UNIVERSITY OF SOUTHAMPTON

FACULTY OF PHYSICAL AND APPLIED SCIENCES

OPTOELECTRONICS RESEARCH CENTRE

High Performance Pulsed Fiber Laser Systems for Scientific & Industrial Applications.

by

Peh Siong TEH

Thesis for the degree of Doctor of Philosophy

March 2015

UNIVERSITY OF SOUTHAMPTON

ABSTRACT

FACULTY OF ENGINEERING AND APPLIED SCIENCE

OPTOELECTRONICS RESEARCH CENTRE

Doctor of Philosophy

HIGH PERFORMANCE PULSED FIBER LASER SYSTEMS FOR SCIENTIFIC & INDUSTRIAL APPLICATIONS

By Peh Siong TEH

This thesis reports an investigation of the power scaling of pulsed fiber laser systems towards the hundreds of Watts regime whilst keeping the impact of fiber nonlinearities such as Stimulated Raman Scattering (SRS) at a manageable level. Two regimes of pulsed operation are investigated: the nanosecond pulse regime and the picosecond pulse regime. Some of the work reported in this thesis was carried out in collaboration with SPI Lasers and Institute for Manufacturing, University of Cambridge under the TSB funded SMART LASER programme.

In the nanosecond regime, two kinds of MOPA configurations are investigated. In the first instance a high accuracy active pulse shaping technique is implemented. Using the combination of a fast electrical Arbitrary Waveform Generator (AWG) and an Electro-Optic Modulator (EOM), optical pulses can be shaped into various custom defined pulse shapes with high temporal resolution feature definition, allowing faster pulse rise and fall times than previously possible. This MOPA has the capability to generate a maximum average output power of ~70 W, pulse energy close to 1 mJ, all within a diffraction limited output beam. The second instance a fully-fiberized system capable of producing up to 45 W of average output power with a pulse energy of ~1 mJ was developed in collaboration with SPI Lasers Ltd. Unlike the first system, which uses an EOM for optical pulse shaping, an Acousto-Optic Modulator (AOM) is instead used to pre-shape the leading edge of the optical seed pulse in order to reduce the impact of nonlinear effects caused by the high peak powers otherwise associated with gain-saturation assisted reshaping of long nanosecond square input pulses, providing a cost-effective solution for the SMART Laser system. The successful development of the SMART Laser system allowed SPI Lasers Ltd to introduce a new product line, namely the G4 pulsed fiber laser system. Both types of fiber laser system were used in material processing experiments to investigate their performance and capabilities.

Using a nanosecond fiber MOPA as a pump source, a synchronously pumped, tuneable, Raman fiber laser is demonstrated both in the near infrared (NIR) and visible regions. A continuous tuning range of 28nm in the NIR and 2.8nm in the visible region are achieved with efficiencies in the range of 12% to 18% respectively. The conversion efficiency can be increased further with the use of a feedback signal. Furthermore, with the presence of a feedback signal, the linewidth of the Raman Stokes lines in both visible and NIR regions shows a significant narrowing effect. This technique will allow the generation of wavelengths which are not easily generated with rare-earth doped fiber lasers and will be useful in the fields of spectroscopy, archaeology, biomedical and many more.

Next, optical pulses in the picosecond regime are investigated. A gain-switching technique is used to generate a stable train of picosecond optical pulses from a semiconductor laser diode (SLD). Gain switching of different types of commercially available SLDs shows different temporal and spectral characteristics which are primarily influenced by the design of the specific chip used. The shortest pulse durations achieved through direct gain switching resulted in ~50 ps pulses; however these were far from transform-limited. However, an external FBG seeded gain switched SLDs was shown to be capable of producing transform-limited optical pulses. I show that a mode-locking mechanism is responsible for the short, transform limited optical pulses observed. This is the first demonstration of a mode locked SLD at the 1.06 μm waveband. With this technique, 18 ps optical pulses with pulse energy of 7.2 pJ and peak power of 400 mW were obtained.

The single polarization, stable, picosecond optical pulses were fed into a chain of polarization maintaining fiber amplifiers to investigate the power scaling capability of this system. A maximum average output power of 513 W is demonstrated in a diffraction-limited output beam. The system operated at a repetition frequency of 215 MHz, corresponding to an estimated pulse energy of 2.4 μJ and a peak power of ~ 69 kW. At the maximum operating output power, the OSNR is measured to be well above 26 dB with a polarization extinction ratio (PER) of 17 dB. A pulse energy of 3.23 μJ is achieved from a similar system at a reduced operating frequency of 53 MHz and an average optical power of 200 W, corresponding to a pulse peak power of 107 kW. In both cases, further power scaling is limited by the SRS.. These results represent the highest optical power demonstrated from a fiber MOPA producing tens of picosecond optical pulses.

Contents

ABSTRACT i

List of Tables 2

List of Figures 3

DECLARATION OF AUTHORSHIP 11

Acknowledgements 12

List Of Abbreaviations 13

Chapter 1. Introduction 15

1.1 Motivations 15
1.2 Historical Overview 18
1.3 Thesis Outline 20
1.4 References 21

Chapter 2. Background 23

2.1 Semiconductor Laser Diodes 23
2.2 Ytterbium Doped Fiber Technology 27
2.2.1 Spectroscopy 27
2.2.2 Principles of Optical Fibers 30
2.2.3 Birefringence in fibers 31
2.2.4 Amplification through Pumping Process 32
2.2.5 LMA Double-clad Fibers 38
2.2.6 Master-Oscillator-Power-Amplifier Configuration 39
2.3 Pulse Propagation and Non-linear Effects in Optical Fibers 41
2.3.1 Dispersion in Pulse Propagation 41
2.3.2 Non-linear Effects in Pulse Propagation: Self Phase Modulation 42
2.3.3 Cross Phase Modulation 46
2.3.4 Stimulated Raman Scattering 46
2.3.5 Stimulated Brillouin Scattering 48
2.4 References 50

Chapter 3. Nanosecond Fiber Laser System 53

3.1 Introduction 53
3.1.1 Pulse amplification and gain saturation 54
3.2 Nanosecond Fiber MOPA with Active Pulse Shaping 59
3.2.1 System Setup 61
3.2.2 Custom Optical Pulse Shapes Demonstration with EOM 63
3.3 SMART Fiber Laser System 65

3.3.1 Seed Laser 67
3.3.2 Pre-amplifier Stage 69
Long pulse amplification 69
Short pulse amplification 71
3.3.3 Power Amplifier Stage 73
3.3.4 Active Pulse Shaping with AOM 76
3.3.5 Characterization of Beam Delivery Fiber 78
3.3.6 Overall Performance of SMART fiber laser 80
3.4 Pulse Tailoring Application on Material Processing 81
3.5 Conclusion 85
3.6 References 87
Chapter 4. Raman Fiber Laser in Visible and Near Infrared Regions 89
4.1 Introduction 89
4.2 Selective excitation of multiple Raman stokes wavelengths (green – yellow – red) using shaped multi-step pulses. 93
4.3 Experimental setup for tunable Raman fiber laser 98
4.4 Tunable Raman fiber laser in the visible 100
4.4.1 Synchronous Pumped Visible Raman Generation 101
4.4.2 Tunability of Synchronously pumped visible Raman laser 103
4.5 Synchronous pumped NIR Raman generation 104
4.6 Discussion 105
4.7 Conclusion 107
4.8 References 108
Chapter 5. Picosecond Pulse Generation Using SLD 111
5.1 Introduction 111
5.2 Gain switching 111
5.3 Demonstration of gain switching technique 113
5.3.1 Gain switched SLD 113
5.3.2 Injection seeding 118
5.4 Active Mode-locking via an inline FBG as external cavity 122
5.4.1 Configuration for Active Mode-locked SLD 123
5.4.2 Performance of mode-locking at various repetition frequencies 124
5.5 Stability of picosecond pulses between direct gain- switching and mode-locking 128
5.6 Chirp measurement with Frequency Resolved Optical Gating (FROG) 133
5.7 Conclusion 137
5.8 References 138
Chapter 6. High Power and High Energy Picosecond Fiber Sources 141
6.1 Introduction 141

6.2 Challenges 143
6.3 Picosecond MOPA configurations 144
6.3.1 Seed Source 145
6.3.2 Amplifier Characterization 146
6.4 Demonstration of High Power Picosecond Fiber MOPA 158
6.4.1 High Average Power Picosecond MOPA 158
6.4.2 Picosecond MOPA with Tunable Repetition Frequency and Diffraction Limited Output 164
6.5 Conclusion 171
6.6 References 173
Chapter 7. Summary and Future Works 177
7.1 Summary 177
7.2 Future works 179
Appendix: List of Publications 181

List of Tables

Table 3.1: Optical pulse width generated from the ns seed diode with various electrical inputs from the Stanford pulse generator at 450 kHz……..67

Table 4.1. Effects of synchronous pumped generation of 3rd Raman Stokes and 5th Raman Stokes in term of linewidth and output peak power……...102

Table 6.1. Measured input and output powers for preamplifier 2 at various repetition frequencies.....151

List of Figures

Figure 2.1. Physical mechanism of gain in a semiconductor laser involving pumping and stimulated emission……..…24

Figure 2.2 Far field patterns for (a) broad area laser and (b) ridge waveguide single mode laser. The illustrations show the influence of optical spatial mode on the far field patterns.....26

Figure 2.3. Typical L-I curve for a semiconductor laser.....26

Figure 2.4. Energy level diagram of Yb3+ consisting of 2 manifolds, the 2F7/2 ground manifold (with 4 Stark levels labeled a, b, c and d) and the 2F5/2 excited manifold (with 3 Stark levels labeled e, f and g).....28

Figure 2.5. Absorption and emission cross section for Yb3+ ions in an germanosilicate glass.....29

Figure 2.6. Light propagation in an optical fiber……..…30

Figure 2.7. Cross section of a high birefringence PM (Panda) fiber with core doped with rare-earth.....32

Figure 2.8. Energy levels diagram involving emission and absorption of photon in a quasi-three-level-Yb-system…….....33

Figure 2.9. Double-clad fiber consists of a rare-earth-doped core surrounded by a much larger and higher-NA inner cladding [16]……..36

.Figure 2.10. Various designs of double-clad fibers. The fiber core is shown in blue, the inner cladding in light gray, and the outer cladding in dark gray. The skew modes are shown in red.[17]……...…….36

Figure 2.11. Free space end pumping configuration for converting low-beam-quality pump light into high beam quality laser output.....37

Figure 2.12. GT Wave multimode fiber coupler schematic with signal port (s) and pump port (p) [19].....37

Figure 2.13. A typical design of double clad LMA fiber with its core doped with rare-earth ions.....39

Figure 2.14. Master oscillator power amplifier (MOPA) configuration. The seed is driven by electronic drivers and the power amplifier consists of a cascaded preamplifier and power amplifier. Delivery fiber and BDO are used for ease of handling and transferring power to the point of application……....….39

.Figure 2.15. Numerical calculation on Gaussian pulse and square pulse and their corresponding spectra due to SPM. The maximum phase shift was set at 4.5 π.....44

Figure 2.16. Numerical calculation showing the effect of temporal pulse shape on spectral broadening due to SPM.....45

Figure 2.17. Raman gain coefficient curve of a silica core single mode fiber. The curve is normalized to 1.0 at 440cm-1. The peak gain for a pump wavelength of 1060nm is 1 x 10-13 m/W and varies with pump wavelength as 1/λp [39].....46

Figure 2.18. Numerical calculation using the coupled equations to illustrate the growth of Raman stokes (1st and 2nd Stokes) as well as the depletion of pump power.....47

Figure 3.1. Optical intensity passing through a short segment of a saturable pulse amplifier.....55

Figure 3.2. The calculated saturation energy for different fiber core radius and 1060 nm operation wavelength. Calculation made with the assumption that Γ_s=1 57

Figure 3.3. The calculated intensity profiles for rectangular shape input pulse (blue) and the output pulses at 10 dB (green) and 30 dB (red) gain respectively.....58

Figure 3.4. Effects of temporal distortion as a result of the gain saturation effect in a fiber amplifier and the mitigation of gain saturation through pre-compensated optical shape.....59

Figure 3.5. Configuration for PM ytterbium-doped fiber MOPA system..... 61

Figure 3.6. Spectrum of PM MOPA with the total output power of 72 W (0.72 mJ).....63

Figure 3.7. Various shapes of the optical pulse at the output of the MOPA measured with a fast photodetector. Insets show the respective electrical pulse shapes generated by the AWG.....64

Figure 3.8. (Top) Schematic of SMART ytterbium-doped fiber laser system and (bottom) the photo of the actual setup……..……66

Figure 3.9: Spectrum of the seed diode for different electrical pulse width……67

Figure 3.10: (a) Division of optical pulse into sections for spectrogram measurement. Spectrogram obtained for (b) 20ns, (c) 40ns and (d) 60ns electrical pulse width……68

Figure 3.11: Pulse shape (100 ns) and spectrum at the input of the pre-amplifier……69

Figure 3.12: Pulse shape and spectrum at the output of the pre-amplifier. The pulse energy was calculated to be 7.3μJ.....70

Figure 3.13: Output power and gain extracted from the pre-amplifier with 100 ns pulse.....70

Figure 3.14: Gain evolution across the output pulse. Fitting was done by using Equation (3. 11).....71

Figure 3.15: Pulse shape (30ns) and spectrum at the output of the seed diode.....71

Figure 3.16: Pulse shape and spectrum at the output of the pre-amplifier. Pulse energy was calculated to be 10 μJ.....72

Figure 3.17: Output power and gain extracted from the pre-amplifier for 30ns pulse……..….72

Figure 3.18: Gain evolution across the output pulse. ……..…73

Figure 3.19: Average output power as a function of pump power. Up to 45W of average power was obtained with a pulse energy of 0.45mJ.....73

Figure 3.20: The evolution of pulse shape and spectra as a function of pump power coupled into the power amplifier.....74

Figure 3.21: Gain evolution G(t) across the output pulse at a pump power of 45W. The estimated saturation energy was 0.1mJ.....74

Figure 3.22: Spectra of backward travelling ASE before and after propagating across the AOM when operating at pump power of 45W.....75

Figure 3.23: Illustration of the function of the AOM in shaping the top of the input signal pulse.....76

Figure 3.24: The input pulse shape into the power amplifier without (left) and with (right) pre-shaping using an AOM.....77

Figure 3.25: Temporal and spectral evolution of the of the optical pulses as a function of pulse energy.....77

Figure 3.26: The output pulse shape (left) measured at an average output power of 15W and the corresponding reflected pulse shape (right) travelling in the backward direction.....78

Figure 3.27: (a) The setup for measuring the SRS threshold at the output of the system and (b) transmission curve of the dichroic mirrors used at AOI of 45˚ and AOI of 60˚.....79

Figure 3.28: The peak power of the signal at 1060nm correspond to the first order Raman threshold for different lengths of beam delivery fiber. The blue squares are the measured values while the red solid line is the best fit calculated from Equation (2.33) with gR = 0.8 x 10-13 m/W.....80

Figure 3.29: The pulse shape of signal and 1st order Raman Stokes as well as the output spectrum obtained for a delivery fiber length of 1m.....80

Figure 3.30. (Top) Unfilled pulse envelopes for (a)50 ns,(b) 60 ns, (c)100 ns and (d)150 ns. (Bottom) The Si material response on unfilled pulses.....82

Figure 3.31. (Top) Energy filled pulse envelopes for (a)50 ns,(b) 60 ns, (c)100 ns and (d)150 ns. (Bottom) The Si material response on energy filled pulses.....83

Figure 3.32. Si material response with tailored pulses having different peaks and tails power levels.....84

Figure 4.1. Simulation result of the cascaded Raman generation of a Gaussian pump pulse…..90

Figure 4.2. Simulation results on the evolution of pump and Raman Stokes components for a perfectly rectangular shape pump pulse.....91

Figure 4.3. Simulation results on the evolution of pump and Raman Stokes components when a rectangular shaped pulse with finite rise and fall time was used.....92

Figure 4.4. Experimental setup of the fiber Raman laser……93

Figure 4.5. (a) 3-step output pulses of MOPA, SHG and Raman lines (inset: initial pulse shape from the EOM); (b) Spectrum of MOPA output; (c) Spectrum of SHG output.....95

Figure 4.6. (a) Spectrum of Raman pulses with simultaneous excitation of green, yellow and red light (inset: picture of the Raman output diffracted by a grating); (b) Overall and separated 3-step output pulses of Raman output.....96

Figure 4.7. (Above) 2-step output pulses of Raman conversion with different pulse energy and separation; (Below) Spectra of the Raman pulses: exciting green and yellow colours simultaneously (inset: picture of the Raman output diffracted by a grating).....97

Figure 4.8. Spectra of the 1st and 4th Raman Stokes with 2-step output pulses in different lengths of Raman gain fiber.....98

Figure 4.9. Experimental setup of the fiber Raman laser synchronously pumped by SHG from a PM MOPA.....99

Figure 4.10. Photo of SPFRL when in operation.....100

Figure 4.11. Spectra of single-pass Raman generation in visible region with a flat-topped rectangular pump pulse and different pump power. Up to 6 orders of Stokes were generated.....100

Figure 4.12. Spectra of 1st Raman Stokes generation with and without feedback. The feedback signal was at 543.1nm. The output peak power obtained was 2.3W.....101

Figure 4.13. Pulse shapes consisting of different components of Raman Stokes orders and residual pump which was spectrally resolved using a bulk grating.....103

Figure 4.14. Spectra of visible tunable Raman laser for (a) 1st Raman Stokes, (b) 3rd Raman Stokes and (c) 5th Raman Stokes.....103

Figure 4.15. Spectra of single-pass Raman generation with a flat-topped rectangular pump pulse and different pump power. Distinct Raman Stokes were generated in a controllable fashion before continuum started to build up as zero dispersion wavelength was within the proximity.....104

Figure 4.16. Spectra of the 4th Raman Stokes with and without feedback signal. The feedback signal was at 1303nm.....105

Figure 4.17. The spectra of wavelength tunability by tuning the feedback signal of 4th Raman Stokes. Up to 28nm of continuous tuning range was achieved.....105

Figure 4.18. Generation of synchronous pumped Raman Stokes when Raman gain medium length was reduced to 25m. The peak power obtained was 400W (1st Raman Stokes) and 590W (2nd Raman Stokes).....106

Figure 5.1. Typical evolution of the photon and carrier density during gain switching cycle in a semiconductor laser diode.....112

Figure 5.2. Experimental configuration for direct gain switching.....113

Figure 5.3. RF amplifier (ZHL-5W) output power at different input signal power for operating frequencies of 1 GHz and 2 GHz. The output power begins to saturate when the input power exceeds -3 dBm.....114

Figure 5.4. Output pulse and spectrum obtained from gain switching an Oclaro SLD.....115

Figure 5.5. Output pulse and spectrum obtained from gain switching of a 3SPhotonics SLD.....115

Figure 5.6. Output pulse and spectrum obtained from gain switching a Qphotonics SLD. The black line spectrum corresponds to a peak-to-peak drive current of 600 mA while the red line corresponds to a peak-to-peak drive current of 300 mA…….....116

Figure 5.7. Numerical calculation for the generation of gain switched optical pulse from SLD with different photon lifetime values.....117

Figure 5.8. Numerical calculation of gain spectra when the carrier density is varied from 1.25 x 1024 m-3 to 1.6 x 1024 m-3.....118

Figure 5.9. Experimental configuration for gain switching with external seeding.....119

Figure 5.10. Output pulses and spectra obtained from external injection seeded gain switched Oclaro SLD at different seeding power……..120

Figure 5.11. Output pulses and spectra obtained from external injection seeded gain switched Qphotonics SLD at different seeding power.....120

Figure 5.12. Output pulses and spectra obtained from a 3SPhotonics SLD when external seeding is applied at different power levels…….……...….121

Figure 5.13. Picosecond pulse generation through active mode-locking with FBG as external cavity…….……..123

Figure 5.14. Spectral profiles of the gain-switched laser diode with (black line) and without (red line) FBG. (Inset) Temporal profiles for the seeded (black line) and unseeded (red line) cases.....124

Figure 5.15. Optical pulse width measured at different repetition frequencies and (color) the corresponding optical pulse shapes……..…125

Figure 5.16. Optical spectra measured for a range of injection current modulation frequencies showing the observed wavelength shift with respect to the central wavelength of the FBG...126

Figure 5.17. Snap shot of the pulse stability with infinite persistence mode when (left) stable mode-locking was achieved while (right) a jittery pulse is observed and locking is no longer stable.....127

Figure 5.18. Interference patterns between the 1st and the 10th optical pulses for two different operating frequencies corresponding to different operating regimes. The separation between peaks corresponds to the temporal separation between the two interfering optical pulses.....128

Figure 5.19. Power spectra of the optical pulse in the frequency domain for (a) direct gain switching and (b) mode locked operations.....129

Figure 5.20. Power ratio plots in frequency domain as a function of frequency harmonics for mode locked and gain switched optical pulses.....132

Figure 5.21. High resolution power spectra measurement for the mode locked optical pulses at (a) fundamental frequency, (b) 3rd harmonics, (c) 7th harmonics and (d) 15th harmonics.....133

Figure 5.22. Experimental setup for FROG measurement via the use of EOM…….....134

Figure 5.23. (Above) Spectrogram measured directly with FROG measurement setup and (below) spectrogram retrieved via deconvolution process.....135

Figure 5.24. (a) The scanned and retrieved spectrogram of the optical pulses from Qphotonics diode and (b) the reconstructed intensity, spectrum and phase profiles.....136

Figure 5.25. (a) The scanned and retrieved spectrogram of the optical output from Oclaro diode and (b) the reconstructed intensity profile and frequency chirp across the optical pulse.....136

Figure 6.1. (Top) Fully fiberized picosecond seed laser based YDFA MOPA system incorporating 4 amplifier stages. (Bottom) Actual photo of the MOPA setup…….....…….....…..145

Figure 6.2. Impulse response of the photodetector measured through the injection of a short 7ps optical pulses……..146

Figure 6.3. Temporal pulse shape and spectrum measured at a repetition frequency of (a-b) 858 MHz and (c-d) 859 MHz.....146

Figure 6.4. Schematic of a forward core-pumped fiber amplifier…….....147

Figure 6.5. The characterization result of a 975/1040 nm WDM using a white light source....148

Figure 6.6. Output signal spectrum from the core-pumping preamplifier measured with different Yb doped fiber length…….149

Figure 6.7. Output signal spectrum measured with forward pumping and backward pumping configurations at 53 MHz repetition frequency.....150

Figure 6.8. Ratio of signal to ASE power and the amount of backward travelling ASE measured at different output signal power……..150

Figure 6.9. The configuration of a forward cladding-pumping fiber amplifier.....152

Figure 6.10. Isolation curve measured at different wavelength for the high power inline isolator. Red dash line shows the operating wavelength with approximately 33 dB isolation.....153

Figure 6.11. Output spectra measured after the 3rd preamplifier with different lengths of doped fiber.....154

Figure 6.12. Spectrum measured at different repetition frequencies, showing the effect of spectral broadening due to SPM. (OSA resolution: 0.1nm)……..….....155

Figure 6.13. Spectral bandwidth measured at -10dB level at different repetition frequencies and output powers.....156

Figure 6.14. (a) Total pump power measured at different injected current and (b) the corresponding pump spectra.....157

Figure 6.15. Output spectrum measured with different input pulse duration (28 ps and 35 ps).....159

Figure 6.16. Average signal output power vs. launched pump power of the power stage amplifier…….....160

Figure 6.17.(a) Spectra measured at various output powers at a resolution setting of 1.0 nm and (b) optical pulse width measured directly with a fast photodetector.....161

Figure 6.18. (a) Measured spectral linewidth as a function of output signal power and (b) broadening in signal linewidth as a result of SPM. In all cases, OSA resolution was set at 0.1 nm……...…...162

Figure 6.19. (Top) Output beams captured with a CCD camera at various output power levels and (Bottom) M2 measurement curve at 200W output power.....163

Figure 6.20. Fully fiberized picosecond seed laser based MOPA with tunable repetition frequency.....164

Figure 6.21. Pulse shape of the seed (black line) and output (red dash line) of the third preamplifier, when operating at a repetition frequency of 214 MHz.....165

Figure 6.22. Output spectra after various amplification stages.....165

Figure 6.23. Average signal output power vs. launched pump power of the power stage amplifier.....167

Figure 6.24. Spectra measured at various repetition frequencies at an average output power of 200 W and an input signal power of 2.6 W. Note that the average output power at 53 MHz was 108 W……..…...167

Figure 6.25. The spectral profiles after the third preamplifier stage (solid lines) as well as the output of the MOPA at 113 W and 171 W of average powers for 1.4 W of input signal power……..169

Figure 6.26. Evidence of pulse width broadening at the highest operating peak power…...…169

Figure 6.27. Signal linewidth measured at different signal output powers across all repetition frequencies.....170

Figure 6.28. SPM effect on signal linewidth at various output average powers with repetition frequency of 53 MHz 171

DECLARATION OF AUTHORSHIP

I, PEH SIONG TEH declare that the thesis entitled

HIGH PERFORMANCE PULSED FIBER LASER SYSTEMS FOR SCIENTIFIC & INDUSTRIAL APPLICATIONS

and the work presented in it are my own. I confirm that:

- this work was done wholly or mainly while in candidature for a research degree at this University;
- where any part of this thesis has previously been submitted for a degree or any other qualification at this University or any other institution, this has been clearly stated;
- where I have consulted the published work of others, this is always clearly attributed;
- where I have quoted from the work of others, the source is always given. With the exception of such quotations, this thesis is entirely my own work;
- I have acknowledged all main sources of help;
- where the thesis is based on work done by myself jointly with others, I have made clear exactly what was done by others and what I have contributed myself;
- Parts of this work have been published (see list of publications).

Signed: PEH SIONG TEH

Date: March 2015

Acknowledgements

I would like to express my upmost gratitude to my supervisor, Prof. David Richardson, for taking me onboard his dynamic research group, Short Pulse Fiber Laser group. I am thankful to him for his endless guidance and support throughout this dissertation.

I am particularly thankful to my co-supervisor, Dr Shaif-ul Alam for his advice and assistance in keeping my progress on track. I am grateful that he helps me to adapt to the new research environment and always be there to provide valuable suggestions which help me to achieve the research goal.

I am fortunate to work among the dedicated group members that are always helpful and supportive. Hereby, I extend my thanks in particularly to Dr Jonathan Price, Dr Martin Bennedt, and Dr Alexander Heidt for their useful advices and contributions. I wish to acknowledge Dr Richard Lewis for his efforts of helping me to setup the high power pulsed laser system. I would like to offer my thanks to Dr Ee Leong Lim for being a supportive senior and his generosity in sharing the optical equipments.

My special thanks are extended to Dr Yongmin Jung and Dr Zhihong Li, for being such good companions and good friends. I really enjoyed our daily discussions on almost everything and of course our regular breaks.

In addition, a thank you to Dr Dejiao Lin for his directly and indirectly help throughout these 4 years. I would like to thank Dr Christophe Codemard and Dr Philip Gorman for their generous insights and sharing. I have to thank Dr Morten Ibsen for his valuable opinions about the fiber Bragg grating.

I am thankful to the Government of Malaysia and Public Service Department for providing me with scholarship for my PhD study.

Most importantly, not of this could have happen without my wife, Tze Wern Yeap who offered her unconditional support and I will forever indebted to her for the sacrifices she made for the past 4 years.

Last but not least, I would like to thank all my family members for providing moral and financial supports during my PhD journey.

List Of Abbreaviations

AOM	Acousto Optic Modulator
ASE	Amplified Spontaneous Emission
AWG	Arbitrary Waveform Generator
BDO	Beam Delivery Optic
CCD	Charge-Coupled Device
CFBG	Chirped Fiber Bragg Grating
CW	Continuous Wave
DC	Direct Current
DCA	Digital Communication Analyzer
DCF	Double Clad Fiber
DFB	Distributed Feedback
DPSS	Diode Pumped Solid State
EOM	Electro Optic Modulator
FBG	Fiber Bragg Grating
FROG	Frequency Resolved Optical Gating
FSR	Free Spectral Range
FWHM	Full Width at Half Maximum
FWM	Four Wave Mixing
GS	Gain Switching
GVM	Group Velocity Mismatch
HWP	Half Wave Plate
ICMF	Injection Current Modulation Frequency
LBO	Lithium Triborate
LIBS	Laser Induced Breakdown Spectroscopy
LIFT	Laser Induced Forward Transfer
LMA	Large Mode Area
MBE	Molecular Beam Epitaxy
MFD	Mode Field Diameter
MOCVD	Metal Organic Chemical Vapour Deposition

MOPA	Master Oscillator Power Amplifier
NA	Numerical Aperture
NIR	Near Infrared
OPO	Optical Parametric Oscillator
OSA	Optical Spectrum Analyzer
OSNR	Optical Signal to Noise Ratio
PBS	Polarization Beam Splitter
PCB	Printed Circuit Board
PCF	Photonic Crystal Fiber
PER	Polarization Extinction Ratio
PM	Polarization Maintaining
RE	Rare Earth
RF	Radio Frequency
RMS	Root Mean Square
SC	Supercontinuum
SBS	Stimulated Brillouin Scattering
SHG	Second Harmonic Generation
SLD	Semiconductor Laser Diode
SMSR	Side Mode Suppression Ratio
SPFRL	Synchronous Pumped Fiber Raman Laser
SPM	Self Phase Modulation
SRS	Stimulated Raman Scattering
TBP	Time Bandwidth Product
TFB	Tapered Fiber Bundle
VBG	Volume Bragg Grating
VECSEL	Vertical External Cavity Surface Emitting Laser
WDM	Wavelength Division Multiplexer
XPM	Cross Phase Modulation
YDF	Ytterbium Doped Fiber

Chapter 1. Introduction

The development of advanced high power pulsed fiber laser systems has come a long way since the first working laser was demonstrated [1]. In terms of performance, there is still much room for improvement especially in power scaling and the suppression of nonlinear effects. This thesis reports the development of short optical pulse fiber lasers giving relatively high energy, high average powers and high peak powers. The attractive features of the pulsed fiber laser systems will be explored in the context of material processing and frequency conversion.

1.1 Motivations

When the laser was first demonstrated in 1960 scientists had no idea of the potential and benefits that lasers could bring. However, the high brightness of lasers made them attractive for many scientific and industrial applications. Just 25 years later, engineers started to incorporate optical fiber amplifiers in telecommunication systems. This was truly the first step towards the development of high power fiber lasers. It did not take long before the first commercial fiber lasers were launched with average power levels in the range of a few Watts to few tens of Watts and they started to penetrate into the industrial and defence applications, which were so far dominated by solid state, and gas based lasers.

The high power pulsed lasers used in industrial applications are based on solid state laser systems. Ti:Sapphire based mode locked laser system is capable of producing ultrafast pulses and is thus a popular system for most high end applications. However, many of these systems are bulky, expensive and require constant maintenance due to the presence of free space optics. Furthermore, thermal effects are a major issue in all solid state based laser systems that need to be addressed as well. Fiber laser system with superior heat management capabilities, a wide gain bandwidth and above all the ability to maintain beam quality irrespective of the output power provides a solution to many of the problems faced by bulk lasers. Ytterbium-doped fiber lasers can operate both in continuous-wave and pulsed modes. It has an excellent optical-to-optical efficiency which helps in reducing the heat load. Furthermore, high power operation is also made possible as the heat generated within the fiber can be dissipated effectively due to the large surface area to volume ratio of the fiber. Moreover, the system can be housed in a small form factor and thus allows a compact system with comparable performance to that of a bulk solid state system. The total cost of manufacturing and the running costs are far lower than for bulk lasers, making this laser system an attractive alternative for a lot of applications such as welding, marking and cutting of metals and other materials. Further development of fiber based laser systems is still underway to explore the potential for even higher average power, peak

power and pulse energy than have been demonstrated thus far with a diffraction-limited output beam.

The ever increasing demands for high average power, peak power and pulse energy from fiber lasers have brought up a number of practical issues those need to be resolved. In the fiber based pulsed Master-Oscillator-Power-Amplifier (MOPA) system, the leading edge of tens of nanosecond optical pulses are preferentially amplified over the trailing edge due to the gain saturation effect, resulting in distortion of the optical pulse. This often manifests itself as a sharp peak at the leading edge whose peak power is many times higher than that of the trailing edge and the width of the optical pulse becomes narrower than the input one. However, when the output pulse energy is less than or comparable with the saturation energy of the active fiber, then the pulse can be amplified without observing any significant distortion.

Pulses with a high instantaneous power at the leading edge will suffer nonlinear phenomena such as Self Phase Modulation (SPM), Stimulated Raman scattering (SRS) and stimulated Brilliouin scattering (SBS). SPM will broaden the output spectrum due to the induced nonlinear phase shifts but this does not affect the system performance adversely unless the associated spectral broadening is limiting (for frequency conversion). The most important nonlinear effect that adversely affects the performance of a fiber laser is the inelastic scattering due to both SRS and SBS. Both nonlinear effects can reduce the total energy contained in the output pulse. SBS travels in the backward direction and has a relatively lower threshold. This can jeopardize the entire system if a high peak power Stokes due to SBS propagates back towards the seed. In order to suppress the SBS effect, the seed diode needs to operate with a broader linewidth (ideally tens of GHz). In the case of SRS, a high peak power exceeding the Raman threshold will cause energy in signal wavelength to become depleted and the generation of Stokes wavelengths. Thus, for a signal with a broad linewidth, the maximum peak power that the system can sustain solely depends on the Raman threshold. This threshold is proportional to the mode area and inversely proportional to the length of the fiber.

I was principally involved in a Technology Strategy Board (TSB) project known as the SMART laser manufacturing project. This was a joint project with two partners; SPI Lasers (UK) Ltd. and the Institute for Manufacturing (IfM) of the University of Cambridge. The aims of this project were to develop an all-fiber, high power pulse source at 1060 nm capable of generating a pulse energy greater than 1mJ, an average power of more than 60W, a pulse duration from a few nanoseconds to tens of nanosecond and a peak power of up to 20kW. For maximum flexibility, a Master-Oscillator-Power-Amplifier (MOPA) approach was adopted. An acousto-optic modulator (AOM) was used to shape the square input pulse in order to reduce the gain saturation effects in the amplifiers. This provided the control needed for tailoring the required

output pulse without triggering too much of a nonlinear effect. However, as the response of the AOM (10 – 100 ns) is slower as compared to Electro-Optic Modulator (EOM), the pulse shaping was limited to a certain extent and may not be ideal for user defined output pulses (i.e. square) in a relatively high gain system. However, due to the higher power handling capability and lower insertion loss characteristics, an AOM has the potential to reduce the number of amplification stages. The SMART laser system was then used for material processing trials and the performance of the system will be discussed in the thesis.

Another nanosecond fiber MOPA system was also built which was a modification from the previously available nanosecond system in our group. In this system, an EOM was primarily used as the pulse shaping element and offered great flexibility in terms of tailoring the arbitrary waveform, i.e. from a single rectangular pulse to a double or triple step optical pulse. This modification involved replacement of the existing Arbitrary Waveform Generator (AWG) (maximum clock speed of 250 MHz) with a faster AWG with a clock speed of up to ~3 GHz. This gave more control and more accurate optical temporal profiles. Furthermore, the power amplifier stage was redesigned with the use of a shorter but higher doping concentration Yb doped fiber. The existing pump source, which was based on a diode stack, was also replaced with a number of fiber coupled pump diodes with improved pump coupling efficiency. This versatile system was used for not only material processing trials, but also for frequency conversion applications including the selective excitation of individual and multiple Raman Stokes lines.

The other work that will be presented here in this thesis is the generation of picosecond optical pulses using a gain switched semiconductor laser diode. A similar technique was demonstrated by one of our group members in the past. However, the output pulses were found to be highly chirped and pulse compression had to be done using a CFBG in order to compress the optical pulses down from ~100 ps to ~21 ps to achieve transform limited optical pulses. The additional components required for compression not only increased the complexity of this setup, but also added additional optical loss. I was involved in developing a new configuration, which required fewer components, and which was able to generate short, transform limited, picosecond optical pulses directly from the gain switched laser diode. Finally the gain switched laser diode operating at 1040 nm was used to seed a cascaded fiber amplifier system. I achieved ~500 W of output power with maximum a peak power of over 100 kW in a single mode, single polarization beam. This is by far the highest optical power demonstrated for a picosecond fiber laser system to date.

1.2 Historical Overview

The theoretical concept of the laser was first proposed by Albert Einstein in the year 1917 [2], however it took almost 40 years before the first working laser could be realized. In 1960, Theodore Maiman constructed and demonstrated the first working laser using a ruby crystal rod as the gain medium [3]. The laser was pumped with a high power flash lamp, creating sufficient inversion for stimulated lasing to occur, with the laser signal wavelength demonstrated at 694 nm. Not long after that, came the first fiber laser demonstrated by Elias Snitzer in the year 1963 [4]. The fibers were fabricated with a neodymium glass core and lower index glass cladding and were pumped with a flash lamp. The efficiency of these fiber lasers was low due to the limitation in pump power and the quality of the doped fiber rod, however, improvements in the Rare Earth doping technique in the 1980's, sped up fiber laser research [5]. The first Ytterbium doped fiber laser was reported in 1997 [6] and soon after a new pumping technique was introduced to scale up the output power [7].

Ytterbium provides several unique features especially a broad absorption band that stretches from 850nm to beyond 1150nm with a peak at 975nm which is useful for amplification purposes[8]. The efficiency obtained from 975nm cladding pumped ytterbium doped fiber can be better than 80% [9]. The low quantum defect and high efficiency also helps in minimizing the heat load and the realization of very high (kW and beyond) average output power. The main limitation is optical nonlinearity due to the long interaction length and tight confinement of laser light in a fiber [10].

The advancement of fiber laser technology came in tandem with the development of semiconductor laser diodes. When the semiconductor laser was first introduced in 1962, the efficiencies were low and the threshold was relatively high [11]. Moreover, the laser only operated at cryogenic temperatures. The slow progress in semiconductor laser development was mainly limited by the fabrication technology that was still immature. The key technology for the realization of high power lasers was the introduction of semiconductor growth technologies namely metallorganic chemical vapour deposition (MOCVD) and molecular beam epitaxy (MBE) [12]. With these techniques combined with continuous refinement on the material and process technology, semiconductor diodes capable of generating optical output powers in excess of 1 W at room temperature were realised.

With the introduction of the double clad fiber concept and the availability of high power semiconductor diodes as pump lasers, the output power from fiber laser systems has grown exponentially[13]. In the CW regime, up to 10kW of output power has been demonstrated with diffraction limited output [14]. The capability of the kW class fiber laser system allows direct replacement of gas lasers in applications such as metal welding, cutting and drilling.

In the pulsed regime, the demands for laser systems operating from long to ultrashort optical pulses are increasing as a result of increasing applications in the medical, material processing and spectroscopy arenas. Significant developments have been reported recently about the performance of pulsed fiber based laser systems. In the femtosecond regime, close to kilowatt level average output power was demonstrated exploiting the chirped pulse amplification technique [15]. On the other hand, in the picosecond regime, over 300 W of average output power was demonstrated by Dupriez et al with pump power as the only limitation to further power scaling [16]. Furthermore, using spectral combination, up to 1.1kW of average power has been demonstrated for nanosecond pulsed fiber lasers [17]. In the case of pulse energies, up to 27mJ has been demonstrated with a peak power up to 2.7MW in a highly multimode Yb-doped fiber amplifier [18]. For diffraction limited output, up to 2mJ of pulse energy has been achieved from a Q-switched fiber laser [19].

In order to reduce the nonlinear effects in high power fiber lasers, Large-Mode-Area (LMA) fibers are used [20]. The large core diameters associated with these fibers allow the mitigation of the detrimental nonlinear effects; raising the Raman threshold up to the hundreds of kilowatts range [21]. However, the downside of the LMA fibers is that they are inherently multi-moded. Various techniques have been introduced to produce clean single mode output from these LMA fibers including fiber coiling technique [22] and tapered fibers [23] that induce higher losses for higher order modes.

Apart from nonlinear effects, the evolution in pulse shape is a significant limiting factor in high energy pulsed laser systems due to the modest saturation energies associated with the confined optical mode within the fiber. This results in pulse distortion within the amplifier chain. Adaptive pulse shaping techniques were introduced to mitigate this limitation with the use of an EOM [24]. This also provides the flexibility to generate arbitrary shaped output pulses as well as controlling the peak power to lie below the Raman threshold.

The ability to scale up the output power from fiber lasers along with the control of the pulse shape, pulse energy, pulse repetition frequency and the operating wavelengths leading to rapid penetration of fiber systems into applications such as drilling, cutting and welding, all of which were previously dominated by other lasers.

1.3 Thesis Outline

The thesis is structured as follows.

Chapter 2 introduces semiconductor and ytterbium doped fiber technologies. The fundamental laser physics is discussed extensively. This includes fiber amplifier design and the constraints imparted due to various nonlinearities.

Chapter 3 discusses the development of a flexible nanosecond fiber MOPA for the SMART project as well as results on the Si processing trials.

Chapter 4 demonstrates the wavelength conversion technique based on controllable Raman Stokes generation. Using a nanosecond fiber MOPA with an EOM as a pulse shaping element and LBO as a frequency doubler, a tunable Raman fiber laser in the visible region is demonstrated.

Chapter 5 describes picosecond pulse generation by means of gain switching and mode locking techniques of semiconductor laser diodes. The physical aspects of SLD and the characteristics of the generated pulses are discussed here.

Chapter 6 demonstrates both high average power and high peak power picosecond MOPA systems using the seed laser discussed in the previous chapter. The results include the highest average power demonstrated to date from an all fiber picosecond MOPA system.

Chapter 7 concludes with a summary of the work in this thesis and discusses possible future research.

1.4 References

1. T. H. Maiman, "Optical and Microwave-Optical Experiments in Ruby," Physical Review Letters **4**, 564-566 (1960).
2. A. Einstein, "On the quantum theory of radiation," Phys. Z (1917).
3. T. H. Mainman, "Stimulated optical radiation in ruby," Nature 187 (1960).
4. E. Snitzer, "Optical maser action in Nd3+ in a Barium crown glass," Phys. Rev. Lett. 7 (12), 444 (1961).
5. L. R. R.J. Mears, I.M. Juancey, D.N.Payne, "Low noise Erbium doped fiber amplifier operating at 1.54um," Electronics Letters, Vol.23, No.19, 1026-1028 (1987).
6. J. N. R.Paschotta, A.C.Tropper, D.C.Hanna, "Ytterbium doped fiber amplifiers," IEEE Journal of Quantum Electronics, 33(7), pp. 1049 - 1056 (1997).
7. R. J. C. H.M.Pask, D.C.Hanna, A.C.Tropper, C.J.Mackechnie, P.R.Barber, J.M.Dawes, "Ytterbium doped silica fiber lasers: Versatile sources for 1 - 1.2um region," IEEE Journal of Selected Topics in Quantum Electronics, Vol.1 No.1 (1995).
8. R. J. C. H.M. Pask, D.C. Hanna, A.C. Tropper, C.J.Mackechnie, P.R. Barber and J.D. Dawes, "Ytterbium doped silica fibers: Versatile sources for the 1 - 1.2 um region," IEEE Journal of selected topics in Quantum Electronics Vol.1 No.1 (1995).
9. A. M. K.T.Vu, D.J.Richardson, L.M.B.Hickey, M.N.Zervas, "Adaptive pulse shape control in a diode seeded nanosecond fiber MOPA system," Opt. Express, Vol.14, pp. 10996-11001 (2006).
10. G. Agrawal, *Nonlinear Fiber Optics (3rd Edition)* (Academic Press, 2001).
11. D. F. Welch, "A brief history of high-power semiconductor lasers," Selected Topics in Quantum Electronics, IEEE Journal of **6**, 1470-1477 (2000).
12. C. R. Abernathy, "Growth of III–V materials by metalorganic molecular-beam epitaxy," Journal of Vacuum Science & Technology A **11**, 869-875 (1993).
13. L. Zenteno, "High-power double-clad fiber lasers," Lightwave Technology, Journal of **11**, 1435-1446 (1993).
14. E.Stiles, "New development in IPG fiber laser technology," (2009).
15. S. H. T.Eidam, E.Seise, T.V.Andersen, T.Gabler, C.Wirth, T.Schreiber, J.Limpert and A.Tunnermann, "Femtosecond fiber CPA system emitting 830W average output power," (2010).
16. P. Dupriez, A. Piper, A. Malinowski, J. K. Sahu, M. Ibsen, B. C. Thomsen, Y. Jeong, L. M. B. Hickey, M. N. Zervas, J. Nilsson, and D. J. Richardson, "High average power, high repetition rate, picosecond pulsed fiber master oscillator power amplifier source seeded by a gain-switched laser diode at 1060 nm," Photonics Technology Letters, IEEE **18**, 1013-1015 (2006).

17. C. W. O. Schmidt, I. Tsybin, T. Schreiber, R. Eberhardt, J. Limpert, and A. Tünnermann, "Average power of 1.1kW from spectrally combined, fiber amplified, nanosecond pulsed source," **Vol.34** (2009).
18. Y.-C. C. Ming-Yuan Cheng, Almantas Galvanauskas, Pri Mamidipudi, Rupak Changkakoti, and Peter Gatchell, "High-energy and high-peak-power nanosecond pulse generation with beam quality control in 200-um core highly multimode Yb-doped fiber amplifiers," **Vol.30** (2005).
19. J. R. O. Schmidt, F. Röser, S. Linke, T. Schreiber, K. Rademaker, J. Limpert, S. Ermeneux, P. Yvernault, F. Salin, and A. Tünnermann, "Millijoule pulse energy Q-switched short-length fiber laser," **Vol.32** (2007).
20. N. D.-R. J. Limpert, I. Manek-Hönninger, F. Salin, F. Röser, A. Liem, T. Schreiber, S. Nolte, H.Zellmer, A. Tünnermann, J. Broeng, A. Petersson, and C. Jakobsen, "High-power rod-type photonic crystal fiber laser," **13** (2005).
21. J. L. C. Jauregui, and A. Tünnermann, "Derivation of Raman treshold formulas for CW double-clad fiber amplifiers," **17** (2009).
22. L. G. P.Koplow, R.P.Moeller, D.A.V.Kliner, "Single mode operation of a coiled multimode fiber amplifier," Optics Letter, Vol.25, pp.442 (2000).
23. A. B. G. J.A.Alvarez-Chavez, J.Nilsson, P.W.Turner, W.A.Clarkson, "Mode selection in high power cladding pumped fiber lasers with tapered sections," in *Conference of Lasers and Electro-Optics (CLEO)* (Washington D.C USA, 1999).
24. K. T. Vu. Andrew Malinowski, Kang Kang Chen, Johan Nilsson, Yoonchan Jeong, Shaiful Alam, Dejiao Lin and David J. Richardson, "High power pulsed fiber MOPA system incorporating electro-optic modulator based adaptive pulse shaping," **17** (2009).

Chapter 2. Background

Since semiconductor based laser diodes and Yb-doped fiber amplifiers are widely used in this thesis, a brief overview of the fundamental science associated with their operation is described in this chapter. It begins with a discussion of the main properties of semiconductor laser diodes followed by the background of ytterbium ion in silica fiber. Next, the physical properties of optical fiber and the technology involved in the development of high power fiber lasers and amplifiers are described. Various pumping techniques commonly used in fiber amplifiers are reviewed as well. The final section describes the impacts of dispersion and nonlinear effects on pulse propagation along the optical fibers. Commonly encountered nonlinear effects in optical fiber such as SPM, XPM, SRS and SBS will be discussed.

2.1 Semiconductor Laser Diodes

Semiconductor lasers, or diode lasers as they are commonly known, are by far the most unique and important piece of technology for laser development. Besides being used in various applications, ranging from compact disc players to laser printers, semiconductor lasers are heavily used in telecommunications systems mainly as signal sources for the transmitter end and pump sources for the fiber amplifiers.

The semiconductor lasers consist of an active medium sandwiched together by n type and p type semiconductors [1, 2]. Most of the semiconductor laser materials are based on the elements from the third group of the periodic table (Al, Ga, In) and elements from the fifth group (N, P, As, Sb). The n type material mainly comes from the fifth group which has a free electron while the p type comes from the third group which has an empty hole. Laser action occurs at the junction between the n and p doped materials when the electrons and holes combine. The CW lasing wavelength of these III-V materials generally ranges between 600 nm to 1600 nm. However, not all the materials are suitable to be used for semiconductor lasers. Most of the semiconductor lasers are made of GaAs and related materials as the recombination process releases energy in the form of a photon instead of just in the form of heat.

The gain in semiconductor lasers is provided by the recombination of holes and electrons which result in the generation of optical radiation. The wavelength of the generated optical radiation is determined by the energy band-gap of the semiconductor materials used [3]. Three key processes are involved in laser action, namely photon absorption, spontaneous emission and stimulated emission. The illustrations of the key processes are shown in the simple two-energy-level diagrams in Figure 2.1 where E_1 is the ground-state energy and E_2 is the excited-state energy.

i. Absorption: A single electron in the valence band can be excited to the conduction band by absorbing a photon of energy $h\nu$ so that $E_2 - E_1 = h\nu$, where E_1 and E_2 represent the energy states of electrons in the valence and conduction bands respectively. However, if the photon energy is lower than the energy difference between the two bands, electron excitation to conduction band will not occur.

ii. Spontaneous emission: An electron in the conduction band can make a downward transition in energy to recombine with the hole in valence band. This spontaneous effect will emit a photon with an energy equivalent the energy difference between the two bands.

iii. Stimulated emission: An electron in the conduction band can be induced to make a downward transition to the valence band by the presence of a photon of equivalent band-gap energy. This stimulated process generates new photons, which are coherent with the inducing photons.

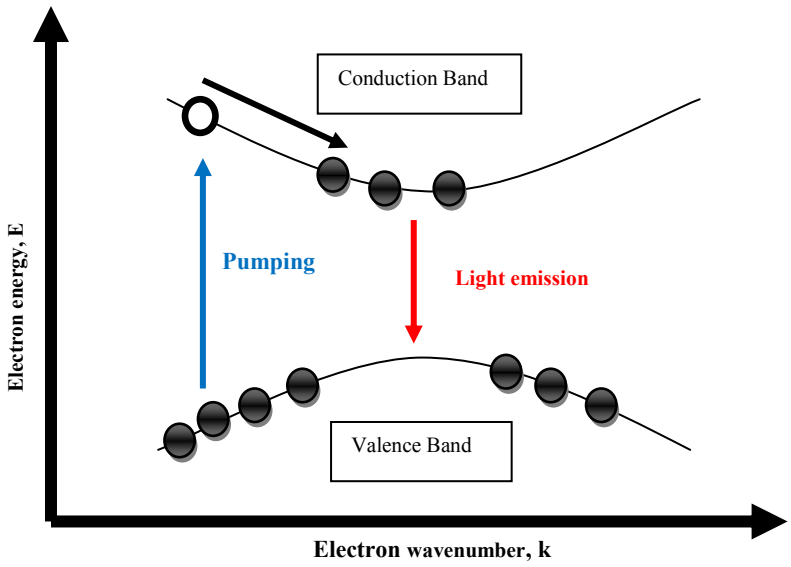

Figure 2.1. Physical mechanism of gain in a semiconductor laser involving pumping and stimulated emission

When the semiconductor laser is in thermal equilibrium, the number of electrons in the valence band is greater than in the conduction band. As a result most of the incident photons will be absorbed reducing the possibility of a stimulated emission process. In order to achieve effective optical gain, the number of electrons in the conduction band has to be greater than in the valence band. This condition is known as population inversion and when this is achieved, stimulated emission will exceed the absorption process. Since population inversion is only achieved when the conduction band is densely filled with electrons, external electrical pumping is required to provide energy to the electrons in the valence band for effectively upward transition. The

pumping process in semiconductor laser is usually done electrically, i.e. forward biasing the p-n junction.

Optical gain via a pumping process alone is not enough for lasing. Optical feedback is required for laser action and this can be achieved by the polished end facets at both ends of the active medium. This effectively creates a Fabry-Perot cavity which has two main roles. First, it dictates the preferred direction for stimulated emission and second, it defines the longitudinal cavity modes [4]. This cavity will create standing waves for a discrete number of frequencies which defines the longitudinal cavity modes. The frequency mode spacing $\Delta\nu_L$ can be determined by the following relationship,

$$\Delta\nu_L = \frac{c}{2nL} \qquad 2.1$$

where c is the speed of light in vacuum, L is the length of active medium and n is the refractive index of the active medium.

The active medium length L will affect the distance between the two modes. For a longer cavity, the longitudinal modes will become very close to each other and a large number of modes will present within the emission band. This is not preferred in data transmission applications because of the potential for enhanced pulse dispersion during propagation along the fiber. Shorter cavity lengths enable an increase in the mode spacing and a fewer number of longitudinal modes within the emission band as long as the total cavity loss can be made low.

Besides the longitudinal modes, which is related to the wavelengths in the cavity, there are spatial modes that represents the standing wave pattern in the cavity transverse to the propagation direction. The mode shape in the device will influence the far field pattern. As the light that is emitted from the output facet gets diffracted as soon as it leaves the facet, a diverging beam in the far field will be created, with both diverging angles in the vertical direction (perpendicular to the plane of the junction) and the horizontal direction (in the plane of the junction) to be different. Figure 2.2 illustrates the dependence of far field on optical mode. In a broad area laser, a number of spatial modes are generated and the higher order transverse modes will have a wider spatial spread as compared with a ridge waveguide single mode laser. The far field pattern in a ridge waveguide is more circular with smaller divergence angle as compared to the broad area device. Coupling of laser light into an optical fiber will be more efficient with the ridge waveguide single mode laser and this is useful for lasers used in the communication.

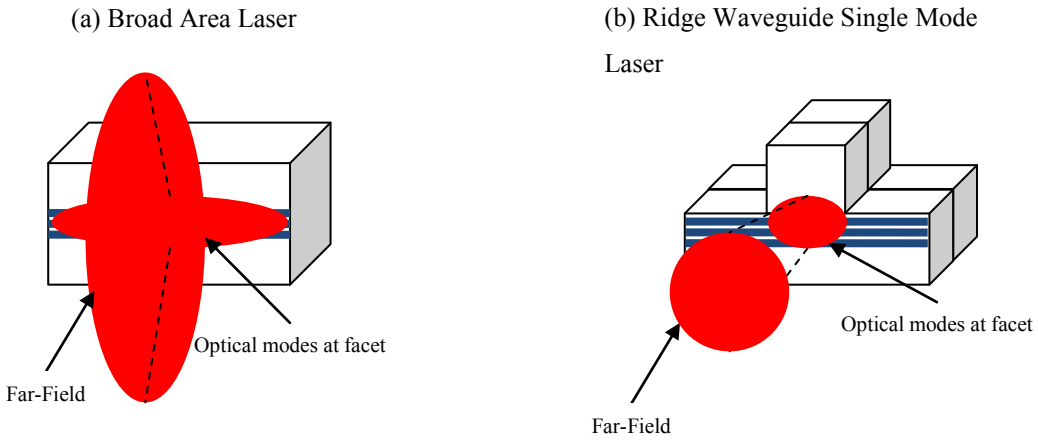

Figure 2.2 Far field patterns for (a) broad area laser and (b) ridge waveguide single mode laser. The illustrations show the influence of optical spatial mode on the far field patterns.

Temperature in the semiconductor laser is an important parameter and needs to be addressed as well. This is to avoid any catastrophic damage that might occur to the diode due to excessive heating. Catastrophic damage is related to the high temperature since the propagation and creation rates of defects are dependent on temperature [5]. Even though the laser is operated below the temperature where damage can occur, the lifetime can still be affected. Apart from damage, temperature is still an important parameter since most of the laser diode characteristics depend on it. These characteristics include power, efficiency, effective intra-cavity refractive index, frequency, spatial modes and gain of the diode. Fluctuation in the temperature will cause a drift in frequency and the occurrence of mode hopping where the longitudinal modes shift during operation. This is because the gain peak continuously drifts towards the lower energy end of the spectrum with increasing temperature and when the diode is operating on a single longitudinal mode, it will shift to the next cavity mode which is closer to the new gain peak resulting in a new output wavelength. (Wavelength shift approximately 0.06nm/˚C).

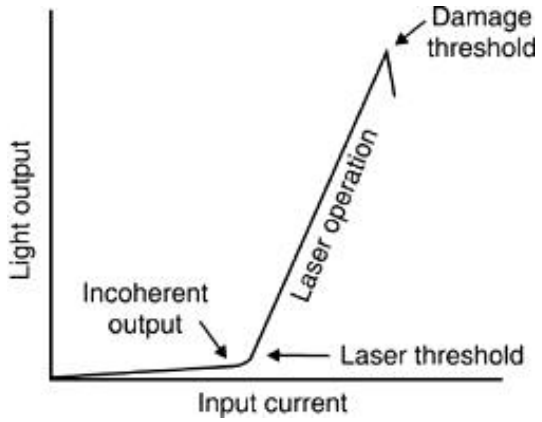

Figure 2.3. Typical L-I curve for a semiconductor laser.

The laser diode output power depends on the injected current. Before reaching threshold, most of the radiation will be from spontaneous emission and the output power is typically very low. Above threshold, the output power increases rapidly and a typical L-I curve (Light-Current) is shown in Figure 2.3. An increase in current will also lead to heating causing a change in the effective cavity refractive index and a corresponding shift in the lasing wavelength.

Another limitation of the semiconductor laser is that it is sensitive to external perturbations due to the low reflectivity of the facets. Although a low reflectivity (~30%) at the cleaved facet is sufficient for maintaining lasing operation, any optical feedback can influence the laser diode characteristics. However, this limitation can be useful when wavelength locking is required. Injection locking with an external laser or from a FBG has been demonstrated and can successfully lock this diode output at a desired lasing wavelength [6]. Furthermore, the locking can be made to just a single longitudinal mode or several modes, depending entirely on the bandwidth of the injected spectrum and the frequency of the mode spacing. Injection locking can enhance the side-mode suppression ratio of the laser diode i.e. the ratio of the power in non-lasing modes adjacent to the main laser mode and the power in the main laser mode.

2.2 Ytterbium Doped Fiber Technology

Rare Earth (RE) ions have been widely used in laser applications due to their superior characteristics over other optically active ions; emission and absorption spectra have narrow wavelength ranges and the transitions are insensitive to the host material. Furthermore, they have long lifetimes for metastable states, and high quantum efficiencies. The rare earths are divided into two groups of 14 elements in the periodic table, namely lanthanides and actinides. Elements in the lanthanide series are primarily used for dopants in silica glass host because many of the actinides are lack of stable isotopes. The lanthanides are characterized by filling of the 4f shell and laser transitions occur between various energy levels of the 4f electrons. The trivalent ions provide the most stable oxidation state amongst the lanthanide ions. Ytterbium is an element belonging to the lanthanides group and is by far the most versatile yet important laser ion in a silica based host.

2.2.1 Spectroscopy

Ytterbium is a member of the rare earth group of elements in the periodic table. Yb^{3+} is useful for having a broad absorption band that stretches from ~850nm up to ~1064nm, an emission band extending from ~950nm up to ~1200nm, and the simplicity of the transition levels involve. The broad absorption band allows the choice of a wide range of pump wavelengths. The Yb^{3+} energy level structure consists of 2 manifolds as indicated in Figure 2.1, the $^2\mathbf{F}_{7/2}$ ground

manifold (with 4 Stark levels labelled **a**, **b**, **c** and **d**) and the $^2\mathbf{F}_{5/2}$ excited manifold (with 3 Stark levels labelled **e**, **f** and **g**). The narrow lines at 975nm correspond to the transitions between the Stark levels labelled **a** and **e** in both emission and absorption plots (Figure 2.4). The absorption peak at shorter wavelength (~915nm) corresponds to the transitions from **a** to **f** and **g**. The longer wavelength of the absorption spectrum corresponds to transitions from **b** to **e, f** and **g**. The second peak in the emission spectrum corresponds to transitions from level **e** to **b**, **c** and **d**. The large energy gap (~10,000cm^{-1}) separating the two manifolds prevents any non-radiative decay via multi-phonon emission. Due to the absence of other energy levels, excited state absorption of pump or signal light and concentration quenching via ion-ion transfer processes are not observed in Yb^{3+} [7]. It is this property that makes Yb^{3+} so efficient to operate and makes it such an attractive gain medium.

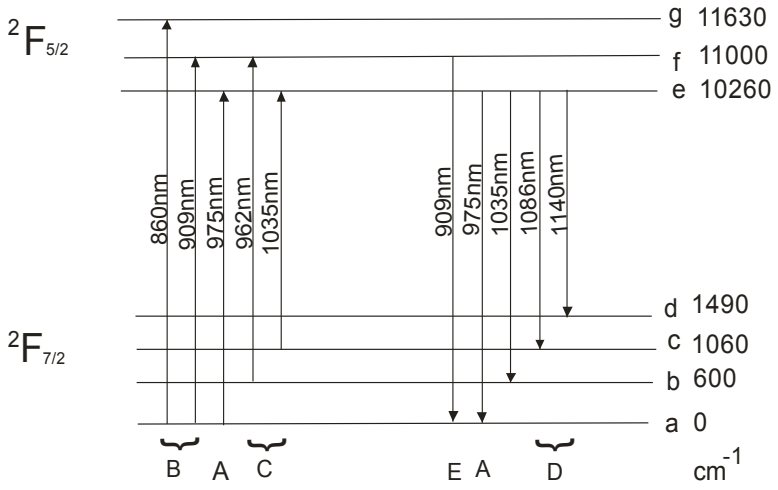

Figure 2.4. Energy level diagram of Yb^{3+} consisting of 2 manifolds, the $^2\mathbf{F}_{7/2}$ ground manifold (with 4 Stark levels labelled **a**, **b**, **c** and **d**) and the $^2\mathbf{F}_{5/2}$ excited manifold (with 3 Stark levels labelled **e**, **f** and **g**).[8]

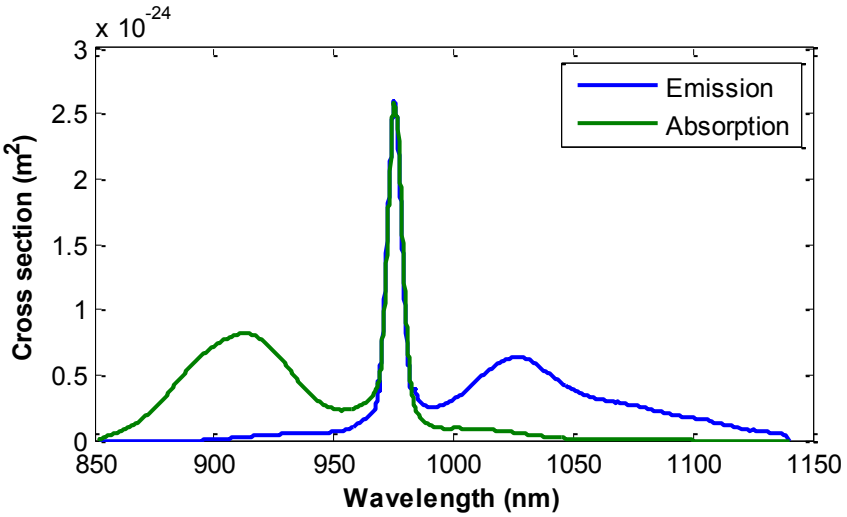

Figure 2.5. Absorption and emission cross section for Yb^{3+} ions in an germanosilicate glass.

The absorption and emission cross section of Yb^{3+} in germanosilicate glass host is shown in Figure 2.5. Both the spectra are normalized to the peak at 975 nm resulting in some degree of discrepancy with the absorption spectrum obtained using the McCumber analysis [9]. The absorption and emission spectra are quite broad. This allows a wide range of possible pump wavelengths (~860 – 1040 nm) and a broad gain bandwidth extending from ~900 - 1130 nm. A broad gain bandwidth is also an attractive feature for amplification of ultrashort pulses. However, there are certain criteria in choosing the pump wavelengths as the signal gain can only be achieved at wavelengths longer than the pump wavelength. Besides, the total doped fiber length will also influence the signal gain and pump absorption as an over length fiber typically results in a signal being reabsorbed due to the nature of the transition levels of Yb^{3+}-ions. Pumping close to the signal wavelength can potentially increase the optical-to-optical efficiency due to the lower quantum defect between pump and signal wavelengths. Finally, the emission wavelength and output power of the pump diodes are important for power scaling in the case of high power fiber lasers and amplifiers.

As for the work reported in this thesis, the operating wavelength for the lasers and amplifiers are set to be at 1040 nm and 1064 nm and therefore the choices of pump wavelengths for direct diode pumping is somewhat limited. I have used 975nm pumping as it allows strong absorption and alters the shortest possible device length which is critical in high peak power applications in order to avoid nonlinear effects. However, pumping at this wavelength reflects a three level behaviour and only 50% population inversion can be created in this scheme. Moreover, as the absorption bandwidth is relatively narrow, the amplifier output will be sensitive to any spectral change of the pump due to the variations of the diode temperature and/or injection current [10]. Up to 97% upper state population can be achieved with 915nm pumping as the active medium behaves like a quasi-four-level System, however a weaker absorption at this pump wavelength

means that a longer length of active fiber will be required to efficiently absorb the pump power resulting in a red shift of the gain peak and a reduction in threshold for fiber nonlinearities..

2.2.2 Principles of Optical Fibers

The unique waveguide structure of an optical fiber allows the electromagnetic (EM) wave to be confined and transmitted along the waveguide. Optical fiber is an example of a dielectric waveguide and usually has a cylindrical shape.

A typical step-index optical fiber usually has the basic structure as shown in Figure 2.6. The whole solid dielectric cylinder is usually made of highly transparent material such as silica. The centre part of the structure is known as the core with a typical diameter of 5-10 μm and has a refractive index of n_1. The core is surrounded by a cladding (typically with a diameter of 125 μm) and has a refractive index n_2 which is less than n_1. Since both regions are based on glass host, refractive indices can be increased or decreased by introducing additional dopants such as Germania (index-raising dopant) and Fluorine (index-lowering dopant). The strength of the entire glass structure is enhanced by a layer of coating which is usually made of a polymer and usually has higher refractive index than silica glass.

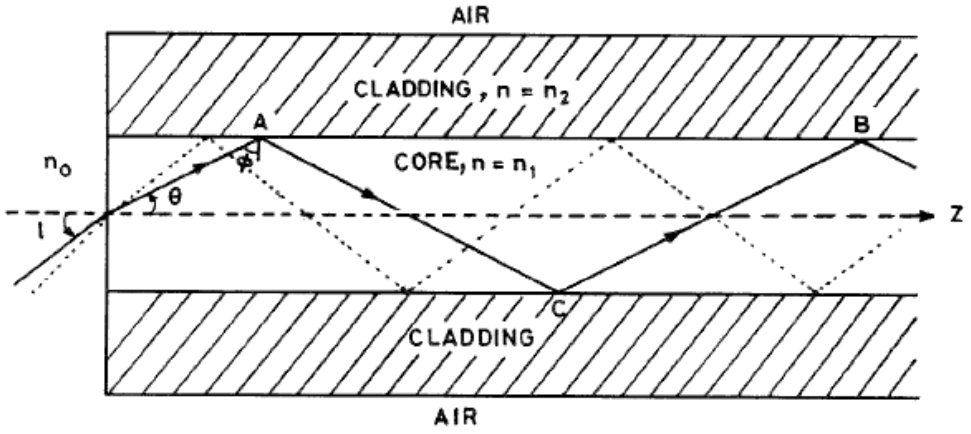

Figure 2.6. Light propagation in an optical fiber [11].

The propagation of EM waves in an optical fiber is governed by total internal reflection between core-cladding boundaries. The conditions required for total internal reflection to occur can be determined through the use of Snell's Law [12]. When a ray enters a fiber (as shown in Figure 2.6), the ray will be able to propagate along the core if the angle of incidence, ϕ at the core-cladding boundary is larger than the critical angle,

$$\phi_c = \sin^{-1}\left(\frac{n_2}{n_1}\right) \qquad 2.2$$

Rays that do not satisfy Equation (2.2) will thus completely leak out after several incident reflections on core-cladding boundaries.

The coupling of light into the fiber is dictated by the angle of incidence at the front facet of the fiber. The allowed incidence angles to ensure total internal reflection can be expressed as a function of the refractive indices of the core and cladding,

$$\phi_a = \sin^{-1}\sqrt{n_1^2 - n_2^2} = \sin^{-1} NA \qquad 2.3$$

The numerical aperture (NA) of a fiber is an important parameter to be considered as it influences the maximum optical coupling into the fiber. As such, a high NA fiber allows a larger amount of light to be efficiently coupled into the fiber.

The combination of fiber core radius, a and NA determine the number of optical modes that can be guided in a fiber,

$$V = \frac{2\pi a}{\lambda} \mathrm{NA} \qquad 2.4$$

where V is the normalized frequency and λ is the signal wavelength. From this relationship, a fiber is considered single-mode when $V \leq 2.405$. If both the core radius and NA of the fiber increases, the fiber will become multimode as it will be able to guide more than one optical mode.

2.2.3 Birefringence in fibers

Birefringence is a phenomenon that occurs in fiber when the light propagation is split into two different paths. This phenomenon occurs as a result of different indices of refraction in the fiber core which is influenced by the polarization direction of light. Ideal optical fiber with a circular core, allows two perpendicularly polarized waves to propagate with both having the same propagation constant. As a consequence, the state of polarization of the waves should remain the same during the propagation. However, this is not the case for real fibers as they typically exhibit variation in the shape of their core along the fiber length meaning the index difference for the two orthogonal modes is different. Furthermore, non-uniform stress due to bending may also occur [13]. Therefore, the two orthogonal modes are coupled to each other due to the changes in fiber birefringence. Hence, the state of polarization will not be preserved in long fiber lengths.

Modal birefringence is usually used to characterize the circular symmetry of a fiber and it is defined as

$$B_m = \left|\overline{n_x} - \overline{n_y}\right| \qquad 2.5$$

where n_x and n_y are the refractive indices for the two polarized waves.

Thus, by increasing the modal birefringence of the fiber, the state of polarization can be maintained. The fiber will not be sensitive towards the changes in polarization states (due to bending or temperature change) as the coupling from one polarization to another will be difficult. The typical birefringence for single mode fiber is ~10^{-6}.

One of the methods that is widely employed to maintain the state of polarization is to use polarization maintaining (PM) fiber. PANDA fibers are the most popular PM fiber type in the industry and are based on strain induced birefringence, a fiber that is extensively used for the experimental work reported in this thesis. The strain birefringence is caused by the presence of stress applying parts (consists of B_2O_3 and $SiO_{2)}$ close to the core, introducing an asymmetric stress [14]. The stress then alters the refractive index of the core. As a result, the modal birefringence of the PANDA fiber is high (typically ~10^{-4}), resulting in large difference in the propagation constants between the two polarized waves. Thus, the coupling of one polarization mode to another will be quite low and polarization states can be maintained along the fibers. PANDA fibers have the advantage compared with other PM fiber types (Bow Tie and elliptical core) because both the fiber core size and numerical aperture are compatible with the standard single mode fiber. These ensure minimum coupling and splice losses between the two types of fibers.

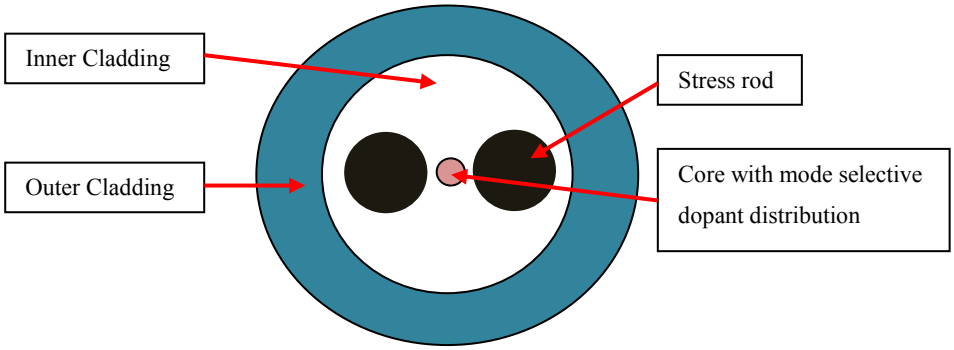

Figure 2.7. Cross section of a high birefringence PM (Panda) fiber with core doped with rare-earth [15].

2.2.4 Amplification through Pumping Process

This section will introduce the current state of fiber optic technology which has the capability of providing pulse amplification with sufficient gain, good beam quality and with low spectral and temporal distortions.

2.2.4.1 Three Level Pumping Scheme

The representation of a quasi-three-level laser is shown in Figure 2.8. In a quasi-three-level Yb system, the lower laser level is a sublevel of the ground state, E_1 and in the upper laser level, E_2, there exist a number of upper state sublevels. Both are separated by a large energy gaps. The total population for the ground state and upper state sub-levels can be represented by N_1 and N_2. In thermal equilibrium, most of the atoms reside in the ground level. Assume that the atoms at the pump level undergo rapid decay to the upper state sub-levels and therefore the population is zero (i.e. $N_3 = 0$).

The interaction between atom and photon can happen in three ways; firstly, a photon can be absorbed when the atom is at the ground level, secondly, when the atom is at the upper level, a photon can be emitted in the presence of another photon and thirdly, an atom emits a photon independently irrespective of the presence of other photons. Absorption process is responsible for the first interaction while stimulated emission governs the second interaction. The third interaction is due to spontaneous emission. All these processes are critical in attenuation and amplification of a signal.

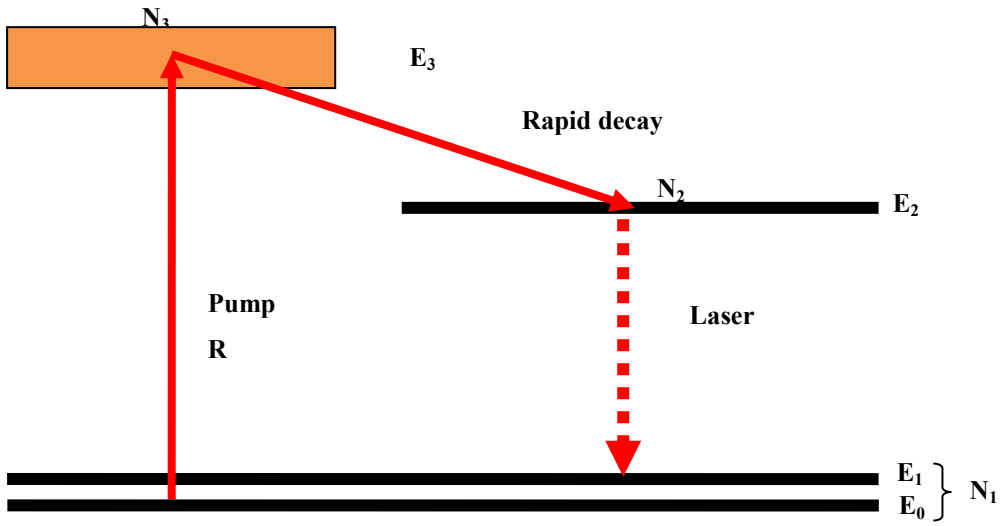

Figure 2.8. Energy levels diagram involving emission and absorption of photon in a quasi-three-level-Yb-system

The absorption and stimulated emission processes are characterized by the probability density

$$W_i = \phi\sigma(v) \qquad 2.6$$

where ϕ is the photon flux density and $\sigma(v)$ is the transition cross section at frequency v. The transition cross section is given by

$$\sigma(v) = \frac{\lambda^2}{8\pi t_{sp}} \mathrm{g}(v) \quad 2.7$$

where $\mathrm{g}(v)$is known as the line shape function and λ is the wavelength. The parameter t_{sp} is the spontaneous emission life time between two energy levels (E_1 and E_2)

The general rate equations are used to represent the quasi-three-level system [16].

$$N_t = N_1 + N_2 \quad 2.8$$

$$\frac{dN_2}{dt} = R - \frac{N_2}{t_2} - (N_2 - N_1)W_i \quad 2.9$$

$$\frac{dN_1}{dt} = -R - \frac{N_1}{t_1} + \frac{N_2}{t_{sp}} + (N_2 - N_1)W_i \quad 2.10$$

Where N_t is the total atomic population in the system; t_2 is the lifetime of the atoms in the upper energy level E_2; t_1 is the lifetime of the atoms in the lower energy level E_1; R is the pumping rate.

Equation (2.9) and (2.10) can be reduced further with $t_1 = \infty$ and $t_2 = t_{sp}$. At steady state, both equations provide similar result:

$$0 = R - \frac{N_2}{t_{sp}} - (N_2 - N_1)W_i \quad 2.11$$

Rearranging Equation (2.8) into

$$N_1 = N_t - N_2 \quad 2.12$$

Substituting Equation (2.12) into Equation (2.11) will result in the following equations:

$$N_1 = \frac{N_t\left(\frac{1}{t_{sp}} + W_i\right) - R}{\frac{1}{t_{sp}} + 2W_i} \quad 2.13$$

$$N_2 = \frac{N_t W_i + R}{\frac{1}{t_{sp}} + 2W_i} \quad 2.14$$

Thus, population inversion is achieved when $\frac{N_2}{N_1} > 1$.

2.2.4.2 Pumping Techniques

The process of exciting the atoms to higher energy level ($F_{7/2}$ to $F_{5/2}$ in ytterbium energy level structure) is known as pumping process. This process is important in optical amplifiers and lasers whereby the pumping process is responsible to achieve population inversion and to generate desired signal light. The number of atoms per second reaching the higher energy level is given by an effective pumping rate,

$$R_p = \eta_p W_p N_0 \quad 2.15$$

where W_pN_0 is the net pumping rate (atoms per second per unit volume) being excited out from the ground level and η_p is the quantum efficiency for pump excitation to the higher energy level. The quantum efficiency usually is quite high and even approaching to unity for many solid state type lasers. There are three types of pumping techniques which are being used throughout this research namely the core-pumped technique, cladding-pumped technique through standard (e.g. free space end pump, fused tapered fiber bundle) and GT wave fiber technology.

In the core-pumped technique, a single mode pump and signal are combined using a wavelength division multiplexer (WDM) with the combined port is spliced to a single mode active fiber. With this technique, the pump and signal overlap with the doped core will be large resulting in a high pump absorption per unit length and a short device length.

In the cladding- pumped technique, multimode pump diodes are coupled into the rare-earth doped double clad fiber (DCF) either via a tapered fiber bundle (TFB) technique or end pumping technique. A double clad fiber (DCF) has a rare-earth doped active core for guiding and amplifying the signal at the centre of the fiber, surrounded by a low-index cladding to guide the pump light. Figure 2.9 shows the typical refractive index profile of a DCF fiber. The single mode signal is guided by the core of the fiber whereas the multimode pump is guided by the low index cladding. Pump absorption is relatively low as the cladding to active core area ratio is quite large resulting in a relatively low overlap of the pump light with the active core. If the DCF has a circular symmetry it can support skew pump modes that do not interact with the core as shown in Figure 2.10. In order to eliminate the skew rays and to improve the absorption of pump light by the active core, the inner cladding of DCF is designed to break the symmetry

through the use of various cladding shapes namely D-shaped, octagonal-shaped and rectangular-shaped. In the work reported in this thesis, an octagonal shaped inner cladding is mainly used.

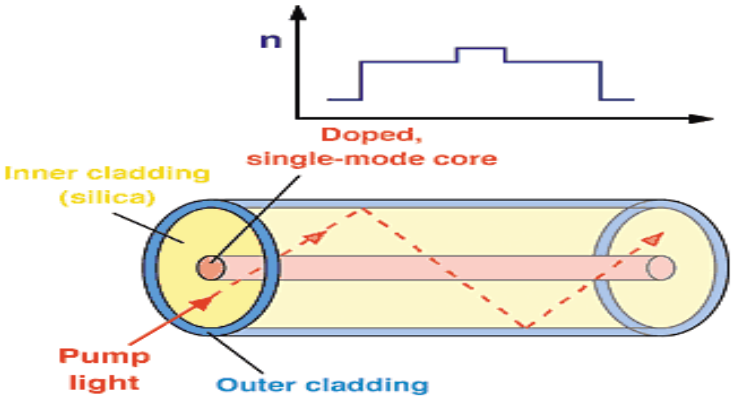

Figure 2.9. Double-clad fiber consists of a rare-earth-doped core surrounded by a much larger and higher-NA inner cladding [17].

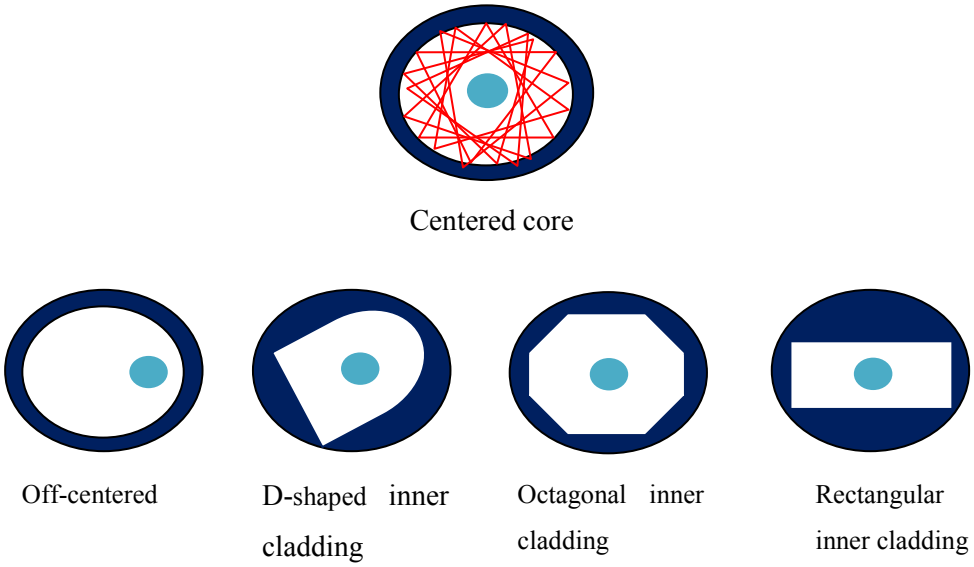

Figure 2.10. Various designs of double-clad fibers. The fiber core is shown in blue, the inner cladding in light gray, and the outer cladding in dark gray. The skew modes are shown in red.[18]

Free-space end-pumping is the simplest method to pump a DCF and is used in most of the experimental work reported here. An illustration of the free space pumping method is shown in Figure 2.11. The pump beam is coupled into the inner cladding using a lens. This method requires good alignment between the launched pump beam and the inner cladding of the fiber and compatible focusing lenses in order to achieve maximum pump launch efficiency. Since the NA of the inner cladding is typically 0.45, directing the pump beam into the fiber cladding will be a relatively easy task given the huge tolerance available for launching the beam. However,

the limitation of this method is that regular adjustment of the launching condition is required to maintain the coupling efficiency.

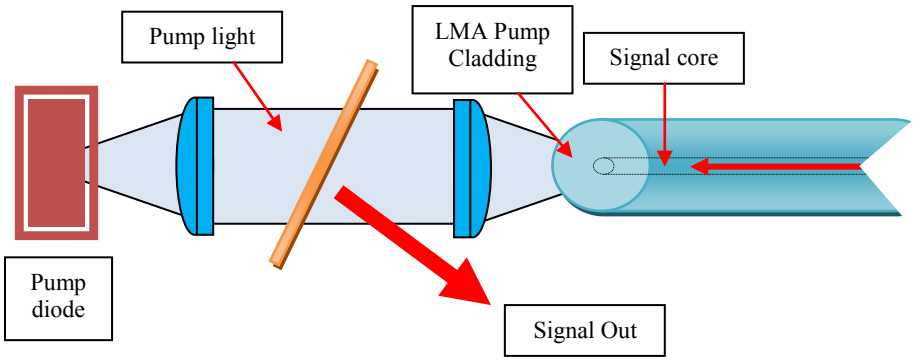

Figure 2.11. Free space end pumping configuration for converting low-beam-quality pump light into high beam quality laser output.

Figure 2.12 shows the GT-wave fiber technology which is invented at the Optoelectronic Research Centre, University of Southampton [19]. In this configuration, a pure silica fiber is held in contact with the doped fiber and encased together in a low refractive index polymer outer cladding. The pure silica fiber acts as the pump ports and the active fiber as the signal port. Pump radiation from the pump fiber *p* transfers into the signal fiber *s* through evanescent field coupling. This technique allows the realization of an all fiber laser system but it comes at a price. Due to the presence of two glass rods in the GT-wave structure, the overlap between the pump radiation and the active core becomes even lower compared to a single glass fiber resulting in a lower pump absorption and longer device length. The long length of fiber required in this scheme compromises the maximum pulse peak power that can be extracted out before the onset of nonlinear effects such as SPM and SRS.

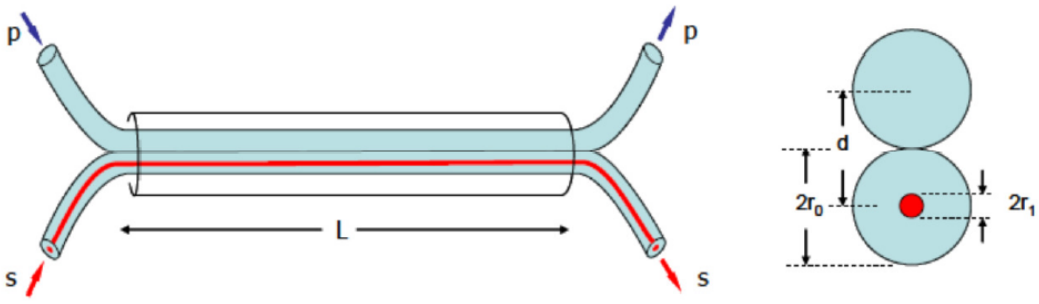

Figure 2.12. GT Wave multimode fiber coupler schematic with signal port (s) and pump port (p) [20].

2.2.5 LMA Double-clad Fibers

Although the growing demand for high power fiber lasers and amplifiers in various applications is increasing rapidly, further power scaling is limited by the onset of nonlinear effects. Even though the silica is not a highly nonlinear material, however, due to the long propagation lengths and the small mode area, the nonlinear effects can still be significant in optical fibers. To circumvent such problems, the peak intensity in the fiber has to be reduced and this can be achieved by increasing the effective mode area, giving rise to an increase in nonlinear thresholds. Therefore, large-mode-area (LMA) fibers are introduced and are widely used in high power fiber lasers for handling high intensity with minimal nonlinear limitations [21].

Initially, LMA fiber design was based on conventional multimode step-index fiber where the core diameter was made large enough to allow an increase of the mode field diameter of the fundamental mode but at the expense of multiple transverse guided modes. As a result the output beam quality was not good as compared to the single mode fiber output because the optical power in the LMA fiber spreads across all the guided modes. In order to obtain better beam quality, a new LMA fiber design was proposed with the core having a low NA [22]. Reduction in NA allows the increase in mode area as the normalized frequency (V number) always satisfies the single-mode condition. However, the LMA fiber with low NA will be sensitive to bending and the lowest NA that can be designed in LMA fiber format is limited to the fabrication process and the bending loss of the fundamental mode [23].

A typical ytterbium doped LMA double cladding fiber is shown in Figure 2.13. This kind of fiber is mainly used in the power amplifier stage where the output consists of high intensity radiation. Both the refractive index profile and the doping distribution of the LMA fiber are tailored for single-mode operation. The core centre consists of a low NA with rare-earth ions selectively distributed across the core x-section to facilitate maximum gain for the fundamental mode and ensuring single mode operation of the fiber laser system. The outer ring with raised index helps to reduce the core bend loss as well as the sensitivity of the mode field diameter to the variation in core size [24].

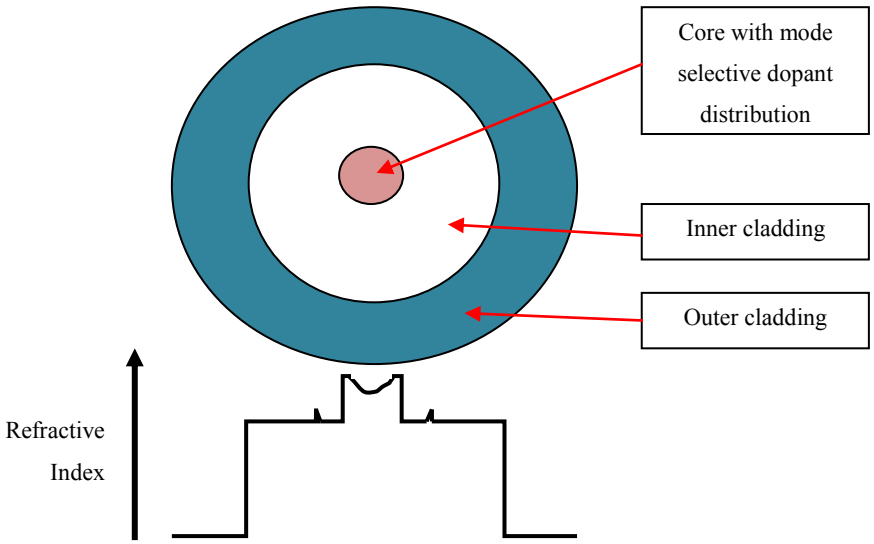

Figure 2.13. A typical design of double clad LMA fiber with its core doped with rare-earth ions.

2.2.6 Master-Oscillator-Power-Amplifier Configuration

In the case of a bulk laser, when the optical power produced by laser oscillator is insufficient for a particular application, an amplifier is usually added in line to the oscillator. Instead of using a higher power oscillator which may result in a low quality output beam and possible severe thermal distortion, the use of an amplifier after the oscillator preserves the spatial, temporal and spectral characteristics of the oscillator. Moreover, the output power can be scaled further with the use of cascaded amplifiers. This configuration is known as a master-oscillator-power-amplifier (MOPA). This configuration has become a catalyst for the development of high power laser systems. In fiber laser systems, MOPA configuration is widely used to enhance the output power without compromising the characteristics of the seed signal.

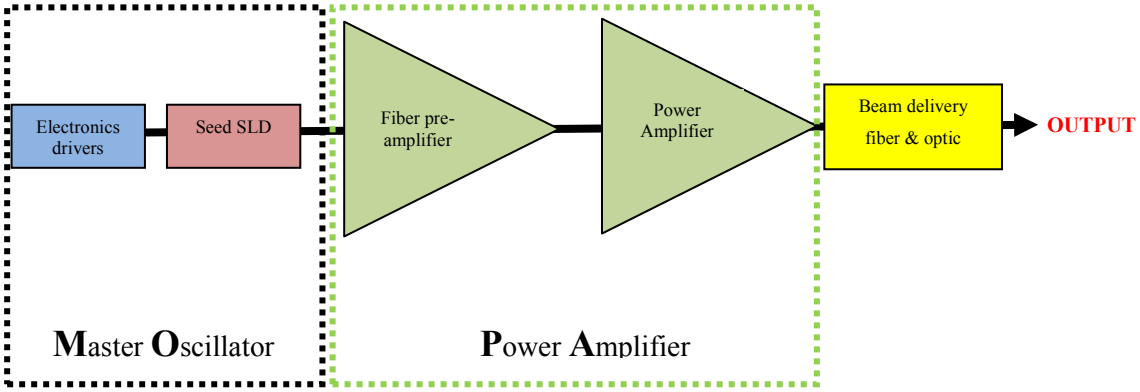

Figure 2.14. Master oscillator power amplifier (MOPA) configuration. The seed is driven by electronic drivers and the power amplifier consists of a cascaded preamplifier and power amplifier. Delivery fiber and BDO are used for ease of handling and transferring power to the point of application.

A semiconductor laser with a fiberised output is commonly used as the seed source or master oscillator. The diode emits single mode, linear/random polarization radiation (depending on design) with a relatively low optical output power. In addition, the seed can operate in both continuous wave and pulsed mode. The signal from the seed is amplified to the desired level with the use of single pass fiber amplifiers. As shown in Figure 2.14, the signal from the seed passes through several amplifiers. The first amplifier is known as the preamplifier, which provides sufficient gain to the signal in order to have adequate optical power at the input of the power amplifier. The amount of gain to be provided by the preamplifier depends on the targeted output power from the power amplifier. Additional preamplifiers may be required if the gain/output power from a single stage preamplifier is not high enough to properly seed the power amplifier. The power amplifier is used to provide the targeted output power. Crucial aspects such as thermal management as well as the suppression of ASE and the nonlinear effects have to be addressed here. The doped fiber used in this stage is usually LMA in nature, which may guide several transverse modes. However, the fundamental mode is usually desired for most applications and techniques such as fiber tapering and bend induced loss for the higher order modes [25, 26] are deployed to obtain single mode output.

With the use of the MOPA configuration, optical power can be scaled to a power level comparable to that of a bulk lasers. Power scaling of single frequency lasers up to 500 W level was demonstrated with MOPA configuration [27]. MOPA based broadband CW lasers with an output well above 1 kW were reported since the year 2004 [28, 29] and in 2009, IPG group has demonstrated single mode fiber lasers with output power of 10 kW [30]. Furthermore, through the use of beam combining method, output power around 100 kW was demonstrated by them in 2013 [31].

On the pulsed MOPA laser side, several significant results with a high energy and high average power were reported. Dupriez et al demonstrated high average power and high peak power in a MOPA configuration based on a VECSEL seed with both femtosecond and picosecond pulses [32]. Using a coherent combination method, Klenke et al demonstrated a femtosecond fiber CPA system with a total average power of 230W and the corresponding peak power of 22 GW [33]. High average powers in the picosecond regime were also demonstrated by Song et al with maximum average power of 157 W [34]. In the nanosecond regime, Yu et al reported an all-fiber MOPA generating square shaped nanosecond optical pulses and with the capability of producing 240 W of average optical power [35].

Most of the experimental setups in this thesis are based on the MOPA configuration with the seed being a semiconductor diode laser. This configuration deemed essential to enable power and energy scaling of pulsed fiber lasers, will be investigated in the following chapters.

2.3 Pulse Propagation and Non-linear Effects in Optical Fibers

Optical pulses propagating along in a nonlinear dispersive system will in general experience nonlinear distortion, with stronger effects expected for larger amplitude pulses. Pulse distortion due to linear dispersion such as group velocity dispersion can result in a complex evolution of the optical pulses. The nonlinear effects can combine with or cancel out the linear dispersive effects and will therefore influence the shape and spectrum of the propagating pulses.

The electric field **E** of a propagating optical pulse can be written as [36]

$$\boldsymbol{E}(r,t) = \frac{1}{2}\,\boldsymbol{x}\{F(x,y)A(z,t)\exp[i(\beta_0 z - \omega_0 t)] + c.c.\} \qquad 2.16$$

where $\boldsymbol{x}$ is the polarization unit vector, A(z,t) is the slowly varying pulse envelope, F(x,y) is the transverse distribution inside the fiber core and β_0 is the propagation constant at the carrier frequency ω_0.

2.3.1 Dispersion in Pulse Propagation

Dispersion plays an important role on pulse propagation in optical fiber because different spectral components associated with the pulse will travel at different speeds. This dispersion manifests through the frequency dependence of the refractive index n(ω). The effect of dispersion with the combination of nonlinearity can cause pulse broadening and soliton formation[36]. In order to understand the effect of dispersion, it is imperative to derive the mode propagation constant using a Taylor series at ω_0, center frequency of the pulse envelope, and can be expressed as

$$\beta(\omega) = \beta_0 + \beta_1(\omega - \omega_0) + \frac{1}{2}\,\beta_2(\omega - \omega_0)^2 + \ldots. \qquad 2.17$$

The parameters β_1 and β_2 are related to the refractive index n and its derivatives through the relations

$$\beta_1 = \frac{1}{v_g} = \frac{n_g}{c} = \frac{1}{c}\left(n + \omega\frac{dn}{d\omega}\right) \qquad 2.18$$

$$\beta_2 = \frac{1}{c}\left(2\frac{dn}{d\omega} + \omega\frac{d^2n}{d\omega^2}\right) \qquad 2.19$$

where n_g is the group index and v_g is the group velocity. Thus β_1 is the inverse of the group velocity which refers to the speed of the envelope of an optical pulse propagating in the fiber. β_2 is the group velocity dispersion parameter.

According to Equation (2.19), when $\beta_2 > 0$, the fiber exhibits normal dispersion. The high frequency (blue-shifted) components will travel slower than the low frequency (red-shifted) components of the same optical pulse. The opposite happens when $\beta_2 < 0$, generally termed as the anomalous dispersion region. The dispersion parameter D is usually used to represent β_2 and the relation between the two are given by [36].

$$D = -\frac{2\pi c}{\lambda^2}\beta_2 \qquad 2.20$$

In the frequency domain, the effect of dispersion on frequency components will cause each and every component to travel at a different velocity. In the temporal domain, the pulse will be either broadened or compressed depending on the dispersion parameter, however in the frequency domain no change will be observed as dispersion alone generates no new frequency components.

2.3.2 Non-linear Effects in Pulse Propagation: Self Phase Modulation

When an electric field **E** is applied to a transparent dielectric medium, it will cause distortion to the electron- charge distributions in the medium. This will lead to an induced polarization **P** in the medium which in the first order approximation will be linear in the applied **E** field. However, if a strong electric field **E** is applied, the polarization response may become nonlinear in the applied field. The total polarization **P** induced by a strong electric field **E** can be represented with this general relation[36],

$$\boldsymbol{P} = \varepsilon_0(\chi^{(1)}.\boldsymbol{E} + \chi^{(2)}:\boldsymbol{EE} + \chi^{(3)}:\boldsymbol{EEE} + \cdots) \qquad 2.21$$

where ε^0 is the vacuum permittivity and $\chi^{(j)}$ (j=1,2,…) is *j*th order susceptibility. The linear susceptibility $\chi^{(1)}$ makes the dominant contribution to P which is related to the refractive index n and attenuation constant α. The second order susceptibility $\chi^{(2)}$ is responsible for nonlinear effects such as second harmonic generation and sum frequency generation. This second order susceptibility will be zero for any material that has a centro-symmetric arrangement of atoms such as silica fibers. As for the third order susceptibility $\chi^{(3)}$, it is mainly responsible for phenomena such as four wave mixing, third harmonic generation and nonlinear variation of the index of refraction.

The third order nonlinearity can lead to an intensity dependent refractive index which is the main cause for phase modulation within a single optical pulse. This leads to the spectral broadening of optical pulses and is known as Self Phase Modulation (SPM). The nonlinear dependence of index of refraction on signal intensity can be defined as[37],

$$n = n_0 + n_2 I \tag{2.22}$$

where n_0 is the linear refractive index value and n_2 is the nonlinear index of refraction. The signal intensity *I* is related to the electric field strength as

$$I = |\boldsymbol{E}|^2 \tag{2.23}$$

The net phase shift in a lossless fiber is proportional to the effective fiber length L_{eff} and intensity[38].

$$\phi(t) = 2\pi(n_0 + n_2 I)\frac{L_{eff}}{\lambda} \tag{2.24}$$

Hence the total phase shift derivatives will be

$$\frac{d\phi(t)}{dt} = \frac{4\pi n_2 L_{eff}}{\lambda}\frac{dI}{dt} = \frac{4\pi n_2 L_{eff}}{\lambda A_{eff}}\frac{dP}{dt} = \omega(t) \tag{2.25}$$

where P is the instantaneous power and A_{eff} is the effective fiber mode area. The instantaneous angular optical frequency of the pulse is related to the rate of change of phase

$$d\omega = \frac{d\phi}{dt} \tag{2.26}$$

Thus, the instantaneous frequency can be derived as

$$\omega(t) = w_0 - \frac{4\pi n_2 L_{eff}}{\lambda A_{eff}}\frac{dP}{dt} \tag{2.27}$$

From Equation (2.27), it is evident that for a fixed length of fiber, the SPM induced spectral change is related to the rate of change of instantaneous power of the pulse. By considering a Gaussian pulse, the leading edge of the pulse will have positive $\frac{dP}{dt}$ value. Thus, the *dω* will be negative; i.e the frequency is down-shifted. Similarly, at the trailing edge of the pulse, *dω* will be positive and the frequency will be up-shifted and the resulting spectrum will be symmetrically broadened from the center frequency due to SPM. If the pulse is asymmetric, the

$d\omega$ will differ between the leading and trailing edges of the pulse and will result in an asymmetrically broadened spectrum.

The shape of the SPM broadened spectrum depends on the optical pulse shape and initial chirp. Figure 2.15 shows the SPM induced spectral evolution of two different optical pulse shapes, specifically a Gaussian and square shaped profiles, for a maximum phase shift of 4.5 π. Both optical pulses are assumed to be chirp free. With the square shaped profile, the spectrum suffers the highest broadening factor because of higher chirp induced at both the leading and trailing edges of the pulse. Moreover, most of the energy resides in the central peak. On the other hand, the Gaussian shaped profile induced a smaller chirp resulting in a smaller broadening factor. In this case, the pulse energy is distributed across the oscillatory peaks with the outmost peaks containing the highest energy. The shapes of the SPM broadened spectra are symmetrical in shape since the induced chirp in the leading and falling edges is equal in strength. However, in real applications, the spectral shape can be influenced by other parameters such as fiber attenuation, amplifier gain and the gain induced by SRS.

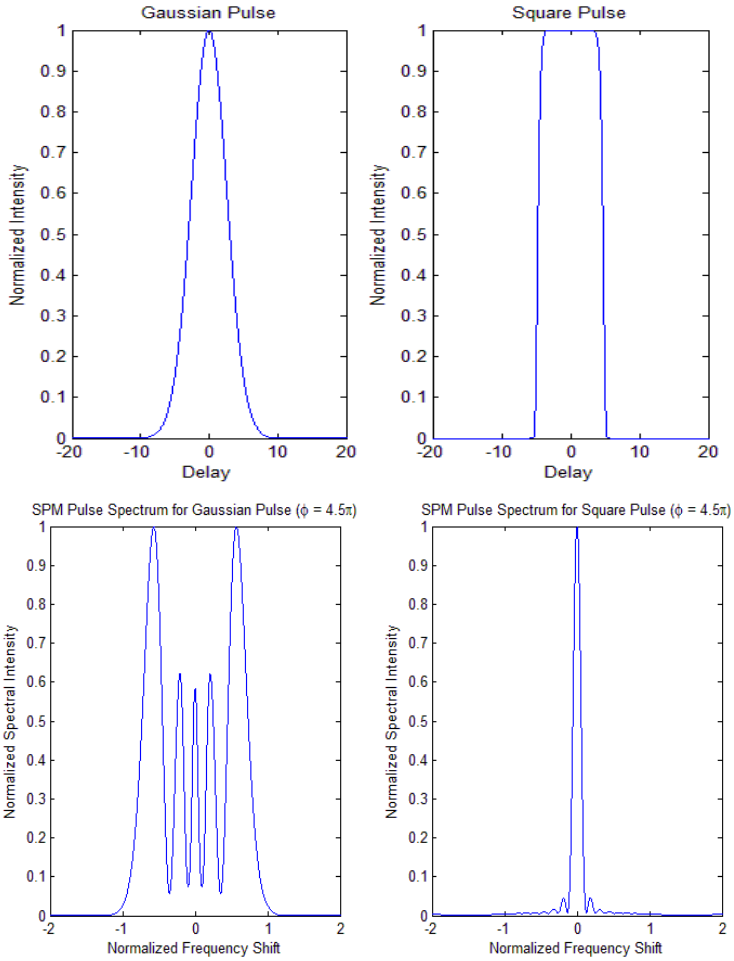

Figure 2.15. Numerical calculation on Gaussian pulse and square pulse and their corresponding spectra due to SPM. The maximum phase shift was set at 4.5 π.

In the case of fiber MOPA amplified nanosecond pulses, the effect of gain saturation within the fiber amplifiers directly influences the output pulse shape. The pulse shape gets distorted with higher leading edge and an exponentially decreasing trailing edge. The higher the gain extracted from the fiber amplifier, the more distortion suffered by the optical pulse. This will also influence the SPM induced spectral broadening. Figure 2.16 shows the impact on the SPM broadened spectrum for different pulse shapes. The numerical calculation of the pulse shape involves flat topped pulse with a pulse duration of 90 ns. The fiber length and peak power are chosen such that $\phi_{max} = 3.5\pi$. In addition, the input pulses are assumed to be unchirped (C=0). With the perfectly square, flat topped pulse (blue line), the shape of the SPM broadened spectrum is perfectly symmetrical and most of the energy is contained in the central peak. When the optical pulse begins to distort due to gain saturation effect (green and red lines), the spectra show an asymmetrical shape with a smaller frequency shift at the higher frequency side as compared to the lower frequency side.

When the pulse is heavily distorted (turquoise line), the spectral bandwidth becomes much larger as compared with a perfectly square, flat topped pulses due to the larger frequency shift of the higher frequency components. Furthermore, the distorted pulse has a trailing edge profile similar to a Gaussian profile, with the chirp induced across the central region of the pulse. Thus, the SPM-broadened spectrum at the pulse trailing edge has identical features as shown in Figure 2.15 (oscillatory structure with the outermost peak containing significant energy).

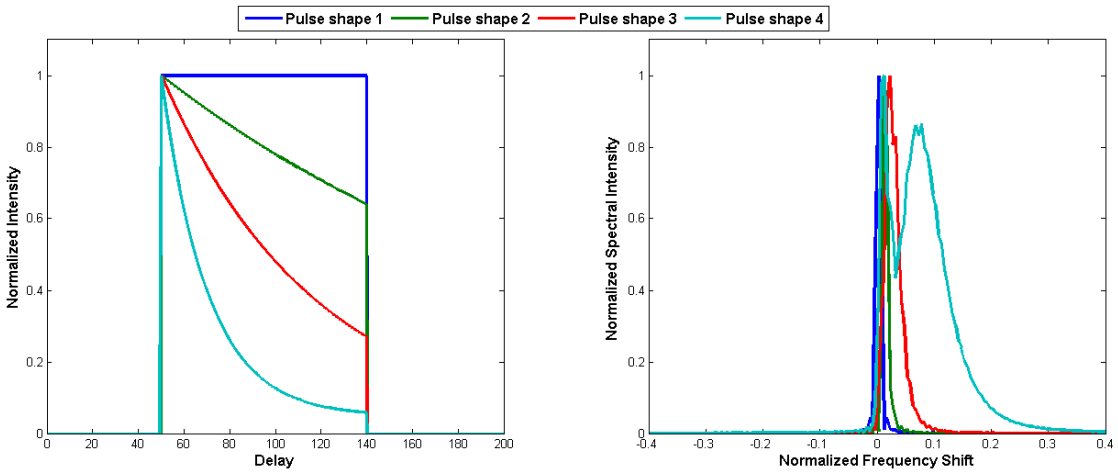

Figure 2.16. Numerical calculation showing the effect of temporal pulse shape on spectral broadening due to SPM.

2.3.3 Cross Phase Modulation

When several waves propagate in an optical fiber in the same direction, the waves can interact with each other, due to the Kerr effect. The co-propagating waves can be coupled due to a phenomenon known as cross phase modulation (XPM). XPM is linked to the change in refractive index of the fiber as a result of the presence of other waves. XPM is always accompanied by SPM and the nonlinear phase change induced by the co-propagating waves depends on the intensity of each wave and the relationship can be expressed by the following equation [39].

$$\phi_j^{NL}(z) = \left(\frac{\omega_j}{c}\right)\Delta n_j z = \frac{n_2\omega_j}{c}\left(\left|E_j\right|^2 + 2\left|E_{3-j}\right|^2\right)z \qquad 2.28$$

The first term in Equation (2.28) is related to the contribution from SPM. The second term represents phase modulation of one wave due the co-propagating wave and is directly linked to the XPM. Moreover, the effect of XPM is a factor of 2 higher as compared to the effect of SPM for the same level of optical intensity. This analysis assumes that the waves are co polarized, if the waves are orthogonally polarized, the interaction is reduced to a 1/3 of the polarized case.

2.3.4 Stimulated Raman Scattering

When a beam of light passes through a transparent material, a small amount of light may scatter to new frequencies different from the incident light due to SRS. SRS is governed by the imaginary part of the third order susceptibility $\chi^{(3)}$. Scattered light to a lower frequency is known as the Stokes wave and to a higher frequency is known as anti-Stokes wave. The amount of frequency change is determined by the vibrational modes of the medium. If the incident light is intense enough, a rapid growth of the Stokes wave will be observed and a significant fraction of the incident light can be frequency shifted.

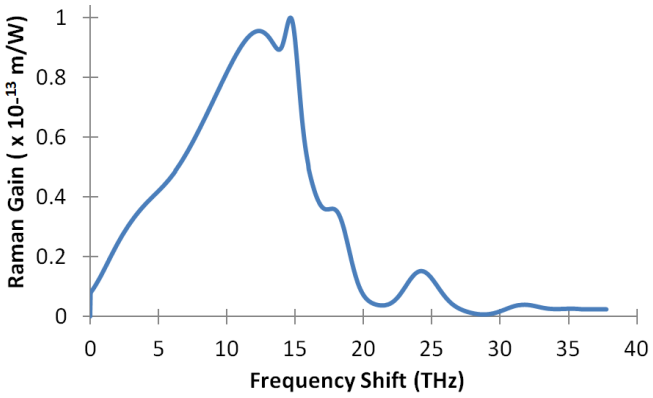

Figure 2.17. Raman gain coefficient curve of a silica core single mode fiber. The curve is normalized to 1.0 at 440cm^{-1}. The peak gain for a pump wavelength of 1060nm is 1 x 10^{-13} m/W and varies with pump wavelength as $1/\lambda_p$ [40].

In silica fibers, the Raman gain coefficient spectrum is very broad and extends up to 30 THz [40]. The measured peak gain at 1.06μm is g_R = 1x10^{-13} m/W with a Stokes shift of Δv = 13.2 THz (440cm^{-1}). If a probe beam of frequency $\omega_{s\ is}$ coincident with the pump, ω_p, it will be amplified if the frequency difference lies within the Raman gain bandwidth. The relationship between the incident pump and Stokes wave can be represented by the following coupled equation (CW case) as shown in Figure 2.18 [36],

$$\frac{dI_s}{dz} = g_R I_p I_s - \alpha_s I_s \qquad 2.29$$

$$\frac{dI_p}{dz} = -\frac{\omega_p}{\omega_s} g_R I_p I_s - \alpha_p I_p \qquad 2.30$$

where g_R is the Raman gain coefficient, α_s and α_p are fiber loss at Stokes and pump frequencies respectively, I_s and I_p are intensities of the Stokes and pump light. By neglecting the pump depletion in Equation (2. 30), it is possible to solve the coupled equation analytically,

$$I_s(l) = I_s(0) \exp(g_R I_0 l_{eff} - \alpha_s l) \qquad 2.31$$

where I_0 is the incident pump intensity at z=0 and l_{eff} is the effective interaction length ($l_{eff} = \frac{1-\exp(-\alpha_p l)}{\alpha_p}$).

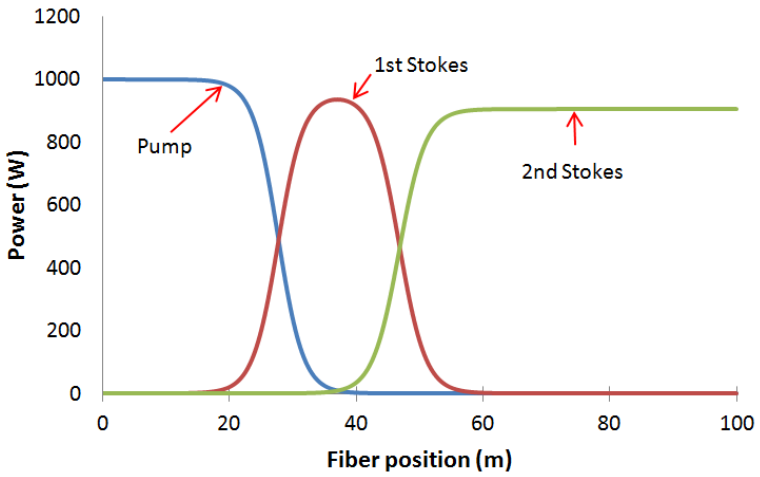

Figure 2.18. Numerical calculation using the coupled equations to illustrate the growth of Raman stokes (1st and 2nd Stokes) as well as the depletion of pump power.

In single pass Raman generation, the pump incident at the fiber input will initiate spontaneous Raman scattering and get amplified along the fiber. The spontaneous Raman scattering will generate photons at each frequency component across the Raman gain bandwidth. Frequency

components lying at the Raman gain peak will build up most rapidly. The Raman threshold is defined as the input pump power at which Stokes power becomes equal to the residual pump power at the fiber output,

$$P_s(l) = P_p(l) = P_0 \exp(-\alpha_p l) \tag{2.32}$$

The critical pump power required to achieve the Raman threshold is given by [41]

$$P_{th} = \frac{20.3 - \ln\beta + \ln\left(\frac{A_{eff}}{g_R l_{eff}}\right)}{g_R l_{eff}} A_{eff} \tag{2.33}$$

where β is the ratio between Raman power and pump power at the output of the fiber when at threshold. Equation (2.33) allows us to estimate the maximum power that can be launched into the fiber without observing any significant growth of Raman Stokes. In order to increase the Raman threshold power, the most effective way is to use a larger core diameter fiber and/or shorter effective fiber length. If the power in the Stokes wave exceeds the Raman threshold, the Stokes will act as a pump for a second order Stokes wave and the process is known as cascaded SRS.

2.3.5 Stimulated Brillouin Scattering

Similar to SRS, stimulated Brillouin scattering (SBS) is a nonlinear process that can occur in optical fiber. It can occur at input intensities much lower than the SRS threshold. SBS occurs when a nonlinear interaction happens between the pump and Stokes fields through an acoustic wave. The pump field will generate an acoustic wave via the electrostriction process [42]. This acoustic wave periodically modulates the refractive index and acts as Bragg grating. Scattered light is downshifted in frequency as a result of Doppler shift associated with grating movement at the speed given by the optical frequency difference between the forward and scattered waves. The Stokes wave will grow exponentially and propagates only in the backward direction for a single mode optical fiber as compared to SRS that can occur in both directions. The frequency shift is much smaller for SBS (~10 GHz) with relatively narrow gain bandwidth (~50 MHz) as it is directly related to the phonon lifetime.

The power at which the Stokes wave at the input end becomes equal to the pump power at the output, is defined as SBS critical power and can be expressed as

$$P^P_{Critical} = 21\frac{A_{eff}K}{g_B L_{eff}} \tag{2. 34}$$

where A_{eff} and L_{eff} are the effective mode area and interaction length as defined in the previous section. K is the polarization factor of the pump with K=1 for polarized light and K = 2 for un-polarized light. The peak value of the Brillouin gain coefficient or g_B = 5 x 10^{-11} m/W, which is higher than the Raman gain by a factor of ~500. This makes the SBS threshold low for a narrow linewidth pump source and becomes a dominant nonlinear process in optical fibers.

The phonon lifetime plays an important role in the process of SBS [43]. When the pulse duration is shorter than phonon lifetime (< 10ns), the Brillouin gain decreases. This means that operation in the picosecond and femtosecond regimes is free from any SBS.

2.4 References

1. J. J. Coleman, "The development of the semiconductor laser diode after the first demonstration in 1962," Semiconductor Science and Technology **27**, 090207 (2012).
2. M. Kondow, T. Kitatani, S. Nakatsuka, M. C. Larson, K. Nakahara, Y. Yazawa, M. Okai, and K. Uomi, "GaInNAs: a novel material for long-wavelength semiconductor lasers," Selected Topics in Quantum Electronics, IEEE Journal of **3**, 719-730 (1997).
3. E. Yablonovitch, and E. O. Kane, "Band structure engineering of semiconductor lasers for optical communications," Lightwave Technology, Journal of **6**, 1292-1299 (1988).
4. M. Yamada, "Transverse and longitudinal mode control in semiconductor injection lasers," Quantum Electronics, IEEE Journal of **19**, 1365-1380 (1983).
5. M. Bou Sanayeh, P. Brick, W. Schmid, B. Mayer, M. Müller, M. Reufer, K. Streubel, J. W. Tomm, and G. Bacher, "Temperature-power dependence of catastrophic optical damage in AlGaInP laser diodes," Applied Physics Letters **91**, - (2007).
6. R. Lang, "Injection locking properties of a semiconductor laser," Quantum Electronics, IEEE Journal of **18**, 976-983 (1982).
7. J. N. R. Paschotta, A.C. Tropper and D.C. Hanna, "Ytterbium doped fiber amplifiers," IEEE Journal of Quantum Electronics Vol.33, pp.1049-1056 (1997).
8. R. J. C. H.M. Pask, D.C. Hanna, A.C. Tropper, C.J.Mackechnie, P.R. Barber and J.D. Dawes, "Ytterbium doped silica fibers: Versatile sources for the 1 - 1.2 um region," IEEE Journal of selected topics in Quantum Electronics Vol.1 No.1 (1995).
9. D. E. McCumber, "Theory of Phonon-Terminated Optical Masers," Physical Review **134**, A299-A306 (1964).
10. Y. Wang, "Optimization of pulse amplification in ytterbium doped double clad fiber amplifiers," Journal of Lightwave Technology, Vol. 23, pp. 2139 - 2147 (2005).
11. A. Ghatak, and K. Thyagarajan., *An Introduction to Fiber Optics* (Cambridge University Press, 1998).
12. J. D. Love, and A. W. Snyder, "Fresnel's and Snell's laws for the multimode optical waveguide of circular cross section," J. Opt. Soc. Am. **65**, 1241-1247 (1975).
13. R. Ulrich, S. C. Rashleigh, and W. Eickhoff, "Bending-induced birefringence in single-mode fibers," Optics Letters **5**, 273-275 (1980).
14. T. Hosaka, K. Okamoto, T. Miya, Y. Sasaki, and T. Edahiro, "Low-loss single polarisation fibres with asymmetrical strain birefringence," Electronics Letters **17**, 530-531 (1981).
15. Y. Sasaki, T. Hosaka, M. Horiguchi, and J. Noda, "Design and fabrication of low-loss and low-crosstalk polarization-maintaining optical fibers," Lightwave Technology, Journal of **4**, 1097-1102 (1986).

16. M. C. T. Bahaa E. A. Saleh, *Fundamental of Photonics* (John Wiley & Sons, 1991).
17. J. K. Dahv Kliner, Fabio Di Teodoro, Sean Moore, "Fiber Laser Technology Reels into High Power Result," (SPIE oemagazine, 2004).
18. R.Paschotta, "Encyclopedia for Photonics and Laser Technology."
19. J. N. A.B.Grudinin, P.W.Turner, C.C.Renaud, W.A.Clarkson and D.N.Payne, "Single clad coiled optical fibre for high power lasers and amplifiers," in *Conference of Laser and Electro-Optic (CLEO)*(Baltimore 23-28 May, 1999).
20. A. M. a. J. K. Michalis N. Zervas, "Effective absorption in cladding pumped fiber," Proceedings Vol. 7914, Fiber Lasers VIII: Technology, Systems, and Applications (2011).
21. J. Limpert, A. Liem, T. Gabler, H. Zellmer, A. Tünnermann, S. Unger, S. Jetschke, and H. R. Müller, "High-average-power picosecond Yb-doped fiber amplifier," Optics Letters **26**, 1849-1851 (2001).
22. N. G. R. Broderick, H. L. Offerhaus, D. J. Richardson, R. A. Sammut, J. Caplen, and L. Dong, "Large Mode Area Fibers for High Power Applications," Optical Fiber Technology **5**, 185-196 (1999).
23. M.-J. Li, X. Chen, A. Liu, S. Gray, J. Wang, D. T. Walton, and L. A. Zenteno, "Effective area limit for large mode area laser fibers," in *Optical Fiber Communication Conference*(Optical Society of America, 2008), p. OTuJ2.
24. J. A. Alvarez-Chavez, H. L. Offerhaus, J. Nilsson, P. W. Turner, W. A. Clarkson, and D. J. Richardson, "High-energy, high-power ytterbium-doped Q-switched fiber laser," Optics Letters **25**, 37-39 (2000).
25. T. Alder, A. Stohr, R. Heinzelmann, and D. Jager, "High-efficiency fiber-to-chip coupling using low-loss tapered single-mode fiber," Photonics Technology Letters, IEEE **12**, 1016-1018 (2000).
26. J. P. Koplow, D. A. V. Kliner, and L. Goldberg, "Single-mode operation of a coiled multimode fiber amplifier," Optics Letters **25**, 442-444 (2000).
27. J. Yoonchan, J. Nilsson, J. K. Sahu, D. N. Payne, R. Horley, L. M. B. Hickey, and P. W. Turner, "Power Scaling of Single-Frequency Ytterbium-Doped Fiber Master-Oscillator Power-Amplifier Sources up to 500 W," Selected Topics in Quantum Electronics, IEEE Journal of **13**, 546-551 (2007).
28. V. Gapontsev, D. Gapontsev, N. Platonov, O. Shkurikhin, V. Fomin, A. Mashkin, M. Abramov, and S. Ferin, "2 kW CW ytterbium fiber laser with record diffraction-limited brightness," in *Lasers and Electro-Optics Europe, 2005. CLEO/Europe. 2005 Conference on*(2005), p. 508.
29. Y. Jeong, J. Sahu, D. Payne, and J. Nilsson, "Ytterbium-doped large-core fiber laser with 1.36 kW continuous-wave output power," Opt. Express **12**, 6088-6092 (2004).

30. M. O'Connor, V. Gapontsev, V. Fomin, M. Abramov, and A. Ferin, "Power scaling of SM fiber lasers toward 10kW," in *Conference on Lasers and Electro-Optics*(Optical Society of America, 2009), p. CThA3.
31. V. Fomin, V. Gapontsev, E. Shcherbakov, A. Abramov, A. Ferin, and D. Mochalov, "100 kW CW fiber laser for industrial applications," in *Laser Optics, 2014 International Conference*(2014), pp. 1-1.
32. P. Dupriez, C. Finot, A. Malinowski, J. K. Sahu, J. Nilsson, D. J. Richardson, K. G. Wilcox, H. D. Foreman, and A. C. Tropper, "High-power, high repetition rate picosecond and femtosecond sources based on Yb-doped fiber amplification of VECSELs," Opt. Express **14**, 9611-9616 (2006).
33. A. Klenke, S. Hädrich, T. Eidam, J. Rothhardt, M. Kienel, S. Demmler, T. Gottschall, J. Limpert, and A. Tünnermann, "22 GW peak-power fiber chirped-pulse-amplification system," Optics Letters **39**, 6875-6878 (2014).
34. R. Song, J. Hou, S. Chen, W. Yang, and Q. Lu, "157 W all-fiber high-power picosecond laser," Appl. Opt. **51**, 2497-2500 (2012).
35. H. Yu, R. Tao, X. Wang, P. Zhou, and J. Chen, "240W high-average-power square-shaped nanosecond all-fiber-integrated laser with near diffraction-limited beam quality," Applied Optics **53**, 6409-6413 (2014).
36. G. Agrawal, *Nonlinear Fiber Optics (3rd Edition)* (Academic Press, 2001).
37. A. E. Siegman, *Lasers* (Oxford University Press, 1986).
38. C. L. R.H. Stolen, "Self phase modulation in silica optical fibers," Phys. Rev. A 17, pp.1448 - 1453 (1978).
39. G. P. Agrawal, *Nonlinear Fiber Optics* (Academic Press, NY, 1995).
40. C. L. a. R. K. J. R.H. Stolen, "Development of the stimulated Raman spectrum in single-mode silica fibers," J. Opt. Soc. Am. B 1, 652-657 (1984).
41. J. L. C. Jauregui, A. Tünnermann, "On the Raman threshold of passive large mode area fibers," **7914** (2011).
42. S. Mauger, L. Bergé, and S. Skupin, "Controlling the stimulated Brillouin scattering of self-focusing nanosecond laser pulses in silica glasses," Physical Review A **83**, 063829 (2011).
43. W. Chen, Z. Meng, and H.-J. Zhou, "Phonon Lifetime Measurement by Stimulated Brillouin Scattering Slow Light Technique in Optical Fiber," Chinese Physics Letters **30**, 074209 (2013).

Chapter 3. Nanosecond Fiber Laser System

Two different configurations of nanosecond fiber MOPA are presented in this chapter. The first configuration is a directly modulated SLD seeded MOPA incorporating a pulse shaping mechanism through the use of an Electro-optic modulator (EOM). The second configuration was jointly developed with SPI Lasers under the Technology Strategy Board (TSB) project, SMART. The SMART system was also seeded with a directly modulated SLD; however, in this case GT-wave fiber based amplifiers were used while an Acousto-optic modulator (AOM) was used as the optical pulse shaper. The advantages and limitations of these two configurations will be discussed. Furthermore, various custom defined pulse shapes produced at the output of the two systems and the impact made in actual material processing trials will be highlighted in this chapter.

3.1 Introduction

The development of industrial based laser sources has been growing at a fast pace in recent years. As of the year 2012, the global market for industrial material processing lasers sat at a record high of € 7.9 billion with laser drilling, cutting, micro processing and marking in the area of automobile manufacturing, semiconductor and aerospace industries [1]. Fiber based laser sources accounted for 18% of the total market share and the fiber laser is ultimately expected to replace gas laser sources and bulk solid state laser sources in the majority of material processing applications.

Before the introduction of fiber laser systems for material processing, this area was mainly dominated by Q-switched solid state lasers with an operational wavelength at 1064 nm or its harmonics [2, 3]. The optical pulses generated from such sources typically have an asymmetrical Gaussian shaped profile and typical repetition rates in few Hz to up to the kHz range. Despite the Q-switched laser system being able to generate different pulse durations and high peak power at low repetition rates, these properties alone are not sufficient for certain material processing applications. For example, Q-switched laser systems are unable to generate short nanosecond optical pulses and offer no control over the pulse profile. Furthermore, the output spatial profile is usually Gaussian in nature which is not efficient for processing applications and results in a spatially non-uniform ablation depth [4].

The introduction of fiber based MOPA systems incorporating directly modulated semiconductor laser diode as the seed laser and rare-earth doped fiber amplifers are the perfect replacement in many instances for the bulky Q-switched laser systems [5, 6]. Moreover laser systems based on fibers are an attractive technology for compact and efficient high performance short pulse laser

systems. Compared with conventional bulk solid state lasers, fiber lasers are superior in terms of beam confinement and heat dissipation. Furthermore, custom defined output pulse shapes (square, step, ramp pulse) with a short (nanosecond) pulse width at mili-Joule pulse energy can now be achieved with fiber based MOPA systems. With the availability of nanosecond fiber sources, more real world applications have emerged demanding high repetition rates, high beam quality and high average power that are simply just not possible with conventional solid state laser system.

With the availability of pulsed laser systems operating between the femtosecond and nanosecond ranges, studies on light matter interactions during material processing can be carried out [7]. Studies on laser ablation threshold, laser induced plasma, ejection mechanisms, heat transfer in material and material characteristics have been widely reported [8-10]. However, not many publications relate to the impact of different optical temporal profiles to laser machining. Recently, the effects of the temporal pulse envelope on the machining of silicon have generated interest and are gaining traction thanks to the availability of nanosecond fiber laser with adaptive pulse shaping. O'Neill reported an improvement in the surface quality in silicon machining that was not possible with conventional Q-switched laser systems [11]. The use of nanosecond fiber MOPAs delivering optical pulse with a sharp leading edge resulted in small heat-affected zones, less recast layers and less micro cracking on the wall of the interaction zone. Hendow et al also demonstrated the use of nanosecond pulse bursts for silicon scribing and showed that the material removal process could be sped up with minimized thermal diffusion [12]. Thus, with the advancement in nanosecond fiber laser technology, a new interesting area of research on controlling the material response on silicon material through the use of designer pulses has now been made possible.

3.1.1 Pulse amplification and gain saturation

When an optical pulse propagates along a laser gain medium with an inverted population inversion, it will experience gain due to the stimulated emission effect. However, the gain distribution along the length of the pulse depends on the width of the optical pulse. If a short optical pulse (sub-nanosecond and below) is launched into the laser medium, the entire length of the pulse will experience uniform inversion and will be amplified uniformly. However, in the case of a longer optical pulse, the leading and the trailing edges of the pulse will experience different levels of population inversion due to gain saturation depletion, resulting in different gains across the pulse profile. The non-uniform gain exerted on a long optical pulse usually introduces distortions to the pulse shape.

The phenomena above can be described by a nonlinear time dependent radiation transfer equation which is based on Siegman and Frantz analysis. Consider a short optical pulse with the intensity I(z,t) propagating in the +z direction along a laser medium with inverted population difference ΔN(z,t) (as shown in Figure 3.1. Optical intensity passing through a short segment of a saturable pulse amplifier. The instantaneous intensity I(z,t) is related to the electromagnetic energy density of the optical signal pulse ρ_{em} (J/m^3) travelling at group velocity v_g, or $I(z,t) = \rho_{em}(z,t)$ x v_g. In a short segment of length Δz in the laser medium, the rate of change of stored signal energy in the length Δz is given by the difference of energy flux between input and output ends plus the net rate of stimulated emission within the segment.

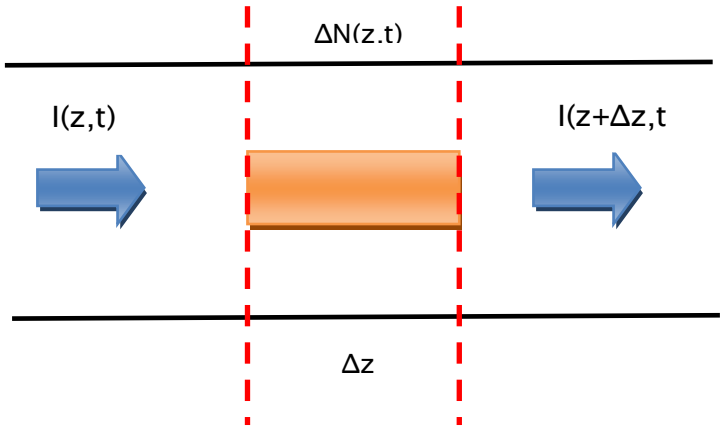

Figure 3.1. Optical intensity passing through a short segment of a saturable pulse amplifier.

The change in pulse intensity and population inversion can be described as [13]:

$$\frac{\partial I(z,t)}{\partial t} = \sigma_e \Gamma_s N(z,t) I(z,t) \qquad 3.1$$

$$\frac{\partial N(z,t)}{\partial t} = \frac{-\sigma_e \Gamma_s}{h\omega} N(z,t) I(z,t) \qquad 3.2$$

where σ_e is the emission cross section for Yb3+ and Γ_s is the power filling factor in the fiber core.

By rearranging the intensity variables and integrating it over the entire fiber, Equation (3. 1) can be rewritten as

$$\int_{I=I_{in}(t)}^{I=I_{out}(t)} \frac{dI}{I} = \sigma_e \Gamma_s \int_{z=0}^{z=L} N(z,t)\, dz \qquad 3.3$$

where $I_{in}(t)$ and $I_{out}(t)$ are the input pulse intensity at z = 0 and the output pulse intensity at z=L respectively. The integral on the right hand side of Equation (3. 3) is defined as the total number of atoms in the amplifier. The solution can be written in the form:

$$I_{out}(t) = I_{in}(t)e^{\sigma_e \Gamma_s N_{tot}(t)} = G(t)I_{in}(t) \quad 3.4$$

where $G(t) = e^{\sigma_e \Gamma_s N_{tot}(t)}$ is the time varying gain at any instant within the pulse. When t =0, $G_0 = e^{\sigma_e \Gamma_s N_0}$, where N_0 is the population inversion at time t = 0 and G_0 is the initial single pass gain of the amplifier.

Equation (3. 2) can now be integrated over the amplifier length,

$$\frac{\partial}{\partial t}\int_{z=0}^{z=L} N(z,t)dz = \frac{dN_{tot}(t)}{dt} = \frac{-1}{h\omega}\int_{z=0}^{z=L}\frac{\partial I(z,t)}{\partial z}\,dz \quad 3.5$$

This can then be simplified as

$$\frac{dN_{tot}(t)}{dt} = \frac{-1}{h\omega}\left[I_{out}(t) - I_{in}(t)\right] \quad 3.6$$

The input and output energy per unit area can be calculated by the following equations:

$$U_{in}(t) = \int_0^t I_{in}(t)dt \quad 3.7$$

$$U_{out}(t) = \int_0^t I_{out}(t)dt \quad 3.8$$

An important parameter that related to the energy storage capability in the laser medium is the saturation energy. The saturation energy per unit area U_{sat} can be defined as[14]:

$$U_{sat} \equiv \frac{hv}{(\sigma_e + \sigma_a)\Gamma_s} \quad 3.9$$

where hv is the energy of a signal photon, σ_e and σ_a are the emission and absorption cross sections at the signal wavelength and Γ_s is the signal overlap with the doped area.

By defining the parameters needed for input and output energies, Equation (3.6) can be further integrated as follow:

$$U_{in}(t) = U_{sat}\ln\left[\frac{1 - e^{-\sigma_e \Gamma_s N_o}}{1 - e^{-\sigma_e \Gamma_s N_{tot}}}\right] = U_{sat}\ln\left[\frac{1 - \frac{1}{G_0}}{1 - \frac{1}{G(t)}}\right] \quad 3.10$$

G(t) represents the instantaneous gain across the optical pulse and can be expressed as functions of $U_{out}(t)$:

$$G(t) = \frac{G_0}{G_0 - (G_0 - 1)e^{-U_{in}(t)/U_{sat}}} \quad 3.11$$

Constants such as G_0 and U_{sat} are dependent on the fiber properties. With the use of the time dependent gain function, the output intensity and shape can be predicted by the following relation:

$$I_{out}(t) = G(t)I_{in}(t) \quad 3.12$$

In the MOPA configuration, the power amplifier stage usually provides the gain required to achieve a significant amount of pulse energy. Knowledge of the saturation energy of the fiber helps to predict the total amount of extractable energy from the MOPA, since the total energy is limited to around 10 times the saturation energy of the fiber. The saturation energy can easily be calculated using Equation (3.9) and the dependence on the fiber core radius is illustrated in Figure 3.2. Since larger core radius provides higher saturation energy, fiber power amplifier usually adopts LMA fiber in order to extract more energy and to have higher threshold for nonlinear distortions.

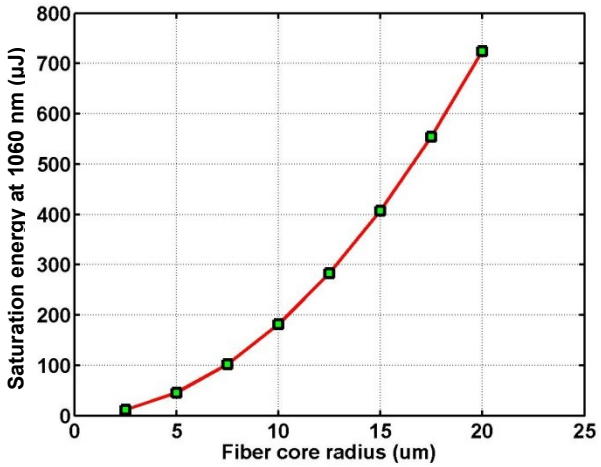

Figure 3.2. The calculated saturation energy for different fiber core radii and 1060 nm operation wavelength. Calculation made with the assumption that $\Gamma_s = 1$.

By utilizing the above equations, the amplification of a rectangular optical pulse in a fiber amplifier can be calculated. Figure 3.3 shows the effect of gain saturation on the optical output pulse shape with 10 dB and 30 dB signal gain. The following parameters are used for the calculation: FWHM pulse width = 90 ns, input pulse energy = 0.1 mJ, signal wavelength = 1060 nm, MFD = 20 μm and fiber saturation energy = 0.18 mJ. When a rectangular shaped input

pulse (blue curve) is launched into a fiber amplifier providing 10 dB of signal gain (green curve), the leading edge of the pulse get amplified more than the trailing edge as a result of the higher gain experienced by the pulse's leading edge as compared to the trailing edge. This pulse reshaping is caused by the gain saturation effect and is partly due to the different gain experienced by the different parts of the pulse as is evident from Equation (3.11). In other words, the gain saturation effect can be attributed to the availability of population inversion to interact with the incoming photons. At the beginning of the input pulse, the gain medium is well inverted and the photons can interact with the available inversion to undergo stimulated emission. However, the available inversion is continuously depleted and towards the end of the pulse there is not enough inversion left to amplify the pulse further. Thus, a significant reshaping of the input pulse can be seen at the output. Further reshaping can be observed when the gain of the amplifier is further increased to 30 dB (red curve). As a result of pulse reshaping, the FWHM of the pulse decreases from 90 ns to 6 ns. The pulse reshaping effect also leads to higher peak powers and may introduce additional nonlinear distortions.

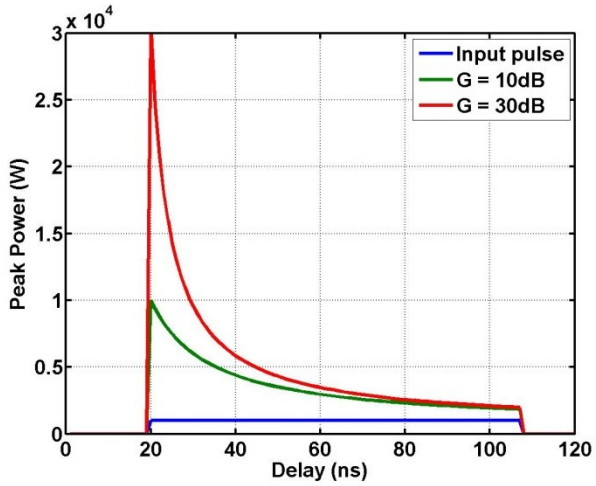

Figure 3.3. The calculated intensity profiles for rectangular shape input pulse (blue) and the output pulses at 10 dB (green) and 30 dB (red) gain respectively.

Although pulse reshaping is not generally desirable in a fiber MOPA system, the effect can be compensated by incorporating a pulse shaping mechanism in the MOPA system. This pulse shaping mechanism will be discussed further in the next section and will be applied in the experimental work presented in this thesis.

3.2 Nanosecond Fiber MOPA with Active Pulse Shaping

The gain saturation effect in a fiber amplifier is a major limitation for high energy (~mJ) nanosecond fiber MOPA systems. The reshaped optical pulses will have a sharp peak at the leading edge, resulting in a reduction in pulse duration (as shown in Figure 3.4(a)). This initial peak with significant peak power combined with relatively long fiber length in the MOPA system will initiate nonlinear effects, mainly SRS. The Raman threshold acts as a cap on the maximum peak power achievable at the signal wavelength. By proper control of the output pulse shape through actively shaping the input pulse so as to pre-compensate for the effects of the gain saturation, flat top pulse shapes can be generated. As a result, the effect of SRS can be minimized and at the same time the energy contained at the signal wavelength is maximized (Figure 3.4(b)).

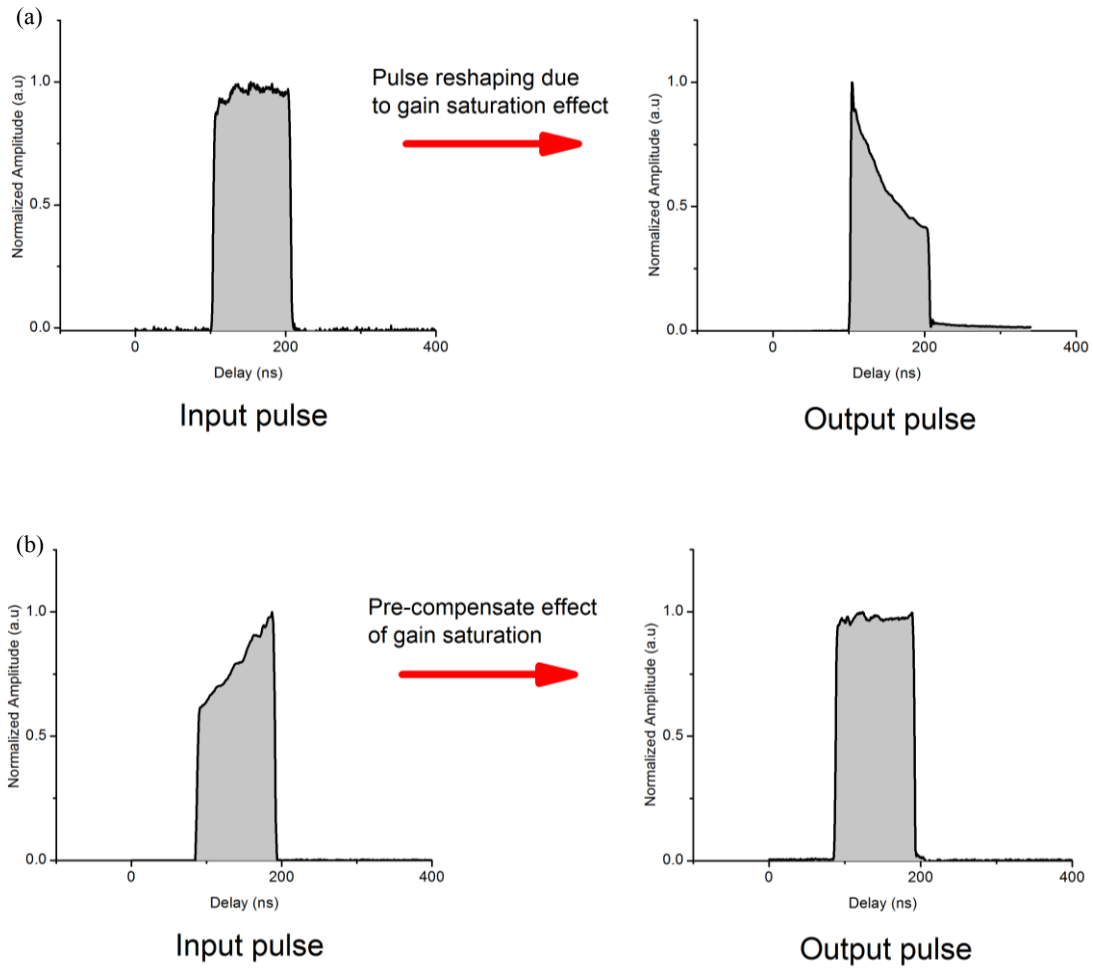

Figure 3.4. Effects of temporal distortion as a result of the gain saturation effect in a fiber amplifier and the mitigation of gain saturation through pre-compensated optical shape.

The development of high performance nanosecond fiber MOPAs was made possible with the use of LMA fiber and exploitation of the cladding pumping technique [15, 16]. The ability of

fiber based amplifiers generating high quality optical signals was demonstrated by Limpert et al in 2002 with a maximum average power of 100 W and a pulse energy of 4 mJ with diffraction-limited beam quality [17]. Two years later, Vu et al demonstrated a diode seeded nanosecond fiber MOPA system and for the first time, demonstrated adaptive shaping of the optical pulses by controlling electrical pulses to the laser diode [18]. The shaping technique not only allows control of the pulse shape at the output of the system but also provides compensation of pulse deformation due to the saturation effect in fiber amplifiers. The pulse shaping technique was further refined with the demonstration of an EOM based shaping technique for use within a MOPA system [6]. With this modification, the quality of the pulses was improved with fewer features introduced by the operation of the diode or its drive electronics. This system not only demonstrated the capability of generating tailored pulse shapes at the output, but significantly improved the extracted pulse energy.

However, the previous laser system lacks the temporal resolution required to shape a shorter optical pulse. The AWG used has a minimum temporal resolution of 4 ns per point. The shortest rectangular shaped optical pulse that can be obtained is ~12 ns (at least 3 points are required for shaping into a rectangular shaped pulse). Thus, optical pulses shorter than 12 ns cannot be shaped in the previous laser system.

Modification of the laser system was carried out with the aim to upgrade the existing AWG used in the nanosecond MOPA system with a higher speed AWG. The new AWG will provide a higher temporal resolution (~ 350 ps) and will allow higher shaping quality. Hence, the capabilities of the modified laser system in terms of pulse shaping and the machining quality will be explored in this chapter.

3.2.1 System Setup

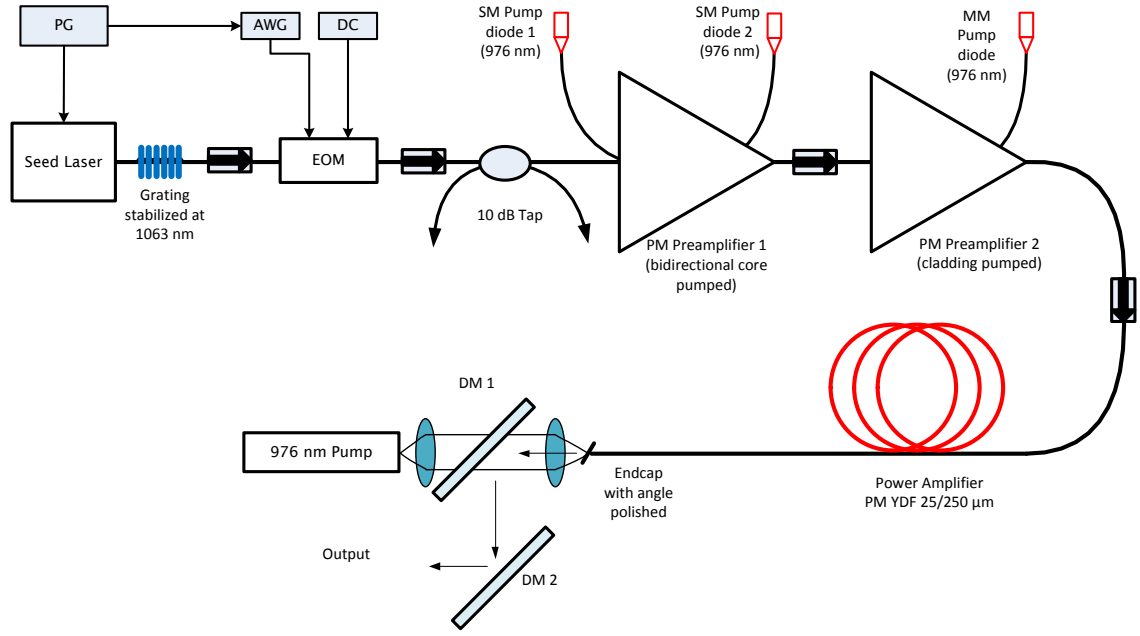

Figure 3.5. Configuration for PM ytterbium-doped fiber MOPA system

A schematic of the system is shown in Figure 3.5. The setup used was an improved version of the system demonstrated earlier [6]. In the present case an arbitrary waveform generator (AWG7000 from Tektronix) with higher bandwidth (~3 GHz) and better temporal resolution (~350 ps) was used instead. Higher resolution allows the generation of rectangular electrical pulses with faster rise and fall times. Besides that, the PM LMA fiber used in the power amplifier (Nufern PLMA-YDF-25/340) was replaced with Nufern PLMA-YDF-25/250 fiber. This PLMA fiber had higher Yb doping concentration and smaller cladding diameter, resulting in ~3 times higher absorption at 975 nm pump wavelength as compared to the previous fiber. Consequently the total fiber length can be reduced to allow higher extracted energy without crossing the Raman threshold.

The seed was a fiber pigtailed Fabry-Perot laser diode (Bookham CPE425) with wavelength stabilized at 1060 nm using an external PM fiber Bragg grating. The optical output of the seed laser passed through an in-line high extinction ratio (~45dB) lithium niobate electro-optic modulator (EOM), which was driven by an arbitrary waveform generator (AWG) with ~350 ps temporal feature resolution. The seed signal was adaptively shaped by the EOM and amplified by an all-fiber three-stage PM amplifier chain to deliver single mode, single polarization output of the required pulse shapes and power levels.

The first pre-amplifier stage is based on a core pumped, Yb^{3+}-doped PM fiber (Nufern PM-YDF-5/130) with a mode field diameter and NA of 6.5 µm and 0.13 respectively. The amplifier

was bi-directionally pumped by wavelength stabilized 975 nm single-mode laser diodes. The core absorption of the fiber was 680 dB/m at 975 nm. A 2.5 meter length of this fiber was used such that the amplifier provides maximum gain around 1060 nm. The output of the first stage amplifier was coupled into the second pre-amplifier stage via an optical isolator. The isolator limits both signal and ASE back-coupling between the two amplifier stages.

The active medium of the second-stage amplifier was a double-clad Yb^{3+}-doped PM fiber (the same Nufern PM-YDF-5/130 but now operated in a cladding pumped configuration). The cladding diameter of the fiber was 130 μm and the pump NA was 0.46. The measured effective cladding absorption for pump light launched into the cladding of the fiber at the pump wavelength (975 nm) was 1.7 dB/m. A 6 m length of fiber was used such that the amplifier provides maximum gain at the signal wavelength. The gain medium was counter-pumped by a 975 nm fiber-pigtailed broad-stripe diode laser through a single (6 + 1) fused tapered fiber bundle (TFB).

The output from the 2nd pre-amplifier stage was spliced to the slow-axis of an in-line fast axis blocking PM isolator to reduce the non-polarized ASE and to increase the optical signal to noise ratio (OSNR) into the final amplifier. The resulting single polarization signal was then coupled into a large mode area (LMA), PM, double-clad, Yb^{3+}-doped active fiber (PLMA-YDF-25/250 from Nufern). The fiber has a core diameter of 25 μm and a core NA of 0.06. The cladding diameter of the polymer coated fiber was 250 μm with a cladding NA of 0.45. The measured cladding absorption of the fiber at the pump wavelength (975 nm) was 5.1 dB/m. A 4 m length of this fiber was chosen such that the amplifier not only provides optimum signal gain but also absorbs most of the launched pump power. To minimize the splice loss between the passive single-mode PM fiber (SM98-PS-U25A from Fujikura) and the LMA active fiber the outer diameter of the LMA fiber was tapered down to 90 μm and a core diameter of 9 μm. This helps to reduce the mode field diameter mismatch between the two dissimilar fibers ensuring lower splice loss. Moreover tapering allowed us to obtain robust single mode operation even though the active fiber core can support several transverse modes. To prevent damage to the output, a 1.3 mm long pure silica mode-expanding end-cap was spliced to the fiber end which was angle-polished to avoid power being retro-reflected back into the fiber core.

The amplifier was end-pumped using a 975 nm diode stack with a maximum pump power of 106 W. The diodes were water-cooled to ensure good wavelength stability. A simple lens combination was used to achieve ~80% coupling efficiency into the fiber. The signal and pump paths were split by dichroic mirrors.

3.2.2 Custom Optical Pulse Shapes Demonstration with EOM

A total average output power of 72 W was measured from the fiber MOPA using a 100 ns shaped optical pulse at 100 kHz repetition frequency. This corresponds to a maximum pulse energy of 0.72 mJ. The OSNR was measured to be ~25 dB. Although short wavelength ASE band started to grow at higher power, most of the energy is confined in the optical pulse. The measured polarization extinction ratio (PER) was 18 dB under full power operation. The peak power was estimated to be approximately 7 kW with no trace of a Raman line. Further increase in output peak power may still be possible by operating the fiber MOPA at a lower duty cycle.

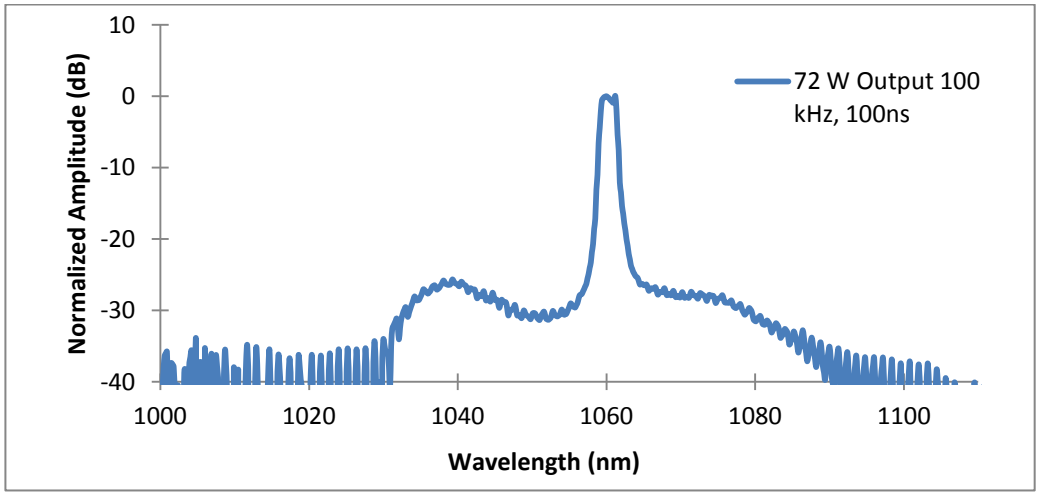

Figure 3.6. Spectrum of PM MOPA with the total output power of 72 W (0.72 mJ).

Optical beam quality is an important parameter for material processing application. For this fiber MOPA, the output M^2 was measured to be 1.1 with circular spot size which is essentially a diffraction limited output beam.

The use of EOM as pulse shaping element allows tailoring of the output optical pulse for specific applications. The limitations of this technique are the higher cost associated with the EOM and that it cannot sustain high optical intensity. As a result, pulse shaping has to be done at the beginning of the MOPA chain where the optical intensity is relatively low and the extra amplifier has to be used to compensate for the loss suffered by the signal due to the high insertion loss of the EOM.

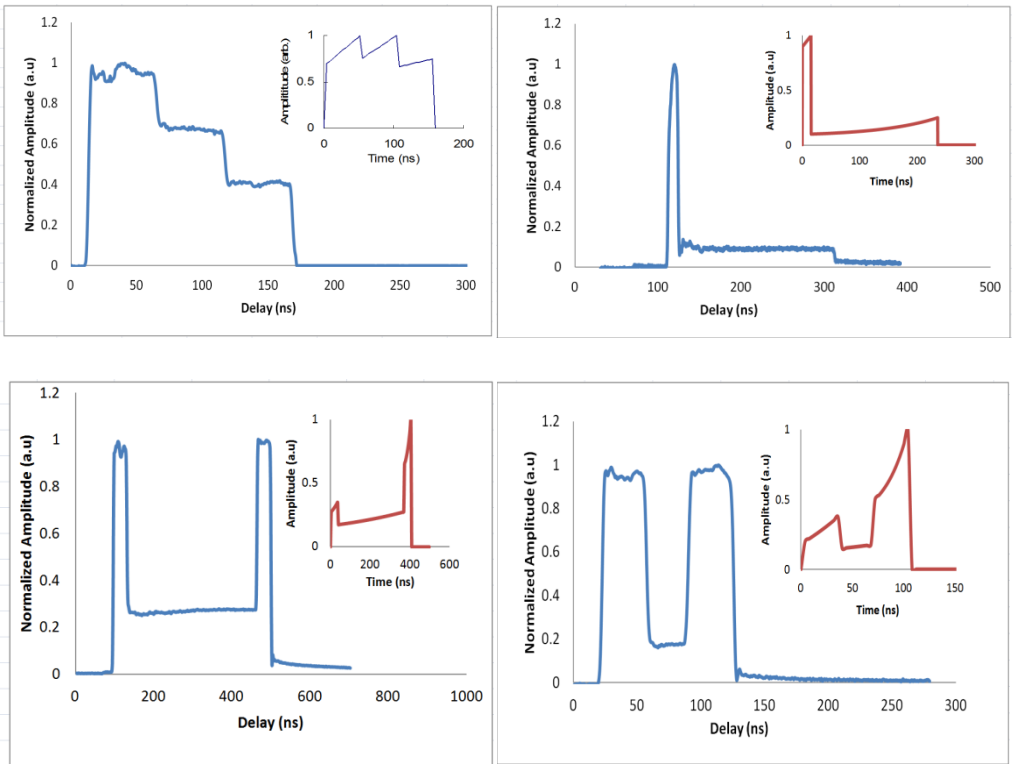

Figure 3.7. Various shapes of the optical pulse at the output of the MOPA measured with a fast photodetector. Insets show the respective electrical pulse shapes generated by the AWG.

As a demonstration of the versatility of this fiber MOPA, we demonstrated a few pulse shapes ranging from double step, triple step, and double peak pulses. Figure 3.7 shows the normalized output pulse and the corresponding electrical input pulse profile generated by the AWG. In the case of triple step pulses, the instantaneous power at every step can be tailored to the desired power. With this demonstration, a whole new class of research on the effects of temporal profile on machining of silicon can be carried out. For example, the use of an energy-bridge between the two peaks in Figure 3.7 helps to maintain the molten state to facilitate the thermal diffusion for deeper material penetration before the second peak arrives and vaporises the material. The upgrade in the shaping component (using faster AWG) has provided more flexibility in tailoring the temporal profile. More results of the tailored temporal pulse profile on material processing obtained with this source are described in Section 3.4.

3.3 SMART Fiber Laser System

The development work of SMART fiber laser was done together with SPI Laser as the project partner. The objective of this work is to develop a nanosecond MOPA laser system in an all fiber configuration at 1060nm region with the capabilities of producing high average power in excess of 50 W and high pulse energy (~1 mJ). The entire MOPA system has to be developed utilizing the least number of amplifier stages and optical components in order to reduce the system complexity and cost. As for the fiber amplifiers, the cladding pumping technique will be deployed, utilizing SPI's proprietary GT Wave technology. The SMART laser system will be fitted with an active pulse shaping capability similar to the nanosecond fiber MOPA discussed in the previous section (Section 3.2). However, EOM will not be used in this system. Instead, the investigation on the pulse shaping capability using an acousto-optic modulator will be carried out. The investigation will include effectiveness of pulse shaping, challenges and the suitable place for AOM to be placed in the MOPA setup. Lastly, the peak power handling of the SMART fiber laser system will be carried out experimentally.

The non-PM ns MOPA system developed solely for material processing applications consisted of a directly modulated seed diode, a pre-amplifier and a power amplifier as shown in Figure 3.8.

The seed diode used in the system is capable of producing pulse durations from 30 ns up to hundreds of nanoseconds with a repetition frequency ranging from hundreds of Hz to hundreds of kHz. The grating stabilized output from the directly modulated seed diode was coupled into the pre-amplifier which consisted of an 8 m long single mode GT Wave fiber with a core diameter of 10 μm and a cladding diameter of 125 μm (for both the signal and pump rods). The pre-amplifier was pumped in the backward direction by a 940 nm multimode pump diode with a maximum pump power of 8 W. The output from the pre-amplifier was fed into an acousto-optic modulator with maximum power rating of 1 W. The AOM was triggered and controlled by an Arbitrary Wave Generator (AWG) at the same frequency as the diode modulation frequency. The output of the AOM was coupled into another GT-Wave fiber-based power amplifier. The core diameter of this fiber was 14 μm while the cladding diameter was 130 μm. The length of the GT Wave fiber was 7m. The amplifier was backward pumped using 7 spatially combined 940 nm pump diodes via a 7x1 TFB producing a total of 80 W of pump power. The output of the power amplifier was spliced to a 1.3 m long delivery fiber followed by a beam delivery optic assembly to safeguard the output end from optical or mechanical damage. There were various taps along the MOPA chain to monitor the system. The inline isolators were used to prevent any backward propagating signal or ASE to cross couple into the previous stage or to the seed diode.

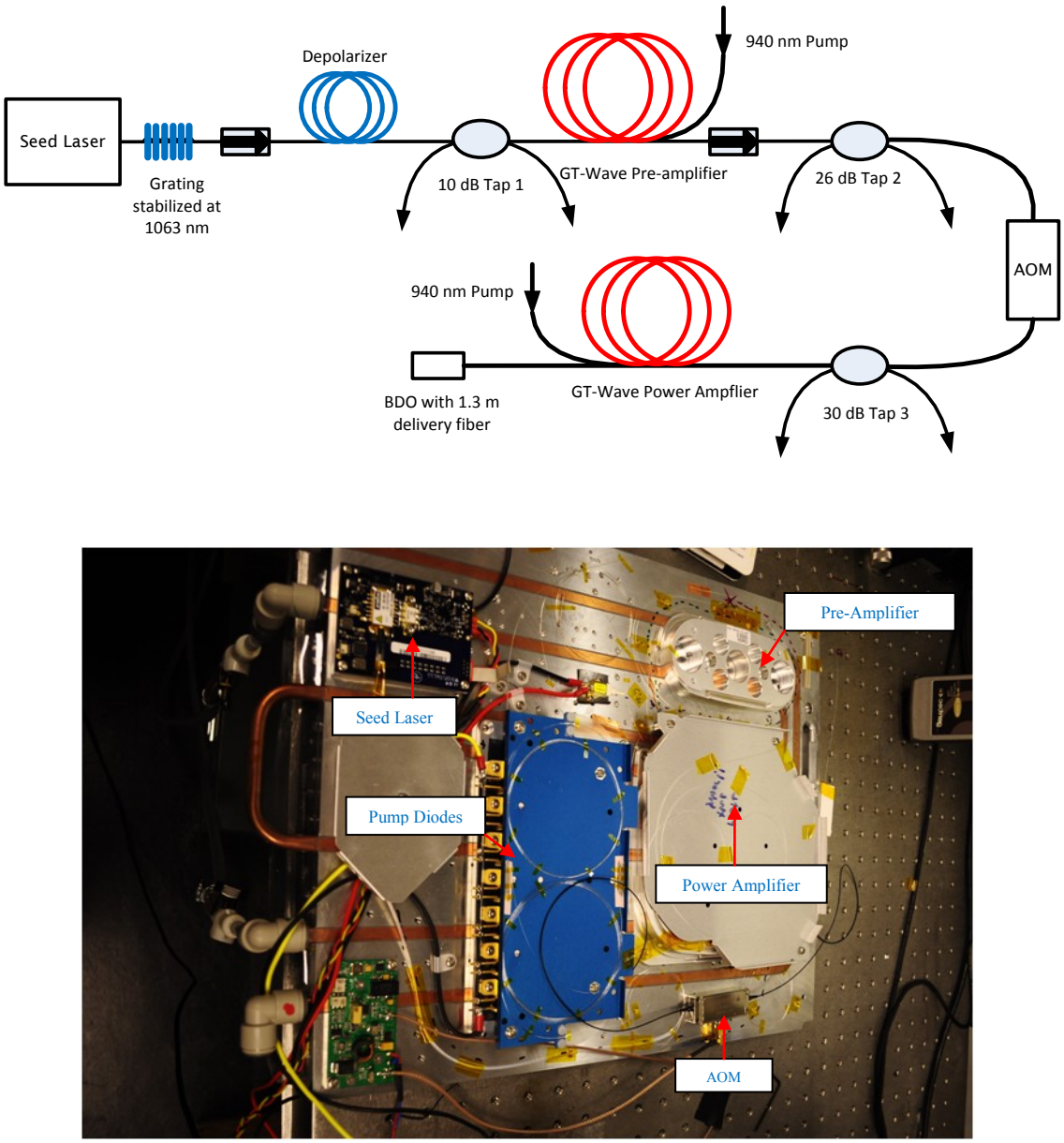

Figure 3.8. (Top) Schematic of SMART ytterbium-doped fiber laser system and (bottom) the photo of the actual setup

3.3.1 Seed Laser

Electrical pulse width (ns)	Optical pulse width (ns)
10	5
20	14
30	21
40	32
50	41
60	52

Table 3.1: Optical pulse width generated from the ns seed diode with various electrical inputs from the Stanford pulse generator at 450 kHz.

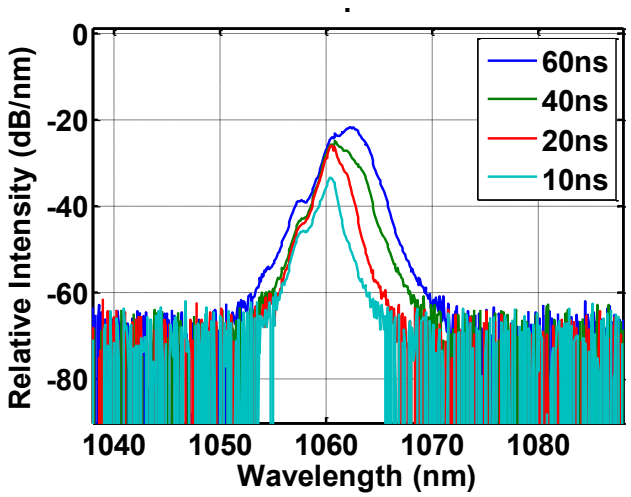

Figure 3.9: Spectrum of the seed diode for different electrical pulse width

The seed diode used in this setup was designed by SPI Lasers. This nanosecond seed diode came together with the driver board and could operate in both pulsed and CW modes. The diode pigtail was spliced to a 1063nm grating to stabilize the output wavelength. In order to operate in the pulsed mode, a Stanford pulse generator (1MHz bandwidth) was used to feed in an electrical pulse signal into the driver to generate an optical pulse. The response of the driver to the input electrical signal (the time delay of the driver to generate signal) was measured to be 9 ns. The various optical pulse widths obtained with different electrical input signals are shown in Table 3.1. The corresponding optical spectra are shown in Figure 3.10, it is apparent that for electrical pulse width shorter than 40ns, the central wavelength is not located at 1063nm. This is because

the feedback from the grating does not arrive back at the diode in time before the diode threshold is achieved and the device begins to lase.

The interaction of optical feedback in the laser diode can be clearly observed by plotting a spectrogram. In order to obtain the spectrogram, an optical pulse will be divided into 'n' section with a fixed step size (as illustrated in Figure 3.10 (a)). The spectrum for each section will be measured and the collected spectrums will be compiled to obtain the wavelength vs time delay spectrogram. From Figure 3.10, it can be seen that the diode only sees the feedback coming from the grating after 35ns. Thus, the shortest optical pulse width that can be generated by this grating stabilized seed diode ensuring a stable output without wavelength and intensity instabilities is around 30ns.

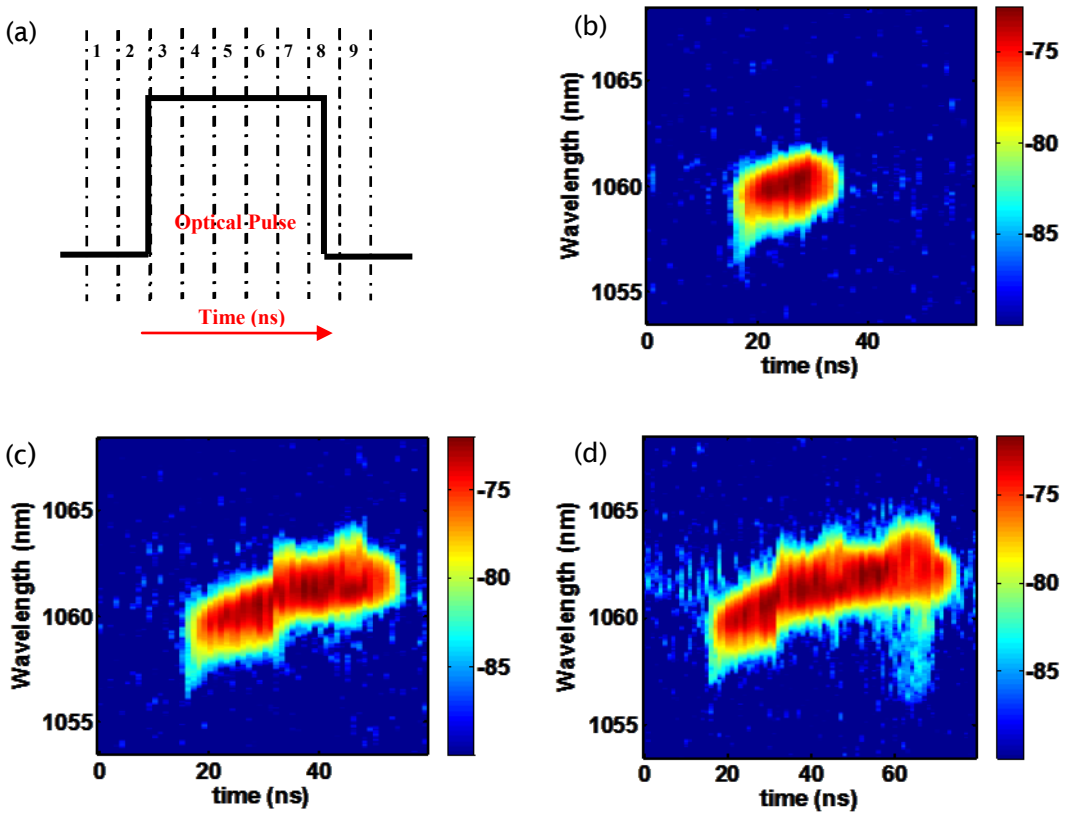

Figure 3.10: (a) Division of optical pulse into sections for spectrogram measurement. Spectrogram obtained for (b) 20ns, (c) 40ns and (d) 60ns electrical pulse width

The maximum average output power of the seed diode in the CW mode was 500mW. However, when operating in the pulsed mode, the output power varied as a function of the duty cycle of the generated optical pulse stream. A depolarizer was so as to avoid Polarization Dependent Gain within the amplifiers. A length of PM980 fiber (~30m) was used to build the depolarizer. The fiber was broken at the midway point and spliced together with the principal polarization

axes misaligned by 45˚. This ensures that the linear polarization of the input signal has polarization components both in the x and y directions.

3.3.2 Pre-amplifier Stage

A single stage pre-amplifier was used in between the seed laser and the final amplifier to boost the output power of the seed source to the 300-400mW power level over a large operating duty cycle of 1-1000. . The amount of output power was found to be adequate to saturate the final amplifier even after 3dB insertion loss at the isolator and AOM pair.

Long pulse amplification

First the amplification of pulses of 100ns temporal width was investigated. The seed diode was modulated with a square electrical pulse of 110ns at a repetition rate of 100 kHz. The average output power from the seed diode was 4mW. The output pulse and spectrum from the seed diode are shown in Figure 3.11. The 3dB spectral bandwidth as measured by an ANDO OSA at a resolution setting of 0.05 nm was1.9 nm.

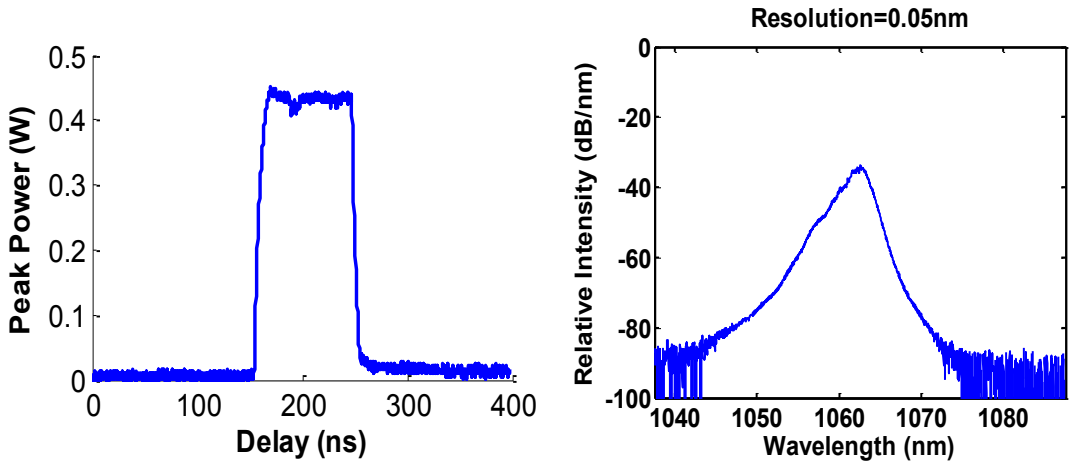

Figure 3.11: Pulse shape (100 ns) and spectrum at the input of the pre-amplifier

The pulse shape and the spectrum at the output of the preamplifier are shown in Figure 3.12. A maximum output power of 730 mW was measured at a pump power of 2.9W corresponding to a signal gain of 22 dB. The spectral bandwidth of the amplified signal was measured to be 2.5 nm. The output power and the signal gain at different pump power are shown in Figure 3.13.

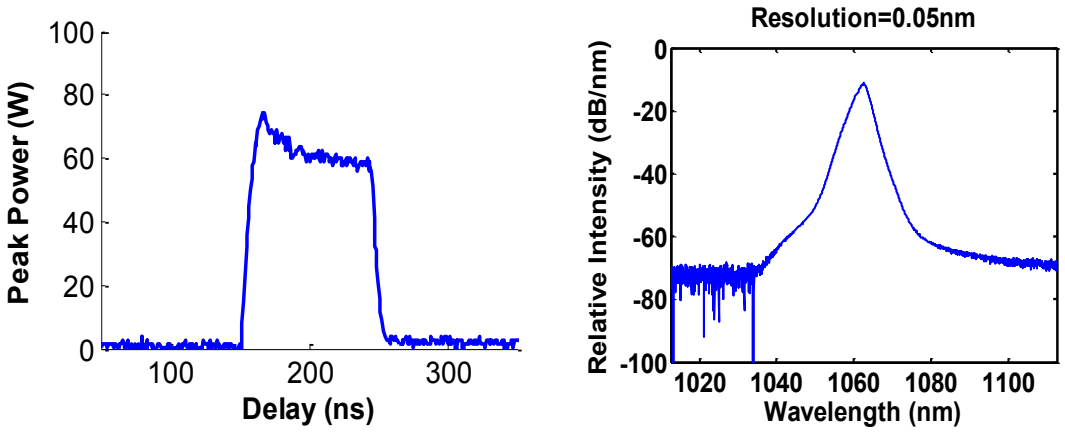

Figure 3.12: Pulse shape and spectrum at the output of the pre-amplifier. The pulse energy was calculated to be 7.3μJ.

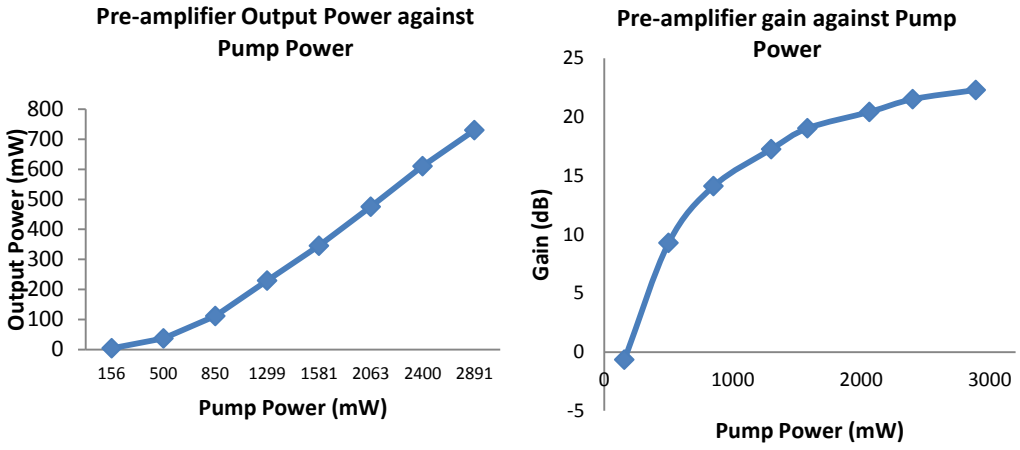

Figure 3.13: Output power and gain extracted from the pre-amplifier with 100 ns pulse.

The plots clearly show that gain saturation occurs within the preamplifier. The value of saturation energy and initial gain can be estimated by fitting Equation (3. 11) to the gain curve across the experimentally obtained optical pulse. The result is shown in Figure 3.14. The small pulse distortion seen at the output of the preamplifier is the result of the time varying gain saturation effect on the pulse during amplification [14]. The saturation energy is estimated to be 45 μJ and the initial gain is 23.6 dB. The gain decreased gradually from 23.6dB to 23dB across the pulse.

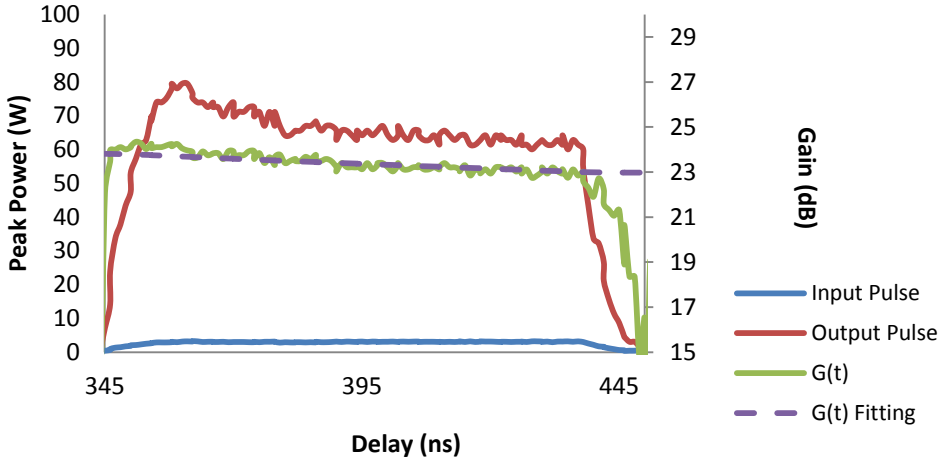

Figure 3.14: Gain evolution across the output pulse. Fitting was done by using Equation (3. 11).

Short pulse amplification

Next, short pulse amplification was investigated to understand the capability of this fiber amplifier to generate amplification of short optical pulses coupled with higher extracted energy and minimal noise generation. As for this investigation, the parameters for the input signal from the seed laser were 40 ns pulse duration at 40 kHz repetition rate. The choice of a 40 ns optical pulse was made to ensure sufficient time for the feedback signal to return before the diode reached threshold. The average output power from the seed diode at this setting was 0.48 mW with a spectral bandwidth of 2.3 nm. The output temporal and spectral profiles of the seed diode are shown in Figure 3.15.

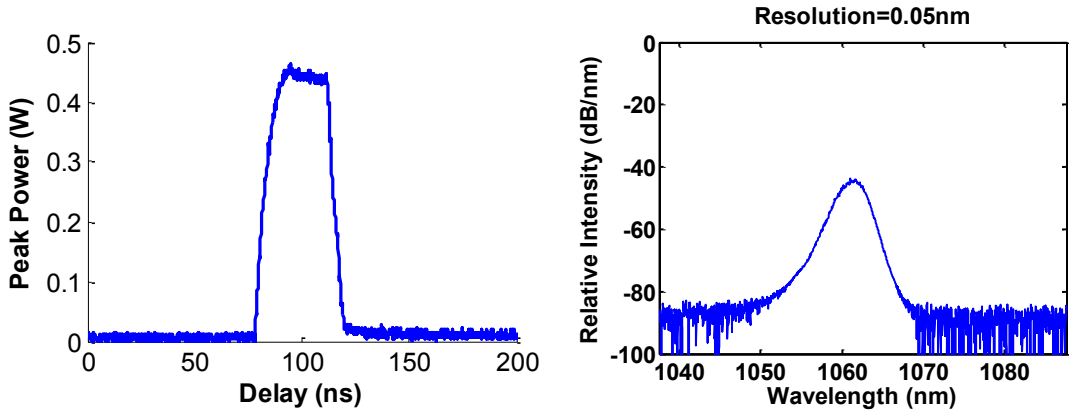

Figure 3.15: Pulse shape (30ns) and spectrum at the output of the seed diode.

The profiles of the amplified pulses after the preamplifier with 31dB of gain (3.1W pump power) are shown in Figure 3.16. The spectral bandwidth measured was 7.12 nm. Introduction of the fiber coupler and isolator after the preamplifier substantially increase the nonlinear fiber length and exacerbate the spectral broadening. The spectral broadening observed here is

believed to be due to the combined effect of SPM and SRS as a result of the high peak power associated with the optical pulses. Because of Raman gain the longer wavelengths experience additional gain resulting in the spectrum becoming asymmetrically broadened as plotted in Figure 3.16.

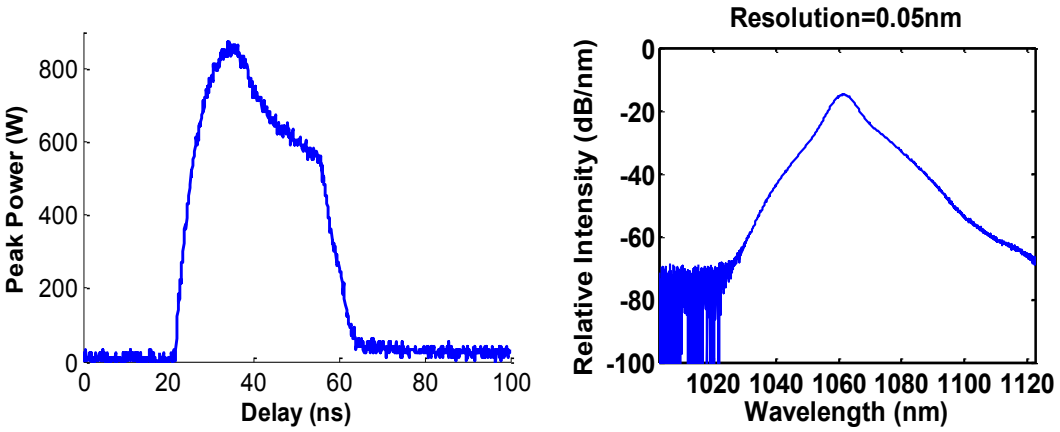

Figure 3.16: Pulse shape and spectrum at the output of the pre-amplifier. Pulse energy was calculated to be 10 µJ.

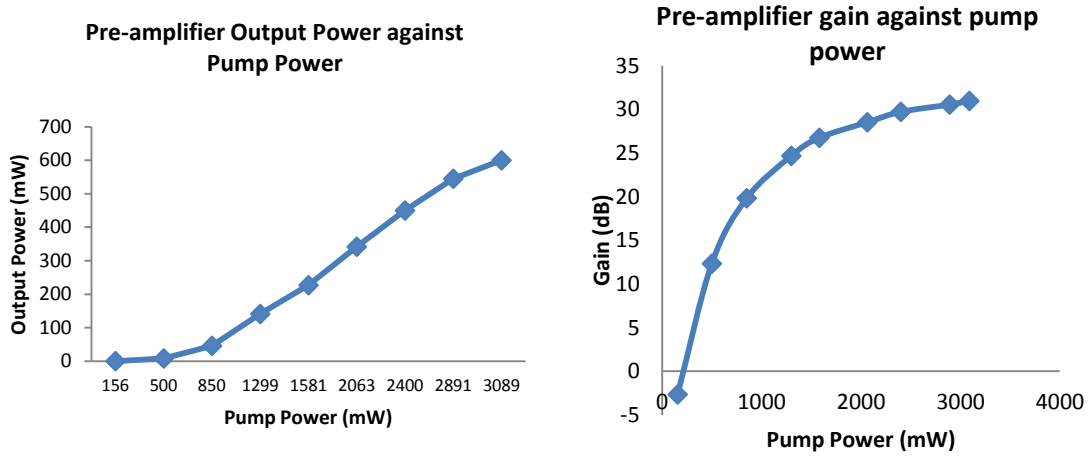

Figure 3.17: Output power and gain extracted from the pre-amplifier for 30ns pulse

The output power and the signal gain at different pump powers are shown in Figure 3.17. The gain started to roll off at the 22 dB level. Nevertheless, the gain curve showed a slower rise with an increase in pump power. The average signal output power was measured as 600mW with an estimated pulse energy of 10 µJ. The estimated initial gain was 36 dB. The shape of the output pulse shows a minor distortion with the gain across it varying from 35dB to 31dB as shown in Figure 3.18.

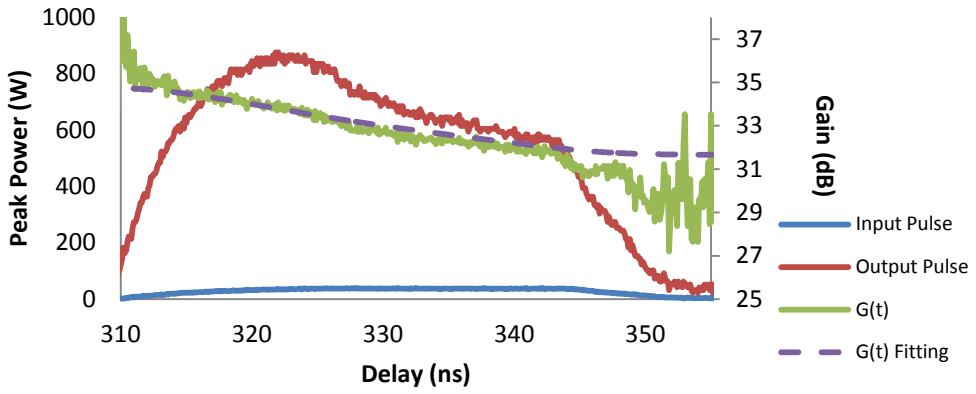

Figure 3.18: Gain evolution across the output pulse.

3.3.3 Power Amplifier Stage

The power amplifier was the final amplification stage of the system. About 400mW of signal was coupled into the power amplifier. Figure 3.19 shows the average output power as a function of launched pump power for pulses with a temporal width of 100ns and repetition rate of 100 kHz. Up to 45W of average output power was achieved. No sign of roll-off in the signal output power shows that further power scaling should be possible with the availability of higher pump power. The slope efficiency with respect to the launched pump power was estimated to be 73% which corresponds to 83% with respect to absorbed pump power. The output from the power amplifier was diffraction limited with a measured M^2 of 1.1.

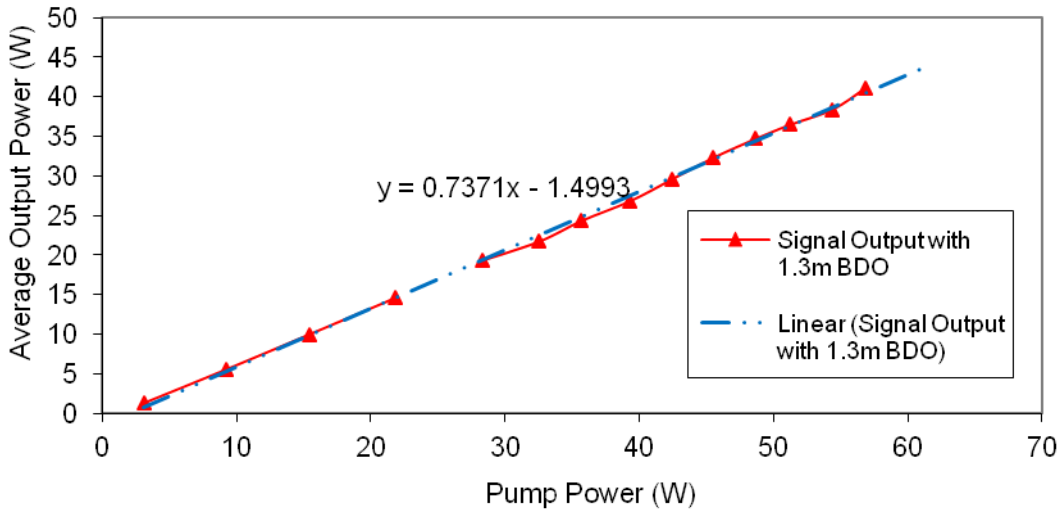

Figure 3.19: Average output power as a function of pump power. Up to 45W of average power was obtained with a pulse energy of 0.45mJ.

Figure 3.20 shows output pulse shapes and spectra at 3 different output powers. The output pulse shape starts to distort as the output crosses the 20W level. Higher gain extraction at the

leading edge as compared to the falling edge causes the pulse shape to turn asymmetrical with a sharp leading temporal feature. The overall pulse duration reduces as the pulse distortion becomes more significant. In addition, the spectrum at 20 W shows a symmetrical shape, but at 39 W and 45 W power levels, the spectrum broadens. The broadening effect is significant towards longer wavelengths. This is likely due to the effect of Raman gain in the fiber.

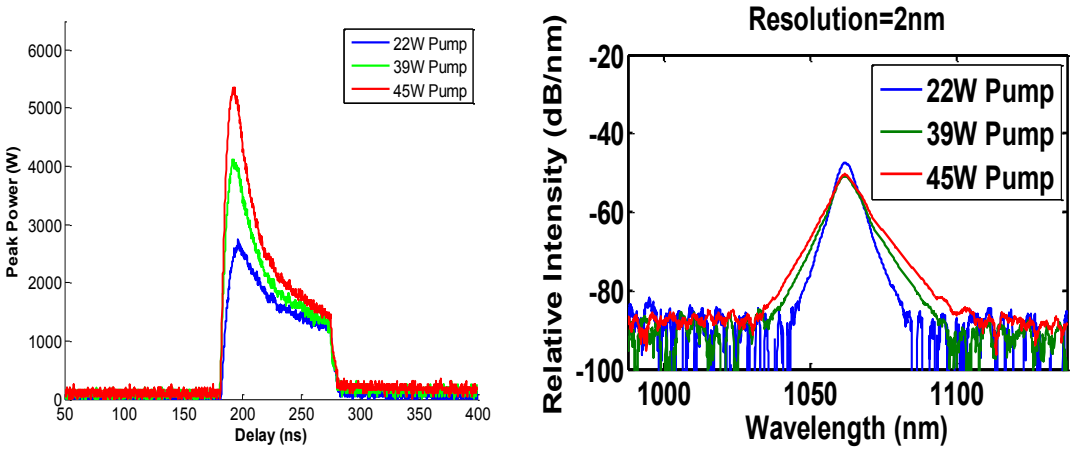

Figure 3.20: The evolution of pulse shape and spectra as a function of pump power coupled into the power amplifier.

In order to estimate the fiber saturation value, fitting of Figure 3.21 using Equation (3. 11) can be performed again. With an initial gain of 21 dB, the saturation energy of this fiber amplifier is estimated to be 0.1 mJ.

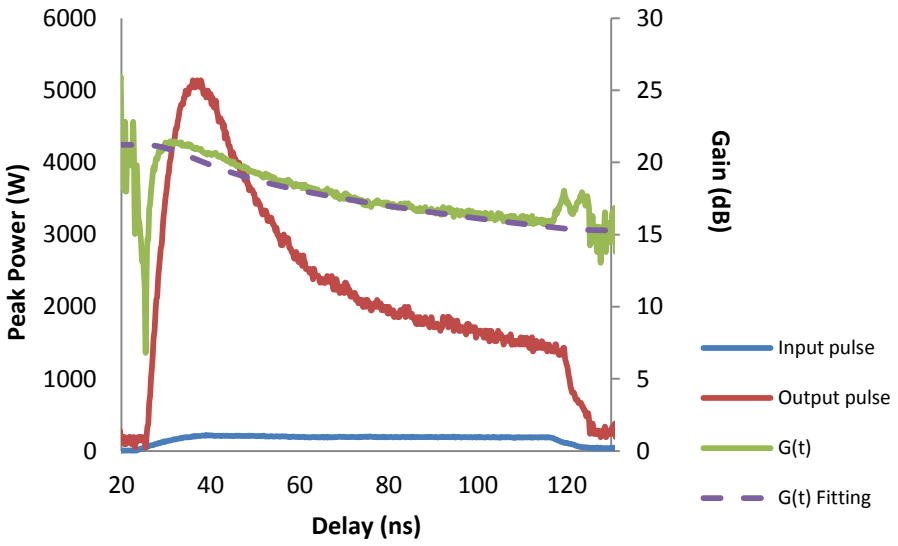

Figure 3.21: Gain evolution G(t) across the output pulse at a pump power of 45W. The estimated saturation energy was 0.1mJ.

Since the estimated fiber saturation energy is 0.1mJ, a maximum extraction energy of ~1.0mJ thus this is possible[19]. However, in order to extract the maximum energy from the amplifier, the gain saturation effect which causes pulse distortion has to be addressed first. This was implemented by using an Acousto-Optic Modulator (AOM) and will be discussed further in the next section.

The ASE propagating in the backward direction is shown in Figure 3.22. It shows that the backward travelling ASE got suppressed by 6dB at the signal wavelength and more than 20dB elsewhere after passing through the AOM. The inline isolator ensured the total suppression of the backward travelling ASE and protected the pre-amplifier from any unwanted feedback. Besides suppressing the backward travelling ASE, the AOM also removed any forward generated ASE. This ensured a clean signal to launch into the power amplifier and prevented any forward ASE from being amplified within the amplifier.

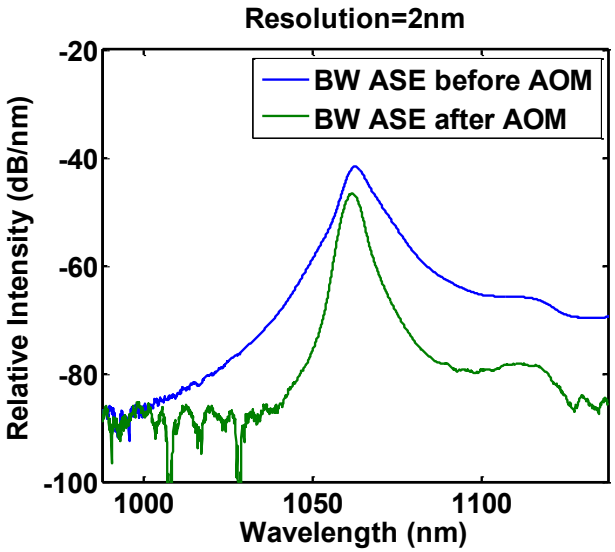

Figure 3.22: Spectra of backward travelling ASE before and after propagating across the AOM when operating at pump power of 45W.

3.3.4 Active Pulse Shaping with AOM

An AOM developed by Gooch and Housego was placed in between the two amplification stages as shown in Figure 3.8. The location of the AOM was chosen such the slightly distorted pulses after the preamplifier can be appropriately manipulated before being amplified further by the power amplifier. The insertion loss of the AOM was measured to be 1.5 dB with an extinction ratio of 50 dB. The measured rise/fall time of the AOM was about 25 ns.

An AWG with compatible RF amplifier was used to drive the AOM. The desired pulse shape required from the AWG can easily be generated and controlled using an in-house developed MATLAB code. Due to the slow rise time of the AOM, the generated shape may not be as accurate as the predicted shape. In fact, due to its relatively modest speed, the usage of an AOM only allows shaping of the top of the optical pulse as shown in Figure 3.23. The opening time of the AOM was set to be much longer than the input pulse width in order to accommodate the entire input pulse without clipping the pulse due to its slow rise or fall time.

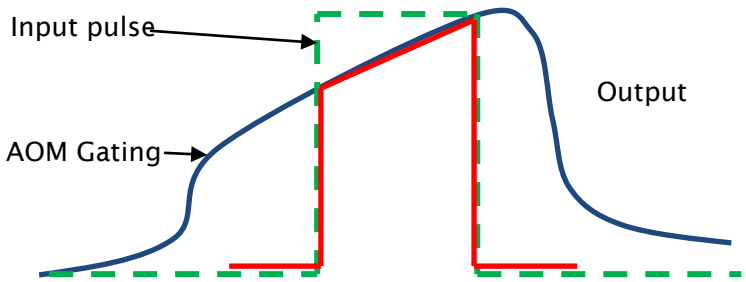

Figure 3.23: Illustration of the function of the AOM in shaping the top of the input signal pulse.

The importance of reshaping the top of the optical pulse especially the leading edge of the pulse is to reduce the gain saturation effect within the power amplifier. This will allow every part of the pulse to get amplified evenly and therefore the pulse energy can be increased without being limited by the gain saturation. Besides, the peak intensity can be varied such that it remains below the Raman threshold at various operating conditions and output powers. This will allow high pulse energy extraction from the power amplifier without sacrificing power to any Raman Stokes lines.

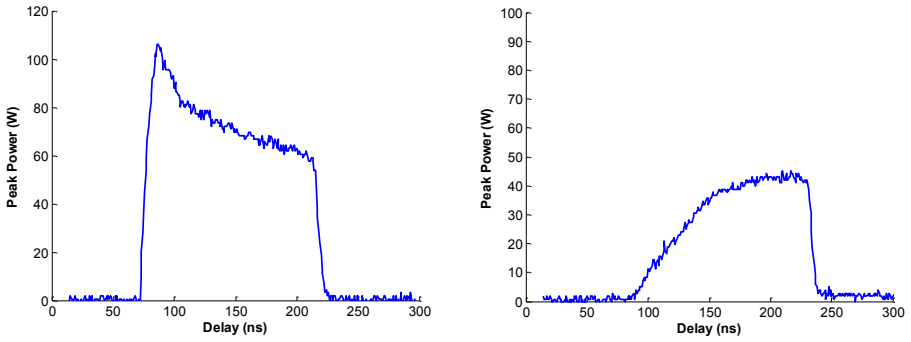

Figure 3.24: The input pulse shape into the power amplifier without (left) and with (right) pre-shaping using an AOM.

In demonstrating the effectiveness of the AOM as a pulse shaper so as to reduce the peak power while achieving maximum pulse energy, an experiment was carried out with a pulse duration of 150ns and repetition rate of 30 kHz. The input pulses before and after the temporal shaping are shown in Figure 3.24. The pulse suffered 3 dB losses in optical power due to the shaping by the AOM. Nevertheless, the input power was still sufficient to saturate the power amplifier and to produce the desired (~1 mJ) output pulse energy. Figure 3.25 shows both the spectral and temporal evolutions of the output pulse as a function of pulse energy.

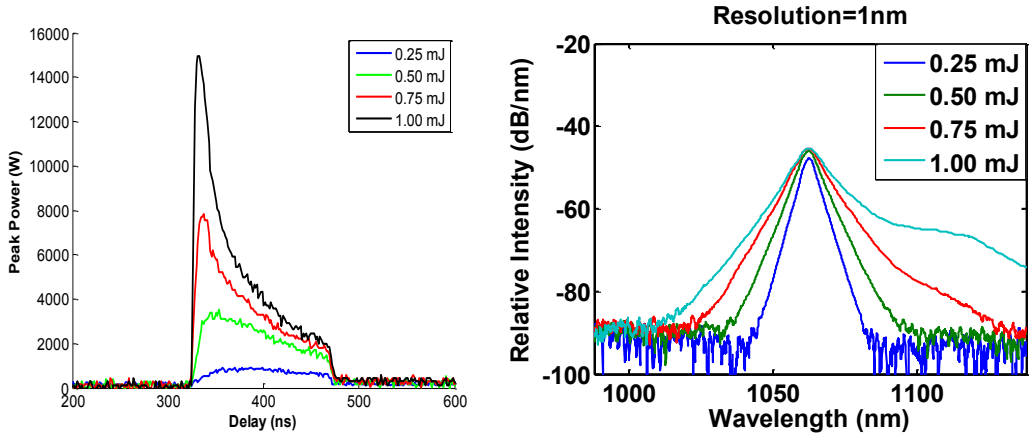

Figure 3.25: Temporal and spectral evolution of the of the optical pulses as a function of pulse energy.

During operation at 30W of output power, it was observed from Tap 3 (shown in Figure 3.8) that a small portion of the pulse travelling in the backward direction leaks through the AOM during the ON state with 120ns gating width. The reflected pulse appears to be 98.4ns delayed from the forward going pulse indicating that the reflection point was likely to be 8m away from Tap 3. This is likely to be the splice point between the BDO and the output of the power amplifier caused by the mode field diameter mismatch. As shown in Figure 3.26, the backward pulse does not look identical to the output pulse. The most probable explanation is that the gain extracted by the backward pulse is low for the first 60ns due to the forward pulse taking out all

the available population inversion. However, the remaining 40ns of the pulse will see more gain because of recovery of the population inversion as continuous pumping replenishes the excited atoms. This explains the reason for the smaller leading edge of the backward pulse. In order to mitigate the effect of the reflected signal leaking through the AOM and affecting the preamplifier from functioning properly, an optimum length of fiber was spliced in between the AOM and the power amplifier stage to provide an adequate delay for the reflected signal to ensure it arrived at the AOM only after the AOM was turned OFF. However, longer length of fiber will enhance the nonlinear effects. Thus, a balance between the length of fiber and the amount of backward signal that leaks through the AOM was devised such that the backward signal power that leaks through the AOM was within the ISO power rating.

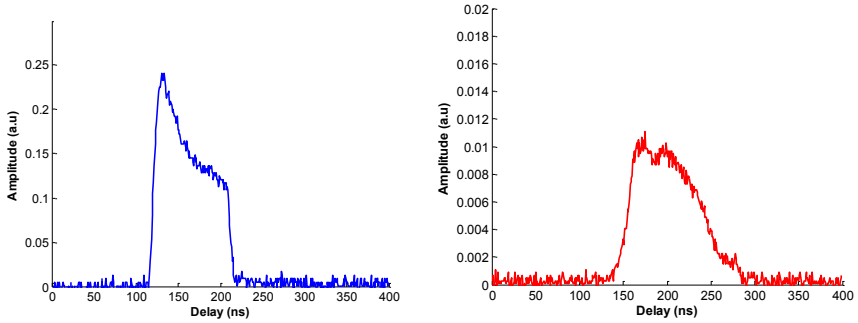

Figure 3.26: The output pulse shape (left) measured at an average output power of 15W and the corresponding reflected pulse shape (right) travelling in the backward direction.

3.3.5 Characterization of Beam Delivery Fiber

At the output of the power amplifier, a passive fiber was spliced and terminated with bulk optics. The passive fiber is known as the beam delivery fiber and the optics as the beam delivery optics. As the output of the power amplifier typically has a peak power in the kW regime. Thus, nonlinear effects such as SRS in the beam delivery fiber are readily generated. The following experiment is designed to study the effect of the length of the beam delivery fiber on the SRS generation.

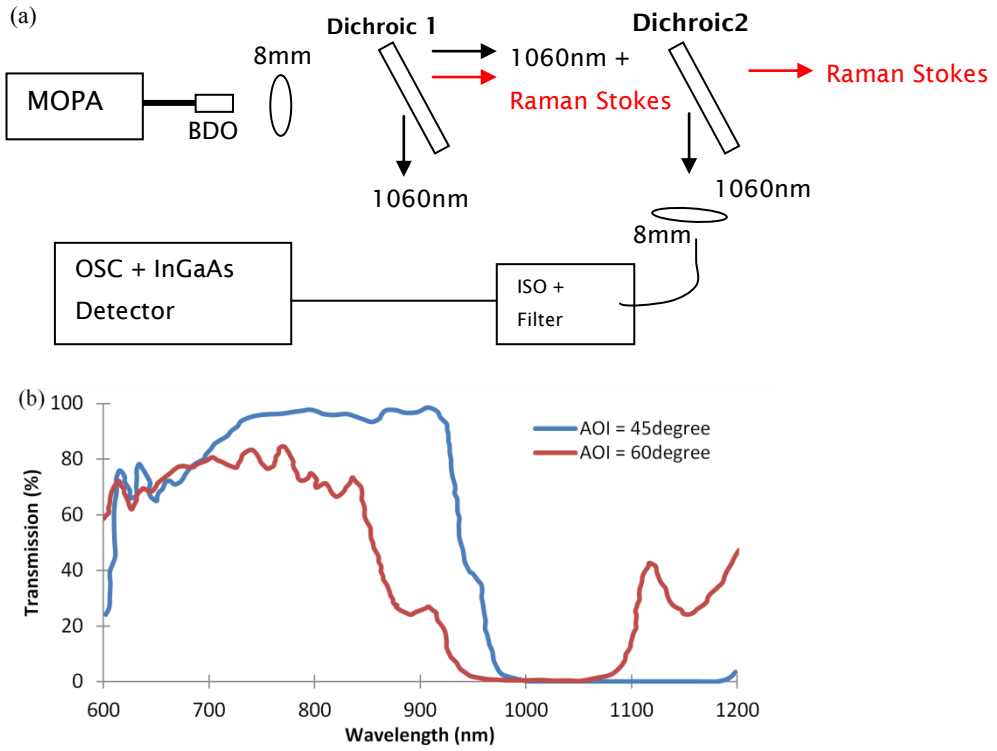

Figure 3.27: (a) The setup for measuring the SRS threshold at the output of the system and (b) transmission curve of the dichroic mirrors used at AOI of 45˚ and AOI of 60˚.

Figure 3.27 shows the setup to measure the SRS threshold. The initial length of the beam delivery fiber was set to 6 m. The operating parameters of the MOPA were 20 kHz repetition frequency and 100 ns pulse duration. In order to measure the SRS threshold, the system was set to operate at average output powers ranging from 5W – 11W. Two dichroic mirrors were used to separate the Raman Stokes and the signal wavelengths. The first dichroic mirror was positioned at 60˚ with respect to the incident beam path to reflect most of the power at the signal wavelength. The second dichroic mirror was also placed at 60˚ with respect to the input beam to reflect the remaining signal at 1060nm. The Raman Stokes wavelength was transmitted through both the dichroic mirrors (~40% at each mirror). The reflected signal was coupled into an ISO with integrated band-pass filter (bandwidth of 16nm) to filter out any additional Raman Stokes that might be present. An InGaAs photo detector was used to cover the wavelengths of the signal and Raman Stokes. This experiment was done by cutting back the lengths of the beam delivery fiber and the Raman thresholds of these lengths of fibers were investigated and plotted in Figure 3.28 together with the fitted curve using Equation (2.33).

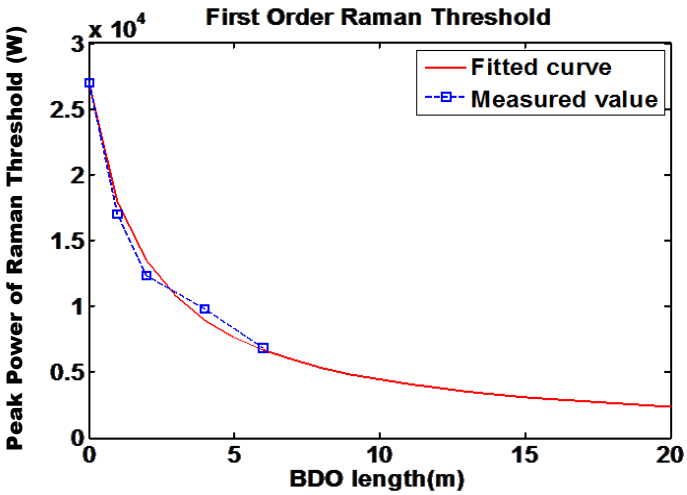

Figure 3.28: The peak power of the signal at 1060nm correspond to the first order Raman threshold for different lengths of beam delivery fiber. The blue squares are the measured values while the red solid line is the best fit calculated from Equation (2.33) with $g_R = 0.8 \times 10^{-13}$ m/W.

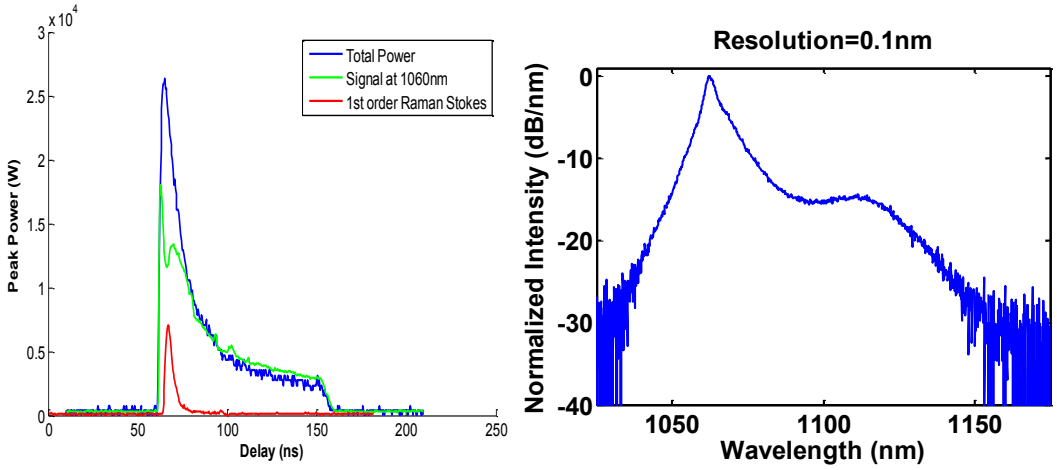

Figure 3.29: The pulse shape of signal and 1st order Raman Stokes as well as the output spectrum obtained for a delivery fiber length of 1m.

3.3.6 Overall Performance of SMART fiber laser

The SMART fiber laser system was successfully developed, utilizing the least number of amplifier stages. The laser system was also less complex as compared to the nanosecond fiber MOPA discussed in Section 3.2. In terms of laser performance, SMART fiber laser produced a maximum average optical power of 45 W. This is 35% less than the total optical power generated from the nanosecond fiber MOPA. However, optical power from the SMART fiber laser can be improved further with the addition of pump power. Furthermore, a pulse energy of up to 1 mJ was successfully extracted. The peak power was limited to 20 kW as a result of the 1m length of delivery fiber used. On the pulse shaping front, an AOM was used in the SMART fiber laser instead of EOM as demonstrated in the nanosecond fiber MOPA. Due to the slow

device response of the AOM as compared to the EOM, the shaping was limited to the leading edge of the optical pulse. This reduced the gain saturation effect in the optical fiber and also the amount of energy shifted to Raman Stokes lines. In addition, the placement of AOM in between the amplifier proved to be effective in isolating any backward propagating pulse from propagating back into the seed laser.

The outcome of the SMART fiber laser had provided SPI Lasers with crucial experimental data. The data was to be used in the development of their upcoming pulsed fiber laser system that is the G4 fiber laser. This G4 fiber laser system will have similarity with the SMART laser system in terms of the configuration and the optical performance.

3.4 Pulse Tailoring Application on Material Processing

This work was done in collaboration with Institute for Manufacturing (IFM), University of Cambridge and SPI Lasers under the SMART project. The objective of this work was to investigate Silicone material removal mechanisms using single pulse ablation with a variety of pulse shapes and pulse parameters (peak power and pulse energy). For short nanosecond pulses, the ablation process is dominated by heat conduction, melting, evaporation and plasma formation [20]. Material removal through vaporization is an energetically costly process. Melt dominated processes, although energetically efficient creates processing artefacts such as a molten lip. The presence of a high front peak in the pulse envelope can increase the absorption coefficient of Silicon material and increase the energy coupling of the remainder from the pulse tail [10]. Thus, by proper designing or tailoring the temporal profile of the pulse, improvements in surface quality can be demonstrated.

The following work was done using the two laser setups described in the earlier sections, which is the SMART fiber laser system and the nanosecond fiber MOPA system. Both systems offer unique capability that is useful for this work. The SMART fiber laser system was used to investigate the effect of pulse energy parameter on the response of the Silicone material. Two types of optical pulse parameters were used; namely the ‘unshaped’ pulses and ‘filled’ pulses. The ‘unshaped’ pulses refer to the context that no additional shaping was done to the seed pulse (rectangular shaped optical pulse). Due to the gain saturation in the amplifiers, the temporal profile for the unshaped pulses has a high front peak with a decaying tail. As for the ‘filled’ pulses, an additional energy (~20%) was added to the pulse envelope by shaping the optical pulse with the use of an AOM as described in Section 3.3.4. The nanosecond fiber MOPA system with the ability to generate the designer pulses was used next. The pulses were designed to have steep front peaks to alter material absorption and were followed by a low energy bridges.

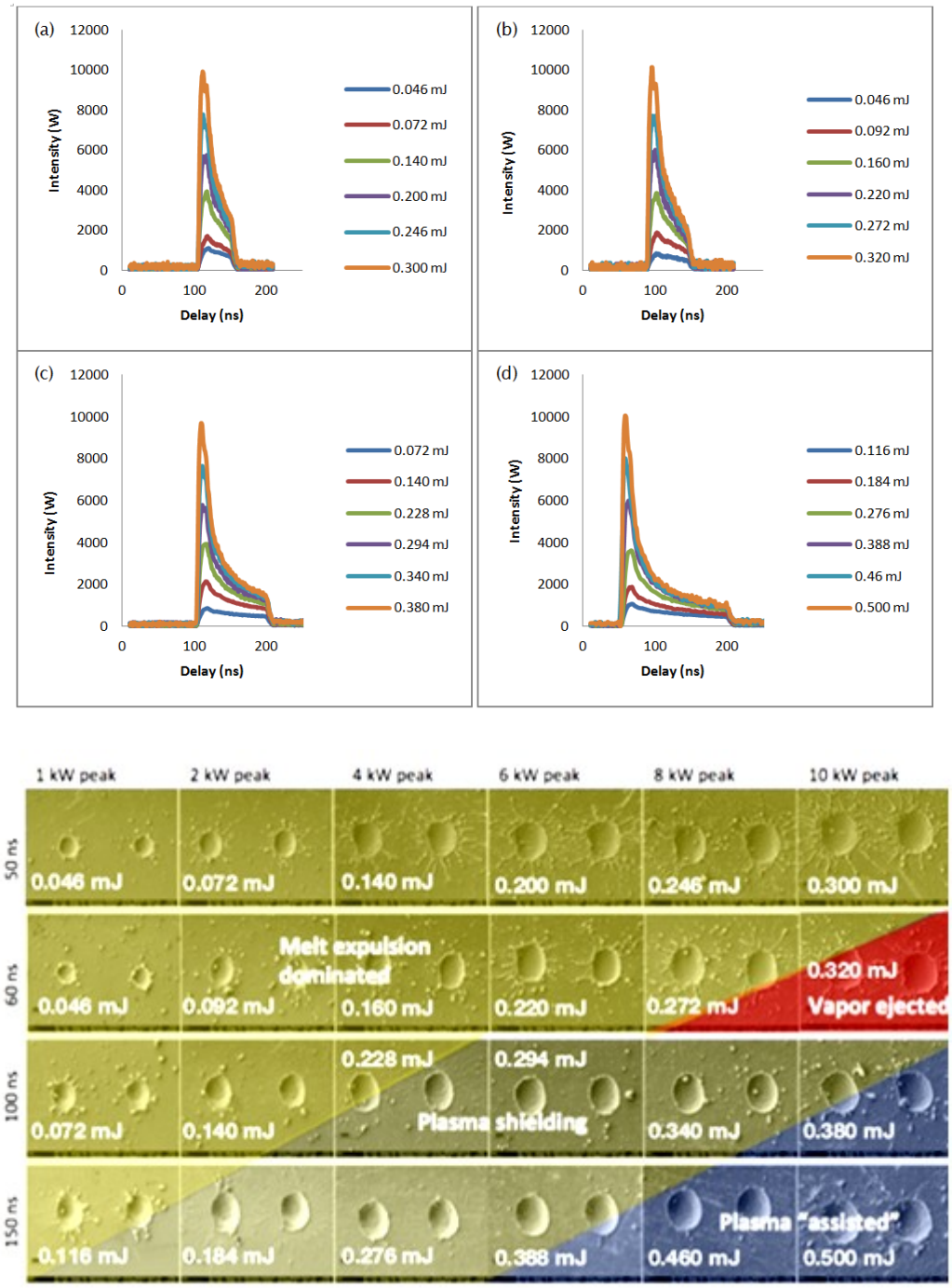

Figure 3.30. (Top) Unfilled pulse envelopes for (a)50 ns,(b) 60 ns, (c)100 ns and (d)150 ns. (Bottom) The Si material response on unfilled pulses.

Figure 3.30 shows the unshaped optical pulses and the response of the Si substrate. Figure 3.31 shows the 'filled' pulses and the corresponding material responses. In both figures, the yellow coloured area shows the parameter space where melt expulsion dominates while red, green and blue areas correspond to the parameter space where vapour ejection, plasma shielding and plasma assisted mechanisms respectively dominate. Four types of pulse duration were used in this work, namely 50 ns, 60 ns, 100 ns and 150 ns.

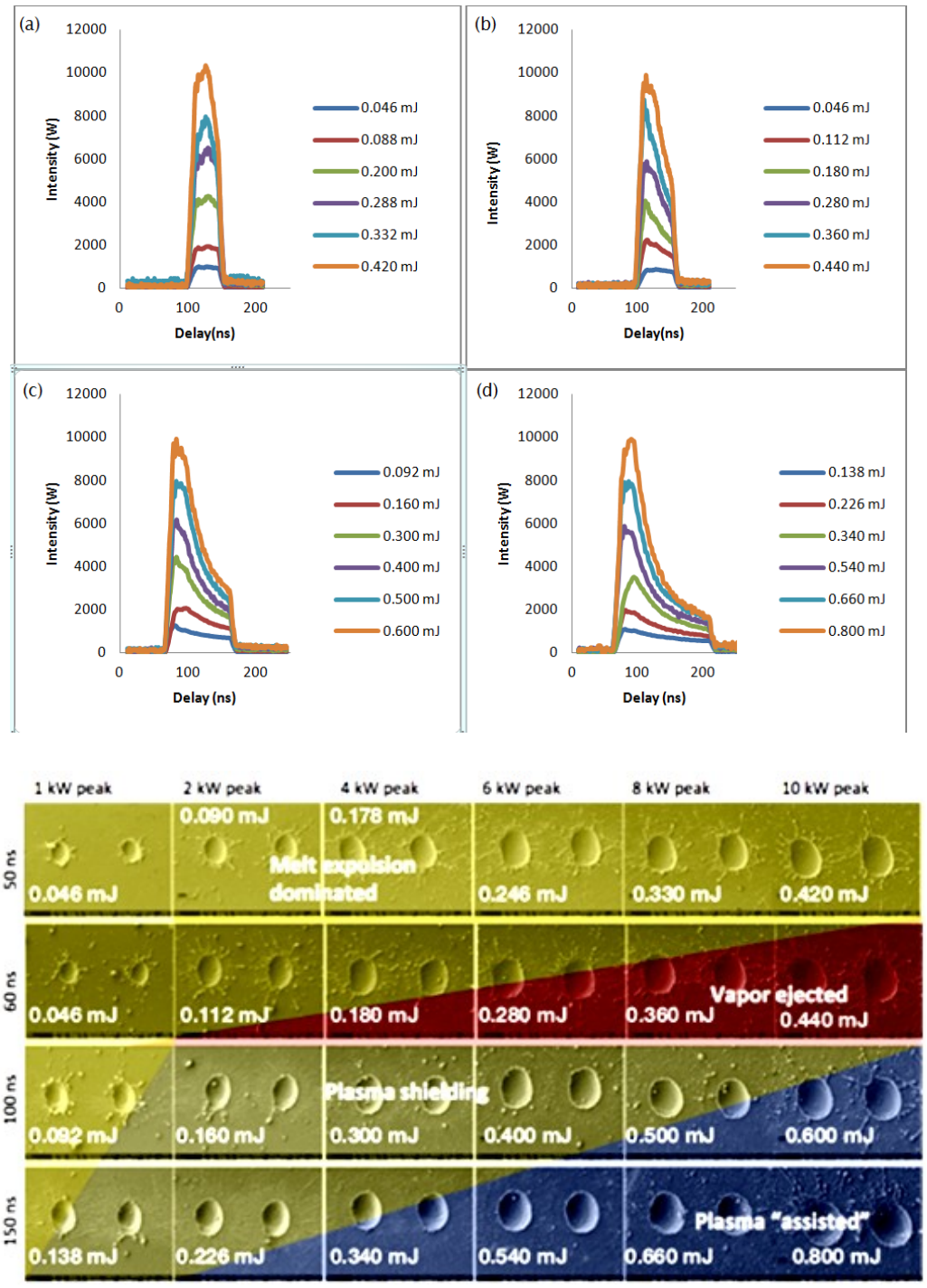

Figure 3.31. (Top) Energy filled pulse envelopes for (a)50 ns,(b) 60 ns, (c)100 ns and (d)150 ns. (Bottom) The Si material response on energy filled pulses.

In Figure 3.30, using 50 ns, unshaped pulse profile on Si material showed that the material removal was dominated by melt explosion. Furthermore, as the peak power increases gradually, the overall size of the hole increases. The ablated depth was measured to be ~2.5 µm and did not show any significant changes at higher peak power. On the other hand, the usage of longer pulses (>100 ns) resulted in cleaner and less splash surrounding the holes. The ablation depth also increased to approximately 4.5 µm and remained constant for different peak powers. The

extension of the pulse duration resulted in an increase in fluence on the material. The energy contained in the tail of the long pulse helps further vaporisation and ejection of molten materials. Furthermore, formation of plasma combined with a high peak power increased the hole diameter instead of the hole depth.

Using the filled pulses, no significant depth advantage were obtained as no changes in ablated depth with 50 ns and 100 ns filled pulses. The added energy purely contributes to replacing the melting dominated regime with plasma/vapour assisted regime.

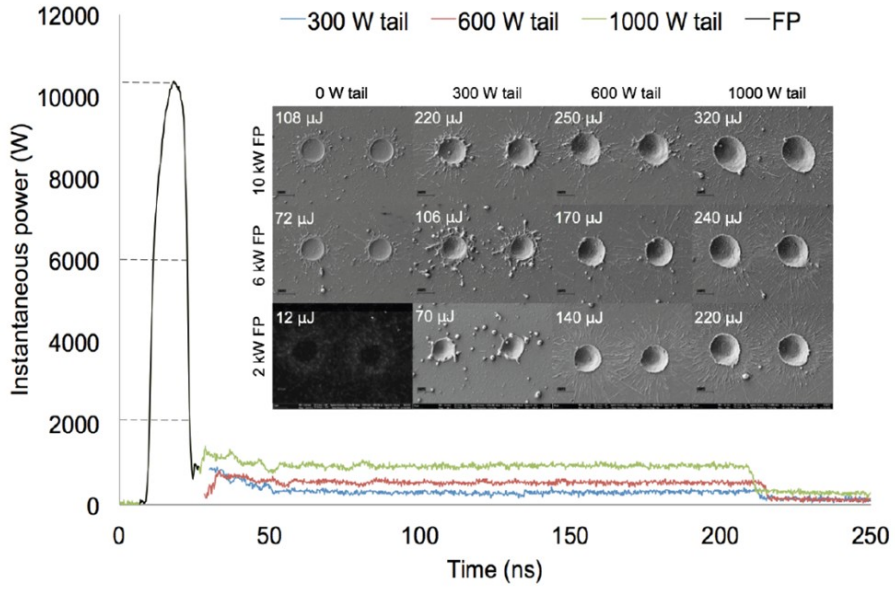

Figure 3.32. Si material response with tailored pulses having different peaks and tails power levels.

Figure 3.32 shows the design of the pulses and the material response. The tailored pulses have a high front peak (~25ns) for affecting the material absorption and are followed by a long energy tail of constant instantaneous power: 300 W, 600 W and 1 kW. The total pulse duration is 200 ns. A maximum hole depth of 8 µm was measured using tailored pulse with 10 kW peak power and with a 600 W tail. However, with 300 W tail, pulse with a 2 kW peak achieved higher penetration depth of 5.7 µm through a melt displacement mechanism with 70 µJ pulse energy. Pulses with 6 kW and 10 kW front peaks achieved a depth of 5 µm and 3.9 µm for 106 µJ and 220 µJ energy respectively. In 6 kW case, the extra energy was used to melt subsequent layers while for the10 kW case, the material was initially removed through a limited vaporization process followed by the remainder of the pulse coupled to the already molten material and created the crater depth through melt displacement.

Silicon responds better to optical pulses with steep front peaks and very low energy bridges as compared to unshaped and filled optical pulses. The designer pulses show a more controlled material response. Furthermore, by comparing the comparable pulse energies for traditional pulse envelopes and designer pulses, it shows that with the use of correct temporal envelope, the quality and material removal rates can be improved further.

3.5 Conclusion

In this chapter two nanosecond fiber MOPAs with slightly different configurations were demonstrated. The first setup was an improved version of the nanosecond MOPA reported earlier [6]. With a maximum average output power of over 70 W and close to 1 mJ of pulse energy, this fiber MOPA system produces a diffraction limited output beam. The use of an AWG with higher bandwidth allows a higher resolution step size and steeper rise/fall time of the optical pulses. Tailored temporal profiles can be done with higher precision and the laser represents an attractive system for investigating the dynamics of material processing.

The second system is SMART fiber laser system which was built in collaboration with SPI Lasers. The system is capable of producing up to 45W of average output power. Pulse energy up to 1.0mJ can be extracted by shaping optical pulse using an AOM before the power amplifier. The output beam quality (M^2) was measured to be 1.1, close to diffraction limited. The SRS limited maximum pulse peak power was measured to be 18kW for 1.3 m of beam delivery fiber. The minimum pulse width is limited to 30ns due to the slow response of the diode driver. The output peak power may be improved further by increasing the Raman threshold through the use of a suitable filter to suppress Raman Stokes generated in the preamplifier seeding into the power amplifier and by reducing the length of the beam delivery fiber.

For the first time I have shown the feasibility of using an AOM to pre-shape the optical pulse so as to control the output peak power irrespective of pulse energy. Unlike an EOM which allows the entire optical pulse to be manipulated as necessary, pulse shaping with an AOM only allows shaping at the leading edge of the optical pulse due to its slow rise and fall times. Nevertheless, it is effective in controlling the peak power and thus can help limit the nonlinear effects within the fiber amplifier. The effectiveness of using an AOM as a pulse shaper in a fiber MOPA system was recently reported by Malinowski et al [21].

The capabilities of both systems were demonstrated for Silicon processing. Using the SMART system, the impact of additional energy contained in optical pulses on the ablation efficiency and quality was investigated. No significant improvement in ablation depth with higher energy pulse was observed and any added energy merely shifted the melting process to a vaporization

process. On the other hand, when the nanosecond fiber MOPA system was used to produce tailored pulses with a sharp initial peak followed by a long tail, material removal rates were shown to be substantially increased.

3.6 References

1. D. A. Belforte, "2012 Annual Economic Review and Forecast: Status-quo for 2013," (2013), http://www.industrial-lasers.com/articles/print/volume-28/issue-1/features/2012-annual-economic-review-and-forecast.html.
2. S. Nikumb, Q. Chen, C. Li, H. Reshef, H. Y. Zheng, H. Qiu, and D. Low, "Precision glass machining, drilling and profile cutting by short pulse lasers," Thin Solid Films **477**, 216-221 (2005).
3. C. X. Wang, G. Y. Wang, A. V. Hicks, D. R. Dudley, H. Y. Pang, and N. Hodgson, "High-power Q-switched TEM00 mode diode-pumped solid state lasers with >30W output power at 355nm," (2006), pp. 610019-610019-610014.
4. J. Bovatsek, and R. S. Patel, "HIGH-POWER, NANOSECOND-PULSE Q-SWITCH LASER TECHNOLOGY WITH FLATTOP BEAM-SHAPING TECHNIQUE FOR EFFICIENT INDUSTRIAL LASER PROCESSING."
5. B. Morasse, S. Chatigny, É. Gagnon, J.-P. de Sandro, and C. Desrosiers, "Enhanced pulseshaping capabilities and reduction of non-linear effects in all-fiber MOPA pulsed system," (2009), pp. 71951D-71951D-71912.
6. A. Malinowski, K. T. Vu, K. K. Chen, J. Nilsson, Y. Jeong, S. Alam, D. Lin, and D. J. Richardson, "High power pulsed fiber MOPA system incorporating electro-optic modulator based adaptive pulse shaping," Opt. Express **17**, 20927-20937 (2009).
7. B. N. Chichkov, C. Momma, S. Nolte, F. von Alvensleben, and A. Tünnermann, "Femtosecond, picosecond and nanosecond laser ablation of solids," Appl. Phys. A **63**, 109-115 (1996).
8. K. Sokolowski-Tinten, J. Bialkowski, A. Cavalleri, D. von der Linde, A. Oparin, J. Meyer-ter-Vehn, and S. I. Anisimov, "Transient States of Matter during Short Pulse Laser Ablation," Physical Review Letters **81**, 224-227 (1998).
9. X. Zeng, X. L. Mao, R. Greif, and R. E. Russo, "Experimental investigation of ablation efficiency and plasma expansion during femtosecond and nanosecond laser ablation of silicon," Appl. Phys. A **80**, 237-241 (2005).
10. Q. Lu, S. S. Mao, X. Mao, and R. E. Russo, "Delayed phase explosion during high-power nanosecond laser ablation of silicon," Applied Physics Letters **80**, 3072-3074 (2002).
11. W. O'Neill, and L. Kun, "High-Quality Micromachining of Silicon at 1064 nm Using a High-Brightness MOPA-Based 20-W Yb Fiber Laser," Selected Topics in Quantum Electronics, IEEE Journal of **15**, 462-470 (2009).
12. S. Hendow, E. Rea, N. Kosa, M. Bengtsson, and S. Shakir, "Bursting for enhanced ablation of materials," (2014), pp. 896110-896110-896111.

13. Y. Sintov, O. Katz, Y. Glick, S. Acco, Y. Nafcha, A. Englander, and R. Lavi, "Extractable energy from ytterbium-doped high-energy pulsed fiber amplifiers and lasers," J. Opt. Soc. Am. B **23**, 218-230 (2006).
14. A. E. Siegman, *Lasers* (Oxford University Press, 1986).
15. Y. Wang, "Optimization of Pulse Amplification in Ytterbium-Doped Double-Clad Fiber Amplifiers," J. Lightwave Technol. **23**, 2139 (2005).
16. H. L. Offerhaus, N. G. Broderick, D. J. Richardson, R. Sammut, J. Caplen, and L. Dong, "High-energy single-transverse-mode Q-switched fiber laser based on a multimode large-mode-area erbium-doped fiber," Optics Letters **23**, 1683-1685 (1998).
17. J. Limpert, S. Höfer, A. Liem, H. Zellmer, A. Tünnermann, S. Knoke, and H. Voelckel, "100-W average-power, high-energy nanosecond fiber amplifier," Appl. Phys. B **75**, 477-479 (2002).
18. K. T. Vu, A. Malinowski, D. J. Richardson, F. Ghiringhelli, L. M. B. Hickey, and M. N. Zervas, "Adaptive pulse shape control in a diode-seeded nanosecond fiber MOPA system," Opt. Express **14**, 10996-11001 (2006).
19. H. L. O. C.C.Renaud, J.A.Alvarez-Chavez, J.Nilsson, W.A.Clarkson, P.W.Turner, D.J.Richardson, A.B.Grudini, "Characteristics of Q-switched cladding pumped ytterbium doped fiber lasers with different high energy fiber designs," IEEE Journal of Quantum Electronics, Vol.37, pp. 199 - 206 (2001).
20. K.-H. Leitz, B. Redlingshöfer, Y. Reg, A. Otto, and M. Schmidt, "Metal Ablation with Short and Ultrashort Laser Pulses," Physics Procedia **12, Part B**, 230-238 (2011).
21. A. Malinowski, P. Gorman, C. A. Codemard, F. Ghiringhelli, A. J. Boyland, A. Marshall, M. N. Zervas, and M. K. Durkin, "High-peak-power, high-energy, high-average-power pulsed fiber laser system with versatile pulse duration and shape," Optics Letters **38**, 4686-4689 (2013).

Chapter 4. Raman Fiber Laser in Visible and Near Infrared Regions

This chapter explores the generation of tunable Raman fiber laser using nanosecond fiber MOPA as a pump source. Generation of selective Raman Stokes will be demonstrated with the use of rectangular shaped profile pump pulses. In addition, a multi-step pump pulse profile will be used to demonstrate simultaneous excitation of multiple Raman Stokes. Further improvement on the Raman fiber laser will be explored including wavelength tunability and conversion efficiency.

4.1 Introduction

Light sources operating between 500 nm and 700 nm are useful for medical and spectroscopic applications. For example in medical application, the conventional method is to use different types of lasers to access different wavelength regions of interest namely the argon laser (400 nm – 500 nm), HeNe laser (630 nm) and semiconductor based laser for various laser therapies and treatments [1-3]. Besides that, laser based spectroscopy has becoming an important method for chemical and biological analysis. Laser Induced Breakdown Spectroscopy (LIBS) for example depends on the wavelength of the laser beam and its intensity [4].

Currently, there are a few methods to generate optical signals in the visible region, namely supercontinuum (SC) generation, frequency conversion through parametric process and frequency doubling. In the case of SC based sources which can span over two octaves, a major portion of the output beam falls outside the visible region and will have to be filtered out. Moreover, the spectral power density of a SC source is usually low and may not be sufficient for some applications. Since the wavelength of the frequency doubled source is defined by the pump wavelength, such sources are not very useful for many applications. In a parametric process such as OPO, the output wavelength is tunable and has been demonstrated recently to tune over the wavelength between 700 nm and 900 nm [5, 6]. However, the downside of this technique is the complexity of the setup which consists of mainly free space optics and requires regular, delicate adjustments.

Fiber Raman lasers on the other hand, have attracted huge interest in recent years because they allow the generation of light across a wide range of wavelengths, which is not possible to achieve with rare-earth doped fiber lasers [7]. SRS is the key mechanism that enables an optical fiber to generate any wavelength subject to the pumping wavelength and the fiber transparency range [8, 9]. The cascading nature of SRS also allows the first-Stokes wavelength to be shifted

to second or higher Stokes orders depending on the interaction length and the intensity of the pump source. The generation of Raman stokes in silica fiber happens when a fraction of the pump light is scattered to a lower frequency This scattered light gets amplified along the length of the silica fiber as long as it remains within the Raman gain bandwidth. However the amplification of a Raman Stokes line depends on a threshold condition as evident from Equation 2.33. Thus, the core size and the total fiber length play important role in the generation and amplification of Raman Stokes. A longer length of fiber will reduce the threshold and allows the generation of Raman Stokes at a lower pump power. Furthermore, multiple Stokes lines can be generated if the group velocity mismatch (GVM) between the successive Stokes lines is negligible.

A substantial body of work has been conducted on CW fiber Raman lasers that are not only attractive from the compactness and versatility point of view but also in terms of efficiency. Such a system is capable of generating hundreds of watts of optical power. For instance, an optical power in excess of 100W at 1120 nm has been demonstrated recently with this technique [10]. Moreover, recently a new architecture based on cascaded Raman lasers has been demonstrated offering significant enhancements in conversion efficiency [11]. With the growing demand for lasers operating at wavelengths away from conventional lasers, Raman based fibers laser are becoming a popular option.

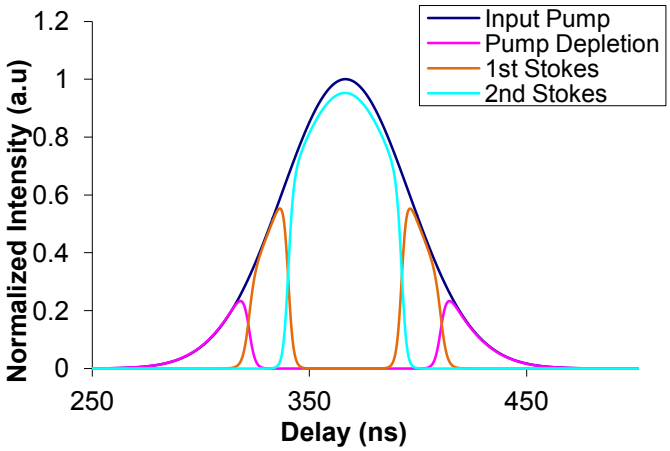

Figure 4.1. Simulation result of the cascaded Raman generation of a Gaussian pump pulse

Pulsed operation on the other hand, is less popular and often compromised by the power dependence of the gain. For instance a pulse propagating along a length of fiber will experience different values of Raman gain across its temporal profile and this usually leads to complex temporal and spectral evolutions [12]. In general, a Gaussian pulse propagating in an optical fiber will generate several Stokes lines of different wavelengths simultaneously as shown in Figure 4.1. This is due to the fact that Raman scattering depends on the instantaneous intensity

of the pump and thus different parts of the pulse will undergo different amount of SRS process. This compromises the quality and efficiency of the generated Raman Stokes lines and does not provide control over selective Stokes line generation.

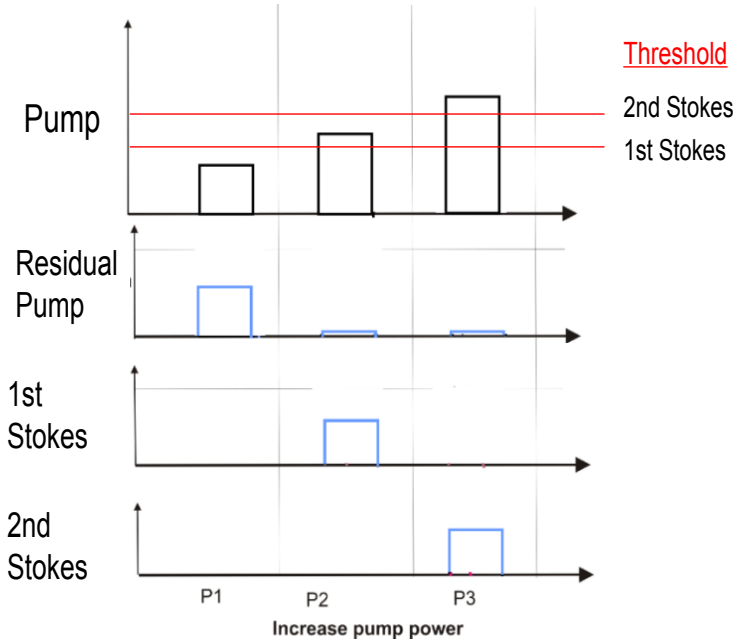

Figure 4.2. Simulation results on the evolution of pump and Raman Stokes components for a perfectly rectangular shape pump pulse.

The issue can be resolved with the use of flat-topped rectangular shape pulse since every point across the pulse will experience equal Raman gain. Figure 4.2 shows that with a perfectly rectangular shaped pump pulse, all the energy from the pump can be transferred to the next Raman Stokes line once the threshold is reached. This allows clean and efficient wavelength generation with a high conversion efficiency. Furthermore, by varying the peak power of the pump, specific Raman Stokes wavelengths can be generated in a controllable fashion. In my actual experiment, a rectangular shaped pulse (Figure 4.3) was generated with a fiber MOPA system incorporating active pulse shaping [13]. The observed residual pump power was due to the limited resolution of the AWG used for pulse shaping introducing finite rise and fall times of the shaped output pulse.

In the work demonstrated by Kang et al, a selective excitation of Raman stokes can be generated with the use of flat-topped rectangular shape pulse [14]. It was shown that Raman stokes up to 11^{th} order can be achieved, accessing close into the ~750 nm region. Such laser system will be attractive for wide area of applications since it can access to one or more visible wavelengths simultaneously just by setting the right pump pulse profile and peak power. For example, in the field of dermatology, various laser sources are required for numerous treatment procedures i.e KTP (532 nm), pulsed Dye (577nm, 585-600nm), gold vapour (628 nm), Ruby (694nm),

Alexandrite (755nm). Moreover, simultaneous generation of multiple Raman stokes will be useful in the medical area i.e laser Doppler imaging of plaque psoriasis with the use of dual wavelength (532 and 632 nm) [15]. Hence, the following work was done with the aim to investigate on the performance of multiple Stokes generated with the multi-step optical pump pulse profiles.

This work was carried out jointly with Dr. Dejiao Lin. The Raman gain medium used was Freelight fiber manufactured by Pirelli, Italy. The silica fiber core is doped with 5 mol% of germanium. The cutoff wavelength of the fiber is at 1450 nm and the propagation loss at 530 nm is estimated to be ~25 dB. In silica based fiber, the Raman gain peak is located 440 cm^{-1} away from the pump wavelength corresponding to a frequency shift of 13.2 THz [7, 8].

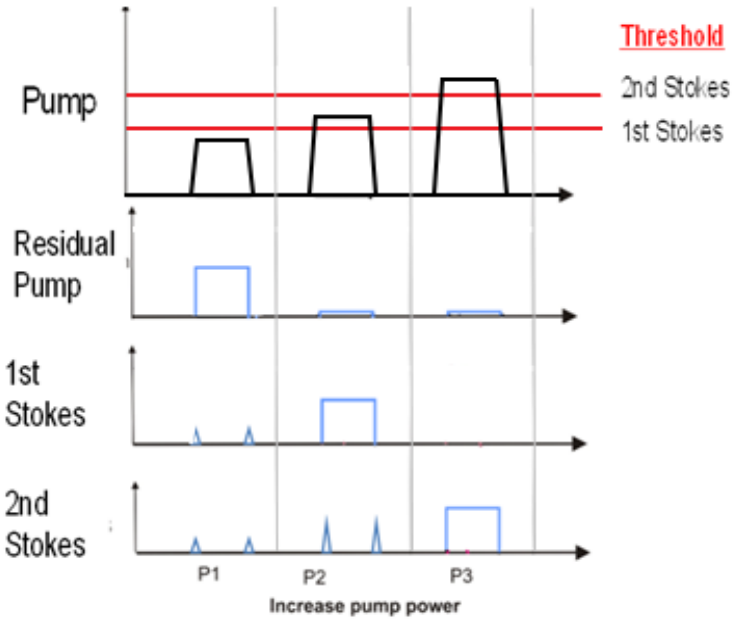

Figure 4.3. Simulation results on the evolution of pump and Raman Stokes components when a rectangular shaped pulse with finite rise and fall time was used.

4.2 Selective excitation of multiple Raman stokes wavelengths (green – yellow – red) using shaped multi-step pulses.

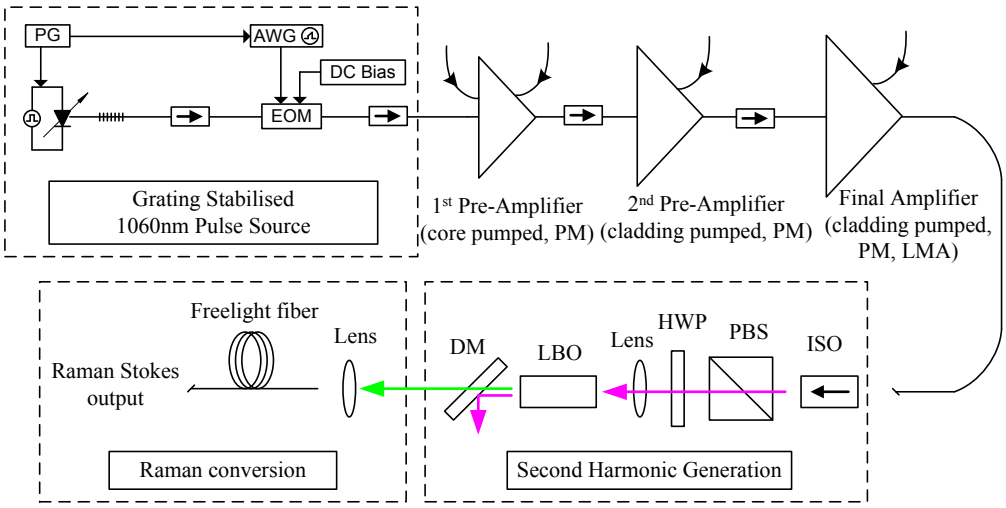

Figure 4.4. Experimental setup of the fiber Raman laser

A schematic of the fiber MOPA pumped Raman laser is shown in Figure 4.4. The seed of the MOPA was a fiber Bragg grating stabilized semiconductor laser diode operating at 1060nm wavelength. The optical output of the seed was passed through an in-line electro-optic modulator (EOM), which was driven by an Arbitrary Waveform Generator (AWG) with temporal resolution of 4ns. The combination of EOM and AWG allowed active pulse shaping to be implemented. The signal from the output of the EOM was then amplified by fiberised three-stage polarization maintaining ytterbium doped amplifier chain to deliver single mode, single polarization output with average power of up to 100W with user defined output pulse shape. A lithium triborate (LBO) crystal was used to frequency double the MOPA output. A free space isolator was placed at the output of the MOPA to protect it from any back reflected beam. A polarization beam splitter (PBS) was used to clean up the output polarization degraded by the isolator. A dichroic mirror was placed at the output of the LBO crystal to separate the unabsorbed pump light at 1060 nm and SHG signal.

The collimated output of the MOPA was launched into a 15mm long LBO crystal using a focusing lens with a focal length of 100 mm. The diameter of the focused beam at the waist position was 70 µm corresponding to a Rayleigh range of 12 mm. The crystal was cut for noncritical phase matching at an operating wavelength of 1060 nm and was placed in an oven at a constant temperature of 155°C for maximum frequency conversion (the FWHM phase matching bandwidth is 3°C) [16]. The linear polarization of the output beam was rotated by a half-wave plate (HWP) to align to the principal axis of the LBO crystal for maximum conversion efficiency. The output from the LBO was passed through a dichroic mirror (DM)

which reflects the unconverted 1060 nm pump light. The transmitted 530 nm light was collimated and coupled into a 250 meter long Pirelli Freelight fiber using an aspheric lens with focal length of 11mm to generate successive Raman Stokes lines.

To obtain the desired spectral-temporal Raman Stokes pulse profiles at the system output we used adaptive pulse shaping to generate multilevel pulse forms at the input to the Raman fiber. First we demonstrate the sequential generation of green (1^{st} Stokes), yellow (4^{th} Stokes) and red (6^{th} Stokes) pulses using a 3-step input pulse. The MOPA was operated at a repetition rate of 50 kHz and the pulse width was set at 50 ns for each step (with a 4ns transition between levels). In order to determine the required ratio of three-step heights, we investigated the respective peak powers required to generate separate orders (1^{st}, 4^{th} and 6^{th}) using simpler rectangular SHG pump pulses [14]. We then established the target multi-level SHG pump pulse shape. This then allowed us to determine the fundamental MOPA output pulse shape as well as the input optical pulse to be created using the EOM. The measured MOPA and SHG pulses are illustrated in Figure 4.5(a) whereas the inset shows the required input pulse shape from the EOM. It is to be noted here that the step height ratios between the MOPA and SHG pulses are different due to the nonlinear power dependency of the SHG (quadratic when operating at relatively low power). The measured average output powers of the MOPA and SHG were 3.1 W and 275 mW respectively and their spectra are shown in Figure 4.5(b) and (c) respectively. The MOPA was operated at a center wavelength of 1060.25 nm with a full width at half maximum (FWHM) spectral width of 0.35 nm. The OSNR was higher than 30 dB and the polarization extinction ratio was better than 20 dB at the output of the MOPA. The center wavelength of the SHG was 530.12nm with a FWHM of 0.17nm.

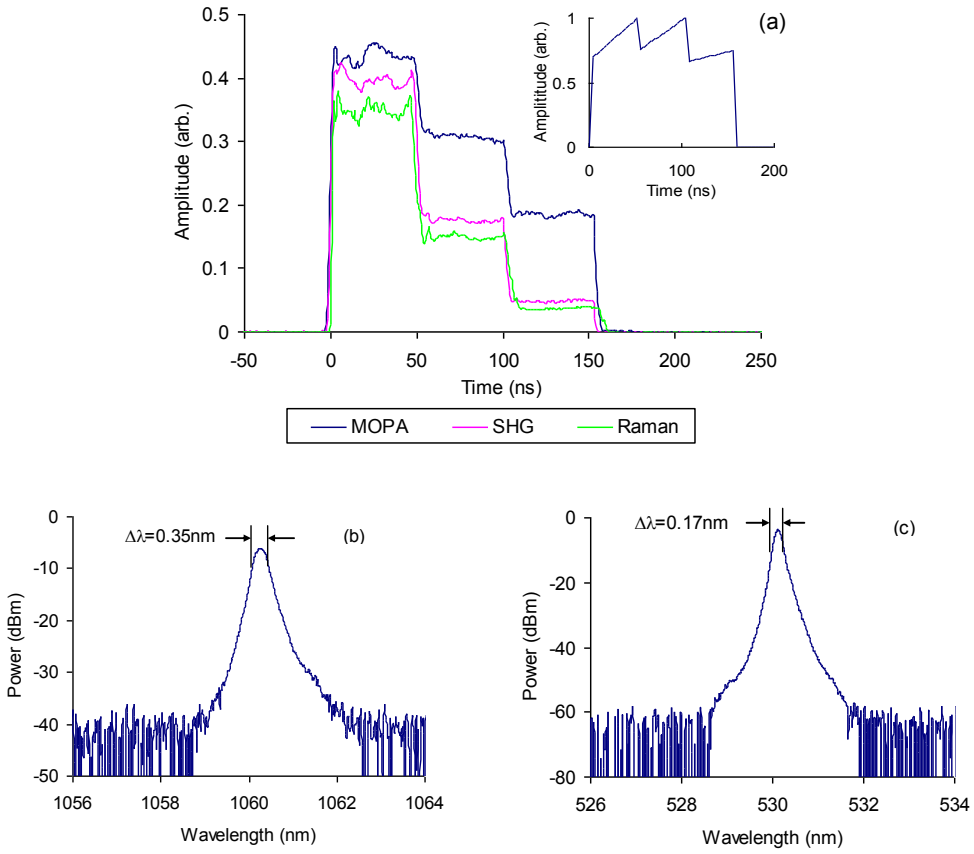

Figure 4.5. (a) 3-step output pulses of MOPA, SHG and Raman lines (inset: initial pulse shape from the EOM); (b) Spectrum of MOPA output; (c) Spectrum of SHG output.

Figure 4.6(a) shows proof of the sequential excitation of 1st (543 nm), 4th (585 nm) and 6th (616 nm) Raman Stokes lines. The extinction ratio of the selected Raman lines was better than 10 dB relative to their nearest neighbours (in terms of the time average powers) whilst the 1060 nm pump depletion was ~15 dB. The spectrum broadened and became asymmetric for higher order Stokes due to the presence of several competing nonlinear processes [17, 18]. The measured peak powers of 1st, 4th and 6th Raman Stokes were 3 W, 9.5 W, 22 W respectively. The higher peak powers for the higher order Stokes lines is predominantly determined by the higher threshold power although the fact that the transmission loss in the Raman fiber decreases at longer wavelengths also has an impact. The pulse shape of the Raman Stokes output is shown as the green plot in Figure 4.5 (a) and blue plot in Figure 4.6 (b). Comparing with the SHG pulse in Figure 4.5(a), the overall pulse width of the Raman Stokes shifted output pulse is slightly longer because of the walk-off among the Raman Stokes and pump wavelengths. We then used a grating to diffract the output from the Raman fiber to establish the temporal distribution of different Stokes orders. The results are shown in Figure 4.6 (b) where it is seen that each of the orders are confined to specific temporal regions across the pulse as expected. Note that the majority of residual 530nm pump remains at the trailing edge of the overall pulse.

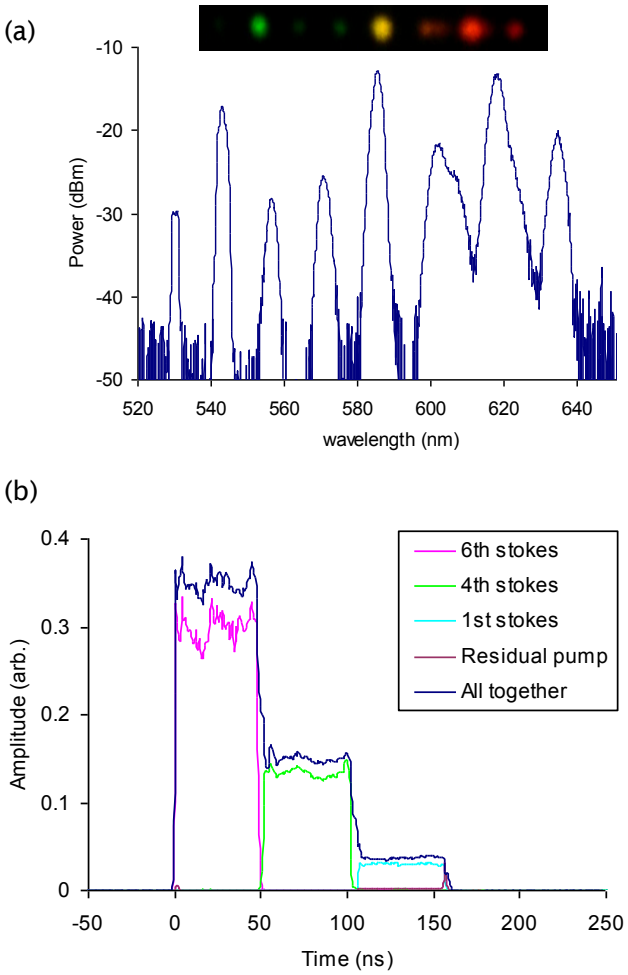

Figure 4.6. (a) Spectrum of Raman pulses with simultaneous excitation of green, yellow and red light (inset: picture of the Raman output diffracted by a grating); (b) Overall and separated 3-step output pulses of Raman output.

Similarly we can generate a combination of two Stokes lines using 2-step pulses as shown in Figure 4.7. The time average power distribution of the different Raman Stokes can be shown to be adjustable by varying the step widths (the peak power is obviously defined by the requirement for a fixed level of gain to achieve complete Raman transfer from the fundamental). The blue plots in Figure 4.7 show the temporal and spectral profiles of the 1st and 4th Stokes orders with average output powers of 7 mW and 22 mW respectively for equal pump pulse step durations of 50 ns. In order to obtain the same average output power at both Stokes lines, the duration of the pump pulse corresponding to the 1st order stokes line was tripled compared to that of the 4th order Stokes line (150 ns and 50 ns respectively) as depicted in Figure 4.7(a) so that both the pump pulse components have equal energies. This resulted in equal output powers of 21 mW for both the Stokes lines as indicated by the pink plot in Figure 4.7(b). This also shows the flexibility of varying the temporal orders of the 1st and 4th Stokes component, as well as incorporating a well defined, user specified temporal separation between the different colored

pulses. Given a specified fiber length, changing the ratio of the peak powers (step height) between the steps, and the order of the step-changes allows the generation of sequences of colored pulses according to any desired combination of Raman Stokes Shift, providing dynamic and agile frequency tuning between well-defined wavelengths.

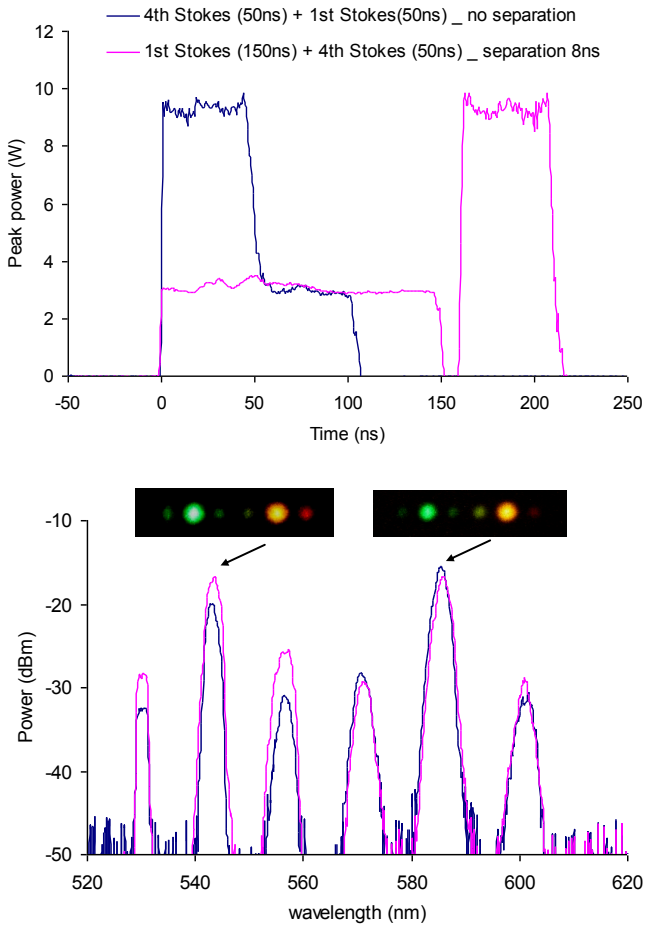

Figure 4.7. (Above) 2-step output pulses of Raman conversion with different pulse energy and separation; (Below) Spectra of the Raman pulses: exciting green and yellow colours simultaneously (inset: picture of the Raman output diffracted by a grating).

We have also investigated potential routes for scaling up the Stokes shifted average output powers. This can be done either by increasing the pulse duration (at fixed pulse repetition rate) so as to increase the energy per pulse at a given Stokes line, or by shortening the Raman gain medium at a fixed pulse duration and repetition rate to increase the peak power required to achieve energy transfer to a given Raman order. Figure 4.8 illustrates an example of scaling using the later approach where the 1st and 4th order Stokes lines were excited in a 100m length of Freelight fiber (the output pulse shapes were kept the same as for the 250 m long fiber case). To obtain the same sequential pattern of excitation of Raman Stokes orders, 284 mW of 532 nm pump was required for the 100 m long fiber giving a total average Stokes shifted power of 115 mW. This is to be compared with values of 34 mW of output for 116 mW of input when the 250

m fiber was used. The numbers are consistent with theoretical predictions when fiber attenuation in the visible and pump coupling loss are taken into account. Note that the long wavelength spectral components appear broadened and more asymmetric for the shorter fiber length which we believe to be induced by the relatively stronger SPM and XPM in this case.

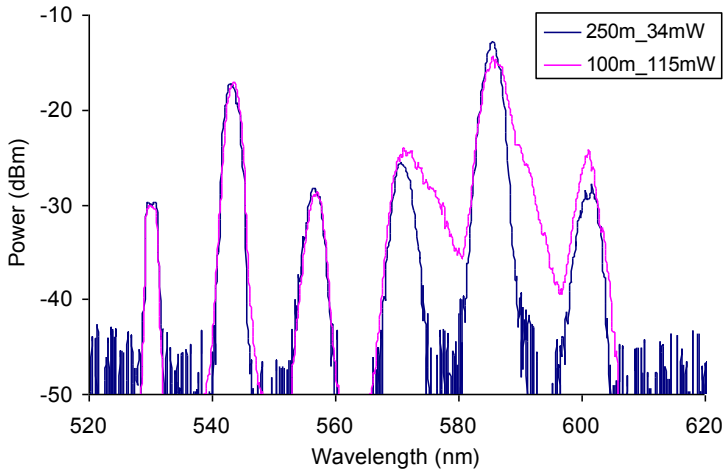

Figure 4.8. Spectra of the 1st and 4th Raman Stokes with 2-step output pulses in different lengths of Raman gain fiber.

4.3 Experimental setup for tunable Raman fiber laser

Synchronous pumped fiber Raman lasers (SPFRLs) were studied both theoretically and experimentally in the 1970s and 1980s [19, 20]. The attractiveness of this technique is that it offers a compact, efficient source of broadly tunable coherent light over the visible and NIR spectral regions [21]. In single pass Raman generation, the pump will initiate the spontaneous Raman scattering which is amplified as it propagates along the fiber. Since the Raman scattering is built up from the noise level, the threshold for the SRS is high for a short length of single mode fiber. For a similar length and type of fiber, synchronous pumped fiber Raman generation offers a lower threshold. Besides, this scheme offers the flexibility of wavelength tuning and a narrow linewidth for Raman Stokes wavelength [22]. Most of the SPFRL demonstrations are operating around the first or second order Raman Stokes peaks in which the experimental setup is relatively simple. However, to achieve higher Stokes order (e.g fourth Stokes order), the configuration becomes more complicated and requires multiple cavity mirrors and a complex arrangement of free space optics. We present a less complicated and yet efficient SPFRL scheme based on selective Raman stokes generation up to 6^{th} orders.

The setup of synchronously pumped fiber Raman laser in the visible region is illustrated in Figure 4.9. It consists of three parts; the first is the MOPA based pump source incorporating

active pulse shaping, the second is the Second Harmonic Generation (SHG) using LBO crystal and the third is the Raman ring laser.

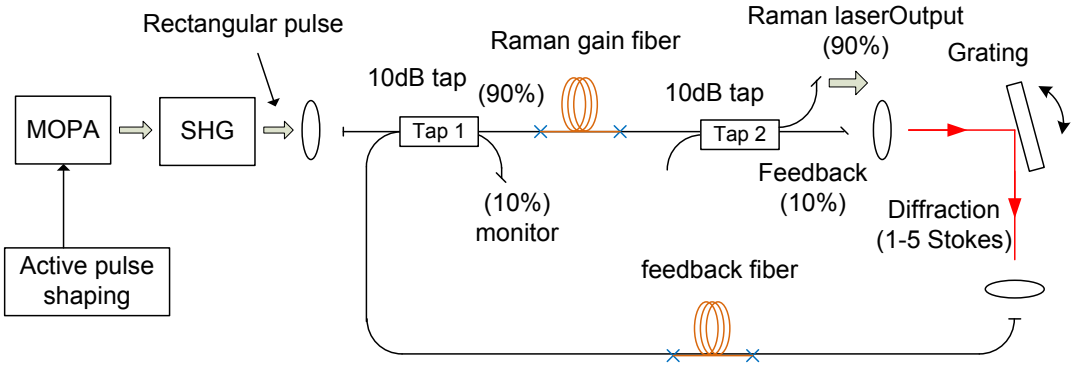

Figure 4.9. Experimental setup of the fiber Raman laser synchronously pumped by SHG from a PM MOPA.

The first two parts have already been described in Section 4.2. As for the third part, the SHG signal at 532 nm was first launched into a 10dB coupler (Tap 1) in which the 90% port was spliced to a 250m long Pirelli Freelight fiber. The other end of the fiber was spliced to a second 10dB coupler (Tap 2). The 90% port was used as the SPFRL output whilst the output of the 10% port was diffracted using a bulk grating mounted in Littrow configuration which can be rotated on its axis. This allows the selection of the wavelength of the feedback signal. The diffracted feedback signal was coupled into another piece of Freelight fiber with a length of 400m. This was to ensure the synchronization of the ~305kHz repetition rate pump and the feedback pulses. This feedback signal was spliced to the 10% input port of the input coupler (TAP 1). In order to ensure both input and feedback signals were in synch, the 10% output port of the input coupler was used as the monitoring port to monitor both in the time and spectral domains.

In the case of the NIR pumped tunable Raman laser, the SHG crystal was removed from the setup. Both of the couplers (Tap 1 & 2) were replaced with ones that work at the NIR wavelengths. The repetition frequency was changed as well due to the difference in group velocities between the pump and Raman Stokes in the NIR.

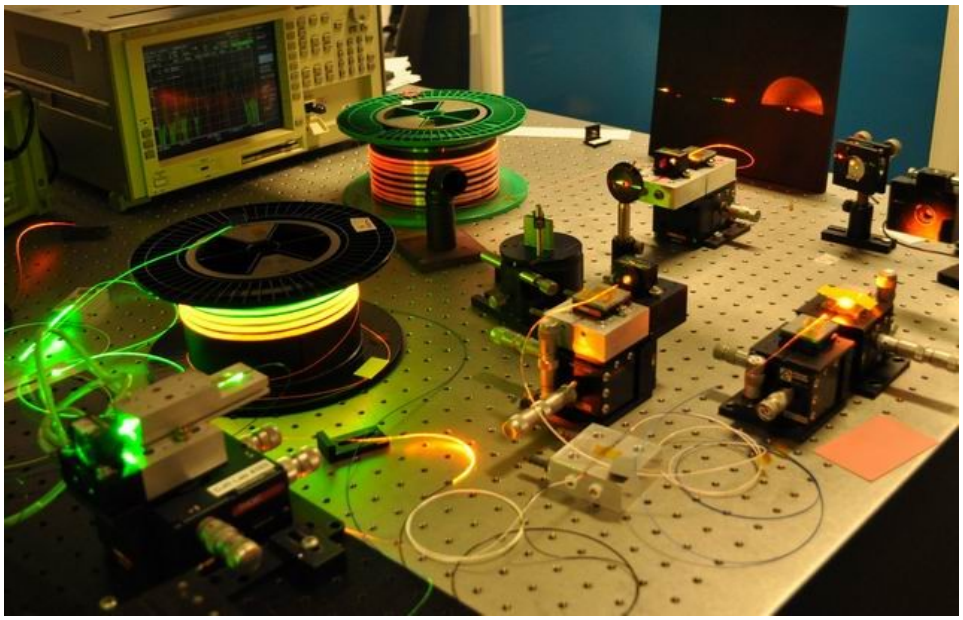

Figure 4.10. Photo of SPFRL when in operation.

4.4 Tunable Raman fiber laser in the visible

For this experimental demonstration, the signal wavelength at 532 nm was used as the pump source. The fiber MOPA pumped frequency-doubled signal has a conversion efficiency of 27% and spectral bandwidth of 0.4nm. A pulse with duration of 100ns and repetition frequency of 100kHz was initially used to generate Raman Stokes in a single pass configuration. As shown in Figure 4.11, up to 6 Stokes orders can be generated by using a flat-topped rectangular pulse. Each Stokes orders had extinction ratio exceeding ~15dB. For higher orders Stokes requiring higher input pulse peak power, nonlinear effects such as SPM and GVM dominates during pulse propagation in Raman gain medium and degraded the extinction ratio.

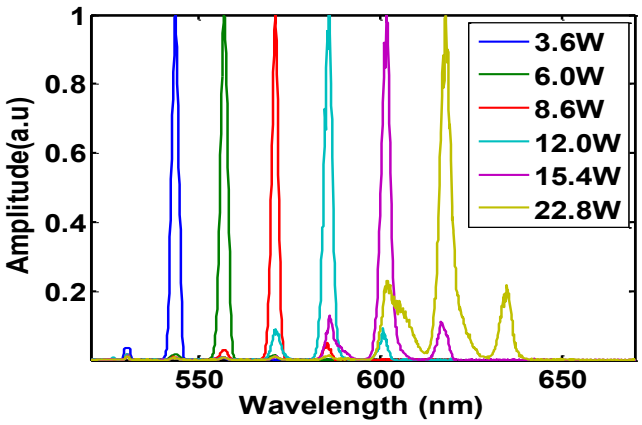

Figure 4.11. Spectra of single-pass Raman generation in visible region with a flat-topped rectangular pump pulse and different pump power. Up to 6 orders of Stokes were generated.

4.4.1 Synchronous Pumped Visible Raman Generation

Firstly the generation of 1st order Raman Stokes lines was investigated for both single pass and synchronous pumping cases. The repetition rate of the pump pulses had to be adjusted to 304.6kHz in order for the feedback pulse to be in synched with the input pump pulse after propagating through the feedback fiber. The pulse duration used in this case was 20ns in order to achieve a similar peak power as that required for the initial experiment to generate 1st order Raman Stokes. A bulk grating diffracted the output beam of the Raman gain medium and the 1st order Raman Stokes was coupled into the feedback fiber. The total feedback signal of the 1st Raman Stokes was estimated to be less than 0.1%. The resultant outcome with and without feedback of the 1st Raman Stokes is shown in Figure 4.12. With a fraction of the feedback signal (0.1%), a significant improvement can be observed. The linewidth decreased by almost a factor of 4 (0.35nm vs 1.5nm). Furthermore, the extinction ratio was improved by >3dB in the presence of a feedback signal. The conversion efficiency achieved was estimated to be ~18%, which is reasonable taking into account the fiber launch efficiency and fiber attenuation in the visible region.

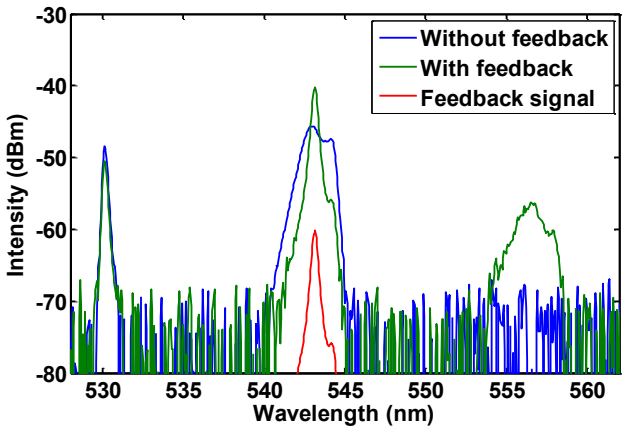

Figure 4.12. Spectra of 1st Raman Stokes generation with and without feedback. The feedback signal was at 543.1nm. The output peak power obtained was 2.3W.

Next, the effects of feedback mechanism on higher Raman Stokes order were investigated. 3rd Raman Stokes and 5th Raman Stokes were of interest in this experiment as the wavelengths were in the yellow (571.2nm) and red-orange (601.6nm) regions. As both Stokes wavelengths had different group velocity dispersion, the repetition rate had to be adjusted to 305.3 kHz for 3rd Raman Stokes and 306.0 kHz for 5th Raman Stokes. Table 4.1 shows the experimental results obtained for feedback at higher Stokes orders. It is to be noted here that the average output powers of the 3rd and 5th Stokes were increased by about 3dB and 2dB in the presence of feedback (the extinction ratios were 15dB and 12dB).

	3rd Raman Stokes	5th Raman Stokes
Center wavelength	571.2nm	601.6nm
Linewidth		
(without feedback)	2.0nm	3.1nm
(with feedback)	0.5nm	0.8nm
Output peak power		
(without feedback)	8.6W	15.4W
(with feedback)	9.5W	18.5W
Conversion efficiency	15%	12%

Table 4.1. Effects of synchronous pumped generation of 3rd Raman Stokes and 5th Raman Stokes in term of linewidth and output peak power.

Figure 4.13 shows the output pulse shapes of the synchronous pumped Raman laser for 3rd Raman Stokes which was measured at Tap 2 output port. A grating was used to separate the lower order Stokes components and residual pump from the Raman output and a multimode fiber was used to collect these components and to couple them into a photodetector. By comparing the width of the SHG output pulse and 3rd Raman Stokes pulse, the Raman Stokes was found to be slightly narrower in terms of pulse width. This happened due to the group velocity mismatch between the pump and 3rd Raman Stokes wavelengths. The total Raman output pulse had a sharp spike at the leading edge and multiple smaller spikes at the trailing edge of the pulse. These smaller spikes were the result of the finite rise and fall time of the pump pulses which was shaped by the AWG. This is also supported by the simulation results (Figure 4.3) with finite rise and fall times. As for the sharp spike at the leading edge, this was the resultant of multiple smaller spikes coalescing together due to the effect of group velocity mismatch between the pump wavelengths and the components of Raman Stokes.

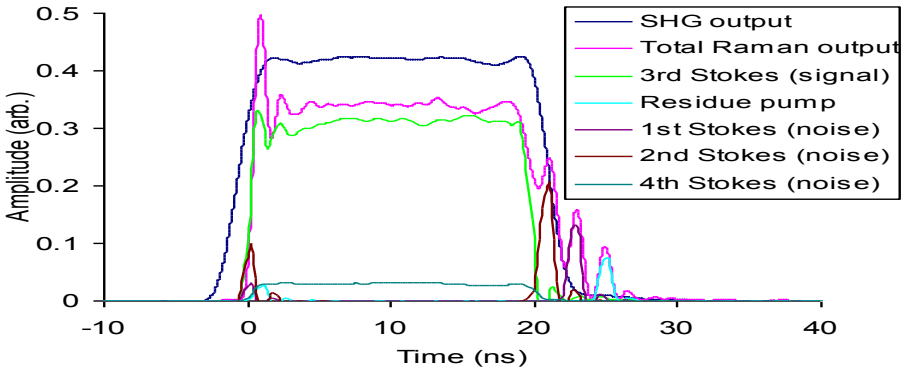

Figure 4.13. Pulse shapes consisting of different components of Raman Stokes orders and residual pump which was spectrally resolved using a bulk grating.

4.4.2 Tunability of Synchronously pumped visible Raman laser

With the use of bulk grating, the wavelength of the feedback signal could be tuned. As shown the in Figure 4.14, a continuous tuning range of 2.2nm - 2.8nm as possible for operation of 1st Raman Stokes, 3rd Raman Stokes and 5th Raman Stokes lines. The observed wide tuning range was due to the broad Raman gain bandwidth in silica fiber as shown in Chapter 2 Section 2.3.4.

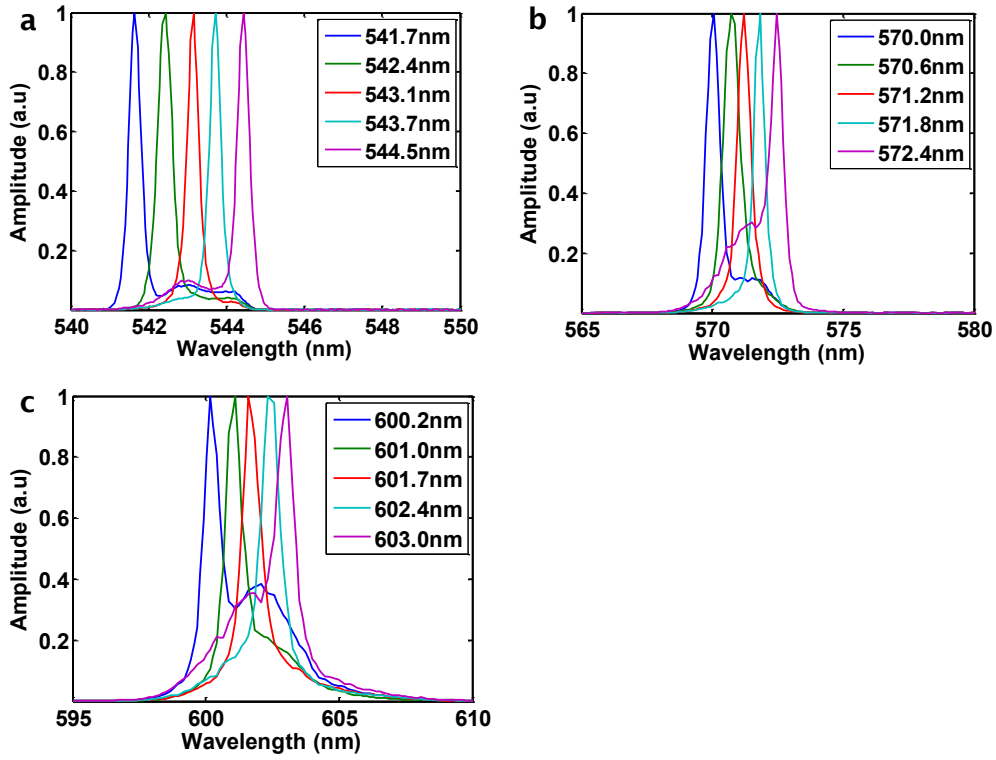

Figure 4.14. Spectra of visible tunable Raman laser for (a) 1st Raman Stokes, (b) 3rd Raman Stokes and (c) 5th Raman Stokes.

The ability to enable fast wavelength tuning with a narrow linewidth opens up to a range of applications. For example in skin treatment, the ability to change the laser from haemoglobin-absorbing yellow to melanin-absorbing green and then to the red for photodynamic therapy could reduce treatment time and enhance treatment selectivity. [23]

4.5 Synchronous pumped NIR Raman generation

Similar investigations were carried out with pump wavelength at 1060nm. This was achieved by removing the LBO from the setup shown in Figure 4.9. The same length of Raman gain medium was used in this case. As shown in Figure 4.15, it was possible to generate up to the 4th Raman Stokes using flat topped rectangular pulses. Beyond which a broad continuum start to develop as the 5th and higher Raman Stokes crosses the zero dispersion wavelength (~1300nm) of the Raman fiber. Thus, the experiment was limited up to the 4th Raman Stokes.

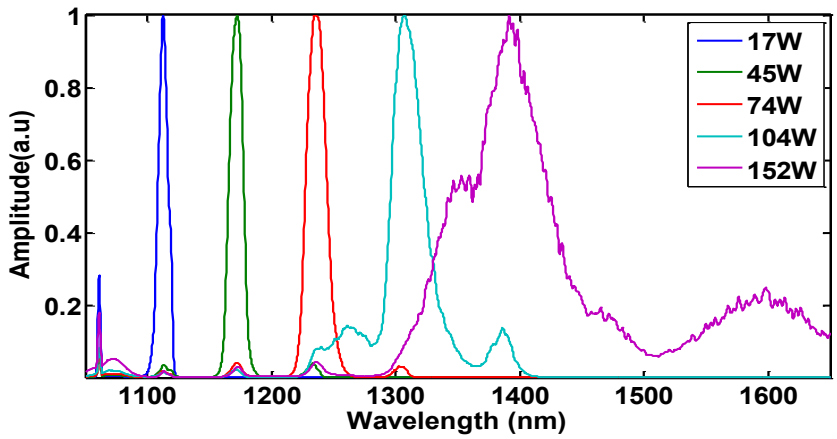

Figure 4.15. Spectra of single-pass Raman generation with a flat-topped rectangular pump pulse and different pump power. Distinct Raman Stokes were generated in a controllable fashion before continuum started to build up as zero dispersion wavelength was within the proximity.

A pulse duration of 16ns with repetition frequency of 400 kHz was used for this experiment. It is to be noted here that in the NIR region, the GVM between the pump and the Raman Stokes is substantially smaller than that in the visible ensuring a longer walk-off length. Figure 4.16 shows the spectrum of the 4th Raman Stokes. An improvement in linewidth and extinction ratio could be seen by utilizing feedback as compared to the single pass Raman generation. The peak power from the MOPA and the synchronous pumped Raman fiber laser output were estimated to be 281W and 119W respectively. The peak power required to achieve Raman threshold was higher in NIR wavelengths than visible. This was due to the lower Raman gain coefficient for 1060nm wavelength as the gain coefficient is wavelength dependent. Higher peak powers triggered nonlinear effects such as SPM and Four Wave Mixing (FWM) and broadened the

spectrum. As a result, the extinction ratio achieved for NIR wavelengths was lower than that achieved in the visible wavelengths for the same Raman Stokes order.

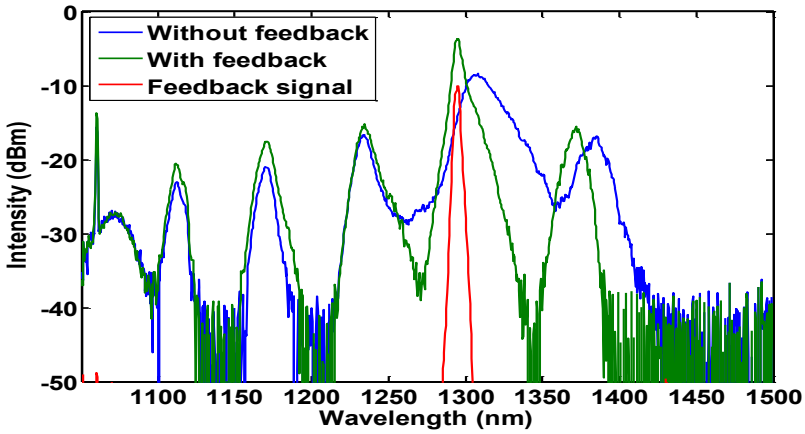

Figure 4.16. Spectra of the 4th Raman Stokes with and without feedback signal. The feedback signal was at 1303nm.

In terms of wavelength tunability, as shown in Figure 4.17, up to 28nm continuous tuning range was achieved for the 4th Raman Stokes which corresponds to 5.0 THz in the frequency domain. This shows an improvement by a factor of 2 as compared to the tuning range in the visible region. As mentioned before, the dispersion in the NIR region provides a longer walk off length between pump and Raman Stokes components leading to the broader tuning range.

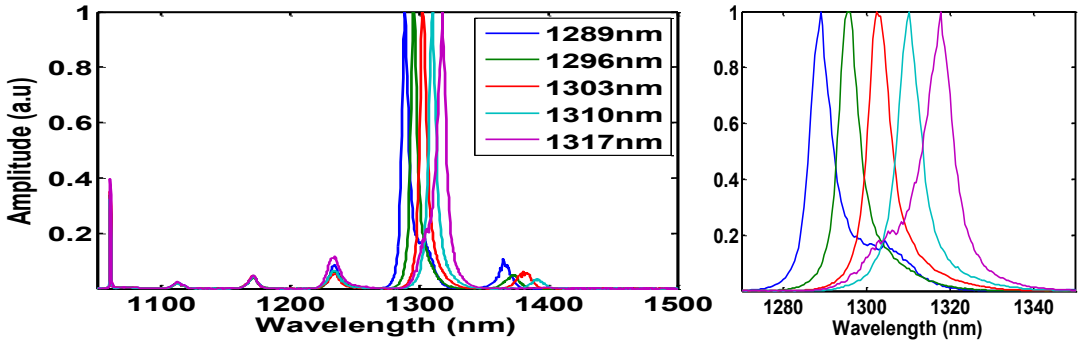

Figure 4.17. The spectra of wavelength tunability by tuning the feedback signal of 4th Raman Stokes. Up to 28nm of continuous tuning range was achieved.

4.6 Discussion

In both visible and NIR cases, the presence of the feedback signal improved extinction ratio of the Raman Stokes while narrowed down the lasing linewidth as compared to the single pass Raman laser. Higher extinction ratio achieved is attributed to the improvement in conversion efficiency as a result of the reduction in Raman threshold. This occurred when a fraction of the Raman Stokes signal is provided through the feedback arm as a seed instead of building up from

noise. This assists the stimulated scattering process. The lower threshold for a particular Raman Stokes line allows a higher energy transfer from the pump and thus increases the conversion efficiency. The reduction in linewidth depends on the linewidth of the feedback signal.

The Raman output can be scaled up further from the currently achieved power level by reducing the gain medium length. This will increase the Raman threshold resulting in higher peak powers required for successful Raman Stokes generation. This in turn will increase the Raman Stokes output power. As shown in Figure 4.18, for a length of 25m of Raman gain medium, an output peak power of 400W (1st Raman Stokes) was obtained as compared to only 41W with 250m length. A reduction in length by a factor of 10 increases the peak power by the same factor. However, at higher peak power, SPM starts to compete with the Raman Stokes generation and degrades the extinction ratio as clearly illustrated by the 2nd Stokes in Figure 4.18. Thus a compromise has to be made in the choice of fiber length to scale up the Raman output power whilst maintaining good side-mode suppression.

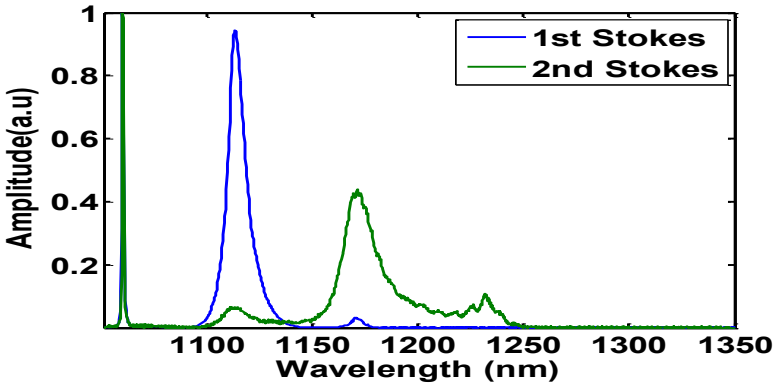

Figure 4.18. Generation of synchronous pumped Raman Stokes when Raman gain medium length was reduced to 25m. The peak power obtained was 400W (1st Raman Stokes) and 590W (2nd Raman Stokes).

During this experiment, it was observed that the Freelight fiber degraded after 48 hours of continuous exposure to the input green laser. With the same peak power fed into the fiber, the Raman stokes generation reduced as compared to the case when the fiber was in a pristine condition. A thorough physical inspection was conducted on the fiber to look for any damage point on the fiber but nothing was found to explain the drop in output power. Furthermore, the Raman gain fiber was re-cleaved but no improvement in performance was observed. The fiber degradation was not observed when the pump source was in the NIR region. We believe that the degradation of fiber as a result of long exposure to visible radiation is caused by a photodarkening effect in the germanium doped fiber [24, 25]. This radiation induced loss effect tends to increase as the signal wavelength becomes shorter.

4.7 Conclusion

We have demonstrated a new technique to realize Raman based pulsed fiber lasers. The use of a pulse shaping technique based on EOM in an all fiber PM MOPA allows the generation of shaped multistep pulses for selective excitation of the Raman stokes. The generation of pulses of several tens to hundreds of nanoseconds in duration with this technique results in output signal wavelengths that changes sequentially from green, to yellow to red (up to 7th stokes orders) using 530 nm pump pulses with a 3 step profile or any other two using 2-step pulses by exploiting the SRS in optical fiber. Operation in the NIR region however is limited to 4 stokes orders before the zero dispersion wavelength of the fiber is reached beyond which a continuum starts to build up.

A tunable, synchronous pumped Raman fiber laser was also demonstrated in the NIR and visible regions. A continuous tuning range of 28nm in the NIR and 2.8nm in the visible region are achieved. The conversion efficiency of pump to Raman signal increased with the use of a feedback signal. The linewidth of the Raman Stokes in both visible and NIR regions shows a significant narrowing effect. The total output power of the Raman fiber laser can still be improved with the right type and length of Raman gain fiber.

The amount of optical power in the form of residual pump can be reduced further by using an AWG with a higher resolution/ faster rise and fall times. By having optical pulses with steeper rise and fall time, a higher conversion efficiency can be attained with better power extinction between the required Raman stokes and the unwanted stokes.

This demonstration will allow the new generation of wavelength agile fiber based laser systems operating across broad and interesting wavelength regimes to be made possible. Such light sources could find great applications in the fields of spectroscopy, archaeology and biomedical to name but a few.

4.8 References

1. D. Hawkins, N. Houreld, and H. Abrahamse, "Low level laser therapy (LLLT) as an effective therapeutic modality for delayed wound healing," Annals of the New York Academy of Sciences **1056**, 486-493 (2005).
2. P. Papageorgiou, A. Katsambas, and A. Chu, "Phototherapy with blue (415 nm) and red (660 nm) light in the treatment of acne vulgaris," British Journal of Dermatology **142**, 973-978 (2000).
3. J. A. Brauer, E. A. Gordon Spratt, and R. G. Geronemus, "Laser Therapy in the Treatment of Connective Tissue Diseases: A Review," Dermatologic Surgery **40**, 1-13 (2014).
4. V. Spizzichino, and R. Fantoni, "Laser Induced Breakdown Spectroscopy in archeometry: A review of its application and future perspectives," Spectrochimica Acta Part B: Atomic Spectroscopy **99**, 201-209 (2014).
5. S. Chaitanya Kumar, O. Kimmelma, and M. Ebrahim-Zadeh, "High-power, Yb-fiber-laser-pumped, picosecond parametric source tunable across 752-860nm," Optics Letters **37**, 1577-1579 (2012).
6. F. Kienle, P. S. Teh, D. Lin, S.-u. Alam, J. H. Price, D. Hanna, D. J. Richardson, and D. P. Shepherd, "High-power, high repetition-rate, green-pumped, picosecond LBO optical parametric oscillator," Opt. Express **20**, 7008-7014 (2012).
7. R. H. Stolen, C. Lee, and R. K. Jain, "Development of the stimulated Raman spectrum in single-mode silica fibers," Journal of the Optical Society of America B **1**, 652-657 (1984).
8. R. H. Stolen, J. P. Gordon, W. J. Tomlinson, and H. A. Haus, "Raman response function of silica-core fibers," Journal of the Optical Society of America B **6**, 1159-1166 (1989).
9. N. Bloembergen, "The Stimulated Raman Effect," American Journal of Physics **35**, 989-1023 (1967).
10. J. Ji, C. A. Codemard, J. K. Sahu, and J. Nilsson, "Design, performance, and limitations of fibers for cladding-pumped Raman lasers," Optical Fiber Technology **16**, 428-441 (2010).
11. V. R. Supradeepa, J. W. Nichsolson, C. E. Headley, M. F. Yan, B. Palsdottir, and D. Jakobsen, "A high efficiency architecture for cascaded Raman fiber lasers," Opt. Express **21**, 7148-7155 (2013).
12. M. Melo, M. O. Berendt, and J. M. Sousa, "Signal Pulse Distortion Induced by Stimulated Raman Scattering in High Power Double-Clad Fiber Amplifiers," Photonics Technology Letters, IEEE **24**, 252-254 (2012).

13. K. T. V. A. Malinowski, K.K. Chen, P.Horak, D.J. Richardson, "Selective Generation of Individual Raman Stokes Wavelength using Shaped Optical Pulses," in *Optical Fiber Communication Conference (OFC)*(San Diego, California, 2008).
14. K. K. Chen, S.-u. Alam, P. Horak, C. A. Codemard, A. Malinowski, and D. J. Richardson, "Excitation of individual Raman Stokes lines in the visible regime using rectangular-shaped nanosecond optical pulses at 530 nm," Optics Letters **35**, 2433-2435 (2010).
15. A. K. Murray, A. L. Herrick, T. L. Moore, T. A. King, and C. E. M. Griffiths, "Dual wavelength (532 and 633 nm) laser Doppler imaging of plaque psoriasis," British Journal of Dermatology **152**, 1182-1186 (2005).
16. C. Kang Kang, S. U. Alam, J. R. Hayes, H. J. Baker, D. Hall, R. McBride, J. Price, D. Lin, A. Malinowski, and D. J. Richardson, "56-W Frequency-Doubled Source at 530 nm Pumped by a Single-Mode, Single-Polarization, Picosecond, Yb3+ Doped Fiber MOPA," Photonics Technology Letters, IEEE **22**, 893-895 (2010).
17. M. N. Islam, J. R. Simpson, H. T. Shang, L. F. Mollenauer, and R. H. Stolen, "Cross-phase modulation in optical fibers," Optics Letters **12**, 625-627 (1987).
18. M. Santagiustina, P. Balan, and C. De Angelis, "Combined effects of self-, cross-phase modulation and stimulated Raman scattering in optical fibers," Optics Communications **100**, 197-203 (1993).
19. M. Nakazawa, M. Kuznetsov, and E. P. Ippen, "Theory of the synchronously pumped fiber Raman laser," Quantum Electronics, IEEE Journal of **22**, 1953-1966 (1986).
20. C. Lin, and W. G. French, "A near-infrared fiber Raman oscillator tunable from 1.07 to 1.32 μm," Applied Physics Letters **34**, 666-668 (1979).
21. K. Smith, P. N. Kean, D. W. Crust, and W. Sibbett, "An Experimental Study of a Synchronously Pumped Fibre Raman Oscillator," Journal of Modern Optics **34**, 1227-1233 (1987).
22. E. Desurvire, A. Imamoglu, and H. J. Shaw, "Low-threshold synchronously pumped all-fiber ring Raman laser," Lightwave Technology, Journal of **5**, 89-96 (1987).
23. H. M. P. a. J. A. P. Richard P. Mildren, "Raman lasers with intracavity nonlinear optics are promising alternatives to multiline lasers and parametric oscillators," (2005).
24. E. J. Friebele, D. L. Griscom, and G. H. Sigel, "Defect centers in a germanium-doped silica-core optical fiber," Journal of Applied Physics **45**, 3424-3428 (1974).
25. L. J. Poyntz-Wright, and P. S. J. Russell, "Spontaneous relaxation processes in irradiated germanosilicate optical fibres," Electronics Letters **25**, 478-480 (1989).

Chapter 5. Picosecond Pulse Generation Using SLD

Apart from the work done on nanosecond regime (in the work of SMART laser discussed in Chapter 3), our project partner, SPI Lasers is looking into developing fiber based laser systems which operate in the picosecond regime as one of their future product line. Such laser system requires a stable optical pulse source as a seed laser for effective amplification in the amplifier chains. The setup complexity and the stability of the pulse generated will be the main requirement for the seed laser. Hence, I was tasked to investigate the techniques for generating picosecond pulses from semiconductor laser diode and with the goal of identifying the best solution to be used as the seed laser.

This chapter investigates two techniques for picosecond pulse generation, namely gain switching and mode-locking of a semiconductor laser diode with an external cavity. Both of these techniques are attractive due to the simplicity of their configurations which make them ideal for seeding fiber MOPAs. The characteristics of the optical pulses such as pulse width, spectral width, frequency chirp and timing jitter will be discussed extensively in this chapter.

5.1 Introduction

The demand for high power fiber lasers producing picosecond optical pulses in the 1.0 μm wavelength region is growing in recent years as they are widely used for laser machining, frequency-doubling, and the pump sources for parametric oscillators and supercontinuum generation [1-3]. Various operating parameters are sought for these types of applications such as variable repetition rate, wavelength tunability, low timing jitter between pulses, pulse widths that can be varied as well as generation of transform-limited optical pulses.

The SLD is well suited for the generation of short optical pulses in the picosecond regime and becomes an important seed source in the MOPA architecture for the generation of high optical power [4]. In order to produce short picosecond optical pulses from a SLD, two major techniques are used, namely gain-switching and mode-locking.

5.2 Gain switching

The development of high speed photonic networks produced high demands for compact pulsed laser sources. A few techniques for short pulse generation using semiconductor based lasers have been introduced; among which the gain switching technique. Gain switching was first demonstrated by Ito et al [5] who showed that by injecting short electrical pulses into the SLD, optical pulses with pulse durations shorter than the injected electrical pulses could be generated.

Since then, the gain switching technique has been widely adopted due to the simplicity of generating picosecond optical pulses directly from a SLD. Moreover, this technique allows operation at essential any repetition rate. Most of the early demonstration of this technique were at the telecommunication wavelength regions round 1550nm. However, in 2005, Piper *et al.* demonstrated gain switching of a 1.06 μm SLD, generating short picosecond optical pulses. [6]

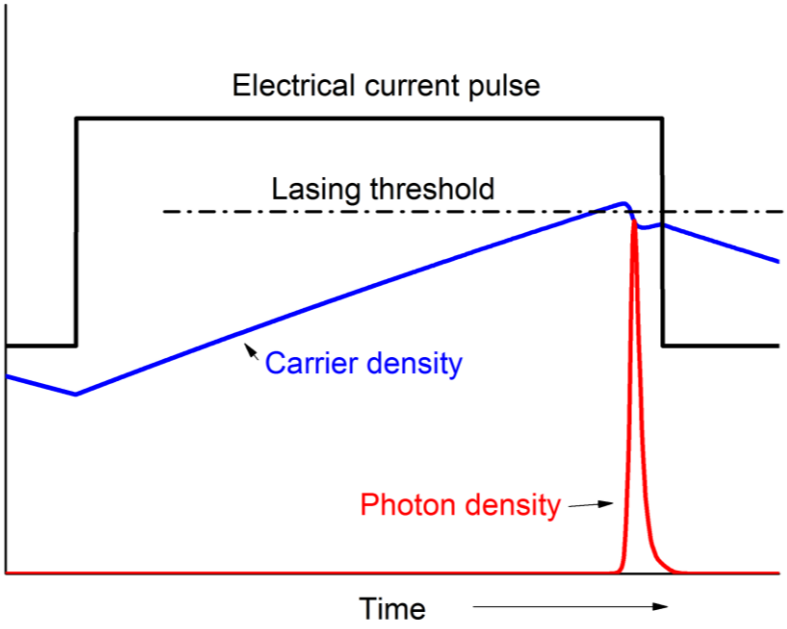

Figure 5.1. Typical evolution of the photon and carrier density during gain switching cycle in a semiconductor laser diode.

When a short electrical pulse is injected into a SLD, the gain of the SLD is switched from below threshold to gain inversion and the diode will generate a series of relaxation oscillation spikes. The principle of gain switching is to excite the first optical spike of the relaxation oscillation without exciting the subsequent ones. The method used is to terminate the current pulse before the onset of the second optical peak and this result in the optical pulse being shorter than the injected current pulse. The evolution of carrier and photon densities during gain switching is illustrated in Figure 5.1. When the electrical pulse is injected into the semiconductor laser, the carrier density build up rapidly to a level far above the lasing threshold. Once the carrier density reaches above the threshold level, a rapid increase in photon density via stimulated emission occurs. This results in a sharp depletion of the carrier density. Since the carrier density cannot be replenished once the current injection stops, photon emission will then stop resulting in a single optical spike or pulse. However, if the electrical current is applied further, the photon density will oscillate resulting in the generation of multiple pulse peaks. Thus, with optimized

operating parameters (bias level, modulation frequency, electrical pulse width and its amplitude), stable, picosecond pulse train generation can be realized through this method.

There are a few drawbacks with this technique. The minimum pulse duration generated is dictated by the device properties and parameters of the modulated current. Furthermore, the optical pulses generated using this technique usually inherit a red shift in lasing wavelength due to the time-varying carrier density within the gain medium which leads to a large refractive index modulation. This results in chirped optical pulses with a corresponding time-bandwidth-product many times that of the Fourier limit.

Several techniques on chirp compensation have been demonstrated in recent years but these bring additional complexity to the setup. For instance, using chirped fiber Bragg gratings (CFBG) [7], dispersive fiber [8], nonlinear optical loop mirrors [9] and spectral filtering techniques using a Mach-Zehnder interferometer [10]. Moreover, gain-switched optical pulses suffer from pulse to pulse timing jitter which originates during the build-up of optical pulses from spontaneous emission, causing random fluctuations in photon density [11].

5.3 Demonstration of gain switching technique

In this section, conventional setup through electrical current injection for achieving gain switched optical pulses will be described. Section 5.3.1 describes the experiment that investigates the characteristics of gain switched optical pulses generated via different SLDs. Section 5.3.2 describes the effects of injection seeding on the optical pulses generated from the gain switching technique.

5.3.1 Gain switched SLD

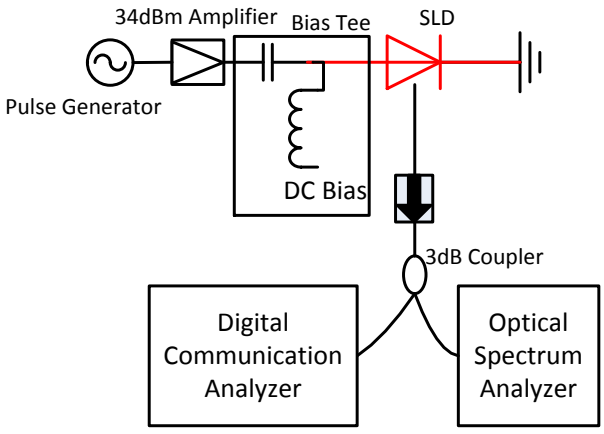

Figure 5.2. Experimental configuration for direct gain switching.

The experimental configuration of the gain switching scheme is shown in Figure 5.2. A 3 GHz pulse generator (Agilent 8133A) was used to generate the electrical sine-wave with a repetition frequency of 1 GHz and duty cycle of 50%. The electrical signal generated was fed into an RF amplifier (ZHL-5W). The RF amplifier used has a limited operation frequency spanning from 800 MHz up to 3 GHz with a maximum saturated output powers of 5W. The performance of the RF amplifier with different input signal power was characterized and is shown in Figure 5.3 It is shown that when the input signal power is above -3 dBm, the output power becomes constant. In this work, the signal power from the pulse generator was set to -6 dBm, resulting in an amplified signal power of 2.5W and the corresponding peak-to-peak current of 600mA in a 50Ω load. If input signal power above -6 dBm was used, the resultant output power will higher than the maximum input power that the bias tee can handle.

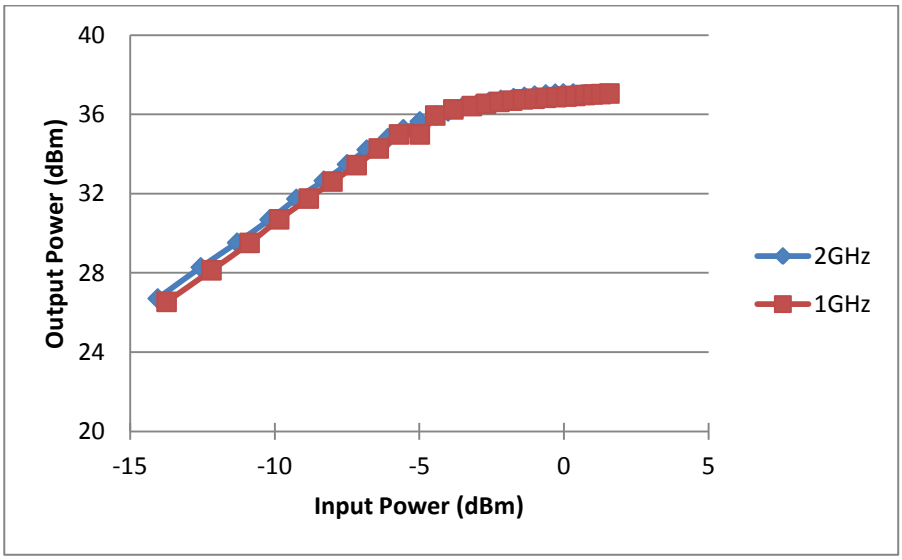

Figure 5.3. RF amplifier (ZHL-5W) output power at different input signal power for operating frequencies of 1 GHz and 2 GHz. The output power begins to saturate when the input power exceeds -3 dBm.

The amplified signal was then combined with an adjustable DC bias current (via a bias-tee) before being fed into the SLD for effective gain-switching. The SLD was mounted on a modified printed circuit board (PCB) with 4 surface mount type resistors in series (48Ω each) in order to match the impedance of the transmission line (50Ω) . The temperature of the SLD was stabilized by using a thermoelectric cooler (TEC) unit. For optimum performance, the temperature of the SLD was maintained at 25˚C. Three SLDs from different manufacturers were used in this work, namely Oclaro, 3SPhotonics and Qphotonics. All three diodes were Fabry-Perot type and housed in 14-pin butterfly packaging. The output signal was fiber coupled with polarization maintaining pigtail, thus preserving the linear polarization from the laser diode. The output pigtail was spliced to a polarization maintaining inline isolator and a 3-dB tap coupler.

Both outputs from the tap coupler were connected to the OSA and a photodetector connected to a Digital Communication Analyzer (DCA) for optical pulse characterizations.

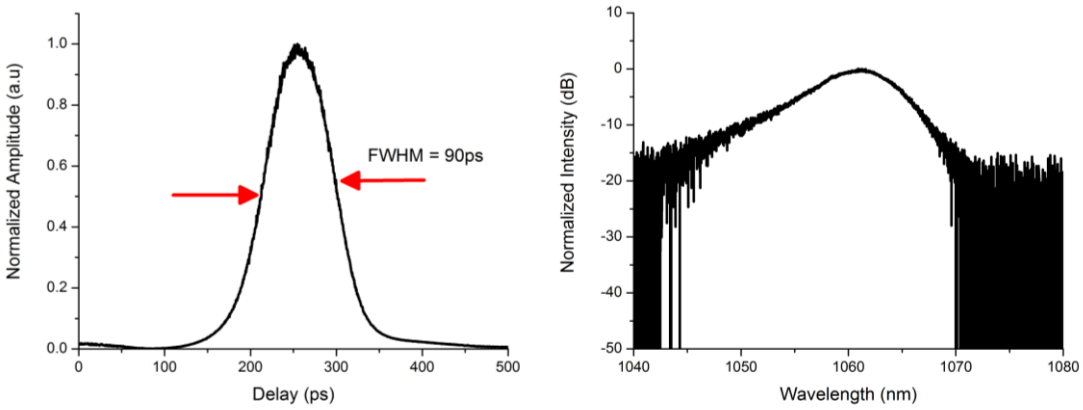

Figure 5.4. Output pulse and spectrum obtained from gain switching an Oclaro SLD.

The first diode tested was an Oclaro SLD (LC96A) capable of producing a maximum optical output power of 400 mW under CW operation at a drive current of 1A. The DC current provided to the diode was 30mA (lower than the threshold current of 40mA) which was combined with the peak-to-peak modulated current of ~600mA at 1GHz repetition frequency. The gain-switched SLD produced a total average output power of 4 mW corresponding to an estimated pulse energy of 4pJ. The generated optical pulse and its spectrum are shown in Figure 5.4. An output pulse width of ~90ps was measured with a broad spectral bandwidth of 7 nm. The shape of the spectrum is asymmetrical and consists of multi-longitudinal modes with a mode spacing of about 0.043 nm. Based on the measured mode spacing, the chip length is estimated to be ~3.5 mm (assuming a refractive index of InGaAs of ~3.5). As for the time-bandwidth product (TBP) of the output pulses, it was estimated to be equal to 168 (i.e very far from transform limited).

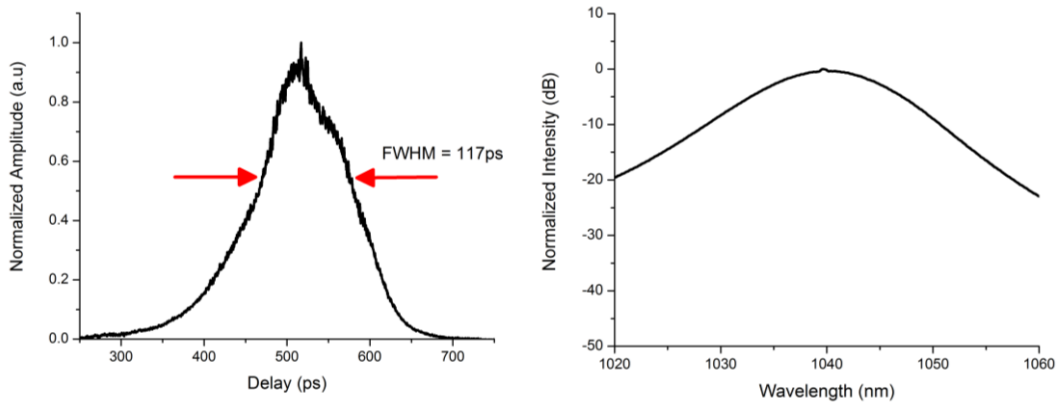

Figure 5.5. Output pulse and spectrum obtained from gain switching of a 3SPhotonics SLD.

The next diode tested was from 3SPhotonics which is designed to operate at 1040 nm. The diode is able to generate a maximum optical output power of 500mW at 1.2A of injected current. In GS mode, 70mA of DC was combined with the modulated current, generating optical pulses with a total optical power of 5mW (~5pJ per pulse). The resulting output pulse and spectrum are illustrated in Figure 5.5. Direct gain switching produced ~117ps optical pulses with a broad spectrum consisting of multi longitudinal modes. The mode spacing for this particular diode was 0.032nm, which was smaller compared to the Oclaro diode. This corresponds to an estimated chip length of ~5 mm, which is 43% longer than the chip length of the Oclaro diode. The shape of the output spectrum is also asymmetrical with a slightly distorted peak. The estimated TBP is 227.

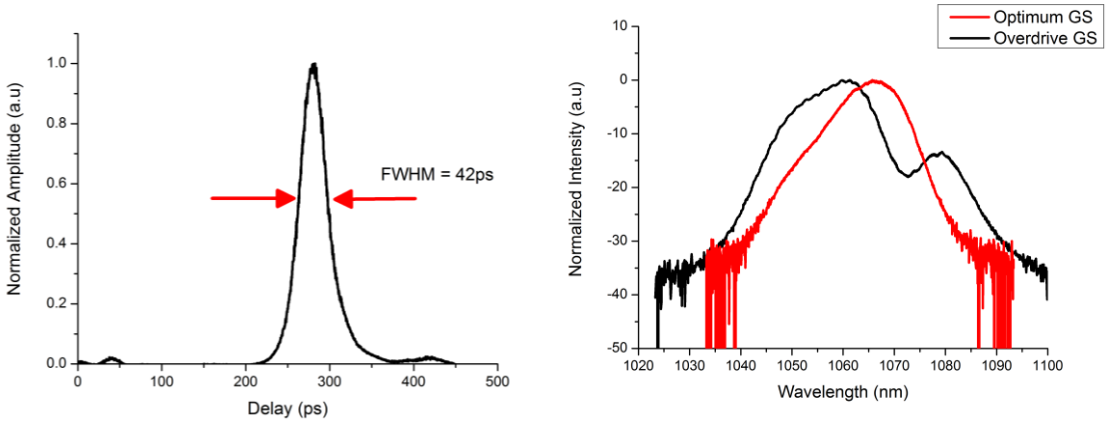

Figure 5.6. Output pulse and spectrum obtained from gain switching a Qphotonics SLD. The black line spectrum corresponds to a peak-to-peak drive current of 600 mA while the red line corresponds to a peak-to-peak drive current of 300 mA.

The final diode tested was manufactured by Qphotonics and has a maximum output power of 30mW at 200mA. The central operating wavelength is located at 1060 nm and has a FBG attached to the diode output for wavelength stabilization. Since the location of the FBG is close to the chip, the reflected signal from the FBG may not be synchronised with the injected modulated current. Initially, the diode was fed with an I_{p-p} of 600mA and a bias current of 40mA. This resulted in a distorted output spectrum as shown in Figure 5.6 (black line). The input modulated current was then reduced down to 300mA peak-to-peak with a DC bias current of 30mA. The corresponding spectrum is illustrated by the red line in Figure 5.6. Optical pulses with a FWHM of 42 ps were obtained with a pulse energy of ~3pJ. Once again a broad, asymmetrical output spectrum was observed with a FWHM of approximately 7 nm. No additional peak was observed at optimum GS operation. The spectrum consists of multi-longitudinal modes with a inter-modal spacing of about 0.16 nm. Again, based on the measured

mode spacing, the estimated chip length is ~1.0 mm (assuming a refractive index of InGaAs of ~3.5). The TBP is estimated to be 79.

From the above set of investigations it is clear that SLDs sourced from different manufacturers resulted in different optical pulse widths at their optimum operating conditions. All 3 SLDs is are shown to have different chip or cavity lengths as calculated from the longitudinal mode spacing. As reported in [12], the cavity length influences the photon lifetime of the SLD through the relationship, $\tau_p = {}^{1}\Big/\left(\nu\left(\alpha_i + \left({}^{1}\Big/_{l}\right)\ln\left({}^{1}\Big/_{R}\right)\right)\right)$ where α_i is the distributed loss, R is the mirror reflectivity, ν is the group velocity and l is the cavity length. A shorter cavity length will result in a shorter photon lifetime and therefore shorter optical pulses can be generated [13, 14]. A simple simulation was carried out using equation in [15] to see the influence of the photon lifetime on the optical pulse width. Four values of photon lifetime are used (1 ps, 2 ps, 5 ps and 10ps) while the other parameters are kept fixed.

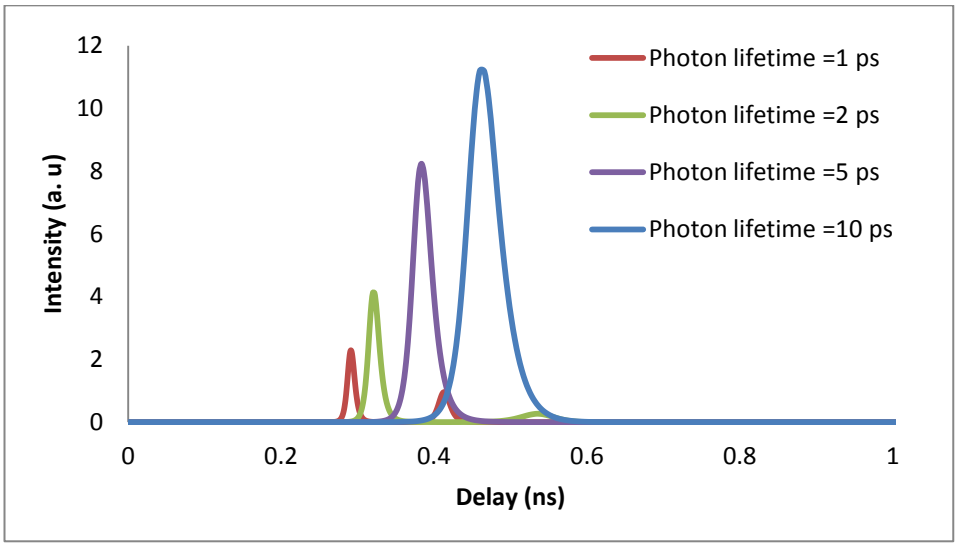

Figure 5.7. Numerical calculation for the generation of gain switched optical pulse from SLD with different photon lifetime values.

When the photon lifetime is 10 ps, optical pulses with a FWHM of approximately 70 ps were obtained. The FWHM reduces to 44 ps for τ_p = 5 ps, 20 ps for τ_p = 2 ps and 12 ps for τ_p = 1 ps. The reduction in optical pulse width also causes the energy contained in the optical pulse to reduce. Although a short optical pulse can be generated with a SLD having a shorter cavity (or chip) length, the average optical power or pulse energy will be low as compared to the SLD with a longer cavity length.

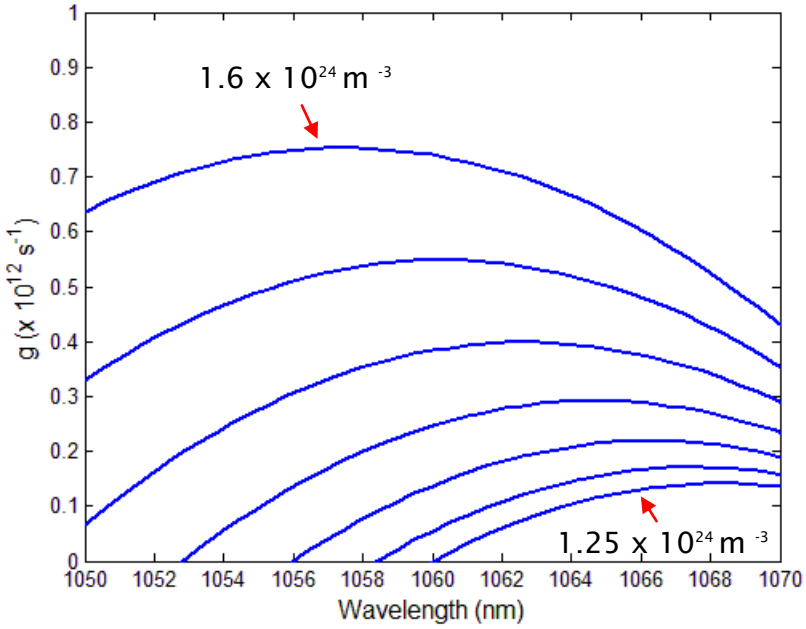

Figure 5.8. Numerical calculation of gain spectra when the carrier density is varied from 1.25 x 10^{24} m^{-3} to 1.6 x 10^{24} m^{-3}.

In all three different SLDs, the output spectra have asymmetrical shapes consisting of multiple longitudinal modes. Similar observation was reported in [16, 17]. The asymmetric spectra result from the band filling effect in the laser diode which is a common phenomenon in laser diodes [18]. When the carrier density is initially built up as shown in Figure 5.8, the gain peak of the laser diode will be blue-shifted, exciting longitudinal modes at shorter wavelengths. However, as the carrier density is slowly depleted due to the stimulated emission process, the gain peak begins to red-shift, resulting in the excitation of the longitudinal modes at longer wavelengths. Since the residual gain will be located at the longer wavelength region, the modes at longer wavelength will experience more gain resulting in asymmetry in the power spectrum of the gain switched pulse.

5.3.2 Injection seeding

The optical spectrum produced from direct gain switching is usually broad as a result of the excitation of multiple longitudinal modes. This broad spectrum output is usually not desired for frequency conversion processes due to the limited acceptance bandwidth of nonlinear crystals. However, it is possible to generate picosecond pulses with narrow spectral bandwidth directly from a SLD using a few techniques reported in [19, 20]. One of the techniques is injection seeding via an external laser source. This technique not only reduces the spectral bandwidth, but also reduces the TBP and the rms timing jitter of the optical pulses.

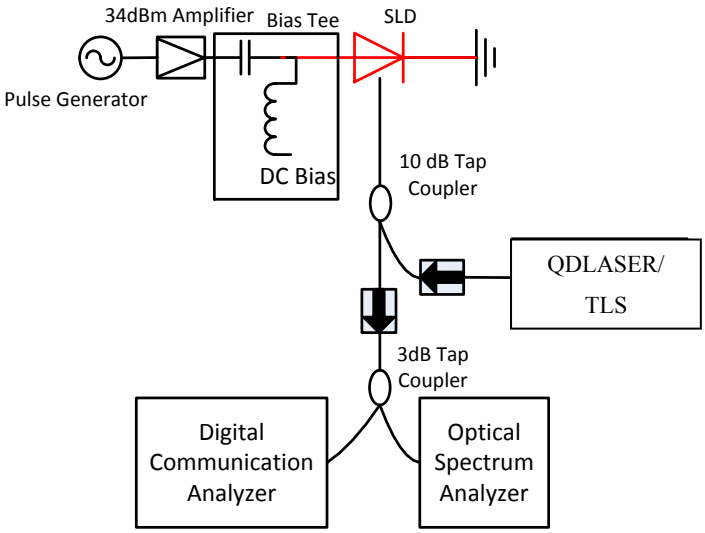

Figure 5.9. Experimental configuration for gain switching with external seeding.

In realizing the external injection seeding, a DFB laser diode (QDLASER) with a 3dB spectral bandwidth of 0.05nm was used as a CW injection seed diode. The DFB laser output was spliced with an inline polarization maintaining isolator to block the incoming optical signal from the GS SLD. A 10 dB tap coupler was spliced after the isolator with the 10% tap port being spliced to the DFB laser and the remaining 90% as the GS signal output. The injection power can be adjusted by changing the injection current to the DFB laser.

With the Oclaro laser diode, direct GS resulted in 90ps optical pulse with 7nm of spectral linewidth. External seeding using a DFB seed diode effectively reduced the spectral linewidth down to 0.07 nm, or by a factor of 100. Moreover, optical pulse duration reduced from ~90ps down to ~45ps. The TBP was reduced to 0.72. However, secondary peaks were observed on either side of the main pulse even at a very low seeding powers as shown in Figure 5.10(a). For 50μW of seeding power the SMSR was measured to be >30dB. Smaller peaks on both sides of the main pulse appeared to be sensitive to diode temperature. The diode temperature was optimized to maximise the energy in the main pulse while minimizing the energy contained in the sidebands. However, sideband free optical pulses could not be achieved. Furthermore, there was no significant changes to the sidebands when the bias current changes.

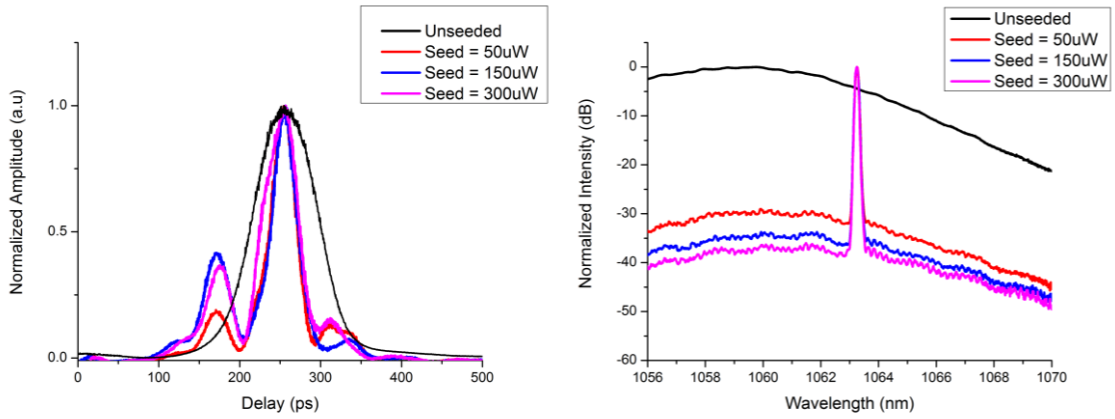

Figure 5.10. Output pulses and spectra obtained from external injection seeded gain switched Oclaro SLD at different seeding power.

Similar observations were made when the Oclaro diode was replaced with a Qphotonics diode. Seeding power appears to affect output pulse shape as shown in Figure 5.11(a). Increasing seeding power into the gain switched laser diode improved the SMSR (>30dB) but at the expense of the output pulse shape. Nevertheless, the extent of pulse deformation is modest with substructures observed only at the trailing edge of the optical pulse. However the substructures became more pronounced when the seeding power exceeds 100µW. For this particular diode, an optimum seeding power was found to be 50µW whereby the optical pulse maintained its original width of 42 ps (as measured with the direct GS scheme) without observing any deformation and an SMSR of ~25dB. The calculated TBP for the external seeding case was 3.1, an improvement by over a factor of 25 to that of the direct GS operation.

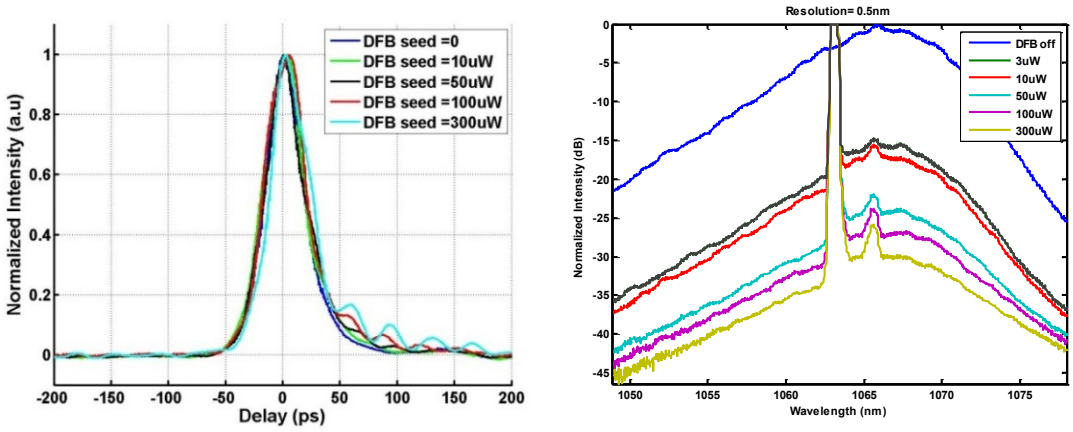

Figure 5.11. Output pulses and spectra obtained from external injection seeded gain switched Qphotonics SLD at different seeding power.

Finally the 3SPhotonics diode was subject to external injection seeding. Since the operating wavelength of this diode was at 1040nm, the DFB diode laser was replaced with a tunable laser

source (TLS) from TOPTICA. Total injected powers from 140μW and up to 375μW were injected into the GS laser diode. The diode behaved similar to that of the Oclaro diode as illustrated in Figure 5.12. The sideband was primarily located at the leading edge of the optical pulse although a small peak also started to appear at the trailing edge at high seeding power. By tuning the temperature of the diode, the energy in the main pulse can be maximised, but the sideband cannot be suppressed completely. The sideband on the leading edge of the pulse is not desirable as it may affect the amplification of the main pulse. ~60ps optical pulses were produced with a maximum output power of 6mW. The spectral bandwidth at the 3dB level was ~0.07nm and the estimated TBP was 0.5, close to bandwidth limited assuming a Gaussian shaped pulse.

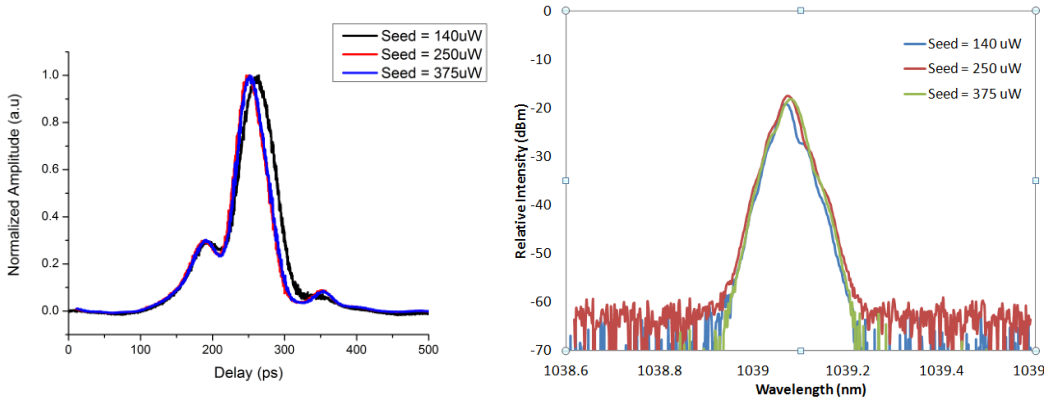

Figure 5.12. Output pulses and spectra obtained from a 3SPhotonics SLD when external seeding is applied at different power levels.

The distorted or substructured optical pulses obtained through external seeding of a gain switched laser diode has been linked to the intrinsic cavity modes. The spectral bandwidth of the external seed plays a crucial role in the output pulse shape. In the Oclaro diode case, the mode spacing is smaller than the bandwidth of the external seed. As a result the injection seed may lock all the cavity modes that lie within the bandwidth of the external seed. Since each cavity mode will have a different pulse build up time due to different propagation delay and gain, the main pulse will be accompanied by structure on either/both the leading and trailing edges.

In the case of the Qphotonics diode, however, no substructure is observed with external seeding because the diode has a larger mode spacing as compared to Oclaro or 3SPhotonics diode by a factor of 4. Thus, external seeding managed to lock just one cavity mode resulting in an undistorted temporal profile. However, when the seeding power is increased, the main pulse starts to broaden while multiple substructures at the trailing edge start to grow. This is related to the interaction between the seed and the cavity modes. When the seeding power is sufficiently high, the seed will start to compete with the cavity modes for gain resulting in a degree of fluctuation of injection locking.

In all 3 cases, however, the TBP was calculated to be larger than the ideal value of 0.44 (assuming a Gaussian profile). Therefore there is a considerable amount of chirp present in the optical pulse. By chirp compensation, transform limited optical pulses can be obtained. Chirp compensation have been demonstrated before using a CFBG [20].

The use of a secondary SLD for external seeding improves the performance of the gain switched laser diode. Spectral bandwidth can be narrowed down with substantial improvement in SMSR and without massive distortion to the pulse temporal profile as seen for the Qphotonic diode. The narrow spectral bandwidth combined with short optical pulse can be used as a seed laser in MOPA configuration. However, incorporating external seeding in the system will be disadvantageous as it added complexity to the seed laser setup. This level of complexity can be tolerated in the laboratory environment but if it is to be manufactured on a large scale, it will not be a cost effective solution.

5.4 Active Mode-locking via an inline FBG as external cavity

Actively mode-locked SLDs with an external cavity grating have become one of the most popular optical sources in the 1.5 μm wavelength region since first reported in 1991 [21]. Short picosecond optical pulses can be generated using this technique and usually operate at high repetition frequency. The optical pulses inherit low timing jitter and a wide locking bandwidth at a fixed operating wavelength [22]. Furthermore, mode-locked SLDs with a fiber Bragg grating (FBG) as an external cavity mirror have been demonstrated experimentally at 2.5 GHz [23] and 10 GHz [24]. Unlike optical pulses generated through gain switching, mode-locked optical pulses are usually transform-limited in kind and offer the prospect of the shortest pulses that can be generated within the bounds of the gain bandwidth of SLD and the spectral bandwidth of the grating [24]. Thus, with this technique, further pulse compression is not required, making the seed configuration simple and economical.

5.4.1 Configuration for Active Mode-locked SLD

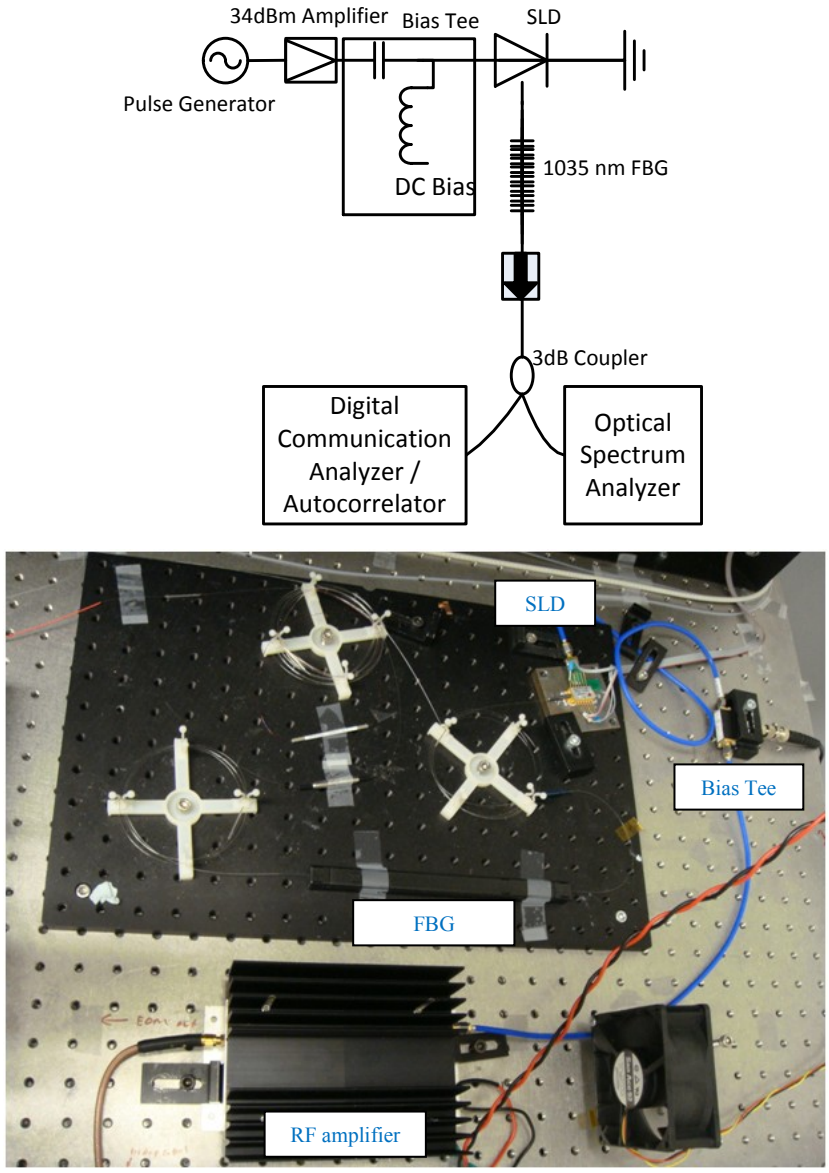

Figure 5.13. Picosecond pulse generation through active mode-locking with FBG as external cavity

Figure 5.13 shows schematic of the experimental setup. The SLD used in this experiment was that sourced from Oclaro which operates at 1035 nm. The measured longitudinal mode spacing was 0.032 nm and the threshold current is 25 mA. A combination of pulse generator and RF amplifier drove the SLD with a stable train of sinusoidal electrical pulses. The drive current had a peak-to-peak current of 632 mA which was superimposed on a DC bias current of 20 mA, slightly less than the threshold current to avoid CW leakage signal. The pigtail of the SLD was spliced to a polarization maintaining 1035 nm FBG with a 3 dB bandwidth of 0.24 nm and a reflectivity of ~12%. The fiber length between the SLD and the FBG was ~2 m. The fundamental frequency of the cavity was ~51.7 MHz and the system was operated at 832.6 MHz

which corresponded to the 16th harmonic. A polarization maintaining 3-dB fused fiber coupler was spliced to the output end of the grating so that both temporal and spectral profiles can be measured simultaneously with a DCA and OSA.

The diodes from 3SPhotonics and Qphotonics were also used in this experimental setup, however, the optical performance was worse compared with the Oclaro device. The 3SPhotonics diode generates longer duration pulses (~30 ps) as compared with Oclaro and the pulse profile was not smooth with random noise peaks. As for the Qphotonics diode, the pulse duration remained similar as compared to the direct gain switching method.

5.4.2 Performance of mode-locking at various repetition frequencies

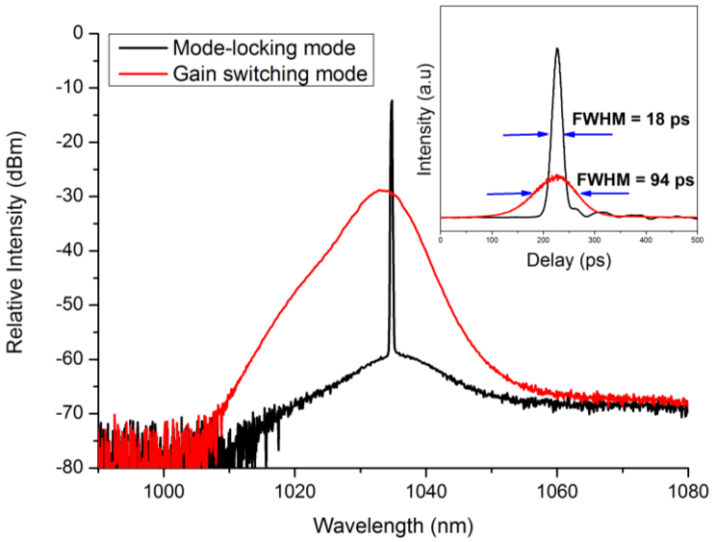

Figure 5.14. Spectral profiles of the gain-switched laser diode with (black line) and without (red line) FBG. (Inset) Temporal profiles for the seeded (black line) and unseeded (red line) cases.

When the injection current modulation frequency (ICMF) was detuned relative to the harmonic of the cavity FSR, pulses with a broad optical spectrum with a full width at half maximum (FWHM) of approximately 6 nm and a pulse width of ~94 ps were measured, as illustrated by the red colored lines in Figure 5.14. In such circumstances the SLD operated in a gain-switching (GS) mode as a result of the high drive current pulse of sub-ns duration. The broad spectrum generated consisted of a large number of longitudinal modes. The emitted optical pulses exhibited a strong red-shift in wavelength from the leading to trailing edge corresponding to a very significant chirp. The estimated time bandwidth product of the pulses is ~158.

Once the ICMF was tuned to 832.6 MHz we observed substantial reductions in both the spectral bandwidth and the pulse width as shown by the black colored lines in Figure 5.14. Furthermore, transform-limited optical pulses of 18 ps were measured with an intensity autocorrelator as

shown in the inset of Figure 5.14. This corresponds to an almost 5 times reduction in pulse width as compared to that of the GS case. A spectral Side-Mode Suppression Ratio (SMSR) of ~50 dB and a FWHM spectral bandwidth of 0.09 nm were measured corresponding to an almost 67 times compression in the spectral domain. The average optical power was measured to be ~6 mW corresponding to a pulse energy of 7.2 pJ.

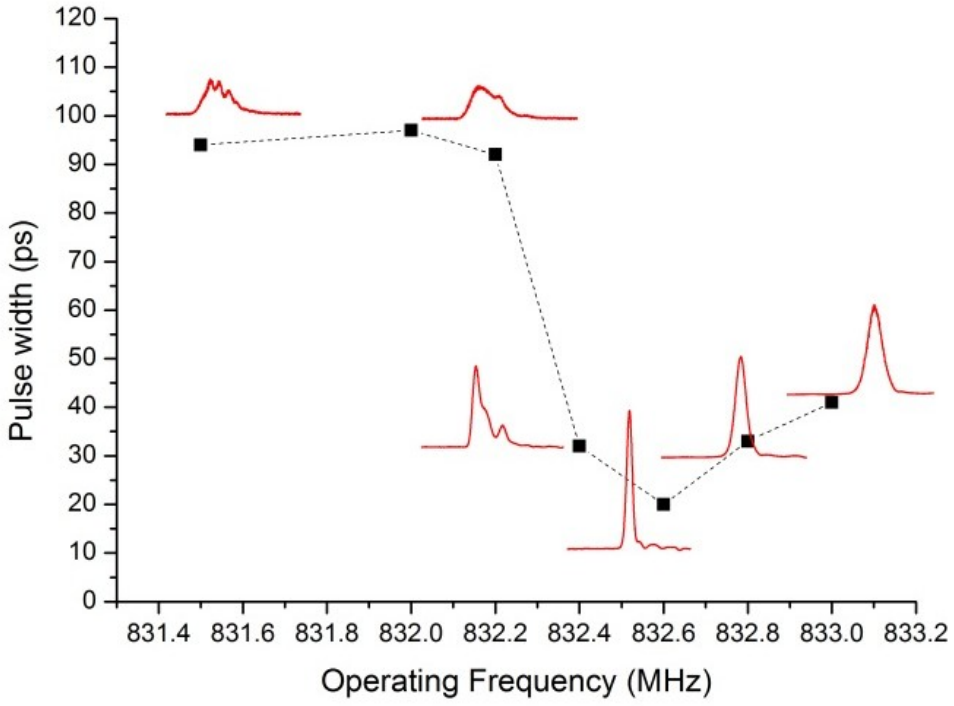

Figure 5.15. Optical pulse width measured at different repetition frequencies and (color) the corresponding optical pulse shapes

A small detuning in the ICMF resulted in a substantial change in pulse widths and pulse shapes, similar to that reported in [25]. Figure 5.15 shows the variation in pulse width as the operating frequency was varied with the inclusion of the detailed pulse shapes observed.

At ICMFs below 832.0 MHz, broad, distorted and unstable optical pulses were observed similar to that of the GS case. Increasing the ICMF to 832.2 MHz resulted in more stable but broader (90 ps) asymmetrical optical pulses with a long trailing edge. Furthermore, the pulses exhibited a double peak structure with the leading peak slightly broader than the trailing peak. The evolution of double peak optical pulses at frequencies just below the cavity resonance frequency can be explained as follows. For a fixed cavity length the time of flight of the pulses remains effectively constant irrespective of the operating frequency. Therefore at frequencies just below the harmonic cavity resonance frequency, the reflected pulses arrive back at the active region whilst the carrier density is still building up due to the ever so slightly longer time interval between the injected current pulses. Consequently a portion of the carrier density gets depleted

through stimulated emission however the carrier density continues to build up in the presence of the current pulse. A second optical pulse evolves when the excess carrier density reaches the threshold condition.

An increase in the ICMF to 832.4 MHz resulted in a reduction in the energy contained within the secondary peak due to insufficient recovery of the carrier density

When the ICMF was tuned to 832.6 MHz, a harmonic of the cavity FSR, short optical pulses with a width of ~18 ps were obtained. In this instance, the returning pulse arrives at the active region when the carrier density is at its maximum. This resulted in the highest peak power of 400mW that can be extracted cleanly from the mode locked laser diode, although a small secondary peak was still observable at the trailing edge of the main pulse. Note however that we managed to eliminate the secondary pulse completely by reducing the DC bias current down from 20 mA to 15 mA.

As the ICMF was further increased to 832.8 MHz and 833.0 MHz, the pulse width broadened to 30 ps and 40 ps respectively and both amplitude and timing jitter started to become significant with increasing frequency detuning. Beyond 833 MHz mode-locking was completely lost and the optical pulses returned to the characteristic of pure GS operation with a pulse width of ~94 ps.

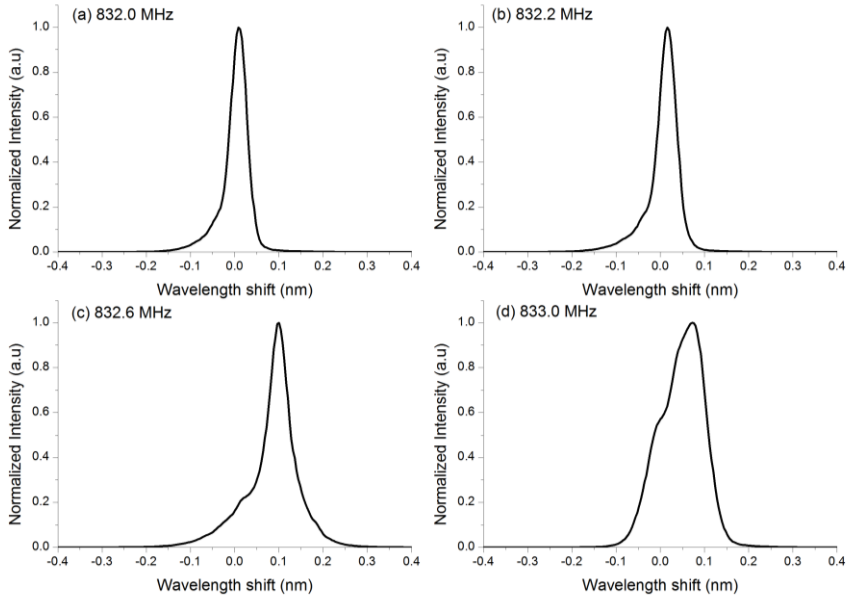

Figure 5.16. Optical spectra measured for a range of injection current modulation frequencies showing the observed wavelength shift with respect to the central wavelength of the FBG.

The lasing wavelength of the output pulses was also affected when the ICMF was detuned. The optical spectra measured at various ICMF are plotted in Figure 5.16. The central wavelength at

different frequency detunings was compared relative to the FBG's peak reflectivity wavelength in order to quantify the accumulated shift in wavelength. We observed a red-shift of the central wavelength as the ICMF was increased to 832.0 MHz and 832.2 MHz. However, as soon as the ICMF was tuned to 832.6 MHz, a maximum wavelength shift of 0.1 nm was measured. We also observed that the spectrum exhibited an asymmetrical shape with a tail in the short wavelength region. Any further increase in repetition frequency resulted in a broader spectrum and a reduction in the wavelength shift. A similar red-shift in central wavelength was also observed in [23, 25, 26] suggesting that when the ICMF was changed, the device self-tuned its operating wavelength in order to maintain the correct effective cavity length needed to maintain resonance with the drive current signal.

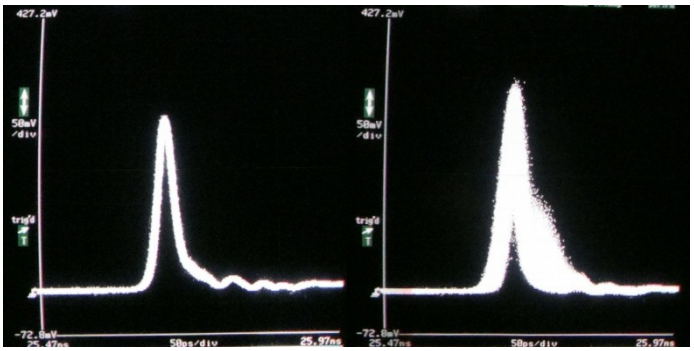

Figure 5.17. Snap shot of the pulse stability with infinite persistence mode when (left) stable mode-locking was achieved while (right) a jittery pulse is observed and locking is no longer stable.

The stability of the mode-locking mechanism depends on the reflectivity of the FBG. In this work, we examined three uniform pitch FBGs of different reflectivity, namely 4%, 8% and 12%. We observed that mode-locking was unstable when a 4% reflectivity grating was used. The stability and shape of the optical pulse varied randomly over a period of time. Much better mode-locking was achieved with a 7% reflectivity FBG. However, environmental conditions such as changes in temperature of the air surrounding the FBG affected the stability of the optical pulses over a longer time scale and fine adjustment of the TEC was necessary from time to time to recover the optimum stable mode-locking condition. On the other hand, when a 12% reflectivity FBG was used stable mode-locked operation was accomplished without the need for periodic tweaking of the temperature controller highlighting the fact that the strength of the external cavity feedback is important in sustaining uninterrupted mode locked operation - mode competition between the SLD modes and that of the external cavity is less well controlled with a weaker grating resulting in unstable mode locked operation.

Since the constituent longitudinal modes of a mode-locked optical pulse will have a defined phase relationship, an interference measurement based on a fiber based Mach-Zehnder interferometer that enabled interference between the 1st and the 10th optical pulses (i.e 10 pulse time slots later) was carried out to confirm that the mode-locking mechanism is indeed responsible for the generation of the short optical pulses observed. Interference patterns are clearly visible in the spectral domains as shown in Figure 5.18 for ICMF of 832.6 MHz and 833 MHz. The interference pattern was lost completely above 833 MHz and at or below 832.0 MHz, indicating that the mode-locking mechanisms no longer exist in these operating regimes. Instead, injection seeding dominates the pulse generation process.

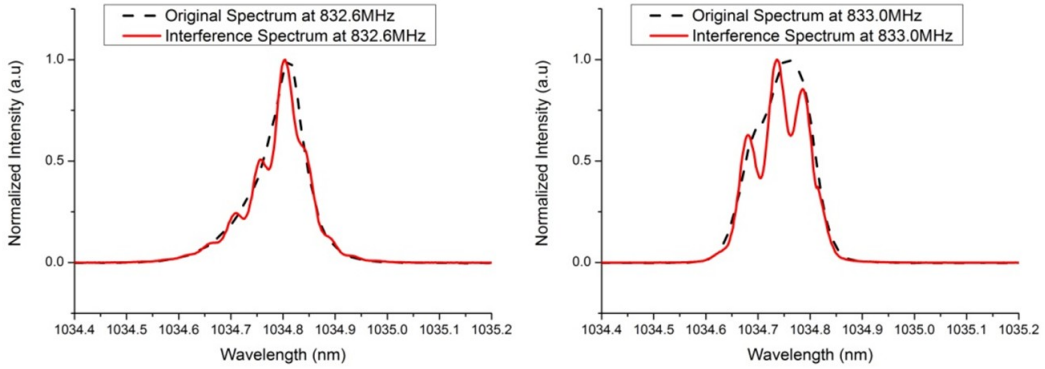

Figure 5.18. Interference patterns between the 1st and the 10th optical pulses for two different operating frequencies corresponding to different operating regimes. The separation between peaks corresponds to the temporal separation between the two interfering optical pulses.

5.5 Stability of picosecond pulses between direct gain- switching and mode-locking

Optical pulses generated from the GS SLD through injection seeding usually exhibit timing jitter as a result of the random photon number fluctuations below the lasing threshold. The RMS timing jitter is proportional to the ratio of the standard deviation to the mean of the photon density at the time when the carrier density reaches the threshold. When current is injected into an unbiased SLD, the random spontaneous emission will dominate and lead to photon fluctuation. Typically, this will result in high timing jitter. Reduction in timing jitter happens when the fluctuation of photon density becomes smaller. This occurred when externally injected light or optical feedback provides initial excitation of the desired mode to a level higher than the spontaneous emission level. Timing jitter can be classified into two categories: correlated and uncorrelated jitter [27]. Correlated jitter is the effect of noise contributed by the drive circuit while the uncorrelated jitter is results from the ‘turn on delay timing jitter’ due to the random spontaneous emission at the onset of an electrical pulse that leads to photon fluctuation.

The optical pulses were measured using a 32 GHz Agilent photodetector and a wideband DCA. The DCA has an intrinsic RMS jitter of 1.5ps and therefore the direct measurement of timing jitter is limited to a resolution of 1.5 ps. Both amplitude and timing jitter can thus be measured directly and the measurement values can be retrieved from the DCA. In the direct gain switching case, the optical pulses produced exhibited significant amplitude jitter (~15%) and RMS time jitter of 5 ps. By introducing an external seed with optical power of 50 µW, the timing jitter improved by approximately 30%. However, the amplitude jitter remains the same as measured for the directly gain switched laser diode.

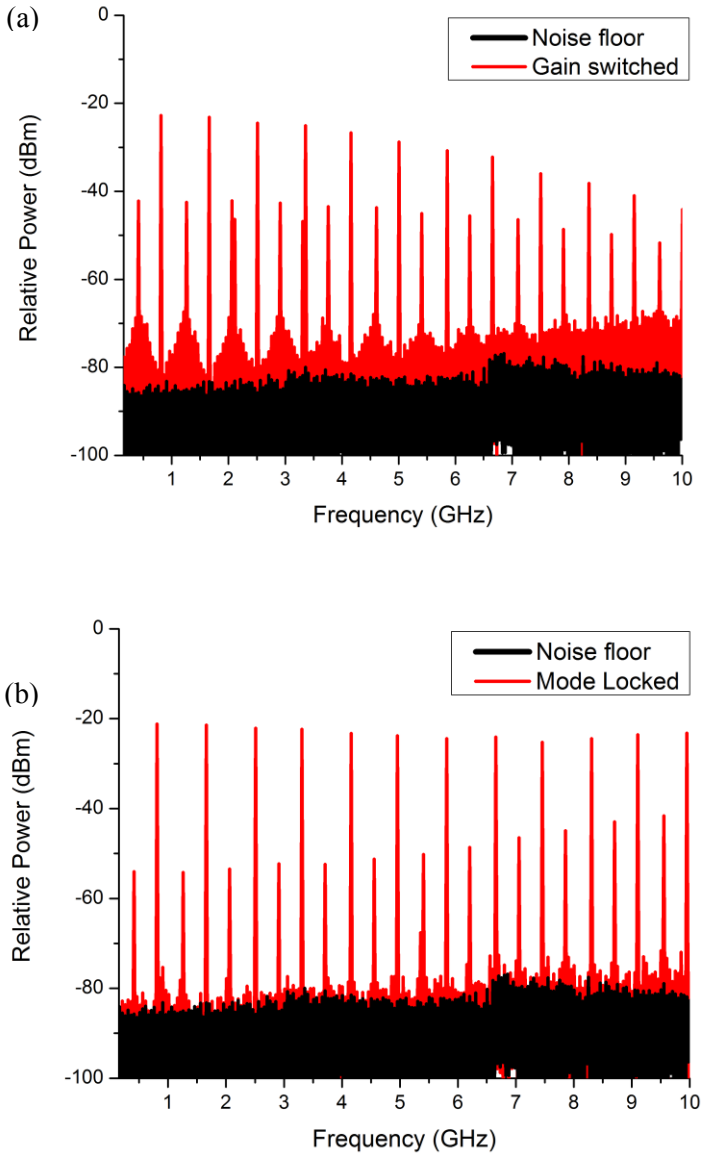

Figure 5.19. Power spectra of the optical pulse in the frequency domain for (a) direct gain switching and (b) mode locked operations.

When the SLD was active mode-locked with a FBG, the timing jitter was measured to be approximately 1.2 ps, which was not accurate due to the resolution limitation of the direct mesurement. However, the amplitude noise remained the same as for the direct gain switching case. In order to obtain an accurate measurement of the timing jitter, frequency domain measurements are required. For the frequency domain measurement, a 50 GHz RF spectrum analyzer from Agilent was used to measure the power spectra of the optical pulses. The analysis was based on frequency domain technique proposed by Von der Linde [28].

Figure 5.19 shows the measured power spectra of the optical pulse train in the frequency domain for both gain switching and active mode locking cases. Both measurements were done with frequency span of 10 GHz and resolution bandwidth of 1 MHz. The noise floor was measured when no optical signal was present in the photodetector originated from the combination of the electrical pulse generator and photodetector. The first peak represents the fundamental frequency of the pulse train and the rest of the peaks are the harmonics of the fundamental. Note that the operating frequencies in these measurements were 832.6 MHz (active mode locking) and 833.2 MHz (gain switching). There is a smaller peak in between the two main peaks; with the frequency value being half the operating frequency. This additional peak exists due to non-uniform amplitude of the pulse train, creating an envelope with a modulation frequency half the laser repetition frequency across the peak of the optical pulses. The electrical pulse generator is the reason behind the non uniform pulse train. From Figure 5.19, it can be seen that there are two types of noise bands present, one which has a narrow bandwidth and lies in between the fundamental and harmonic frequencies while the other has a uniform noise band across all the harmonics and is mainly uncorrelated noise. It was observed that for gain switching operation, the pulse train incurred higher RMS uncorrelated timing jitter, with the base noise level increased by approximately 10 dB. On the other hand, with active mode locking operation, the base noise level only had a small increase, indicating a small uncorrelated noise floor. Using the extension of the method proposed by Leep et al [29], the RMS uncorrelated timing jitter was calculated by using Equation 5-1.

$$\sigma_\tau = \frac{1}{2\pi\sqrt{\mu^2 + \frac{1}{12}}f} \cdot \sqrt{\frac{P_n}{P_c} \cdot \frac{f}{\Delta\Delta f_{res}}}$$

Equation 5-1

where σ_τ is the RMS uncorrelated timing jitter, μ is the harmonic order, f is the repetition frequency, Δf_{res} is the resolution bandwidth and P_n/P_c is the ratio of peak power of the noise band and peak power of the carrier.

In addition, both timing and amplitude jitter can be calculated based on the equations proposed by Von de Linde. Equation 5-2 is used for the estimation of the amplitude jitter.

$$\frac{\Delta E}{E} = \frac{1}{2\mu\pi}\sqrt{\left[\left(\frac{P_A}{P_C}\right)_{\mu=0}\frac{\Delta f_j}{\Delta f_{res}}\right]}$$

Equation 5-2

where $^{\Delta E}/_{E}$ is the percentage of amplitude jitter, μ is the harmonic order, Δf_j is the repetition frequency, Δf_{res} is the resolution bandwidth and $^{P_C}/_{P_A}$ is the ratio of peak power of one of the noise band and peak power of the carrier. As for RMS timing jitter, Equation 5-3 was used.

$$\frac{\Delta t}{T} = \frac{1}{2\mu\pi}\sqrt{\left[\left(\frac{P_C}{P_j}\right)_{\mu}\frac{\Delta f_j}{\Delta f_{res}}\right]}$$

Equation 5-3

where Δt is the RMS amplitude jitter, T is the round trip time, μ is the harmonic order, Δf_j is the repetition frequency, Δf_{res} is the resolution bandwidth and $^{P_C}/_{P_j}$ is the ratio of peak power of the noise band and peak power of the carrier.

Figure 5.20 shows the power ratio plot as a function of nth harmonics with the power ratio being measured directly. The power ratio is influenced by the sum of the two different noise contributions, the first is the high frequency temporal jitter and the second is the amplitude fluctuations. In direct gain switching, the power ratio increases from -80 dB to -30 dB as the nth harmonic becomes higher. Increases in power ratio indicate that more noise is accumulated in the frequency band. It clearly shows that gain switched optical pulse suffers significant jitter noise from the high frequency components. The optical pulse from the active mode locked laser diode shows a slower rise in power ratio. For low frequency components, the gradient of the mode locked pulse is almost the same as for the gain switched pulse and this is mainly attributed to amplitude jitter. At higher harmonics, the power ratio curve for the mode locked pulse shows a slower rise, indicating that the high frequency jitter is low. At a resolution bandwidth of 1 MHz, $^{P_n}/_{P_c}$ = -53 dB at the 8th harmonic for gain switching operation and $^{P_n}/_{P_c}$ = -62 dB at the 8th harmonic for mode locking operation. Based on this, the calculated rms uncorrelated timing jitter is 1.4 ps for gain switching and 0.55 ps for mode locking operations.

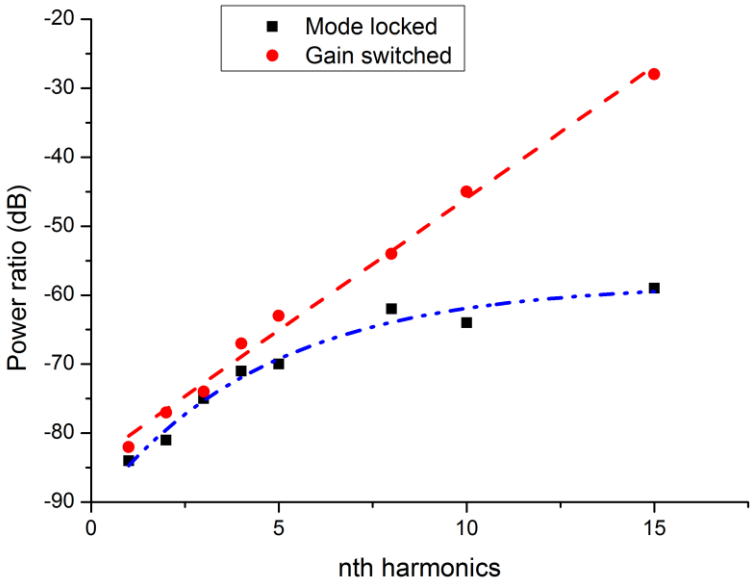

Figure 5.20. Power ratio plots in frequency domain as a function of frequency harmonics for mode locked and gain switched optical pulses.

Figure 5.21 show the RF power spectrum measured at the fundamental frequency, 3rd harmonic and 7th harmonic for the mode locked optical signal and the electrical signal from the pulse generator. The frequency resolution used was 10 kHz with a frequency span of 1 MHz. The sweeping time for this measurement was 98 ms with a total of 1000 sampling points. Based on Equation 5-3 the calculated RMS amplitude jitter is approximately 15%, similar to the value obtained through direct measurement with the DCA. It was identified that a large portion of this amplitude jitter originated from the electrical pulse generator. As shown in Figure 5.21(a,b,c) the pulse generator spectrum (doted red line) overlapped perfectly with the spectrum of the optical signal. Moreover, similar observations were made for the 3rd and 7th harmonics. The narrow noise band lies -25dB below the main peak in Figure 5.21(a) and is believed to originate from the electrical pulse generator.

The timing jitter measurement for the mode locked case was calculated based on the RF power spectrum obtained at the 15th harmonic as shown in Figure 5.21(d). The frequency resolution was set to 10 kHz for this set of measurements. The FWHM of the pedestal was measured to be 615 kHz while the difference between the peak of the power spectrum and that of the pedestal was -50 dB. Using Equation 5-3, the calculated RMS timing jitter turned out to be 316 fs.

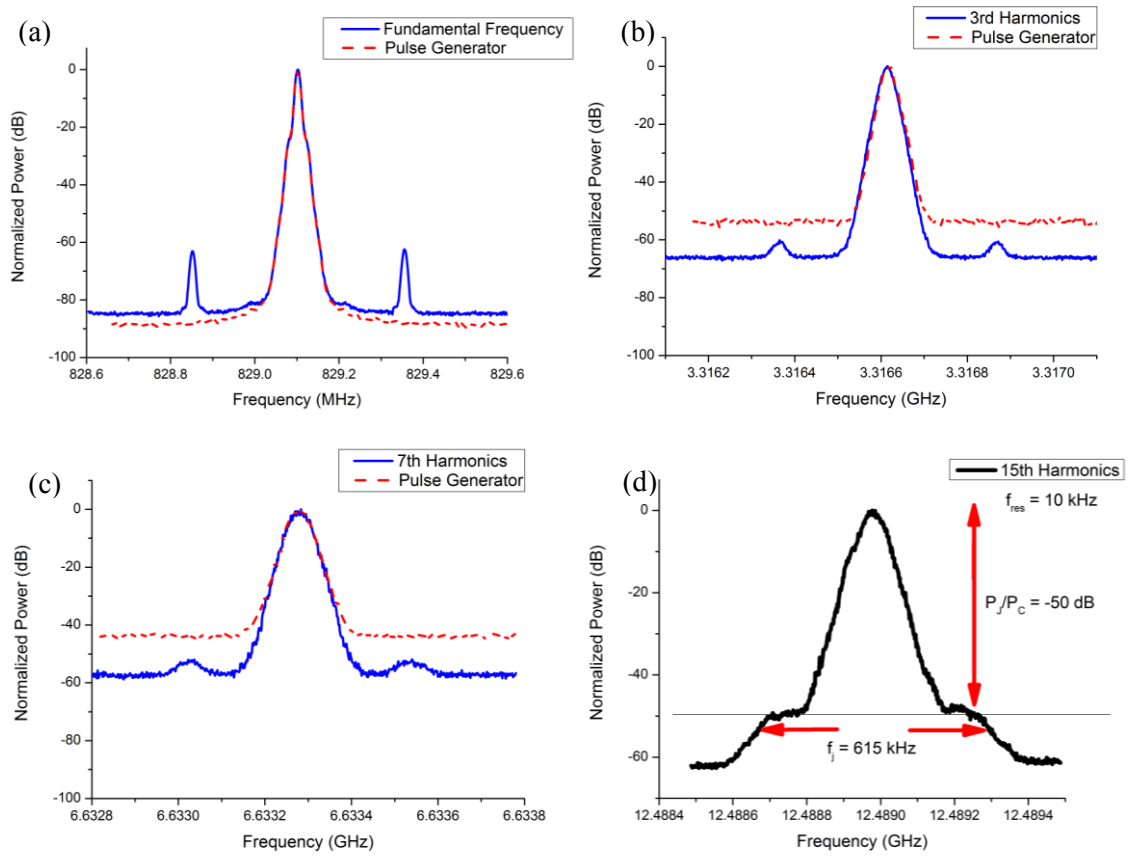

Figure 5.21. High resolution power spectra measurement for the mode locked optical pulses at (a) fundamental frequency, (b) 3rd harmonics, (c) 7th harmonics and (d) 15th harmonics.

5.6 Chirp measurement with Frequency Resolved Optical Gating (FROG)

The optical pulses generated from the GS SLD are usually chirped and result in TBPs many times the transform limited value. The effect of band filling combined with carrier depletion in SLD for instance, leads to shifting of the SLD's gain peak to longer wavelength. This causes the optical signal to be chirped, with the leading edge populated with short wavelength components and the falling edge with long wavelength components. Since the optical pulse is linearly chirped, the pulse can be in principle, compressed down to transform limited via an external compressor or dispersion tailored fiber. Measurement of the chirp parameter associated with the optical pulse is thus crucial.

One of the techniques used for chirp measurement is Frequency-Resolved Optical Gating (FROG) [30, 31]. This technique utilizes a temporal modulator (an intensity modulator in this case) as a gate instead of using nonlinear interaction in the typical FROG configuration. A spectrogram of the pulse is constructed by measuring the spectrum of the gated pulse as a function of the delay between the optical pulse and the gate. Complete information about the pulse shape and phase can then be extracted from the time-frequency spectrogram. Through the

use of a broadband intensity modulator, it is possible to characterise both short and long optical pulses. Furthermore, the entire setup is fully fiberised and high delay resolution can be achieved with an electronic delay generator.

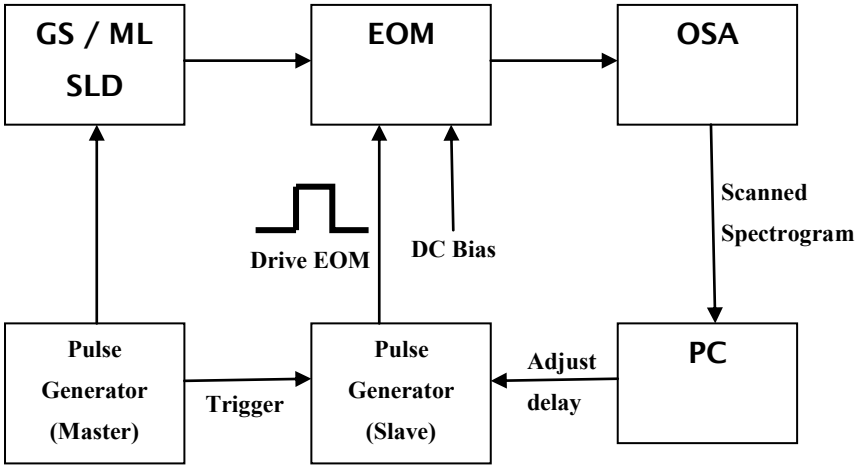

Figure 5.22. Experimental setup for FROG measurement via the use of EOM.

The detailed setup for the FROG measurement using an EOM (intensity modulator) is shown in Figure 5.22. A 10dB optical coupler was spliced to the seed, with the 90% output port fed to a fiberised EOM. The EOM was driven by a square waveform, generated from a secondary pulse generator. The master pulse generator triggered the secondary unit as well as modulating the SLD. In order to have a full extinction of the EOM, the amplitude of the square waveform was set to 5V. The square wave generator with the ability to vary both pulse duration and output delay was controlled directly using a PC. The gate width used in this experiment was 100 ps, and was limited by the bandwidth of the EOM. The delay step used was 1ps. The output from the EOM was fed into an OSA with resolution set to 0.01 nm. At every delay step, a spectral trace was taken and by overlapping all these traces the time-frequency spectrogram can be produced with a spectrogram sample shown in Figure 5.23. Numerical retrieval was carried out on the spectrogram using the blind deconvolution code developed at the ORC, University of Southampton [32, 33].

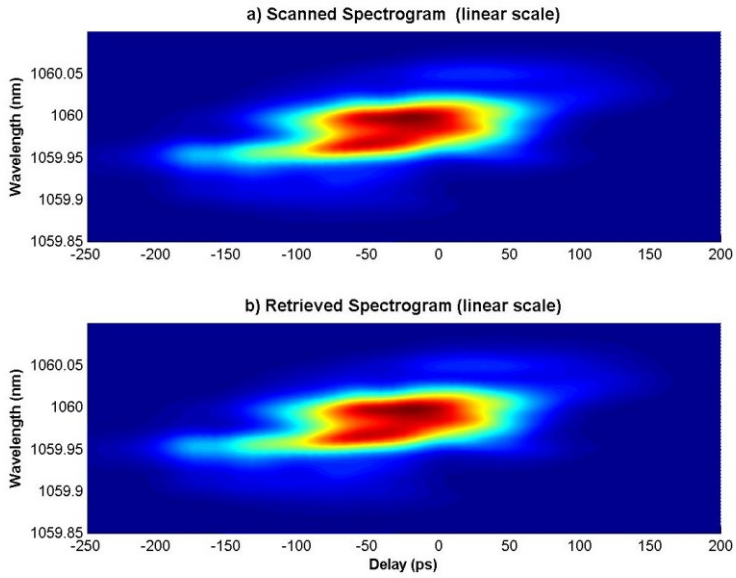

Figure 5.23. (Above) Spectrogram measured directly with FROG measurement setup and (below) spectrogram retrieved via deconvolution process.

Figure 5.24(a) shows a spectrogram obtained for the output pulses of a Qphotonic diode externally seeded by a DFB. With the use of the deconvolution program, a spectrogram was also retrieved. The retrieval error was < 0.004 on a 128 x 128 point grid indicating that there is good agreement between the measured and reconstructed spectrograms. In order to verify the accuracy of the deconvolution algorithm, the set of results were compared with the intensity and spectrum measured directly via photodetector and OSA. As shown in Figure 5.24(b) (blue lines), the traces from direct measurement overlapped nicely with the retrieved results. As for the spectrum, the agreement was very good down to 30dB from the maximum level. From the measured spectrogram, the frequency shift was clearly observed with the leading edge being blue shifted and the trailing edge was red shifted. The phase at every point across the intensity profile was different. This indicate that the pulse inherited frequency chirp as a result of the phase difference. Furthermore, the pulse experienced negative chirp with the calculated TBP (TBP = 3.1) many times the transform limited value.

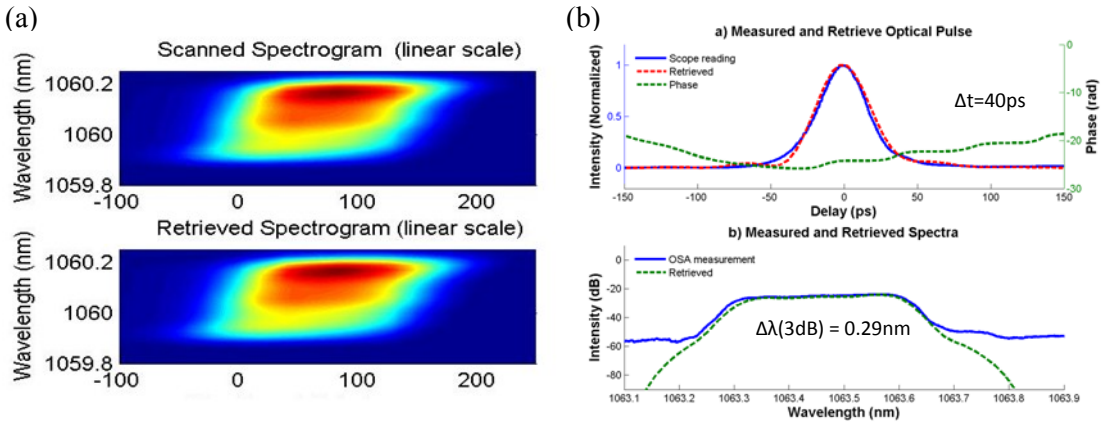

Figure 5.24. (a) The scanned and retrieved spectrogram of the optical pulses from Qphotonics diode and (b) the reconstructed intensity, spectrum and phase profiles.

The same measurement was repeated for the mode locked pulses. The results are shown in Figure 5.25. The retrieved error achieved for this measurement was < 0.002. Information such as the temporal shape (black line) and chirp (blue dash line) across the optical pulses can be retrieved with this method as shown in Figure 5.25. It clearly shows that the measured chirp was constant across the central region of the optical pulse and increases linearly at the trailing edge due to the existence of a small secondary peak which is ~35 ps away from the main pulse. The estimated time bandwidth product (TBP) of 0.45 indicates that the output pulses were time-bandwidth limited (assuming a Gaussian shaped optical pulse).

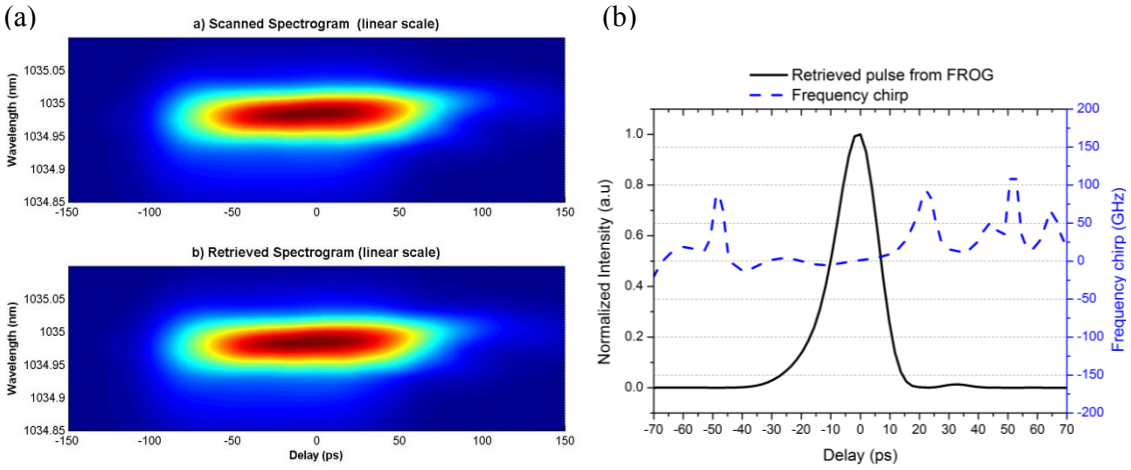

Figure 5.25. (a) The scanned and retrieved spectrogram of the optical output from Oclaro diode and (b) the reconstructed intensity profile and frequency chirp across the optical pulse.

5.7 Conclusion

In this chapter, gain switching of SLDs sourced from different manufacturers (Oclaro, 3SPhotonics and Qphotonics) were investigated in detail. The Qphotonics SLD generated the shortest gain switched optical pulses with 42 ps of optical duration. The output spectral bandwidth was over 7 nm in the case of direct gain switching, but can be narrowed down significantly with external seeding. However, SLDs sourced from Oclaro and 3SPhotonics generated long optical pulses (90 ps and 117 ps respectively) with a similarly broad output spectrum. Like the Qphotonics SLD, using external injection seeding technique, it was possible to narrow the output spectrum significantly; however, the output pulse profiles appeared to be distorted or to have secondary peaks.

It has also been demonstrated that external FBG seeded gain switched SLDs can produce transform limited optical pulses. I have shown that a mode locking mechanism is responsible for the observed short, transform limited optical pulses. This is the first demonstration of a mode locked SLD at the 1.06 μm waveband. With this technique, a short 18 ps optical pulse with a pulse energy of 7.2 pJ and peak power of 400 mW was obtained.

Further characterisation on the stability of the optical pulses generated via direct gain switching and mode locking was carried out. The frequency domain measurement technique was carried out and concluded that the timing jitter of the mode locked pulses was smaller as compared to the gain switched pulses. Furthermore, direct gain switched pulse suffered significant noise jitter at higher harmonic frequencies.

Finally, a FROG technique was applied to investigate the frequency chirp of the optical pulses generated via injection gain switching and mode locking techniques. From the measured spectrogram and retrieved phase information, it can be concluded that the gain switched pulses inherit a negative frequency chirp and can be compressed with an external compressor such as a chirped fiber Bragg grating (CFBG), dispersive fiber etc. FROG also revealed that the mode locked optical pulse was chirp free and that the output optical pulse is transform limited.

The combination of the excellent stability of the optical pulse produced and simplicity of this mode locking configuration make this SLD based system an attractive seed source for picosecond MOPA systems.

5.8 References

1. F. Kienle, P. S. Teh, D. Lin, S.-u. Alam, J. H. V. Price, D. C. Hanna, D. J. Richardson, and D. P. Shepherd, "High-power, high repetition-rate, green-pumped, picosecond LBO optical parametric oscillator," Opt. Express **20**, 7008-7014 (2012).
2. A. Ancona, S. Döring, C. Jauregui, F. Röser, J. Limpert, S. Nolte, and A. Tünnermann, "Femtosecond and picosecond laser drilling of metals at high repetition rates and average powers," Opt. Lett. **34**, 3304-3306 (2009).
3. K. K. Chen, S.-u. Alam, J. H. V. Price, J. R. Hayes, D. Lin, A. Malinowski, C. Codemard, D. Ghosh, M. Pal, S. K. Bhadra, and D. J. Richardson, "Picosecond fiber MOPA pumped supercontinuum source with 39 W output power," Opt. Express **18**, 5426-5432 (2010).
4. J. Yoonchan, J. Nilsson, J. K. Sahu, D. N. Payne, R. Horley, L. M. B. Hickey, and P. W. Turner, "Power Scaling of Single-Frequency Ytterbium-Doped Fiber Master-Oscillator Power-Amplifier Sources up to 500 W," Selected Topics in Quantum Electronics, IEEE Journal of **13**, 546-551 (2007).
5. H. Ito, H. Yokoyama, S. Murata, and H. Inaba, "Picosecond optical pulse generation from an r.f. modulated AlGaAs d.h. diode laser," Electronics Letters **15**, 738-740 (1979).
6. A. Piper, A. Malinowski, B. C. Thomsen, D. J. Richardson, L. M. B. Hickey, and M. N. Zervas, "11.1 W average power, 20 ps pulses at 1 GHz repetition rate from a fiber-amplified gain-switched 1.06 μm Fabry-Perot laser diode," in *Lasers and Electro-Optics, 2005. (CLEO). Conference on*(2005), pp. 1141-1143 Vol. 1142.
7. K. K. Chen, J. H. V. Price, S.-u. Alam, J. R. Hayes, D. Lin, A. Malinowski, and D. J. Richardson, "Polarisation maintaining 100W Yb-fiber MOPA producing μJ pulses tunable in duration from 1 to 21 ps," Opt. Express **18**, 14385-14394 (2010).
8. K. A. Ahmed, H. F. Liu, N. Onodera, P. Lee, R. S. Tucker, and Y. Ogawa, "Nearly transform-limited pulse (3.6 ps) generation from gain-swtiched 1-55 um distributed feeback laser by using fibre compression technique," Electronics Letters **29**, 54 (1993).
9. C. de Dios, and H. Lamela, "Improvements to Long-Duration Low-Power Gain-Switching Diode Laser Pulses Using a Highly Nonlinear Optical Loop Mirror: Theory and Experiment," Lightwave Technology, Journal of **29**, 700-707 (2011).
10. A. Consoli, and I. Esquivias, "Pulse shortening of gain switched single mode semiconductor lasers using a variable delay interferometer," Opt. Express **20**, 22481-22489 (2012).
11. D.-S. Seo, H.-F. Liu, D. Y. Kim, and D. D. Sampson, "Injection power and wavelength dependence of an external-seeded gain-switched Fabry--Perot laser," Applied Physics Letters **67**, 1503-1505 (1995).

12. P. Downey, J. E. Bowers, R. Tucker, and E. Agyekum, "Picosecond dynamics of a gain-switched InGaAsP laser," Quantum Electronics, IEEE Journal of **23**, 1039-1047 (1987).
13. G. J. Aspin, J. E. Carroll, and R. G. Plumb, "The effect of cavity length on picosecond pulse generation with highly rf modulated AlGaAs double heterostructure lasers," Applied Physics Letters **39**, 860-861 (1981).
14. R. J. Helkey, and Y. Arakawa, "Cavity optimization for minimum pulsewidth of gain-switched semiconductor lasers," Photonics Technology Letters, IEEE **7**, 272-274 (1995).
15. K. Y. Lau, "Gain switching of semiconductor injection lasers," Applied Physics Letters **52**, 257-259 (1988).
16. L. Pao-Lo, C. Lin, I. P. Kaminow, and J. J. Hsieh, "Picosecond pulse generation from InGaAsP lasers at 1.25 and 1.3 μm by electrical pulse pumping," Quantum Electronics, IEEE Journal of **17**, 671-674 (1981).
17. M. Osinski, and M. J. Adams, "Picosecond pulse analysis of gain-switched 1.55 µm InGaAsP laser," Quantum Electronics, IEEE Journal of **21**, 1929-1936 (1985).
18. K. Wada, H. Yoshioka, J. Zhu, T. Matsuyama, and H. Horinaka, "Simple form of multimode laser diode rate equations incorporating the band filling effect," Opt. Express **19**, 3019-3036 (2011).
19. J. Lawrence, and D. Kane, "Injection locking suppression of coherence collapse in a diode laser with optical feedback," Optics communications **167**, 273-282 (1999).
20. A. Piper, A. Malinowski, B. C. Thomsen, D. J. Richardson, L. M. Hickey, and M. N. Zervas, "11.1 W average power, 20 ps pulses at 1 GHz repetition rate from a fiber-amplified gain-switched 1.06 μm Fabry-Perot laser diode," in *Conference on Lasers and Electro-Optics*(Optical Society of America, 2005), p. CTuCC3.
21. P. A. Morton, R. Adar, R. C. Kistler, C. H. Henry, T. Tanbun-Ek, R. A. Logan, D. L. Coblentz, A. M. Sergent, and K. W. Wecht, "Hybrid soliton pulse source using a silica waveguide external cavity and Bragg reflector," Applied Physics Letters **59**, 2944-2946 (1991).
22. Z. Ahmed, L. Zhai, A. J. Lowery, N. Onodera, and R. Tucker, "Locking bandwidth of actively mode-locked semiconductor lasers," Quantum Electronics, IEEE Journal of **29**, 1714-1721 (1993).
23. P. A. Morton, V. Mizrahi, P. A. Andrekson, T. Tanbun-Ek, R. A. Logan, P. Lemaire, D. L. Coblentz, A. M. Sergent, K. W. Wecht, and P. F. Sciortino, Jr., "Mode-locked hybrid soliton pulse source with extremely wide operating frequency range," Photonics Technology Letters, IEEE **5**, 28-31 (1993).
24. R. Paoletti, D. Bertone, R. Fang, G. Magnetti, M. Meliga, G. Meneghini, G. Morello, G. Rossi, L. Tallone, and M. Scofet, "Repetition rate, using a mode-locked hybrid distributed

Bragg reflector (ML-HDBR) laser source," Photonics Technology Letters, IEEE **12**, 245-247 (2000).

25. A. J. Lowery, N. Onodera, and R. Tucker, "Stability and spectral behavior of grating-controlled actively mode-locked lasers," Quantum Electronics, IEEE Journal of **27**, 2422-2430 (1991).
26. N. Dogru, "Effect of Grating Parameters on Mode-Locked External Cavity Lasers," Selected Topics in Quantum Electronics, IEEE Journal of **15**, 644-652 (2009).
27. M. Jinno, "Correlated and uncorrelated timing jitter in gain-switched laser diodes," Photonics Technology Letters, IEEE **5**, 1140-1143 (1993).
28. D. Linde, "Characterization of the noise in continuously operating mode-locked lasers," Appl. Phys. B **39**, 201-217 (1986).
29. D. A. Leep, and D. A. Holm, "Spectral measurement of timing jitter in gain switched semiconductor lasers," Applied Physics Letters **60**, 2451-2453 (1992).
30. C. Dorrer, and I. Kang, "Simultaneous temporal characterization of telecommunication optical pulses and modulators by use of spectrograms," Optics Letters **27**, 1315-1317 (2002).
31. K. T. Vu, A. Malinowski, M. A. F. Roelens, M. Ibsen, P. Petropoulos, and D. J. Richardson, "Full Characterisation of Low Power Picosecond Pulses From a Gain-Switched Diode Laser Using Electro-Optic Modulation Based FROG," (Optical Society of America, 2007), p. CFF4.
32. M. A. Roelens, B. C. Thomsen, and D. J. Richardson, "Multi-wavelength EAM based optical sampling for performance monitoring in high bit-rate systems," (2004).
33. M. A. Roelens, M. Forzati, A. Djupsjöbacka, P. Petropoulos, A. Berntson, and D. J. Richardson, "Linear frequency resolved optical gating as a line monitoring tool," in *Optical Fiber Communication Conference*(Optical Society of America, 2006), p. OWN2.

Chapter 6. High Power and High Energy Picosecond Fiber Sources

After investigating and analyzing the best solution for generating stable pulses in Chapter 5, the seed laser will be amplified in a chain of fiber amplifiers to investigate the power scaling capability. This chapter will present the work which explicitly targets a high energy and high average power picosecond fiber MOPA. The challenges and laser efficiency will be discussed with the experimental work on the fiber MOPA. Furthermore, the factor limiting the output power will be analyzed.

Apart from this, both our project partners, SPI Laser and IFM have great interest for the work done here. The improvement in power scaling capability in the picosecond fiber MOPA will allow IFM to carry out more specific machining tests. As for SPI Lasers, valuable experimental data can be obtained on the performance and capability of the fiber MOPA and will be useful for their upcoming products.

6.1 Introduction

High-power lasers operating in the picosecond regime are becoming increasing useful for various applications. With the cost of pump lasers coming down significantly from a few hundreds of dollars per Watt to close to a dollar per Watt, manufacturers are looking at reliable and cost effective laser systems as a replacement for some manufacturing processes. Many of these applications require high average powers and high peak power picosecond pulses with pulse repetition frequencies ranging from kHz to MHz ranges. Titanium sapphire lasers are commonly employed for many of these applications but emerging fiber laser and amplifier systems provide an attractive alternative solution [1]. Ytterbium-doped fiber amplifiers (YDFAs) in particular have been demonstrated to be capable of providing high single-pass gain, very high optical-to-optical efficiencies, diffraction-limited output beams and to be highly robust with regards to thermal effects due to the fiber geometry which allows for the efficient dissipation of heat generated in the lasing process [2-4].

In recent years, operation in the picosecond regime has become popular and various demonstrations with high average power and high energy pulses are reported. The simplicity and alignment free picosecond fiber MOPA system has attracted a lot of research interest and the introduction of new fiber laser based applications. One of them is the high power green laser generated through frequency doubling using a nonlinear bulk crystal. Dupriez et al reported an 80 W green laser generated through frequency doubling using an LBO crystal and with a total

conversion efficiency of 46% [5]. Other than that, there are also a growing number of demonstrations using picosecond pulses to pump optical parametric oscillators (OPO), allowing large wavelength tunability and representing an essential tool for spectroscopic applications [6-8]. The use of picosecond optical pulses packed with high energy and operating at high repetition frequency (MHz range) in processes such as Laser Induced Forward Transfer (LIFT) has also been reported recently and has shown great results in device fabrication [9, 10]. The picosecond-LIFT process has the advantage over ns-LIFT that the thermal effect is minimum, thus avoiding cracking, melting and other common defects which often occur with the nanosecond pulses.

In micromachining applications, picosecond optical pulses offer great advantages over other tools due to the non-thermal ablation process. One of the main application of picosecond pulses is the machining of hard transparent materials. A high precision cut with good edge quality on glass materials can be achieved using a high power picosecond laser [11]. Besides, the capability of high energy picosecond optical pulses to modify and polish the surface of stainless steel was demonstrated recently [12, 13]. This opens up the possibility to produce ultra-smooth substrates.

A key approach to generate high average power is the implementation of MOPA architecture. The technique has been used successfully in the picosecond regime allowing pulses from either a mode-locked or a gain-switched seed laser to be amplified to high optical output powers. Piper et al demonstrated amplification of gain switched picosecond pulses in 2003 with 1 GHz repetition frequency and 21 ps pulsewidth [14]. Further amplification of up to 341 W was demonstrated with a similar setup by Dupriez et al [15]. However, the output was slightly multimoded with M^2 of 2.4 due to the use of a large diameter core fiber. The setup was not fully fiberized with the power amplifier stage relying on free space in and out coupling. Kang et al demonstrated a fully fiberized, gain switched seeded MOPA with a linearly polarized output of up to 100 W over the operating frequencies between 908 MHz and 56 MHz[16]. The system is capable of generating optical pulses tunable between 1 ps and 21 ps using an external compressor. In addition, Chen et al demonstrated amplification of mode locked picosecond pulse in a fiberized MOPA at a maximum power of 157 W at a repetition frequency of 480 MHz [17].

A growing number of applications require significant amounts of optical energy in the short pulse regime. Although DPSS systems can offer such optical parameters, bulk systems are no longer the preferred option. The emerging fiber based laser systems are slowly replacing DPSS system. Although the cw optical power achieved from fiber based laser system is comparable to other competing technologies, the energy extraction is still modest. The advancement of fiber

fabrication technology and the availability of high brightness, high average power pump diodes will be the catalyst for scaling both the optical power and energy in the fiber based laser system.

6.2 Challenges

Similar to solid-state lasers, fiber lasers also faces thermal management issues while scaling to higher average output power. The fiber geometry which provides a large surface area to volume ratio allows a better heat dissipation capacity than in bulk solid state laser counterparts. However the use of short lengths of DC YDF in fiber amplifier so as to manage nonlinear effects causes a significant amount of thermal loading. Furthermore, any splice loss also contributes to the overall heat load. Thermal loads caused by the quantum defect in active fiber and splice loss have to be managed properly to ensure that the fiber polymer coating does not reach the critical temperature (80 ~ 150˚C). This can be achieved by sandwiching the active fiber in between graphite sheets in order to spread the heat quickly since graphite has a good thermal conductivity of approximately 1600 W/m-K [18] along the plane. Besides, forced air or water-cooling may have to be incorporated for efficient thermal management.

Another challenge faced is damage to the fiber facet. The output end of high power fiber MOPAs is usually prone to surface damage. This effect is known to affect picosecond and nanosecond optical pulses and is caused by electron avalanche [19]. When the intensity of the output beam exceeds the damage threshold of the fiber core material, it leads to fracture or melting of silica glass. Typically, the surface damage threshold is lower than the bulk damage (bulk optical damage irradiance ~4.75 kW/μm^2) [20]. This is because surface cracks, scratches or dust can concentrate the optical field locally and lead to plasma formation at a lower threshold. It is reported [19-21] that by proper end face polishing, surface damage can be made equal to the bulk value. Moreover, fiber with a larger mode field diameter can handle higher peak intensity as the damage threshold scales with the mode area. Another option is to splice a large silica rod of appropriate length at the output of the MOPA to allow the beam to expand appreciably so as to reduce the intensity at the silica-air interface [22] resulting in a higher damage threshold.

Although substantial progress has been made in scaling the average output power from fiberized systems to the hundreds of watts level, the maximum peak power in these experiments has often been limited by nonlinear effects such as SPM and SRS [23] due to the relatively long lengths of active fiber required to absorb the coupled pump power in cladding pumped schemes. SPM in particular will increase the signal linewidth and reduce its spectral purity. This will impact the performance of the laser system when it is used as a pump source for frequency conversion e.g. OPO, SHG etc. [7, 24].

SRS on the other hand is responsible for transferring energy from the signal to a longer wavelength once the threshold has been reached. This is often the main limiting factor of a fiber MOPA designed to generate high peak power pulses. These effects can be minimized by using large-mode-area (LMA) fibers which incidentally also help in shortening the device length due to the higher pump absorption per unit length that results from their relatively large core-to-clad area ratio. LMA fiber with an even larger core diameter should in principle allow even further scaling up of the peak power, but this may rapidly lead to higher bending loss, a larger heat load per unit length and a tendency to multi-mode operation [25, 26]. Thus, a compromise needs to be made when designing the LMA fiber in terms of extractable peak power, ease of fiber handling and the output beam quality under high power operation.

6.3 Picosecond MOPA configurations

Throughout this chapter, an operating wavelength of 1040 nm is chosen over the more commonly used 1060 nm in order to minimize the overall amplifier length by exploiting the fact that the emission cross-section in YDF is much higher at 1040nm than at 1060 nm [27]. This leads to a higher gain per length and better energy extraction compared to the conventional 1060 nm operation (refer Chapter 2 in Section 2.2). Having a shorter device length especially in a MOPA system will be beneficial as the system can operate at higher peak power due to the reduction in effective length and increase in nonlinear threshold leading to higher pulse energy at the output.

Generation of stable, picosecond optical pulses from a semiconductor laser diode via a gain switching technique typically produces low energy optical pulses. The energy usually ranging from pJ to nJ depending on the driving conditions and characteristics of the laser diode. If the target output energy is in the μJ range , a total gain of 50 – 60 dB has to be provided. Since a fiber amplifier only provides a total average gain of ~20 dB, multiple amplifiers have to be used to achieve the target output pulse energy. For the work reported in this chapter, 4 fiber amplifiers are being used to provide sufficient gain to the pulses generated by the gain switched seed laser. The details of each stage of the MOPA system are elaborated below.

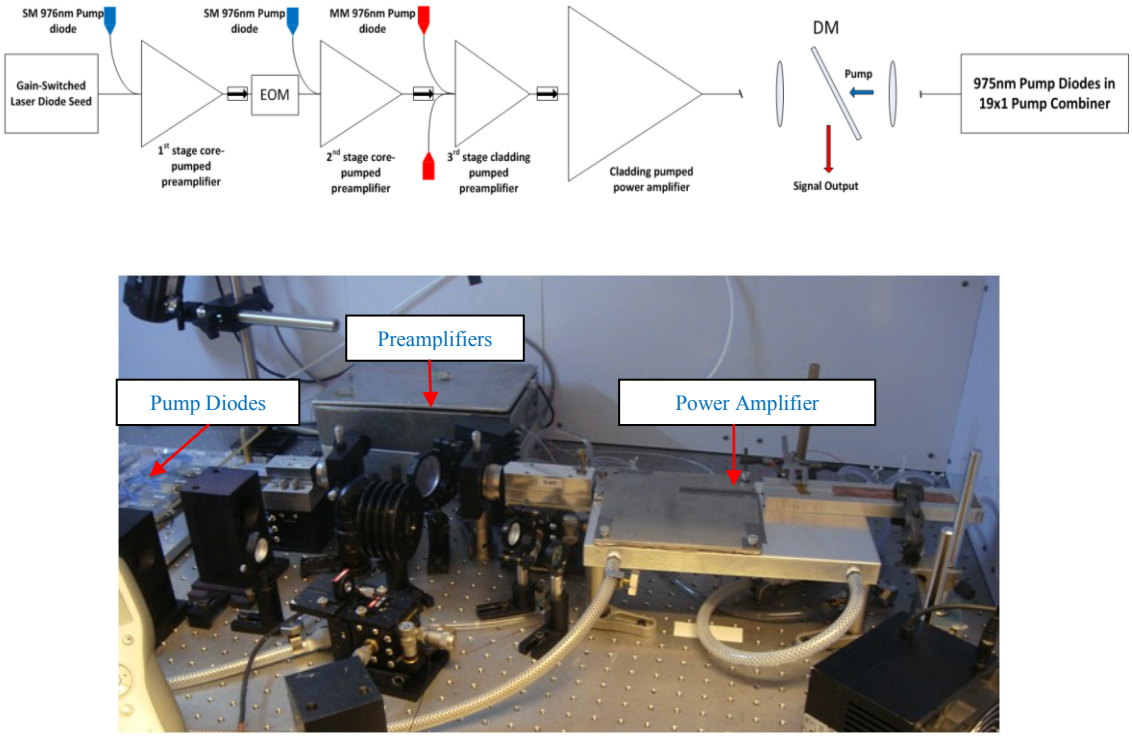

Figure 6.1. (Top) Fully fiberized picosecond seed laser based YDFA MOPA system incorporating 4 amplifier stages. (Bottom) Actual photo of the MOPA setup

6.3.1 Seed Source

The SLD used as the seed source is a commercially available Fabry-Perot laser diode with PM fiber pigtail (3SPhotonics). The SLD is gain-switched using the same setup as shown in Fig. 5.13 of Chapter 5. The pigtail of the SLD was spliced to a PM FBG with a 3 dB bandwidth of 0.24 nm and a reflectivity of 7.2 %. By tuning the repetition frequency, synchronization between the emitted pulses from the diode and reflected pulses from the FBG can be achieved and this eventually locks the cavity modes.

Two different optical pulse widths were achieved when the repetition frequency is tuned to either 858 MHz or 859 MHz. The optical pulses are measured directly with a fast photo-detector (Agilent 83440D) and a digital communication analyzer (Agilent Infiniium 86100C). Figure 6.2 shows the impulse response of the detection system measured by injecting a very short (7 ps) optical pulse indicating that the detection system can clearly resolve pulses as short as 16 ps. The measured optical pulses are illustrated in Figure 6.3. The shortest optical pulse is produced when the repetition frequency is tuned to 858 MHz, with a pulse duration of 28 ps. The optical pulse becomes slightly broader at higher repetition frequency and was measured to be 35 ps at 859 MHz. The measured average output power was ~6 mW corresponds to a pulse energy of ~7 pJ.

Both spectra show OSNR of over 45 dB as shown in Figure 6.3(b,d). The output spectrum at 858 MHz has a broader bandwidth (0.12 nm) as compared to that at 859 MHz (0.09 nm). The polarization extinction ratio (PER) was measured to be >20dB.

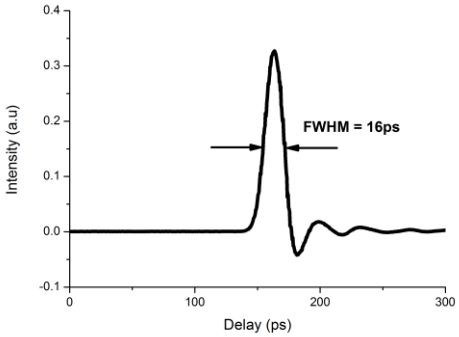

Figure 6.2. Impulse response of the photodetector measured through the injection of a short 7ps optical pulses

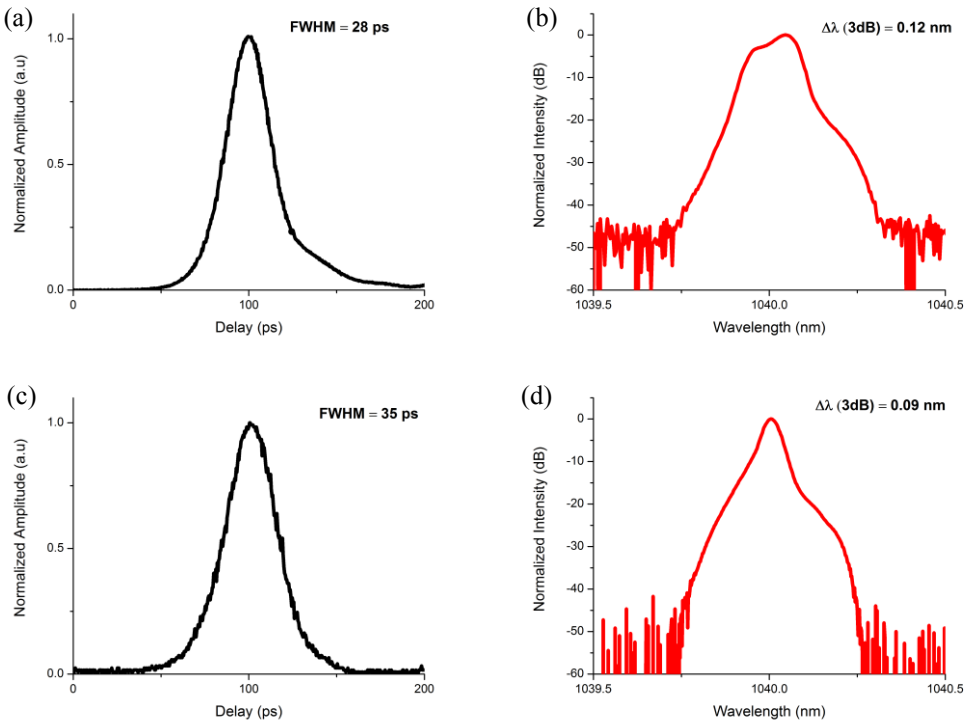

Figure 6.3. Temporal pulse shape and spectrum measured at a repetition frequency of (a-b) 858 MHz and (c-d) 859 MHz.

6.3.2 Amplifier Characterization

Given the low average optical power and thence the pulse energy available from the gain switched laser diode, amplification of the diode output is necessary for any real life application.

In order to scale up the output power to the desired level, a ytterbium-based fiber MOPA system was adopted.

6.3.2.1 Configuration of pre-amplifiers

The preamplifiers refer to the type of fiber amplifiers which provide low noise but sufficient amplification of the seed laser output. This is a crucial stage as it needs to amplify the small signal from the seed laser to a level sufficient to saturate the power amplifier stage. Moreover, noise performance in the preamplifier stages is a critical parameter. A low noise output will ensure signal purity and good OSNR as input to the power amplification stage.

In this work, two types of pump configurations were used for the fiber amplifiers, namely the core-pumping configuration and cladding-pumping configuration. The active medium used in both the preamplifiers was a double-clad ytterbium doped fiber (DC YDF).

Core Pumping Pre-amplifiers

Two stages of core-pumped amplifiers were used in the setup, the first being used to amplify the seed signal whilst the second is used to re-amplify the signal after the losses incurred in the EOM. The schematic of the core-pumped amplifier is shown in Figure 6.4. This setup consists of a 975nm/1040nm WDM coupler, isolator and a short length of polarization maintaining DC YDF. The WDM used here is to effectively couple the pump and signal wavelengths together into the active fiber for signal amplification. An inline isolator was spliced at the output of the active fiber to prevent any reflected signal or backward propagating ASE from the next stage amplifier to couple back into the amplifier.

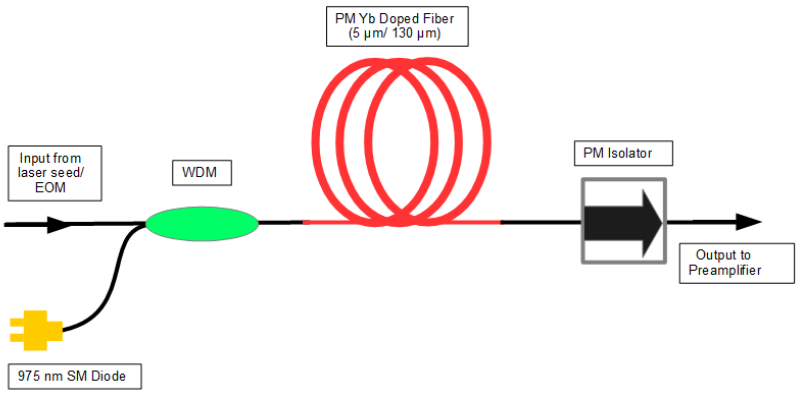

Figure 6.4. Schematic of a forward core-pumped fiber amplifier.

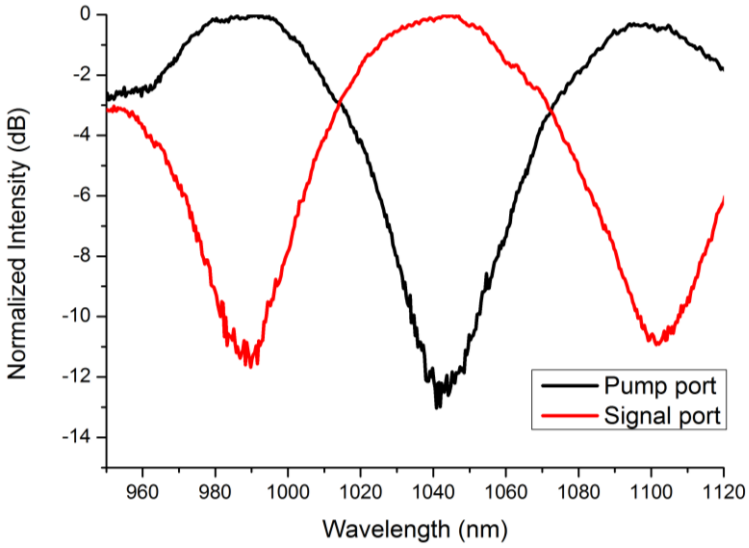

Figure 6.5. The characterization result of a 975/1040 nm WDM using a white light source.

In order to understand the coupling ratio of the signal and pump ports, I characterized the WDM using a white light source (Bentham WLS100) and OSA (AQ6370B). Figure 6.5 shows the measured coupling ratios as a function of wavelength for both the pump and signal ports. The extinction between the signal and the pump port at 1040 nm is over 12 dB which is deemed adequate to prevent backward propagating signal or ASE coupling into the pump port and causing damage to the pump diode.

The pump diode used in this setup is a single mode semiconductor laser diode from Lucent Agere with an external fiber Bragg grating as a wavelength stabilizer. The pump diode operates at 976 nm and emits a maximum average output power of 180 mW. An electrical driver board (EU-39 from Roithner Lasertechnik GmbH) provides a spike free, constant current of 300 mA to drive the pump diode.

Choosing the length of the Yb doped fiber is also a crucial parameter. Doped fiber that is too short will limit the gain of the signal and produce short wavelength ASE whilst an over length doped fiber will cause signal reabsorption and the generation of long wavelength ASE.

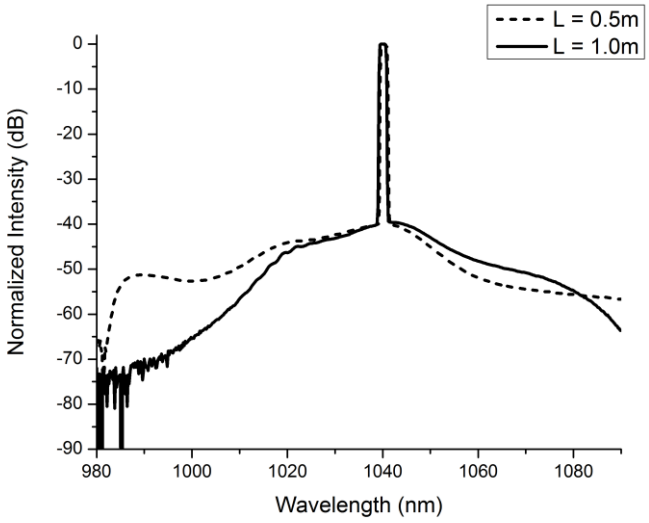

Figure 6.6. Output signal spectrum from the core-pumping preamplifier measured with different Yb doped fiber length

The Yb doped fibers used in this work are all commercially available from Nufern. For the core pumped preamplifiers, polarization maintaining, Yb doped double clad fibers are used (PM-YDF-5/130). This fiber has a core diameter of 5 μm and an octagonal shaped cladding diameter of 130 μm. It is a single mode fiber with NA of 0.12 and with an estimated mode field diameter of 6.5 μm. Figure 6.6 shows the output spectra of the first stage preamplifier output with different lengths of gain fiber. Both lengths produced a total optical output power of 50 mW for a seeded signal of ~6 mW corresponding to a total signal gain of ~9 dB. With L = 0.5 m, short wavelength ASE was observed whilst long wavelength ASE emerged as the fiber length increased to L =1.0 m. The ASE noise generated between these 2 fiber lengths are quite low and a total OSNR of over 40 dB was measured for both. This observation shows that the optimal length lies in between these two fiber lengths. For the 1st preamplifier however I have opted for 50 cm long Yb doped fiber.

The second stage preamplifier is located after the EOM. This amplifier is required to provide sufficient gain with low ASE noise for different pulse repetition frequencies. Optimization on the amplifier is required since the operating frequency varies between maximum pulse repetition frequency of 858 MHz and minimum pulse repetition frequency of 53 MHz. The total Yb doped fiber length used in this stage is 1.0 m.

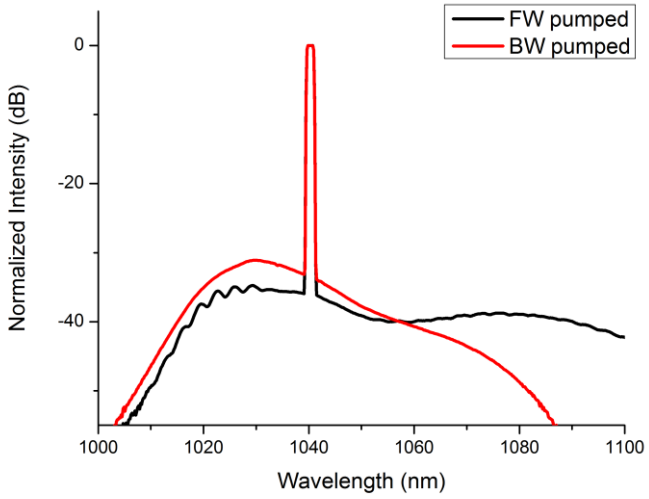

Figure 6.7. Output signal spectrum measured with forward pumping and backward pumping configurations at 53 MHz repetition frequency.

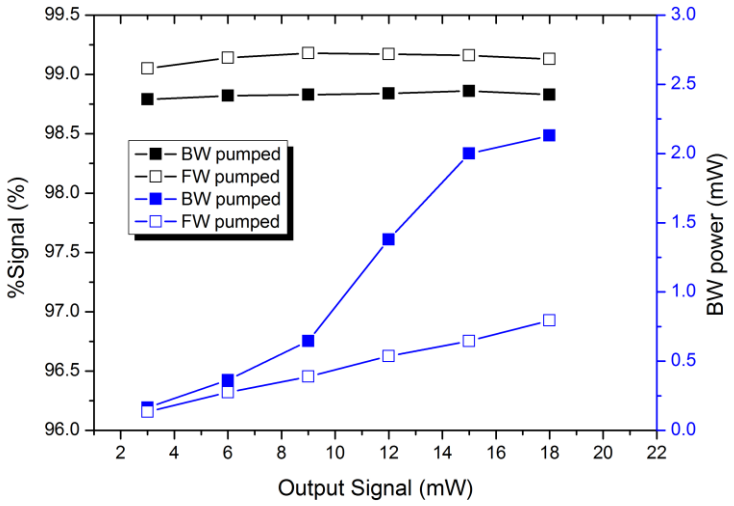

Figure 6.8. Ratio of signal to ASE power and the amount of backward travelling ASE measured at different output signal power.

For this preamplifier both the forward pumping and the backward pumping schemes were investigated. Figure 6.7 and Figure 6.8 shows the comparison between the two pumping schemes when operating at 53 MHz with an input power of 0.8 mW. The forward pumping scheme is shown to be a preferable choice since it produced an output signal with lower noise (over 99.1% is estimated to be signal in forward pumping as compared to 98.8% in backward pumping). At a maximum output power of 18 mW, the backward propagating optical power (referring to signal/noise propagating in the opposite direction to the optical signal) is higher for the backward pumping configuration. This indicates that the input signal was low and not

sufficient to saturate the amplifier especially towards the end of the doped fiber where the inversion is the highest. Thus, a significant amount of ASE is generated.

Table 6.1 shows the average optical power measured at the input and output of the second stage preamplifier at various repetition frequencies

Repetition Frequency (MHz)	Input to Preamplifier 2 (mW)	Output of Preamplifier 2 (mW)
858	17	43
430	6.4	32
214	3.5	23
107	1.6	17
53	0.8	13

Table 6.1. Measured input and output powers for preamplifier 2 at various repetition frequencies.

Cladding Pumping Pre-amplifier

A cladding pumped pre-amplifier was introduced after the second stage preamplifier to boost the output power such that it was sufficient to saturate the power amplifier with a target average output power of 100W and beyond. As mentioned in Chapter 2, the use of DC YDF allows high power, low brightness pump radiation to be launched into the inner cladding region. One of the limitations of the cladding pumping scheme is that the pump absorption could be incomplete due to the weak overlap between the cladding modes and the doped core. In order to increase the pump absorption, a long length of YDF has to be used as compared to core-pumping configurations. However, this will lead to nonlinear effects especially SPM and SRS. Thus, an appropriate choice of fiber type and length are crucial in building a cladding pumped fiber preamplifier.

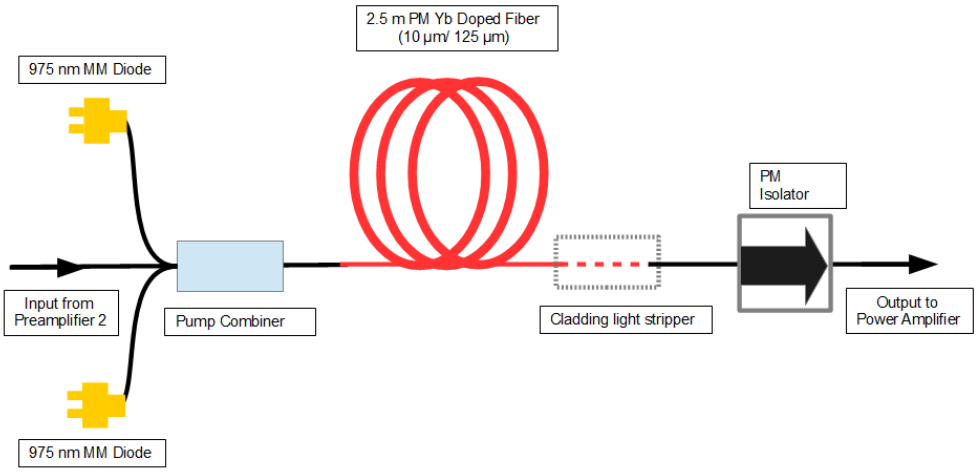

Figure 6.9. The configuration of a forward cladding-pumping fiber amplifier.

Figure 6.9 shows the configuration of cladding pumped preamplifier used in this work. In this preamplifier, proper management of the nonlinear effects is crucial since the signal peak power and the length of fiber used can easily trigger SPM and SRS. We adopted a forward pumping configuration in order to reduce the length of the passive fibre (associated with the fused pump and signal combiner) at the output of the amplifier and therefore the impact of nonlinear effects.

The aim of this preamplifier is to produce an average output power in excess of 2 W sufficient enough to seed the power amplifier stage. At this average power, the extracted pulse energy could be substantial when operating at low repetition frequency. This will lead to a very high pulse peak power at the output of the preamplifier. Therefore, in order to reduce the nonlinear effects in this preamplifier, we use a larger core diameter active fiber. The PM YDF used in this stage has a core diameter of 10 µm with a core NA of 0.08 and an inner-cladding diameter of 125 µm with 0.46 NA.The total length of doped fiber used in this preamplifier was 2.5 m and the cladding absorption for this doped fiber is ~1.8 dB per meter with a 975 nm pump wavelength. The fiber was co-directionally pumped by a 975 nm multi-mode (MM) pump diode through a fiberized (2+1)x1 PM pump combiner. The fiber type at the input of the pump combiner is matched to PM980 fiber while the output is matched to 10 µm /125 µm fiber and thus reduces any additional loss due to mode field diameter mismatch.

Due to the very low pump absorption, a cladding light stripper or pump dump is used at the end of the YDF to remove any unabsorbed pump. The in-house pump dump consists of a ceramic holder and high index (n ~= 1.6) UV curable polymer gel. A small section of the YDF coating was removed and cleaned before placing it on a ceramic holder filled with the polymer gel. Then, it was cured with a UV lamp. By removing the coating, the cladding was directly exposed

to the polymer gel which has a higher refractive index than the silica cladding. As a result light in the cladding will not be guided anymore and therefore will leak out from the YDF.

An inline isolator was placed at the output of the preamplifier to prevent backward travelling signals consisting of ASE noise, any reflection of the forward propagating signal, SRS etc. coupling back into the preamplifier and destabilizing the MOPA chain. The isolator is capable of handling 3 W of CW power and a peak power of 10 kW. The effective isolation at various optical signal wavelengths was investigated using an ASE light source. Figure 6.10 shows the measured result. At the signal wavelength (1040 nm), approximately 33 dB of isolation was provided by the isolator. Moreover, the peak isolation of 35 dB is located at 1030 nm which nicely overlaps with the short wavelength ASE band and therefore provides a good filter for the backward propagating ASE.

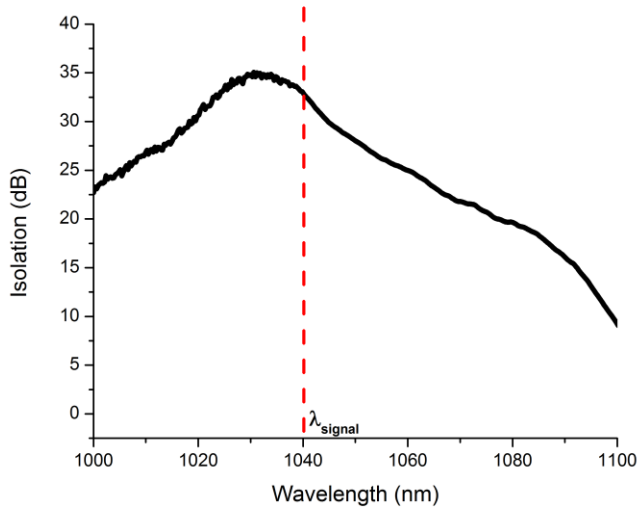

Figure 6.10. Isolation curve measured at different wavelength for the high power inline isolator. Red dash line shows the operating wavelength with approximately 33 dB isolation.

Other than isolating backward propagating optical signals, the inline isolator also acts as a polarization filter. The isolator is designed to transmit only the slow axis while completely blocking the signal in other polarization directions including the fast axis. This resulted in a cleaner single polarization output. The polarization extinction at the output was measured to be 23 dB by using the combination of a PBS and a HWP.

In order to find out the suitable YDF length to be used, 3 different fiber lengths were investigated in terms of total gain and ASE noise. Figure 6.11 shows the spectra obtained with different YDF lengths. The measurement was conducted at 53 MHz repetition frequency and with an input signal power of 13 mW. For a 90-cm YDF length, a total optical power of 1.3 W was measured when a total pump power of 3.8 W was launched into the YDF. Residual pump

power measured was 1.2 W, which means over 68 % of the total pump power being absorbed effectively by the YDF.

However, the measured OSNR was only 28 dB with significant amount of short wavelength ASE, which is not ideal to seed the power amplifier. Further scaling of output power was limited by the rapid degradation of the OSNR. However, with an increase in the YDF length, the ASE was found to shift to longer wavelengths. Moreover, the OSNR improved with the use of a longer YDF length, from 28 dB for 90-cm YDF to 31 dB for 1.5m of YDF and 34 dB when the YDF length was increased to 2.5m. A total output power of 2.6 W and signal gain of 23 dB were obtained with 2.5 m of YDF.

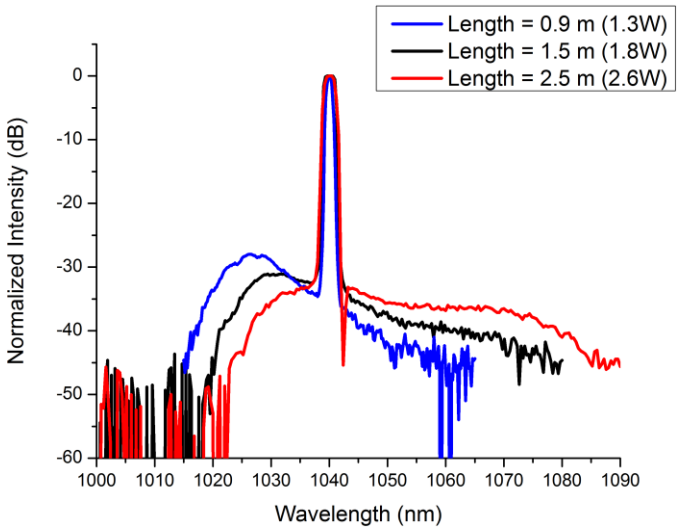

Figure 6.11. Output spectra measured after the 3rd preamplifier with different lengths of doped fiber.

The peak power associated with the maximum average power of 2.6 W is estimated to be 1.7 kW at 53 MHz repetition frequency. Even at this peak power level, the spectrum in Figure 6.11 does not show any sign of SRS build up which is predicted to peak around 1090 nm for a 1040 nm signal wavelength. However, the peak power was sufficient to initiate SPM assisted spectral broadening. Figure 6.12 shows the output spectra obtained at various repetition frequencies. The dotted line plot was measured at the input of the 3rd preamplifier which corresponds to the output spectrum of the 2nd preamplifier. When operating at higher repetition frequencies such as at 214 MHz, the signal linewidth show a smaller broadening effect due to the reduction in peak power. The estimated peak power was only ~430 W in this case. The signal linewidth begins to broaden rapidly when the repetition frequency was reduced to 107 MHz corresponding to a pulse peak power of ~ 860 W.

The broadening of the spectral bandwidth at different repetition frequencies is measured at the 10 dB level and is plotted in Figure 6.13. Based on the measured data, SPM begins to have an effect on the signal linewidth when the peak power was ≥300 W. At 53 MHz, since the peak power was > 300W at 450 mW of average power, the linewidth begins to broaden and the broadening continues up to 1.06 nm at the maximum output power. The rollover in spectral broadening may have been caused by the onset of SRS which may not be clearly evident from Figure 6.11 due to the high noise floor level. On the other hand, the broadening only occurs when the average power is ~1 W for 107 MHz and ~2 W for 214 MHz repetition frequencies.

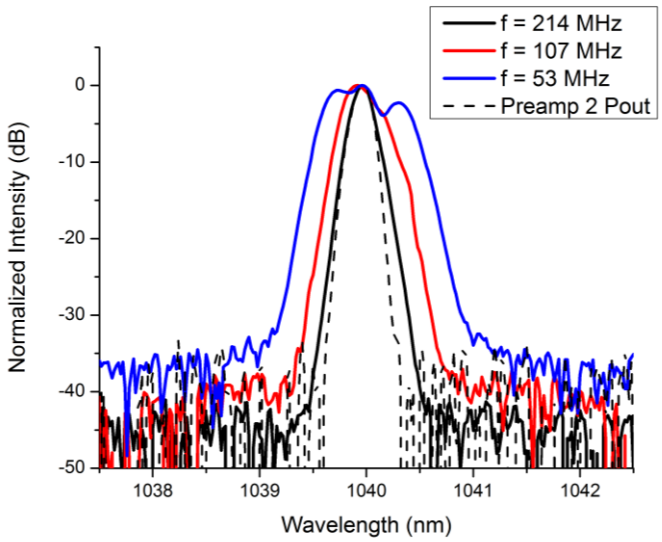

Figure 6.12. Spectrum measured at different repetition frequencies, showing the effect of spectral broadening due to SPM. (OSA resolution: 0.1nm)

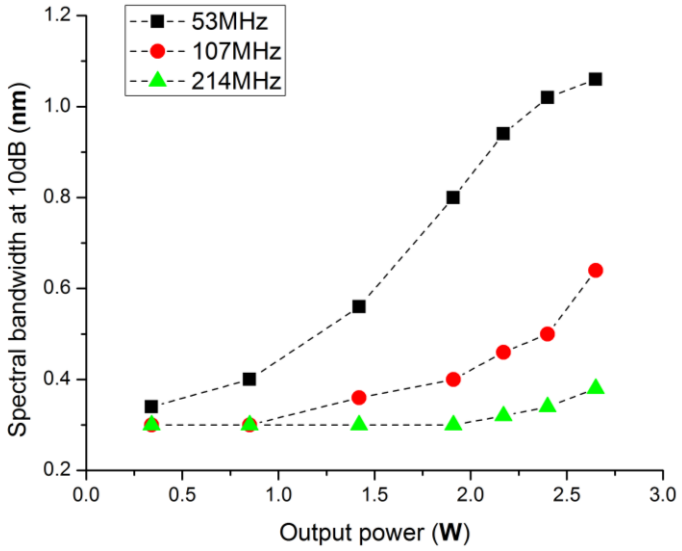

Figure 6.13. Spectral bandwidth measured at -10dB level at different repetition frequencies and output powers.

6.3.2.2 Configuration of Power Amplifier

This fiber amplifier stage is capable of providing gain of up to 24 dB and can lead to high optical output power. The power amplifier stage in a fiber MOPA is crucial especially in pulsed operation as the combination of high average power and high peak power can easily damage the amplification stage unless adequate precautions in terms of thermal and nonlinearity management have been taken into account. Therefore, the preamplifiers in this system were designed in a way such that sufficient optical power can be generated with very low noise and nonlinear distortion. This is to ensure a clean signal seeding the power amplifier.

A 3 m long, polarization maintaining Yb-doped LMA fiber with core and cladding diameters/NAs of 25 µm/ 0.06 and 250 µm/ 0.46 respectively was used in this stage. The estimated V number of the core of the LMA fiber is 4.5 and this fiber is able to support a total of 9 transverse modes. Direct splicing of the LMA to PM085 (polarization maintaining, single mode fiber with a core diameter of 10 µm and a cladding diameter of 125 µm) will lead to higher splicing losses due to mismatch in the mode field diameters and the possibility of random excitation of the transverse modes in the LMA fiber leading to a very poor output beam quality. In order to ensure a single mode output, preferential excitation of the fundamental mode is important. This can be achieved by adiabatically tapering the LMA fiber such that the tapered section only guides the fundamental mode and is matched to the MFD of the 10µm core fiber. Fiber tapering was carried out using a glass processing device from Vytran (GPX-3300). A section of fiber coating with length of approximately 10 cm was stripped off using a modified fiber stripper. The fiber was then tapered down from 250 µm cladding diameter to 100 µm with

the total tapered length of 3 cm. This resulted in a core diameter of 10 µm, with an estimated V number of 1.8 and this supports the fundamental mode only. The centre of the tapered section was then cleaved and spliced to a 15 cm length of PM085 fiber. The total splice loss was measured to be 0.6 dB. The taper-spliced section was then placed onto an in-house made aluminium fiber holder for thermal management. The uncoated section that includes the splicing point was protected with a polymer gel of high refractive index. The polymer gel was UV cured to permanently attach to the aluminium holder. The use of a high refractive index gel on the uncoated fiber allows optical signal propagating in the cladding and any residual pump power to leak out from the fiber.

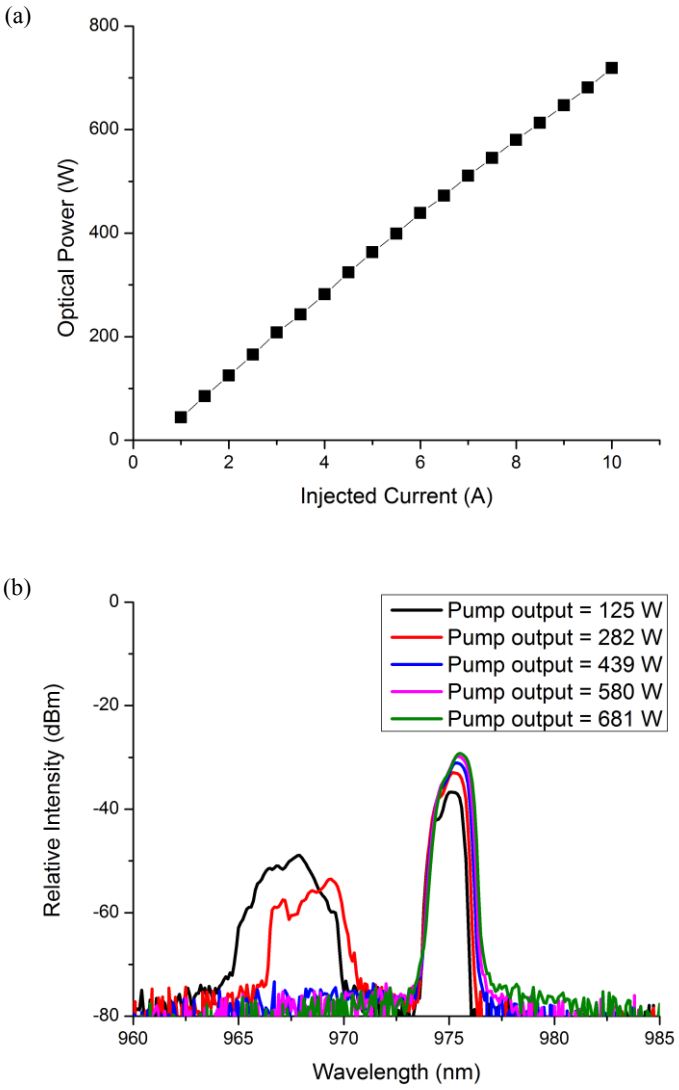

Figure 6.14. (a) Total pump power measured at different injected current and (b) the corresponding pump spectra.

Both the LMA fiber and the aluminium fiber holder were then placed onto a water cooled plate maintained at a constant temperature of 19˚C using a standalone chiller. The LMA fiber was manually coiled at a diameter of 80 mm to introduce additional bend induced loss to the guided LP_{11} mode and sandwiched between two graphite sheets for efficient removal of heat along the length of the doped LMA fiber.

The pump for the power amplifier consisted of 16 multimode laser diodes each of which was capable of producing a maximum output power of 50W at a drive current of 12 A. The operation wavelength of each diode was locked at 975 nm using a volume Bragg grating (VBG). To maintain the recommended case temperature of 20˚C, all the laser diodes were mounted onto a separate water-cooled plate. A 19x1 pump combiner was used to spatially combine the multimode laser diodes. The output pigtail of the combiner had a outer cladding diameter of 200 μm and NA of 0.46. The transmission efficiency of the pump combiner was measured to be 90%. Figure 6.14 shows the spatially combined power plot of the pump module and the spectra at various power levels. The total pump power available was 715 W at 10 A drive current. At low drive current, the output wavelength of the diode was found to be not entirely locked to 975 nm region due to the gain peak being located at around 967nm, quite far away from 975 nm. However as the pump current was increased, the gain peak shifts to the 975 nm region, allowing the locking of the diode and clean output spectra were produced.

Both the pump output fiber and the LMA YDF fiber were then mounted onto 3-axis translational stages for free-space pumping. A short length of end cap (1.3 mm) was spliced onto the LMA to avoid any facet damage due to the intense optical power at the output of the MOPA. The end cap was also angle polished in order to prevent a 4% Fresnel reflected signal coupling back into the core of the LMA fiber. A pair of aspherical lenses with a focal length of 20 mm were used. Dichroic mirrors with high transmission at 975 nm and high reflectivity at 1040 nm were used to separate the pump and the output signal beams. The pump coupling efficiency into the LMA fiber was measured to be ~95%.

6.4 Demonstration of High Power Picosecond Fiber MOPA

6.4.1 High Average Power Picosecond MOPA

Given that the total available pump power in our laboratory was over 700W, an experiment was carried out to investigate the power scaling capability of the MOPA system. This includes scaling not only the average power but also the pulse energy at the output of the MOPA. The fundamental repetition frequency was tuned to 858 MHz, resulting in 28 ps time-bandwidth limited optical pulses (refer to section 5.3.1). The EOM was set to operate at 214 MHz and

effectively pulse picked at a duty cycle of 1/166. The 2nd preamplifier was used to compensate for the insertion loss of the EOM and power loss due to the reduction in repetition frequency. The output of the 3rd preamplifier was increased from 2.6 W to 3.4 W by increasing the launched pump power. This is to ensure that sufficient signal is injected to saturate the power amplifier.

The critical peak power at which SRS become significant (SRS peak lies ~23 dB below the signal peak) with this 25 μm core and 3 m long LMA fiber is estimated to be ~75 kW [23]. However, at an output power of 351 W (corresponding to an estimated peak power of 59 kW), a significant amount of SRS started to appear as shown in Figure 6.15, which according to our calculation is still lower than the predicted threshold. One possible explanation for the low SRS threshold may be related to the ASE noise generated from the 3rd preamplifier. The long wavelength ASE noise can act as a seed and effectively decrease the SRS threshold. A simple solution to this could be to use a bandpass filter based isolator in between the preamplifier and the power amplifier, however, this could not be manufactured within the timeframe of my doctoral degree.

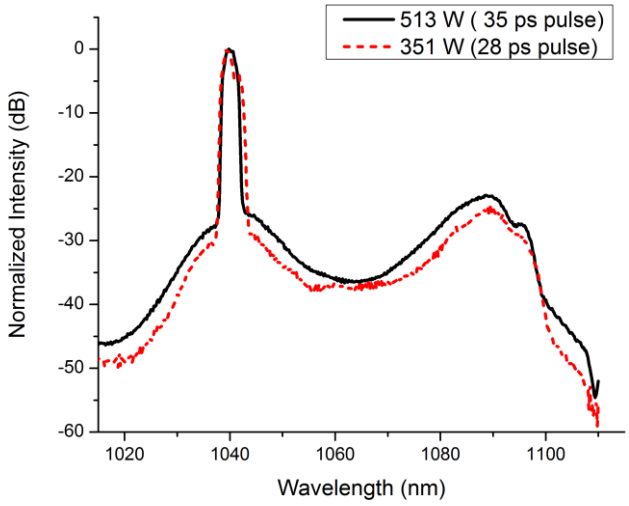

Figure 6.15. Output spectrum measured with different input pulse duration (28 ps and 35 ps).

In order to further increase the average power from the MOPA, the optical peak power has to be reduced. Increasing the optical pulse duration by 25% should reduce the peak power to ~47 kW at 351 W. This should allow further power scaling to beyond 500 W with an estimated peak power of ~61 kW.

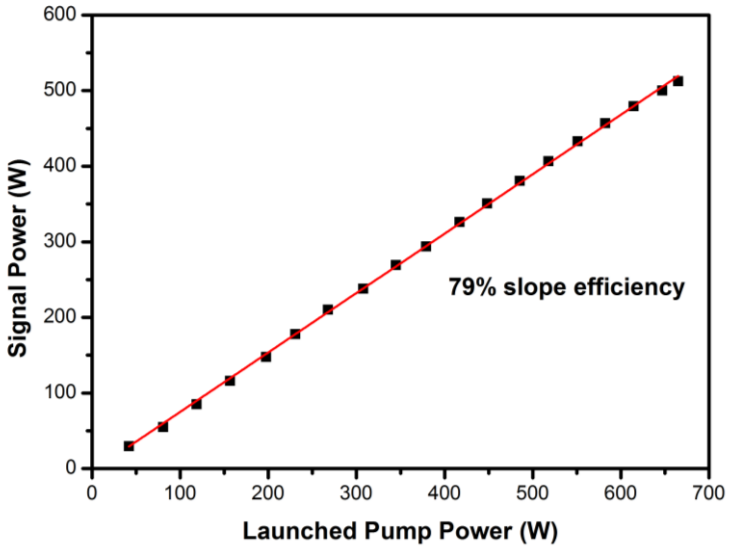

Figure 6.16. Average signal output power vs. launched pump power of the power stage amplifier

In order to increase the pulse duration the repetition frequency of the seed was tuned to 859 MHz resulting in 35 ps optical pulses however the average power from the seed remained the same. The EOM was then modulated at 215 MHz corresponding to a new duty cycle of 133. The resulting amplified output signal vs pump power is plotted in Figure 6.16. A thermal power head (Ophir BDFL500A-BB-50) was used to measure the optical output power. For a total launched power of 670 W, the average signal output power was measured to be 513 W. This corresponds to an amplified signal gain of 21.8 dB assuming no excess loss introduced by the tapered splice. The slope efficiency was measured to be 79% with respect to the launched pump power. No roll off in signal power was observed even at the highest pump power, indicating that further power scaling is still possible. The pulse peak power at the highest operating average power level was estimated to be ~69 kW and the maximum pulse energy was 2.4 μJ. A polarization extinction ratio of 17 dB was measured at the output of the system.

The optical spectra measured at the output of the system with 1.0 nm OSA resolution are shown in Figure 6.17(a). At the maximum average output power, the measured OSNR was recorded to be 26 dB, which corresponds to an OSNR degradation of 11 dB as compared to the input signal to the final stage amplifier. Furthermore, a hump with the peak at 1090 nm started to appear for output powers beyond 250 W due to the onset of SRS. However, the power contained in the Raman Stokes line at the maximum operating output power of 513 W is not significant (~0.25 % of the total optical power) and most of the optical power remained at the signal wavelength. For further power scaling, however, the mitigation of SRS has to be addressed first as the Raman Stokes line grows much faster than the signal at this power level as evident from Figure 6.17(a). The core size of the ytterbium doped fiber in the power amplifier can be further

increased to 40 μm to increase the Raman threshold but this will have an impact on the preservation of the fundamental mode within the fiber. Another possible way is to use specialty fiber such as micro-structured fiber [28] or chirally-coupled-core fiber [29].

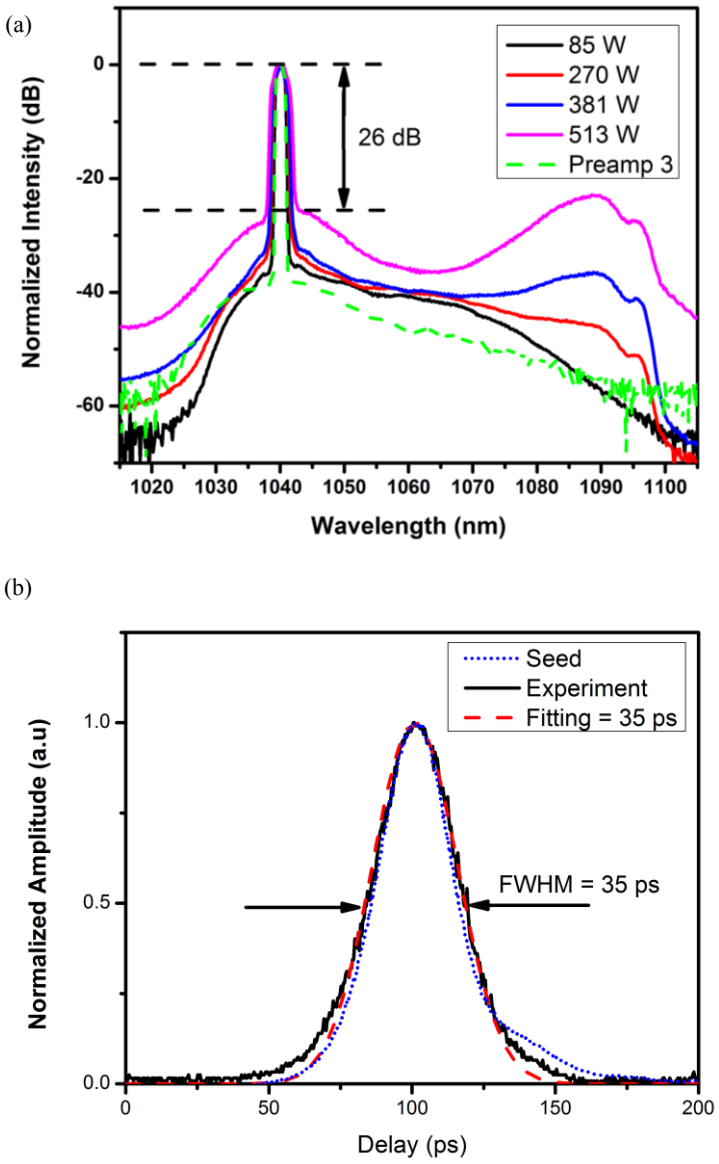

Figure 6.17.(a) Spectra measured at various output powers at a resolution setting of 1.0 nm and (b) optical pulse width measured directly with a fast photodetector.

The optical pulse measured at the maximum output power is shown by the solid black line in Figure 6.17(b). A clean optical pulse with no pedestal was observed. By using a Gaussian fit (red dashed line), the full width at half maximum of the optical pulse was estimated to be 35 ps which is similar to the width of the seed pulses. Moreover, no significant temporal distortion was observed even at the maximum output power.

Figure 6.18(a) shows the rms 3 dB spectral bandwidth obtained through numerical modelling and experimental measurement. The spectral broadening is primarily caused by SPM along the amplifier chain. The measurement results agree well with the numerical estimation. The linewidth of the seed source broadened from 0.12 nm to 2.4 nm at the output of the MOPA chain at 513 W of average output power. The high resolution (0.02 nm) output signal spectra for two different output powers are shown in Figure 6.18(b) plotted on a linear scale to emphasize the detailed features resulting from SPM. At low average output power (29 W), the effect of SPM is not that significant due to the low pulse peak intensity and the spectrum here is measured to be only slightly broader than the seed spectrum. However, at the maximum output power, the effect of SPM becomes significant, creating characteristic sidebands on either side of the central wavelength, resulting in an increased spectral bandwidth. Such spectral broadening which induces a near linear chirp across the pulse profile can be beneficial as it can be exploited to compress the pulses using an external grating pair, thereby increasing the pulse peak power [16].

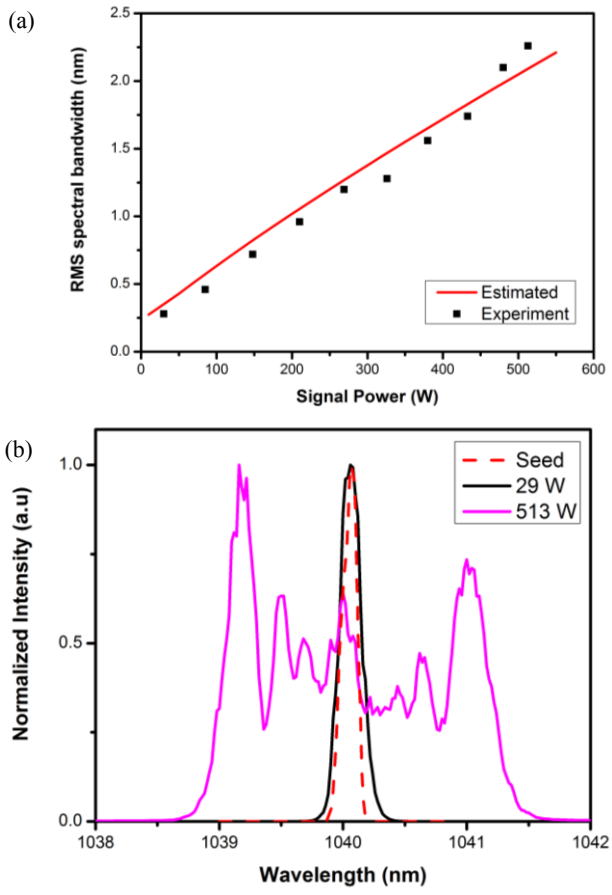

Figure 6.18. (a) Measured spectral linewidth as a function of output signal power and (b) broadening in signal linewidth as a result of SPM. In all cases, OSA resolution was set at 0.1 nm.

In order to assess the output beam quality, a fraction of the output beam at various output powers was imaged with a silicon based CCD camera. Figure 6.19 shows the captured beam profiles at 4 different power levels. As the signal output power was progressively increased a Gaussian shaped intensity profile was maintained. Furthermore, we did not observe any distortion on the captured mode profile even at the maximum output power. The quality of the output beam was also measured using a commercial M^2 measurement instrument. The M^2 measurement was based on the D4σ method yielding an estimated M^2 of 1.1 as shown in Figure 6.19 at 200 W of output power.

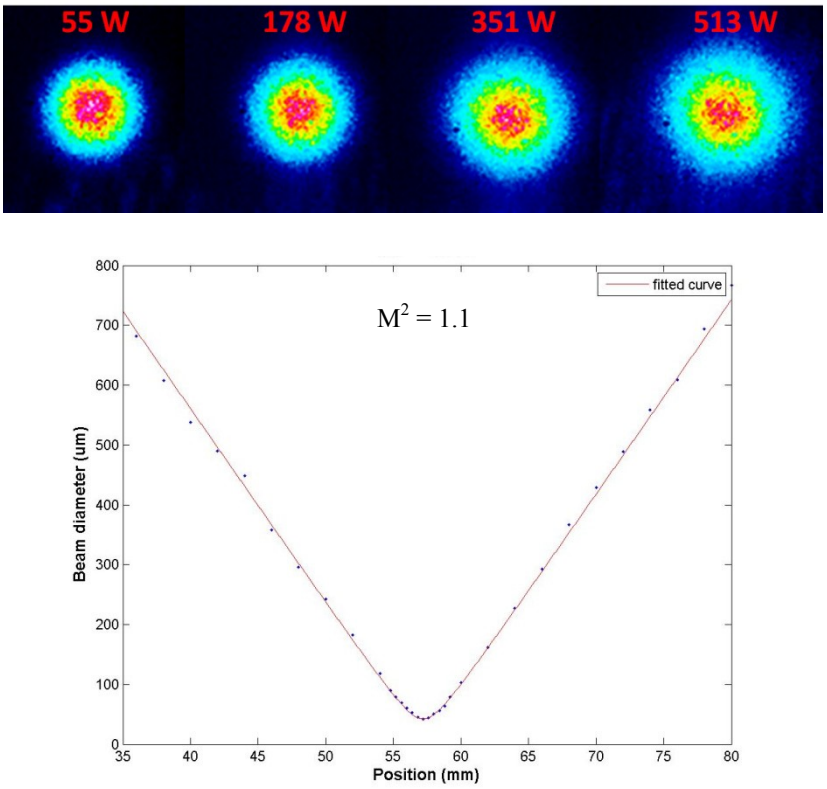

Figure 6.19. (Top) Output beams captured with a CCD camera at various output power levels and (Bottom) M^2 measurement curve at 200W output power.

6.4.2 Picosecond MOPA with Tunable Repetition Frequency and Diffraction Limited Output

Power scaling up to tens of kW is possible from YDF system if sufficient amount of pump power can be injected. However, two key aspects that require attention are the thermal effect in the fiber and the overall OSNR. Proper management of these two aspects will ensure maximum intensity generated and transmitted along the fiber. However, in pulsed regime, the interest is not only on the average optical power, but also the extracted pulse energy and the peak intensity that can be achieved. Compared to the bulk solid state laser, fiber based laser system has limited capability in term of energy extraction with good beam quality.

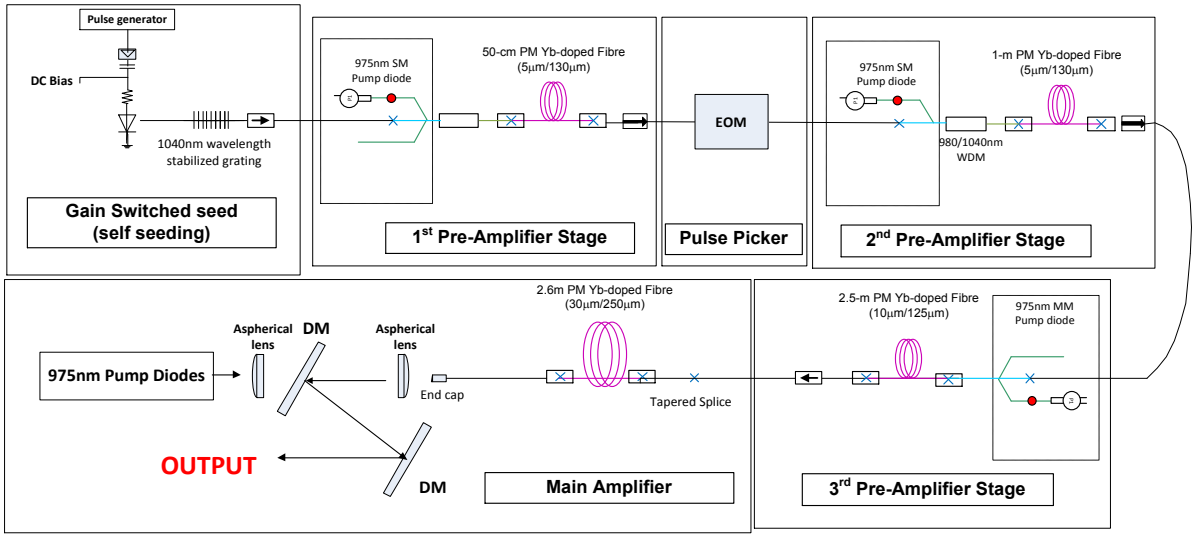

Figure 6.20. Fully fiberized picosecond seed laser based MOPA with tunable repetition frequency.

In section 6.4.1, the maximum peak power achieved was only ~69 kW by using an LMA fiber with 25 μm core diameter. In order to increase the nonlinear threshold, the 25 μm core diameter LMA fiber was replaced with a 30 μm core diameter fiber (NUFERN PLMA-YDF-30/250-VIII), which accounted for 44% increase in core area. Given that the new fiber had the same outer cladding diameter, it improved pump absorption and helped in reducing the overall device length. This should allow the fiber to have much higher SRS threshold and consequently higher energy extraction capacity. A 2.6 m length of LMA fiber was used in the final-stage amplifier).

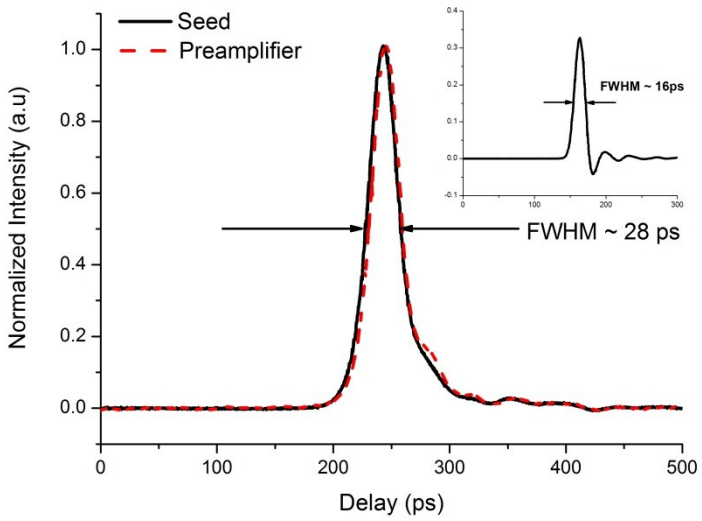

Figure 6.21. Pulse shape of the seed (black line) and output (red dash line) of the third preamplifier, when operating at a repetition frequency of 214 MHz.

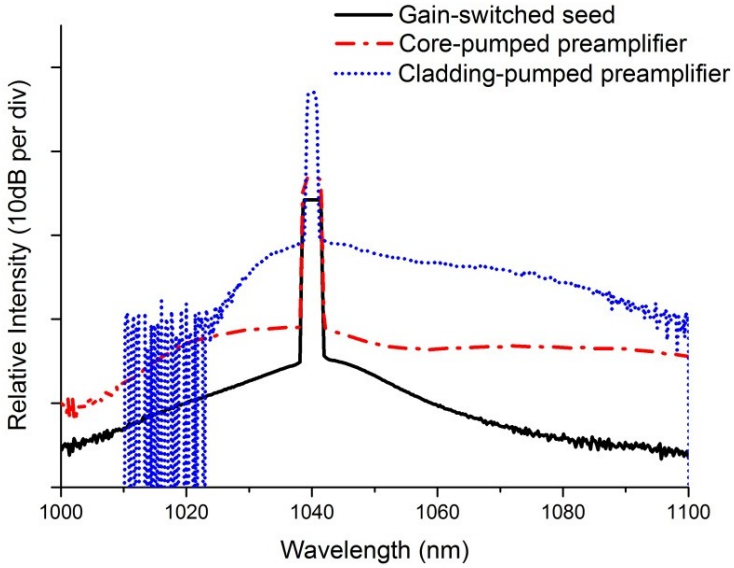

Figure 6.22. Output spectra after various amplification stages.

The performance of the MOPA at different repetition frequencies (858 MHz, 430 MHz, 214 MHz, 107 MHz and 53 MHz) were investigated. The maximum average optical power was estimated to be around 200 W across all operating frequencies before SRS became significant. The EOM located after the 1st preamplifier was used to define the operating frequencies. As for the MOPA system, the seed laser was operating at a repetition frequency of 858 MHz, resulting in optical pulses with FWHM of 28 ps as shown in Figure 6.21.

A maximum average output power of 2.6 W was obtained after the third stage cladding pumped preamplifier. The shape and duration of the pulse were preserved after the preamplifiers as shown by the red dashed plot in Figure 6.21. The corresponding low resolution (1.0 nm) optical spectra measured with an OSA after different preamplifier stages at a reduced repetition frequency of 214 MHz are shown in Figure 6.22. The seed had an optical signal to noise ratio (OSNR) of 40 dB. The short wavelength ASE around 1030 nm started to build up after the second stage preamplifier (red dash-dot line) due largely to the short length of the gain medium. A moderate gain of 8 dB was extracted from this stage. The length of the gain medium of the third stage amplifier was chosen such that the short wavelength ASE after the second stage gets reabsorbed inside the gain medium whilst providing over 20 dB signal gain. This gain partitioning scheme ensured the maximum optical signal to noise ratio (OSNR) before seeding into the power amplifier stage, as illustrated by the blue dotted line.

The output power as a function of the launched pump power from the final stage amplifier is shown Figure 6.23 with an estimated slope efficiency of 77% with respect to the launched pump power. A maximum output power of 200 W was obtained for a total launched pump power of 270 W at all frequencies except for 53 MHz for which a maximum output power of 171 W was measured. Further power scaling was limited by significant nonlinear distortions experienced by the amplified pulses as well as transfer of energy to the SRS line. The polarization extinction ratio (PER) of the output signal at maximum operating power was measured to be 15 dB and an M^2 of ~1.1 which qualifies that the output beam was diffraction limited.

The maximum peak power extraction of a fiberized picosecond MOPA system is usually limited by the onset of SPM and SRS. Several techniques have been used to reduce these nonlinear effects, such as: (i.) minimizing the total fiber length including both active and passive fibers, (ii.) increasing the fiber core diameter while preserving the single-mode propagation, and (iii.) reducing the pulse peak power. In our system, we managed this by gain partitioning the various amplification stages as well as keeping the passive fiber length down to only 1.5 m after the third pre-amplification stage.

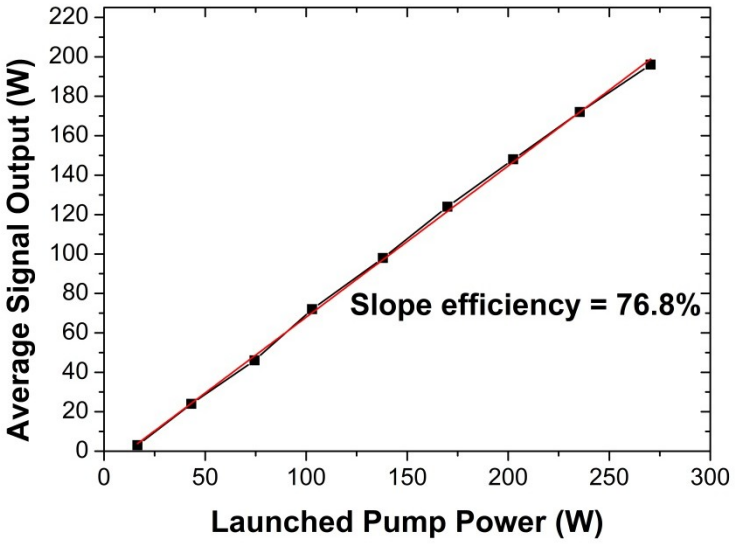

Figure 6.23. Average signal output power vs. launched pump power of the power stage amplifier.

At the maximum operating output power of 200 W, a reasonable OSNR of >30 dB was achieved for repetition frequencies ranging from 214 MHz to 858 MHz as shown in Figure 6.24 which shows that most of the amplified powers was contained in the signal band. A maximum pulse peak power (pulse energy) of 33.4 kW (0.93 µJ) was achieved whilst the pulse maintained its temporal shape as evident from the black dash-dot line in Figure 6.26.

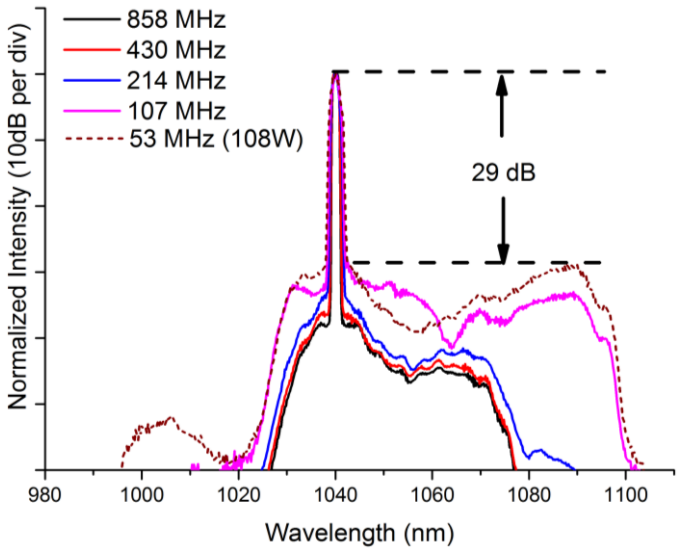

Figure 6.24. Spectra measured at various repetition frequencies at an average output power of 200 W and an input signal power of 2.6 W. Note that the average output power at 53 MHz was 108 W

When the repetition frequency was reduced to 107 MHz or lower, significant nonlinear distortion was observed and the SRS assisted peak at around 1090 nm started to build-up as shown by the solid pink and dotted brown lines in Figure 6.24, restricting the maximum pulse

peak power extraction from the system to around 73 kW and pulse energy to ~2.0 μJ at 53 MHz repetition frequency (corresponding to a maximum average output power of 108W). The broad SRS peak at around 1090 nm was measured to be 29 dB below the signal peak. One of the factors that led to the relatively low SRS threshold is the seeding of ASE around the SRS region from the third preamplifier stage. Figure 6.25 shows the output spectra from the third preamplifier stage for two different output powers represented by the solid black and red line plots. Approximately 0.08% (2.1 mW) of the ASE power was estimated to be within the SRS region at 2.6 W of total optical output power. In an attempt to increase the SRS threshold, the seeding to the power stage amplifier was reduced from 2.6 W to 1.4 W so as to reduce the total ASE seeding power down to 1.1 mW. Furthermore, reduction in the seeding power increased the amplifier gain which in turn reduced the effective length of the amplifier [30]. We estimated the effective length to be around 0.54m, a 23% reduction compared to when operating at 2.6 W. The combined effects of reduced ASE seeding and effective length of the amplifier helped in increasing the SRS threshold.

Figure 6.25 clearly shows the improvement brought about by the reduction in seeding power to the booster amplifier. At an output power of 113 W, the SRS peak is measured to be approximately 40 dB below the signal peak whilst it is only 29dB at 108 W of output power when 2.6W of seeding power was used. This increased SRS threshold allowed us to scale up the power to 171W and resulted in an approximate 1.6 fold increase in the extractable pulse energy. We estimated that 96% of the total output power was contained in the signal band. The corresponding peak power and pulse energy achieved were 107 kW and 3.23 μJ respectively. We noticed that the output pulses broaden from 28 ps to 30 ps as shown in Figure 6.26 due to the combined effect of SPM and dispersion within the active fiber.

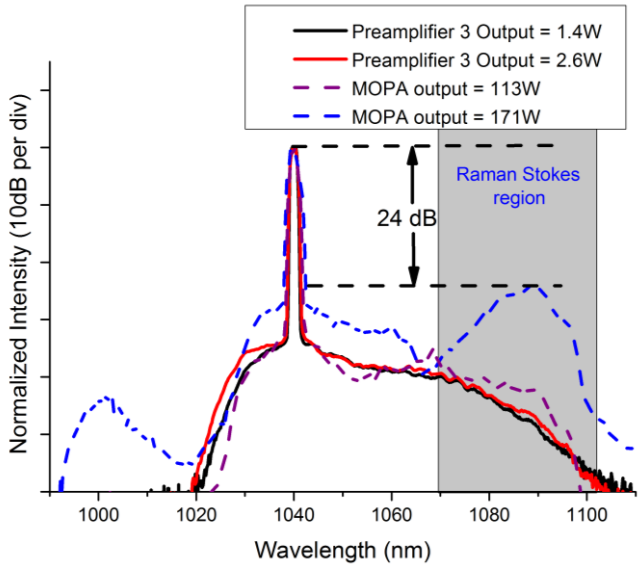

Figure 6.25. The spectral profiles after the third preamplifier stage (solid lines) as well as the output of the MOPA at 113 W and 171 W of average powers for 1.4 W of input signal power

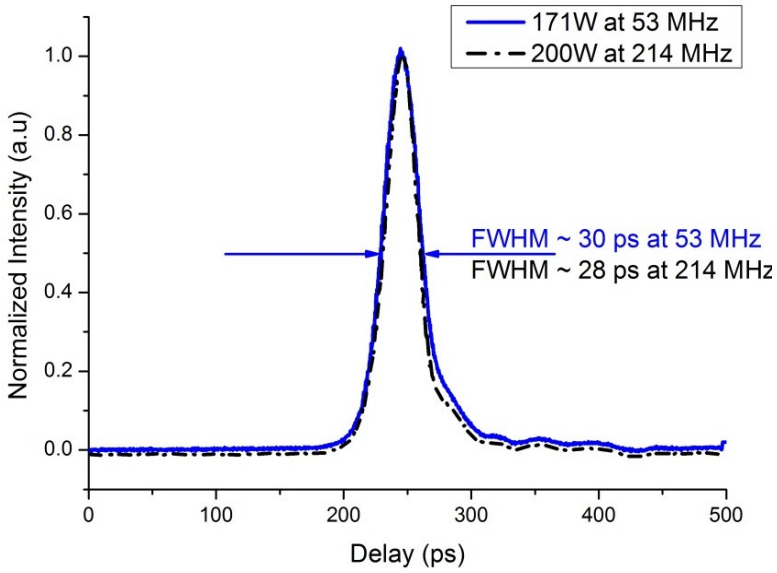

Figure 6.26. Evidence of pulse width broadening at the highest operating peak power

The influence of SPM on the broadening of the signal line-width is shown in Figure 6.27. The level of spectral broadening depends on the pulse peak power. For the same average output power, the pulse peak power increased with a decrease in repetition frequency, resulting in a linear increase in spectral bandwidth with power as shown in Figure 6.27. However, as the pulse peak power was increased far above the SRS threshold, the intra-band Raman scattering also plays a part in the broadening of the spectral bandwidth causing the lineshape to broaden asymmetrically towards the long wavelength side as illustrated by the solid blue line in Figure 6.28. The green dash-line plot in Figure 6.27 shows the nonlinear increase in spectral bandwidth

due to the combined effect of SPM and SRS when the pulse peak power exceeds 80kW. The degree of spectral broadening is relatively modest in absolute terms – only a few nm at the lowest repetition frequencies investigated. The nonlinear phase shift accumulated in the final stage amplifier was estimated by fitting the measured output spectrum through the use of an in-house developed numerical modeling tool. We estimate a total nonlinear phase-shift of 28.3 radians at the maximum pulse peak power of 107 kW whilst the seed spectral width broadened by ~25 times from its original value [31]. It is to be noted here that the input linewidth to the final stage amplifier also increased with a decrease in operating frequency. However, the drop in seed power from 2.6 W to 1.4 W helped in keeping the nonlinear broadening factor down as is evident from the solid purple and dashed green lines as long as the pulse peak power does not exceed a critical power for intra-pulse Raman scattering to play a domineering role.

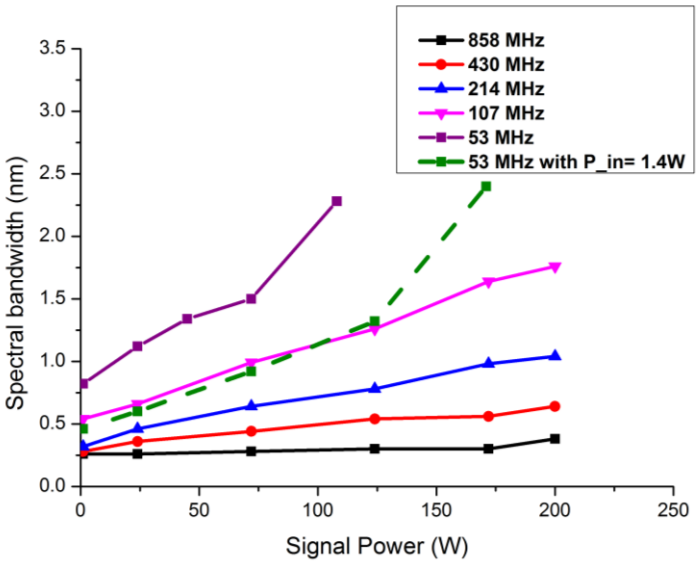

Figure 6.27. Signal linewidth measured at different signal output powers across all repetition frequencies.

Despite the significant spectral broadening due to SPM, this linear chip can be exploited to compress the optical pulses and enhanced the peak power significantly. As reported in [7] and [16], the optical pulses from the MOPA system were compressed down from 21 ps down to between 1 ps and 5 ps with the use of a grating based compressor at the output. This method allows a maximum compression factor of 17 and increased in optical peak power by 7 times. This compressed output can be useful for industrial material processing or a pump source for green signal generation through nonlinear frequency doubling [24].

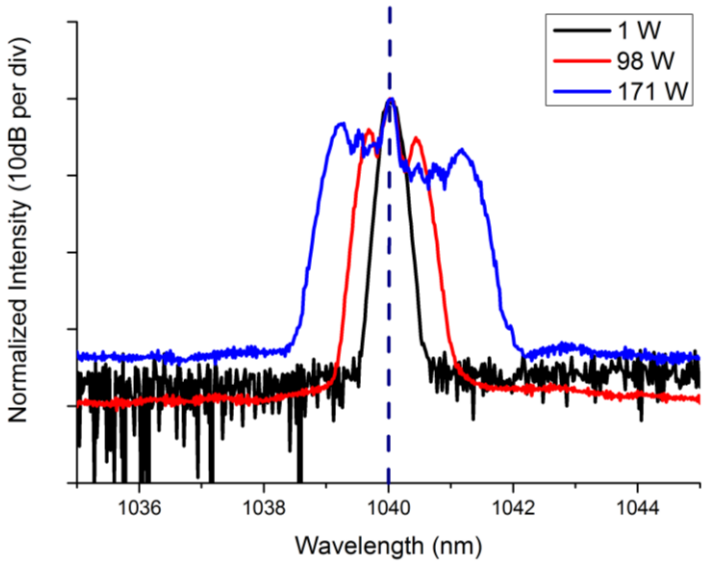

Figure 6.28. SPM effect on signal linewidth at various output average powers with repetition frequency of 53 MHz.

6.5 Conclusion

Chapter 6 has described the design considerations and strategies to power scale picosecond fiber laser. The MOPA setup is mainly based on commercially available optical components and standard single/double clad fiber with step refractive index core. Two different MOPA configurations are demonstrated, each with different set of optical parameters.

In the first configuration, a gain-switched diode-seeded all-fiber ytterbium doped MOPA with 35 ps optical pulses and up to 513 W of average output power at 1040 nm is demonstrated. The system operates at a repetition frequency of 215 MHz corresponding to an estimated pulse energy of 2.4 μJ and a peak power of ~ 69 kW. At the maximum operating output power, an OSNR of 26 dB was recorded, indicating that the ASE was well controlled throughout the MOPA chain. A polarization extinction ratio of 17 dB was measured signifying that the amplified output signal is single polarized. Output beam quality measurements using a CCD and a commercial M^2 measurement system indicate that the output mode is essentially Gaussian in nature and close to diffraction limited. The effect of SPM within the fiber amplifier chain, which causes the signal linewidth to broaden, is in good agreement with the numerical estimation. Furthermore, the amount of energy effectively transferred to the Raman Stokes (peak at 1090 nm) was small.

As for the second configuration, a gain-switched diode-seeded all-fiber MOPA amplifying 28 ps optical pulses up to an average output power of 200 W at 1040 nm with variable repetition frequencies is demonstrated. The ASE was well suppressed at the maximum operating output

power across all the operating frequencies with OSNR values ranging between 25 dB to 35 dB. A maximum pulse energy of 3.23 μJ was achieved at the lowest operating frequency of 53 MHz corresponding to a pulse peak power of 107 kW. Further energy scaling was primarily limited by the rapid build-up of the SRS peak at around 1090 nm. It may be possible to enhance the output pulse energy by filtering out the long wavelength signal components after the third pre-amplifier stage using a narrow band-pass filter (<0.5 nm) which otherwise acts as a seed for the SRS line.

Both configurations demonstrated that SRS is the main limiting factor for achieving high pulse energy. The spectral purity of the input signal to the final amplifier plays crucial role in the build-up of SRS peak. Proper management or filtering of the long wavelength ASE (>1070 nm) generated from the 3rd preamplifier is required to avoid SRS seeding in the final amplifier. Moreover, the use of larger core fiber helped in increasing nonlinear threshold and allowed scaling of the pulse peak power and pulse energy. However, mode preservation in fiber with even larger core diameter will be challenging and specialty fiber (e.g. PCF) may need to be explored for further energy scaling whilst maintaining good beam quality.

6.6 References

1. D. J. Richardson, J. Nilsson, and W. A. Clarkson, "High power fiber lasers: current status and future perspectives [Invited]," J. Opt. Soc. Am. B **27**, B63-B92 (2010).
2. H. M. Pask, R. J. Carman, D. C. Hanna, A. C. Tropper, C. J. Mackechnie, P. R. Barber, and J. M. Dawes, "Ytterbium-doped silica fiber lasers: versatile sources for the 1-1.2 μm region," Selected Topics in Quantum Electronics, IEEE Journal of **1**, 2-13 (1995).
3. Y. Jeong, J. Sahu, D. Payne, and J. Nilsson, "Ytterbium-doped large-core fiber laser with 1.36 kW continuous-wave output power," Opt. Express **12**, 6088-6092 (2004).
4. Y. Fan, B. He, J. Zhou, J. Zheng, H. Liu, Y. Wei, J. Dong, and Q. Lou, "Thermal effects in kilowatt all-fiber MOPA," Opt. Express **19**, 15162-15172 (2011).
5. P. Dupriez, J. K. Sahu, A. Malinowski, Y. Jeong, D. J. Richardson, and J. Nilsson, "80 W Green Laser Based on a Frequency-Doubled Picosecond, Single-Mode, Linearly-Polarized Fiber Laser," in *Conference on Lasers and Electro-Optics/Quantum Electronics and Laser Science Conference and Photonic Applications Systems Technologies*(Optical Society of America, Long Beach, California, 2006), p. CThJ1.
6. F. Kienle, K. K. Chen, S.-u. Alam, C. B. E. Gawith, J. I. Mackenzie, D. C. Hanna, D. J. Richardson, and D. P. Shepherd, "High-power, variable repetition rate, picosecond optical parametric oscillator pumped by an amplified gain-switched diode," Opt. Express **18**, 7602-7610 (2010).
7. F. Kienle, P. S. Teh, D. Lin, S.-u. Alam, J. H. V. Price, D. C. Hanna, D. J. Richardson, and D. P. Shepherd, "High-power, high repetition-rate, green-pumped, picosecond LBO optical parametric oscillator," Opt. Express **20**, 7008-7014 (2012).
8. Z. Wei, G. McConnell, and M. Parsons, "Optical parametric oscillator system for CARS microscopy," in *Lasers and Electro-Optics 2009 and the European Quantum Electronics Conference. CLEO Europe - EQEC 2009. European Conference on*(2009), pp. 1-1.
9. L. Rapp, C. Cibert, A. P. Alloncle, and P. Delaporte, "Characterization of organic material micro-structures transferred by laser in nanosecond and picosecond regimes," Appl. Surf. Sci. **255**, 5439-5443 (2009).
10. D. A. Willis, and V. Grosu, "Microdroplet deposition by laser-induced forward transfer," Applied Physics Letters **86**, - (2005).
11. D. Ashkenasi, T. Kaszemeikat, N. Mueller, A. Lemke, and H. J. Eichler, "Machining of glass and quartz using nanosecond and picosecond laser pulses," (2012), pp. 82430M-82430M-82437.
12. K. Pangovski, K. Li, and B. O'Neill, "Application of picosecond lasers for surface modification and polishing."

13. M. Trtica, B. Gakovic, D. Batani, T. Desai, P. Panjan, and B. Radak, "Surface modifications of a titanium implant by a picosecond Nd: YAG laser operating at 1064 and 532nm," Appl. Surf. Sci. **253**, 2551-2556 (2006).
14. A. Piper, A. Malinowski, B. C. Thomsen, D. J. Richardson, L. M. B. Hickey, and M. N. Zervas, "11.1 W average power, 20 ps pulses at 1 GHz repetition rate from a fiber-amplified gain-switched 1.06 μm Fabry-Perot laser diode," in *Lasers and Electro-Optics, 2005. (CLEO). Conference on*(2005), pp. 1141-1143 Vol. 1142.
15. P. Dupriez, A. Piper, A. Malinowski, J. K. Sahu, M. Ibsen, B. C. Thomsen, Y. Jeong, L. M. B. Hickey, M. N. Zervas, J. Nilsson, and D. J. Richardson, "High average power, high repetition rate, picosecond pulsed fiber master oscillator power amplifier source seeded by a gain-switched laser diode at 1060 nm," Photonics Technology Letters, IEEE **18**, 1013-1015 (2006).
16. K. K. Chen, J. H. V. Price, S.-u. Alam, J. R. Hayes, D. Lin, A. Malinowski, and D. J. Richardson, "Polarisation maintaining 100W Yb-fiber MOPA producing μJ pulses tunable in duration from 1 to 21 ps," Opt. Express **18**, 14385-14394 (2010).
17. R. Song, J. Hou, S. Chen, W. Yang, and Q. Lu, "157 W all-fiber high-power picosecond laser," Appl. Opt. **51**, 2497-2500 (2012).
18. A. A. Balandin, S. Ghosh, W. Bao, I. Calizo, D. Teweldebrhan, F. Miao, and C. N. Lau, "Superior thermal conductivity of single-layer graphene," Nano letters **8**, 902-907 (2008).
19. A. V. Smith, and B. T. Do, "Bulk and surface laser damage of silica by picosecond and nanosecond pulses at 1064 nm," Applied Optics **47**, 4812-4832 (2008).
20. A. V. Smith, B. T. Do, G. R. Hadley, and R. L. Farrow, "Optical Damage Limits to Pulse Energy From Fibers," Selected Topics in Quantum Electronics, IEEE Journal of **15**, 153-158 (2009).
21. A. Wetter, M. Faucher, B. Sévigny, and N. Vachon, "High core and cladding isolation termination for high-power lasers and amplifiers," (2009), pp. 719521-719521-719528.
22. S. Sinha, K. E. Urbanek, A. Krzywicki, and R. L. Byer, "Investigation of the suitability of silicate bonding for facet termination in active fiber devices," Opt. Express **15**, 13003-13022 (2007).
23. G. Agrawal, "Nonlinear Fiber Optics," in *Nonlinear Science at the Dawn of the 21st Century*, P. L. Christiansen, M. P. Sørensen, and A. C. Scott, eds. (Springer Berlin Heidelberg, 2000), pp. 195-211.
24. C. Kang Kang, S. U. Alam, J. R. Hayes, H. J. Baker, D. Hall, R. McBride, J. Price, D. Lin, A. Malinowski, and D. J. Richardson, "56-W Frequency-Doubled Source at 530 nm Pumped by a Single-Mode, Single-Polarization, Picosecond, Yb^{3+}-Doped Fiber MOPA," Photonics Technology Letters, IEEE **22**, 893-895 (2010).

25. A. Tünnermann, T. Schreiber, F. Röser, A. Liem, S. Höfer, H. Zellmer, S. Nolte, and J. Limpert, "The renaissance and bright future of fibre lasers," Journal of Physics B: Atomic, Molecular and Optical Physics **38**, S681 (2005).
26. S. Wielandy, "Implications of higher-order mode content in large mode area fibers with good beam quality," Opt. Express **15**, 15402-15409 (2007).
27. R. Paschotta, J. Nilsson, A. C. Tropper, and D. C. Hanna, "Ytterbium-doped fiber amplifiers," Quantum Electronics, IEEE Journal of **33**, 1049-1056 (1997).
28. J. Kim, P. Dupriez, C. Codemard, J. Nilsson, and J. K. Sahu, "Suppression of stimulated Raman scattering in a high power Yb-doped fiber amplifier using a W-type core with fundamental mode cut-off," Opt. Express **14**, 5103-5113 (2006).
29. X. Ma, I. N. Hu, and A. Galvanauskas, "Propagation-length independent SRS threshold in chirally-coupled-core fibers," Opt. Express **19**, 22575-22581 (2011).
30. G. P. Agrawal, *Nonlinear Fiber Optics* (Academic Press, NY, 1995).
31. S. C. Pinault, and M. J. Potasek, "Frequency broadening by self-phase modulation in optical fibers," J. Opt. Soc. Am. B **2**, 1318 - 1319 (1985).

Chapter 7. Summary and Future Works

In this chapter, I will summarize the work presented here in this thesis and suggest possible improvements and future research directions.

7.1 Summary

In Chapter 3, two different configurations of nanosecond fiber MOPA are demonstrated. The first system was the improved version of the nanosecond MOPA with the use of EOM as pulse shaping. The improvement towards the pulse shaping mechanism allows greater resolution and faster rise/fall time for more accurate shaping. Pulse shape with higher complexity can now be tailored with this system. The second system is known as SMART fiber laser system, which was built in collaboration with SPI Lasers. The system is capable of producing up to 60W of average power. AOM was used as pulse shaping for the first time and the high damage threshold of the AOM allows it to be placed before the power amplifier. However, shaping is only limited to the pulse leading edge due to the response of the AOM. Nevertheless, pulse energy up to 1.0mJ can be extracted by shaping optical pulse using an AOM before the power amplifier. Output beam quality (M^2) was measured to be 1.1, close to the diffraction limited beam. The SRS limited maximum pulse peak power was 18kW for 1.3 m of beam delivery fiber. The capabilities of both MOPA systems were successfully tested with Si material processing experiment.

Chapter 4 introduces to a new technique of generating pulsed Raman based fiber laser. The use of nanosecond MOPA with EOM as pulse shaping mechanism in an all fiber PM MOPA allows the generation of shaped multistep pulses for selective excitation of the Raman stokes. With the pump wavelength at 530 nm, Raman Stokes across different visible regions can be generated via this technique. This resulting in output signal wavelength that changes sequentially from green, to yellow to red (up to 7th stokes orders) using 530 nm pump pulses with 3 step profile or any other two using 2-step pulses by exploiting the SRS in optical fiber. Operation in the NIR region however is limited to 4 stokes order before zero dispersion wavelength of the fiber is reached. Across that wavelength, a continuum started to build up. With the similar configuration footprint and a small modification, a tunable, synchronous pumped Raman fiber laser was developed. This Raman fiber laser can operate in the NIR and visible regions with continuous tuning range of 28 nm in NIR and 2.8 nm in the visible regions. Efficiency of the Raman laser increased with the use of feedback signal. Furthermore, linewidth of the Raman Stokes in both regions shows narrowing effect. Although the average output power demonstrated is still modest, however with the right fiber type (microstructured fiber) and length of Raman gain, further power scaling is possible.

Chapter 5 demonstrates the use of SLD for gain switching. The SLD used are of different manufacturers and both the characteristics of the temporal and spectral are investigated. Most of the outputs have broad spectral as a result of excitation of multiple longitudinal modes in the diode cavity. By using external seeding, the output spectrum can be compressed down. Throughout the investigation both with and without external seeding, narrow output spectrum was observed. However, this was accompanied by distorted output pulses. Next, with the use of gain switched driving technique combined with a simply cavity consisting an external FBG, both spectrum and temporal compression were observed. Optical pulses with transform limited duration was obtained and mode-locking mechanism is believed to be the mechanism behind this observation. With this technique, a short 18 ps optical pulse with a pulse energy of 7.2 pJ and corresponding peak power of 400 mW was obtained. Further characterization works were carried out resulting in the optical pulse with chirp free and with high stability (low timing jitter).

Power scaling of picosecond seeded fiber MOPA is demonstrated in Chapter 6. Furthermore, the design considerations and strategies to power scale picoseconds fiber laser are discussed in this chapter. The MOPA setup is mainly based on commercially available optical components and standard single/double clad with step refractive index fibers. Two different MOPA configurations are demonstrated, each with different set of optical parameters. Both configurations was seeded by a gain switched SLD and with operating wavelength of 1040 nm. The first configuration demonstrated up to 513 W of optical output power with 35 ps pulses and at 215 MHz repetition frequency. The corresponding peak power was estimated to be ~69 kW. Furthermore, the output was single polarization, with PER of over 17 dB recorded. The second configuration has 28 ps output pulses and with a total average power of 200 W. This configuration is able to operate at repetition frequency between 858 MHz and 53 MHz with maximum output power of 200 W (except for 53 MHz where maximum output power is only 171 W). The maximum peak power achieved was estimated to be ~107 kW. Both configurations showed SRS is the main limiting factor for further power scaling. The spectral purity of the input signal to the power amplifier plays crucial role in the build-up of SRS peak. Moreover, spectral broadening as a result of SPM becomes significant when operating at high peak power. EOM offers a continuous tunable repetition rate which enable generation of different peak powers at a fixed average optical power, allowing control on the spectral broadening due to SPM.

7.2 Future works

Demands for pulse energy from fiber based laser systems are increasing with more and more new applications especially in material processing. It is a challenging task to extract more energy from the fiber amplifiers since gain saturation, ASE, nonlinear effects and pump power dictate the maximum energy that can be extracted from the amplifiers. The use of specialty fiber such as Yb doped PCF can be the direct solution for obtaining higher pulse energy. Another method worth venturing is operating the laser in burst mode with pulse tailoring profiles. The first few pulses may consists of short nanosecond pulses but with high peak intensity sufficient to melt the target area and followed by long nanosecond pulses packed with energy to help further vaporisation and ejection of molten materials.

In the pulsed Raman based fiber laser, the performance can be further improved with better selection of Raman gain fiber. Fiber resistance to photodarkening has to be used since the operating signal is in visible regions. Thus, further works with the use of PCF as gain media can be carried out to investigate the efficiency of Raman stokes generation. With large effective mode area and the use of sufficiently short piece of PCF, Raman threshold can be further increased, allowing more optical power to be transferred to the selected Raman stokes. Increase in optical power in the selected Raman stokes will allow the system to be used effectively in the field of spectroscopy, medical and many more.

The generation of transform limited optical pulses via gain switched SLD with FBG as external cavity is an attractive scheme due to its simplicity and efficiency. By replacing the FBG with a tunable Bragg grating, it is possible to achieve similar transform limited optical pulses across all wavelengths tuning. Furthermore, since the gain of the SLD depends on the operating wavelength, it is possible to achieve even shorter pulse duration if the gain and grating bandwidth are both sufficiently wide.

Performance of picosecond all fiber MOPA has reached a new height with the recent demonstration of over 500 W of optical power. This demonstration is by far the highest record achieved by all fiber picosecond laser system to date. However, the experimental results showed that there are still rooms for further power scaling. New fibers with better doping concentration and larger effective mode area can improve the peak power of the system by a factor of 5. Ultimately, peak power in MW range will be made possible and may replace bulk laser in most applications. Besides that, the availability of high power pulsed source as pump source allows high impact experiments to be done using various nonlinear frequency conversion media. For example, record level optical power in green (via frequency doubling) or super bright white light (via supercontinuum generation) can be achieved with such laser system. Furthermore, the configuration can be further improvised to operate in burst mode. The burst picosecond optical

pulses can be shaped similar to nanosecond MOPA system. It has great advantage compared to nanosecond MOPA as the picosecond burst MOPA is free from SBS.

Appendix: List of Publications

Journals related to this thesis

1. **P. S. Teh**, S.-u. Alam, R. J. Lewis, and D. J. Richardson, "Single polarization picosecond fiber MOPA power scaled to beyond 500 W," Laser Physics Letters **11**, 085103 (2014).
2. **P. S. Teh**, S.-u. Alam, D. P. Shepherd, and D. J. Richardson, "Generation of mode-locked optical pulses at 1035 nm from a fiber Bragg grating stabilized semiconductor laser diode," Opt. Express **22**, 13366-13373 (2014).
3. K. Pangovski, M. Sparkes, A. Cockburn, W. O'Neill, **T. Peh Siong**, L. Dejiao, and D. Richardson, "Control of Material Transport Through Pulse Shape Manipulation: A Development Toward Designer Pulses," Selected Topics in Quantum Electronics, IEEE Vol. **20**, 51-63 (2014).
4. **P. S. Teh**, R. J. Lewis, S.-u. Alam, and D. J. Richardson, "200 W Diffraction limited, single-polarization, all-fiber picosecond MOPA," Opt. Express **21**, 25883-25889 (2013).
5. D. Lin, S.-u. Alam, **P. S. Teh**, K. K. Chen, and D. J. Richardson, "Selective excitation of multiple Raman Stokes wavelengths (green-yellow-red) using shaped multi-step pulses from an all-fiber PM MOPA," Opt. Express **19**, 2085-2092 (2011).
6. D. Lin, S.-u. Alam, **P. S. Teh**, K. K. Chen, and D. J. Richardson, "Tunable synchronously-pumped fiber Raman laser in the visible and near-infrared exploiting MOPA-generated rectangular pump pulses," Optics Letters **36**, 2050-2052 (2011)

Conference contributions related to this thesis

1. **T. Peh Siong**, S. U. Alam, C. Ho-Yin, D. P. Shepherd, and D. J. Richardson, "Generation of transform-limited picosecond pulses at 1.0um from a gain switched semiconductor laser diode," in *Photonics (ICP), 2013 IEEE 4th International Conference on Photonics, Melaka, Malaysia* (2013), pp. 240-243.
2. **P. S. Teh**, H.-Y. Chan, R. J. Lewis, S.-u. Alam, D. P. Shepherd, and D. J. Richardson, "200W Gain-Switched-Diode-Seeded, Single-Polarization, Narrow-Linewidth, All-Fiber, Picosecond MOPA," in *CLEO: 2013*(Optical Society of America, San Jose, California, 2013), p. CW3M.2.

3. S. Alam, L. Dejiao, **T. Peh Siong**, C. Kang Kang, and D. J. Richardson, "A fiber based synchronously pumped tunable Raman laser in the NIR," in *Lasers and Electro-Optics Europe (CLEO EUROPE/EQEC), 2011 Conference on and 12th European Quantum Electronics Conference*(2011), pp. 1-1.

Other publications

1. F. Kienle, S.-u. Alam, **P. S. Teh**, D. Lin, J. H. V. Price, D. C. Hanna, D. J. Richardson, and D. P. Shepherd, "High power high repetition rate picosecond optical parametric oscillator pumped by frequency doubled all-fiber Yb-doped MOPA," In SPIE Photonics Europe, pp. 843302-843302. International Society for Optics and Photonics, 2012.
2. F. Kienle, **P. S. Teh**, D. Lin, S.-u. Alam, J. H. V. Price, D. C. Hanna, D. J. Richardson, and D. P. Shepherd, "High-power, high repetition-rate, green-pumped, picosecond LBO optical parametric oscillator," Opt. Express **20**, 7008-7014 (2012).
3. S. Jindan, F. Xian, P. Horak, C. Kangkang, **T. Peh Siong**, S. Alam, W. H. Loh, D. J. Richardson, and M. Ibsen, "1.06 μm Picosecond Pulsed, Normal Dispersion Pumping for Generating Efficient Broadband Infrared Supercontinuum in Meter-Length Single-Mode Tellurite Holey Fiber With High Raman Gain Coefficient," Lightwave Technology, Journal of **29**, 3461-3469 (2011).
4. X. Feng, J. Shi, C.-C. Huang, P. Horak, **P. S. Teh**, S.-u. Alam, M. Ibsen, and W. H. Loh, "Laser-induced crystalline optical waveguide in glass fiber format," Opt. Express **20**, B85-B93 (2012).
5. Y. Jung, Q. Kang, V. A. J. M. Sleiffer, B. Inan, M. Kuschnerov, V. Veljanovski, B. Corbett, R. Winfield, Z. Li, **P. S. Teh**, A. Dhar, J. Sahu, F. Poletti, S. U. Alam, and D. J. Richardson, "Three mode Er3+ ring-doped fiber amplifier for mode-division multiplexed transmission," Opt. Express **21**, 10383-10392 (2013).
6. Z. Li, A. M. Heidt, **P. S. Teh**, M. Berendt, J. K. Sahu, R. Phelan, B. Kelly, S. U. Alam, and D. J. Richardson, "High-energy diode-seeded nanosecond 2μm fiber MOPA systems incorporating active pulse shaping," Optics Letters **39**, 1569-1572 (2014).